INFORMATION TO USERS

This manuscript has been reproduced from the microfilm master. UMI films the text directly from the original or copy submitted. Thus, some thesis and dissertation copies are in typewriter face, while others may be from any type of computer printer.

The quality of this reproduction is dependent upon the quality of the copy submitted. Broken or indistinct print, colored or poor quality illustrations and photographs, print bleedthrough, substandard margins, and improper alignment can adversely affect reproduction.

In the unlikely event that the author did not send UMI a complete manuscript and there are missing pages, these will be noted. Also, if unauthorized copyright material had to be removed, a note will indicate the deletion.

Oversize materials (e.g., maps, drawings, charts) are reproduced by sectioning the original, beginning at the upper left-hand corner and continuing from left to right in equal sections with small overlaps.

Photographs included in the original manuscript have been reproduced xerographically in this copy. Higher quality 6" x 9" black and white photographic prints are available for any photographs or illustrations appearing in this copy for an additional charge. Contact UMI directly to order.

ProQuest Information and Learning
300 North Zeeb Road, Ann Arbor, MI 48106-1346 USA
800-521-0600

UMI®

CHARACTERIZATION OF Ti-6%Al-4%V/TiC PARTICULATE REINFORCED METAL MATRIX COMPOSITES CONSOLIDATED BY SINTERING AND THERMOMECHANICAL PROCESSING

by

Priti Wanjara

Department of Mining and Metallurgical Engineering
McGill University
Montreal, Canada

A Thesis Submitted to the
Faculty of Graduate Studies and Research
in partial fulfillment of the requirements for the degree of
Doctor of Philosophy

November, 1999

0-612-64690-4

To my parents for making it all possible, to my sister, Mona, for her everlasting friendship and to my husband, Jitendra, for his unfailing love and encouragement.

ABSTRACT

TiC reinforcement particles were incorporated into a Ti-6%Al-4%V matrix and processed by two powder metallurgy techniques, namely elevated temperature pressureless sintering and hot deformation-assisted sintering (also known as hot pressing). For these composites, processing by sintering alone necessitated high temperatures (> 1500°C) for near-complete density consolidation, whilst the conditions for temperature and hold time were reduced (*i.e.* 1000°C and ½ hour) through deformation-assisted sintering. During high temperature processing in the absence of deformation, considerable coarsening of the lamellar matrix microstructure occurred. The interfacial reaction between the reinforcement and matrix was characterized by *in situ* neutron diffraction sintering studies at temperatures between 1100°C and 1350°C. Initial reaction occurred by carbon diffusion from the TiC particle to the titanium alloy, as evidenced through the increase in the lattice parameter of the matrix phase with holding time at the various sintering temperatures. Beyond the carbon solubility limit of the matrix phase, a stable stoichiometric phase formed as shown by the appearance of distinct peaks in the neutron diffraction patterns. Room temperature lattice parameter measurement gave a value of 4.290 Å with a fractional occupancy of carbon of 0.45 ± 0.04, which corresponds to a stoichiometry of Ti_2C. For the various isothermal sintering temperatures, change in the Ti_2C volume fraction with hold time was determined and growth of this interfacial phase was reasoned to occur by carbon diffusion from the TiC particles, through the reaction zone and to the Ti-6%Al-4%V alloy. Transformation of the entire TiC particle to Ti_2C occurred in the composites sintered at 1500°C. For the composites processed by sintering only, the mechanical properties determined by shear punch testing indicated that the strength and ductility are limited at low temperature sintering because of high porosity, and at high temperature sintering because of the interfacial phase. To improve the properties, the composites need to be processed to high densities at low temperatures using deformation-assisted sintering. The interfacial layer thickness in the deformed composites processed to near-complete densities at temperatures between 1000°C and 1200°C was less than 0.3 μm. Moreover microstructural modification of the initial lamellar structure was possible and a refined bimodal microstructure (5 μm alpha plate size) was obtained in the composites deformed just below the beta transus temperature (~1017°C). A combination of low porosity, small interfacial reaction thickness, and microstructural refinement increased the strength and ductility close to that typical of these composites. Subsequent heat treatment of these composites at 1100°C rapidly increased the interfacial reaction layer and degraded the mechanical properties. Hence further processing to increase the density should involve low temperature mechanical working techniques to minimize additional interaction of the matrix and reinforcement and maximize the properties of the composite.

RÉSUMÉ

Des particules de renforcement en carbure de titane (TiC) ont été incorporées dans un alliage Ti-6%Al-4%V par deux techniques de métallurgie des poudres, par frittage sans pression à haute température et par frittage sous déformation (ou pressage à chaud). Pour les composites obtenus par frittage seul, une température très élevée (>1500°C) est nécessaire pour obtenir une densification quasi-complète, alors que les conditions de température et de temps sont réduites (1000°C, ½ heure) pour le pressage à chaud. Au cours du frittage à haute température sans déformation, il se produit un grossissement important de la microstructure lamellaire de la matrice. La réaction interfaciale entre les particules de renforcement et la matrice a été caractérisée par diffraction de neutrons *in-situ* en cours de frittage entre 1100°C et 1350°C. La réaction se produit initialement par diffusion du carbone des particules de TiC vers l'alliage de titane, ce qui se traduit par l'accroissement du paramètre de maille de la matrice en fonction du temps de maintien. Au-delà de la limite de solubilité du carbone dans la matrice une phase stœchiométrique stable génère de nouveaux pics dans le diagramme de diffraction de neutrons. La mesure du paramètre de maille à la température ambiante donne une valeur de 4,290Å avec un taux d'occupation du carbone de 0,45 ± 0,04, ce qui correspond à la stœchiométrie Ti_2C. On a mesuré la fraction volumique de la phase Ti_2C en fonction du temps de maintien aux différentes températures de frittage, on en a déduit que la croissance de Ti_2C s'effectuait par diffusion de carbone des particules vers l'alliage de titane au travers d'une zone de réaction. La phase TiC disparaît complètement au profit de Ti_2C pour les composites frittés à 1500°C. Les propriétés mécaniques mesurées par des tests de poinçonnement montrent que, pour les composites obtenus par frittage seul, la porosité importante limite la résistance et la ductilité à basse température, pour les composites frittés aux températures élevées la phase interfaciale en est responsable. Afin d'améliorer leurs propriétés mécaniques, les composites doivent être densifiés à basse température par frittage sous contrainte. L'épaisseur de la couche interfaciale dans les composites presque totalement densifiés sous pression entre 1000°C et 1200°C est inférieure à 0,3μm. Par ailleurs, il possible de modifier la microstructure de la structure lamellaire, une structure bimodale affinée (lamelles α de 5 μm) a été obtenue pour des composites déformés juste au dessous de la température du *transus* beta (~1017°C). Une combinaison entre une faible porosité, une faible épaisseur de la zone de réaction interfaciale et un affinement microstructural augmente la résistance et la ductilité à des valeurs voisines de celles typiques pour ces composites. Au cours d'un traitement ultérieur du matériau à 1100°C l'épaisseur de la couche de réaction interfaciale augmente rapidement et les propriétés mécaniques se dégradent. Les procédés ultérieurs de densification devraient donc faire intervenir des techniques de déformation plastique à basse température pour minimiser les réactions entre la matrice et les particules et optimiser les propriétés du composite.

ACKNOWLEDGEMENTS

Few people are able to successfully complete the research required for a doctoral thesis without the support and commitment from advisors, family and friends. I certainly am no exception for along this challenging journey many individuals aided me directly or indirectly. As I write this, I wonder how a simple acknowledgement will do them any justice.

To begin, I express my sincere gratitude to my thesis supervisors, Professors Steve Yue and Robin A.L. Drew, for their guidance, patience and encouragement. They have provided me with numerous opportunities to participate in conferences worldwide to strengthen my knowledge of materials science. Their dedication to scientific inquiry and enthusiasm for physical metallurgy will remain an inspiration to me.

I am also grateful to Professor John J. Jonas for providing me the opportunity to use the CSIRA Steel Processing Laboratory. I am appreciative to Dr. John Root and the research staff at Atomic Energy of Canada Limited (Chalk River Laboratories) for access to the neutron diffraction facilities and their technical support. I would also like to acknowledge the assistance of Yves Giroux and John Cole of Hitachi Canada for providing access to the S-4500 field emission gun scanning electron microscope.

Considering the working environment, the support staff is instrumental in solving administrative and research difficulties. I extend my appreciation to the administrative personnel in general, but in particular to Lorraine Mello and Vicki Pedicelli for also providing a pleasant and friendly atmosphere. I am also grateful for the advice and laboratory assistance of Terry Maccagno, Edwin Fernandez, Helen Campbell, Glenn Poirier and Ray Langlois.

I have many fond memories of my association with the CSIRA Steel Processing Laboratory, the Ceramics and Composites Processing Laboratory and the McGill Metals Processing Centre. I am privileged to call all the students, both past and present, working there my friends. Their association added immeasurably to the quality of my education, either through their invaluable suggestions and support or through our various social gatherings.

On a personal level, the unceasing love, encouragement and support provided by my parents and sister, Mona, throughout the years has enabled me to realize my greatest aspirations. Words fail to describe their compassion and enormous sacrifices during the years of intensive effort of my studies. My husband, Jitendra, has enlightened my perception of life and strengthened my belief that anything is possible. His unconditional love, understanding, and patience have comforted me through many rough moments.

Last, but not least, the financial support received through the Natural Science and Engineering Research Council of Canada, les Fonds pour la Formation des Chercheurs et l'Aide à la Recherche and the McGill Metals Processing Centre is greatly appreciated.

TABLE OF CONTENTS

LIST OF FIGURES

Chapter 2

Chapter 4

Chapter 5

Chapter 6

Chapter 7

Chapter 8

Appendix III

LIST OF TABLES

Chapter 2

Chapter 4

Chapter 6

Chapter 7

Chapter 8

Appendix III

CHAPTER 1

INTRODUCTION

The advancement of science and technology has required materials with ever-increasing performance characteristics, which may be specified by various criteria including reduced weight, lower cost, and higher strength and stiffness. In an effort to improve the physical and mechanical properties, materials scientists and engineers are striving to either modify existing materials or develop novel materials. Exemplary of this latter category are *composite materials*, as these have been developed by combining two or more distinct phases to form a system having properties, not only markedly different from the constituent properties, but also ingeniously tailored for the specific application.[1]

Historically, composites have existed since ancient civilizations (*e.g.* adobe bricks and wood).[2] However, a composite, in the present context, will be restricted to material synthetically fabricated from chemically dissimilar phases that are separated by a distinct interface. Heightened interest in composites has occurred in the last few decades in which these have been designed for various engineering applications by incorporating *reinforcing* phases within a *matrix* phase.[3] The matrix, a continuous phase in the composite, is frequently present in a greater quantity and its properties are improved by incorporating the second constituent, the reinforcement or reinforcing phase.

One simple scheme for the classification of composites is to separate the matrix and reinforcing phase constituents, and divide them into several groups. The first classification is based on the type of the matrix constituent: Polymer Matrix Composite, Metal Matrix Composite or Ceramic Matrix Composite. Composites can also be classified based on the type of reinforcement used: fiber reinforced (continuous or discontinuous) or particulate reinforced (flakes, chopped fibers, shaped particles, and whiskers).

Polymeric matrices are mainly based on thermosetting and thermoplastic polymers.[4] Thermosets (*e.g.* epoxy and phenolic) undergo a soft plastic stage only once and then harden irreversibly whereas thermoplastics (*e.g.* polyethylene, nylon, and acetyl) can be repeatedly heated, fabricated and cooled. Polymeric composites are currently used in a variety of applications including primary and secondary load bearing structures, tubing, electronic packaging, as well as automobile and aircraft components. Criteria for selection of polymeric composites include aspects of weight, impact resistance, strength and stiffness, ease of manufacturing and flexibility, flammability requirements and corrosion resistance. The main disadvantages of these composites are their low maximum working temperature, high thermal expansion coefficient and sensitivity to moisture.

Metallic composites usually have a lightweight matrix of an alloy of aluminium, magnesium, or titanium, and, where weight is not a critical parameter, alloys of nickel, copper, cobalt, silver and zinc have also been used.[5]. Generally, metallic composites possess high specific strength and stiffness (*i.e.* strength or modulus divided by density), good wear resistance and fatigue strength, high electrical and thermal conductivities, as well as higher operating temperature capabilities than polymeric composites. On account of these attributes, metallic-based composites are being considered as substitutes for conventional alloys especially in automotive and aerospace components.

Although light weight (combined with increased strength and stiffness) is often the driving force for the development of polymeric and metallic composites, ceramic-based composites are selected or developed because of their potential for high temperature applications.[6] Ceramic matrices include various oxides (*e.g.* stabilized zirconia and alumina), nitrides (*e.g.* boron nitride and aluminium nitride), carbides (*e.g.* silicon carbide and tungsten carbide), as well as glasses (*e.g.* borosilicates) and glass-ceramics (*e.g.* lithium and magnesium aluminosilicates). Typically, ductile or ceramic reinforcements in the shape of particles, whiskers and fibers are incorporated to improve the rather poor fracture toughness and fracture strength of the matrix phase. Difficulties facing the development and application of these composites are related to their processing requirements.

Selection of the reinforcement material and type is a function of the matrix constituent, the properties required of the composite and the processing route.[7-8] Common reinforcement materials include carbides (*e.g.* silicon carbide and titanium carbide), nitrides (*e.g.* silicon nitride and aluminium nitride), oxides (*e.g.* alumina and silica), glass fibers as well as elemental materials (*e.g.* boron, carbon, tungsten, and silicon). Also, fibers of silica glasses (*e.g.* E-glass or S-glass) are the most common reinforcements for polymeric composites. Incorporation of these reinforcing phases (in volume fractions of 5 to 50%) into the matrix phase improves the performance of the composite system. The main parameters in determining the effectiveness of the reinforcement are its shape, size, distribution and orientation. In general, fiber reinforcements offer a higher potential for improvement in the mechanical properties than particulate reinforcing phases.[9-10] However, stemming from the difficulty in fabricating fibers and incorporating these into the matrix phase during processing, particulate reinforcements are preferred for applications not requiring extreme loading or thermal conditions.

This represents the current status of composite science and technology in which research and development has enabled the processing of a range of composite systems.[11] While polymeric composites have experienced expansive use,[12] metallic and ceramic composites still remain subject to research and development efforts to resolve processing and performance difficulties.[13] For metallic composites, the most important driving force has been the aerospace industry, as great expectations have been placed on these materials as weight reducing engineering solutions.[14] Hence, the central theme to metallic-based composite development has been light weight and enhanced properties. Though metallic composites have exhibited many advantages and improved properties, the processing costs still represent barriers to more widespread application of these materials.[15] Such barriers are particularly significant as these composites now progress from relatively low volume, high cost applications in aerospace technology to high volume, low cost applications in the automotive and consumer goods industries.[16-17]

Early activities related to metallic composites focused on the development and behavior of continuous fiber reinforced materials based on aluminium and titanium matrices.[18-19] Despite their highly promising mechanical properties, these composites have been afforded only limited application due to shortcomings stemming from the cost of fiber fabrication, as well complex processing requirements in incorporating these into the matrix. Specifically the problems associated with the manufacturing of continuous fiber reinforced metal matrix composites (including fiber damage, microstructural non-uniformity, fiber-to-fiber contact, and extensive interfacial reactions) led to the development of discontinuously reinforced composites for applications not requiring the ultimate in performance.[7]

Discontinuously reinforced metallic composites have attracted attention in recent years as these can exhibit isotropic properties and are easier to process using standard processing methods, such as powder metallurgy. The availability of various reinforcement types at relatively low cost, and the existence of metal working technology for the processing of these composites, have also contributed to lower cost of the final component. Aluminium and its alloys as matrix materials have been the focus of much of the research and development effort on discontinuously reinforced composites.[20-22] Lower processing temperatures and compatibility with various reinforcements has enabled the advancement of aluminium-based composites to the stage of commercial production.[23] Alternatively, development of titanium-based composites has been delayed by processing problems stemming from the high reactivity of titanium with many reinforcements, as well as higher fabrication temperature requirements.[24] However, there are many potential applications for titanium composites in advanced engineering components, especially for high temperature operation where the properties of rival aluminium composites deteriorate.[25]

In this last decade, considerable development of the science and technology related to particulate reinforced titanium-based composites has been initiated.[26-30] An increased understanding of the high temperature consolidation behavior is required to assess the effect of the processing parameters on the interaction of matrix and reinforcement which forms the interface. Also, the influence of processing and, more specifically, that of the matrix microstructure and interface, on the mechanical properties of the composite material need to be assessed. This is the basis for the present work.

A literature review of the developments in the particulate reinforced titanium metal matrix composite field is given in *Chapter 2*. This chapter also includes the basic concepts and mechanisms involved in the processing of these materials using powder metallurgy technology. *Chapter 3* reviews the objectives of the present work. In *Chapter 4*, the experimental materials and methods are described. High temperature processing of the composites was performed by vacuum sintering and thermomechanical processing. Optical microscopy, scanning electron microscopy, electron probe micro-analysis and neutron diffractometry were used to characterize the matrix microstructure and interfacial reaction zone. Mechanical property assessment was accomplished using microhardness testing, hardness testing and shear punch testing techniques. The development of the shear punch testing technique for mechanical property assessment of discontinuously reinforced composites is presented in *Chapter 5*. The sintering results, given in *Chapter 6*, consist of the consolidation behavior, microstructural and interfacial characterization and mechanical property determination. The deformation behavior during thermomechanical processing and its influence on the microstructural and interfacial development, as well as the resulting mechanical properties are presented in *Chapter 7*. The results obtained in *Chapters 6 and 7* are discussed and rationalized in *Chapter 8*. Finally, conclusions and recommendations for future work are given in *Chapter 9*.

CHAPTER 2

LITERATURE REVIEW

Particulate reinforced composites based on titanium metal and alloys are considered as potential replacements for conventional materials used in various applications including wear parts such as gears, shafts and bearings, erosion-corrosion resistant tubing and creep/fatigue resistant engine components. The main limitation to the development of titanium-based composites is the high reactivity of titanium, which adversely affects the stability of many reinforcing materials and results in the formation of reaction products at the interface region. The extent of reaction and the nature of bonding between the reinforcement and matrix determine the load transfer capability and crack resistance of the composite.[31-33] Generally, this reaction zone between the matrix and the reinforcement is considered to be a weak region.[34] Also, the relative degradation in the properties of the composite usually increases as the thickness of the interfacial reaction zone increases.[35] An explanation for this degradation is that the reaction zone acts as a circumferential flaw on the reinforcement, which weakens the reinforcing material and, thus, the composite. Alternatively, the reaction zone may act to degrade the intrinsic strength of the reinforcement by forming stress concentrations or causing debonding.

The degradation in the mechanical and physical[36] properties of the composite, due to the interfacial reaction, has necessitated characterization of the nature of the reaction products formed, as well as minimization or optimization of the extent of reaction between the matrix and reinforcement in the interface region.[37] Essentially, there have been three basic approaches to solving the interfacial reaction problem in titanium-based composite systems: (1) to modify the matrix by alloying with (a) slower diffusing elements that reduce the reactivity of titanium and thereby reduce the reaction zone thickness directly or (b) with elements that decrease the melting temperature, and thus reduce the reaction layer thickness indirectly by lowering the fabrication temperature; (2) to select or develop chemically stable reinforcements; and (3) to develop lower temperature processing techniques that minimize the reaction zone.

Research on the effects of alloying on reducing the reactivity of titanium was performed in the late 1960s and early 1970s.[38] Additionally, considerable work has been performed to alloy the titanium matrix so as to produce a material that can be processed at a lower temperature. Techniques include alloying to achieve grain size refinement and stability for superplastic forming,[39-40] using hydrogen as a temporary alloying element during processing[41-43] and alloying with beta-stabilizers to form metastable beta-compositions.[44-45] However, Ti-6%Al-4%V remains the most readily available and most widely applied titanium alloy in industry. Thus, the current work will be directed towards employing this material as the matrix phase in the composite system to be developed. As such, this chapter will be divided into three sections: (1) an overview of the Ti-6%Al-4%V matrix alloy, (2) a selection of a suitable reinforcement material and (3) a review of the processing techniques applicable to titanium-based composites.

2.1 Ti-6%Al-4%V Matrix Characteristics

Elemental titanium undergoes an allotropic transformation from hexagonal closed-packed (hcp) α to body-centered cubic (bcc) β at a temperature of 882°C.[46] Elements which when dissolved in titanium produce little change in the transformation temperature or cause it to increase (*e.g.* aluminium, carbon and oxygen) are known as alpha-stabilizers, while alloying additions which decrease the phase-transformation temperature (*e.g.* vanadium) are referred to as beta-stabilizers.[47] In two-phase alloys, the single-phase α and single-phase β regions are separated by a two-phase α+β region, the width of which increases with increasing solute concentration. In general, alloys of titanium are classified as 'α', 'α+β' or 'β'. The 'α+β' alloys have compositions containing mixtures of both α and β stabilizers, and thus a mixture of α and β phases are present in equilibrium at room temperature.

The simplest α+β alloy is Ti-6%Al-4%V (the composition is in weight percent). The addition of aluminium stabilizes the α phase to higher temperatures while vanadium stabilizes the β phase to lower temperatures. For Ti-6%Al-4%V, the transformation temperature from the single-phase β region to the α+β phase region, referred to as the β-transus temperature, is approximately 988°C ± 10°C,[48] as observed from the section of the pseudo-binary Ti-6Al-V phase diagram shown in Figure 2.1.[49]

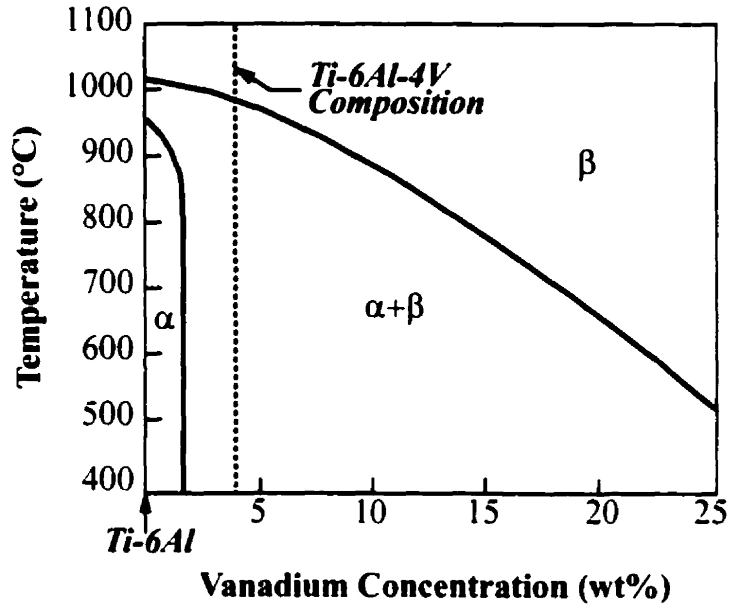

Figure 2.1 Schematic phase diagram of (Ti-6Al)-V.[49]

For the Ti-6%Al-4%V alloy, there are two basic morphological types of room temperature microstructures, lamellar and equiaxed. The lamellar structure forms upon heating to above the β-transus temperature and cooling into the α+β phase region. Slow cooling (*e.g.* furnace cooling) leads to the nucleation and growth of the α phase in plate form at prior β grain boundaries. The resulting lamellar structure consists of plate-like α separated by very thin layers of β. The cooling rate from above the β-transus temperature greatly affects the size of the lamellae. In general, the prior β grain size controls the length of the lamellae, while their width is diffusion controlled and can be refined by increasing the cooling rate.[50] Higher cooling rates (*e.g.* air or water cooling) result in a finer α phase and the microstructure is referred to as acicular, Widmanstätten or basket-weave depending on the exact appearance of the lamellae. Alternatively, the equiaxed structure can only be formed by work hardening the lamellar structure (by plastic deforming in the α+β phase field at either ambient or elevated temperatures) and then recrystallizing the microstructure. Break-up of the β grains during the deformation stage enables the α phase to nucleate and grow at sites other than the prior β grain boundaries during recrystallization.[51-53] Hence, by manipulating the heat treatment and thermomechanical processing parameters, a variety of microstructures based on the lamellar and equiaxed morphologies can be formed. Moreover, the morphology of the α phase must be tailored judiciously, as the microstructure significantly influences the properties of the material; for example equiaxed microstructures have higher tensile ductility and are resistant to fatigue crack initiation, whereas lamellar microstructures have superior crack propagation resistance.

In general, Ti-6%Al-4%V possesses excellent corrosion resistance, high specific strength, good fatigue resistance and moderate fracture toughness values.[54] However, the low elastic modulus, poor wear resistance and low hardness of Ti-6%Al-4%V limit the service life of this material at elevated temperatures and in tribological applications. To improve these properties, particulate reinforcement can be employed to combine the rigidity, wear resistance and high hardness of a ceramic phase with the ductility, machinability, specific strength and corrosion resistance of Ti-6%Al-4%V.

2.2 Reinforcement Selection

The selection criteria for ceramic reinforcements include[7,33]

(1) Superiority in mechanical properties such as rigidity (*i.e.* high elastic modulus), high yield and tensile strengths and high hardness.

(2) Superiority in physical properties such as high melting temperature, low density and high thermal conductivity.

(3) Thermodynamic stability in titanium alloys at the temperatures required for consolidation and secondary processing.

(4) Small difference in the coefficient of thermal expansion between the reinforcement particle and the titanium alloy.

(5) Containing elements that have a low solubility in the titanium alloy matrix at the processing temperatures.

(6) Strong bonding between the reinforcement and matrix with a uniform thin reaction zone.

The reinforcement-matrix interfacial interaction remains an outstanding problem in metallic composite systems, but is particularly difficult for titanium-based matrices, on account of the reactivity of these materials. In the case of fiber reinforced composites, chemical stability of various fibers in titanium-based matrices may be achieved by adjusting the surface composition through the use of multiple-layer coatings having a reduced reactivity, which thereby enables the correct degree of compatibility to be attained in the matrix during processing.[55] On account of the smaller dimensions (*i.e.* smaller aspect ratio and diameter) of particulate reinforcements, such reactivity problems are magnified for the latter and are often very difficult to avoid (*i.e.* stable barrier layers are difficult to produce on particles).[8,56] As such chemical interactions between the matrix and reinforcement usually have deleterious effects on the properties of the composite, selection of the appropriate discontinuous reinforcement is critical, more so than in the case of continuous fibers.

Considering the above criteria, the range of reinforcing materials available which have suitable properties that would make them useful additions to titanium-based matrices is short. For example, the rare earth oxides are stable in titanium and can be incorporated into the matrix using a rapid solidification route or powder metallurgy processing.[57-58] However, the mechanical properties of these oxides are such that the potential for improvement in the elastic modulus, wear resistance and hardness of titanium-based materials is small, especially at the low volume fractions (*i.e.* 10-20 vol.%) commonly utilized in particulate reinforced titanium matrix composites.

Recent studies have examined various ceramic phases, including Al_2O_3,[59-60] SiC,[61-64] Si_3N_4,[65-68] B_4C,[69-70] TiB_2,[71-73] TiB,[74-81] TiN,[82] TiAl,[83-84] BN[85] and TiC[86-89] as reinforcement materials in titanium alloy matrices. Table 2.1 summarizes the observations for various candidate reinforcement materials.[90-92]

With regard to mechanical property improvement, B_4C and SiC offer the greatest potential by virtue of their high specific strength and stiffness. However, the lower coefficient of thermal expansion of these reinforcements, as compared to that of most titanium alloys, which is approximately 9 x 10^{-6} K^{-1}, results in a high thermal mismatch and generates internal stresses which degrade the properties of the composite. In addition, B_4C particulates react with titanium-based matrices to form a region of TiB and TiC phases with TiB needles growing into the matrix.[69-70] In the case of SiC particulates, the reaction products that have been observed for Ti-SiC interfaces depend on the temperature of exposure during processing. At temperatures below 850°C, TiC is the only reaction product observed.[71] At higher temperatures, the extent of reaction with the titanium matrix is greater and a complex multiple-layer reaction zone of various interfacial products, including TiC and Ti_5Si_3, forms.[93-94] Accompanying the formation of these reaction products is a large decrease in volume (*i.e.* -4.6%), which generates radial tensile stresses at the interface. These oppose the differential thermal contraction stresses, and tend to cause interfacial cracking and further degradation of the room and elevated temperature properties of the composite.[71] Examination of the reaction kinetics of the Ti and SiC system has shown that the formation of the interfacial constituents is diffusion controlled.[61] Hence, by decreasing the exposure time at the compaction temperature using, for example, shock processing technology or solid state pressure assisted methods (*e.g.* forging or hot pressing), the interfacial reaction products in SiC particulate reinforced titanium composites can be minimized.[95]

Table 2.1 - Compatibility of reinforcement particles for titanium matrix composites

Particle	Knoop Hardness (GPa)	Elastic Modulus (GPa)	Density (g/cm^3)	Coefficient of Linear Expansion (1×10^{-6} K^{-1})	Maximum Solubility Matrix (at.%)	Particle (at.%)	Nature of interfacial bond and property assessment
TiB	28	550	4.57	8.6	0.001	1.0	Very good
TiB_2	15-45	530	4.53	8.1	Unstable in Ti alloys		Failure
TiC	28-35	462	4.92	7.4-8.6	1.8	15.0	Very good
B_4C	27	449	2.51	4.5	Unstable in Ti alloys		Failure
SiC	25	414	3.21	4.3	Unstable in Ti alloys		Poor
TiN	16-20	251	5.43	8.0	22.0	26.0	Failure
Si_3N_4	8-19	304	3.20	3.0	Unstable in Ti alloys		Failure
BN	2[a]	85	2.25	7.5	Unstable in Ti alloys		Failure
AlN	12	340	3.30	5.6	Unstable in Ti alloys		Failure
TiAl	3	176	3.91	-	Unstable in Ti alloys		Failure
Al_2O_3	18-23	380	3.97	8.1	Unstable in Ti alloys		Failure

[a] Mohs scale

Amid the remaining reinforcements, TiB_2 has attracted recent interest for improving the thermal properties of titanium alloys.[69-71] Results indicate that TiB_2 would be preferable to SiC as a reinforcement in titanium for situations where high thermal conductivities would be beneficial. The slower reaction rate kinetics (as compared to SiC and B_4C) between the TiB_2 reinforcement and the titanium matrix forms a thinner interfacial layer of TiB, which does not mechanically weaken the interface to the same degree as that in the Ti-SiC system.[72] This may be at least partly a consequence of the much lower volume change (*i.e.* decrease of 1.4%) accompanying the formation of the TiB reaction product.[71-72] However, the morphology of the TiB is needle-like in form, and local microcracking, porosity and general damage in the vicinity of the interface weakens the composite and leads to premature failure.[73] Recent research with titanium aluminides indicates that the reaction kinetics of this interface, and thus the thickness of TiB reaction product, decreases with increasing aluminium content such that in Ti-47Al, TiB_2 has been reported to remain stable at 1200°C for 7 days.[96] Moreover reinforcement of titanium aluminides, with low volume fractions of TiB_2, has resulted in improved elevated temperature workability, higher strength and improved toughness through grain refinement of the matrix alloy.[97-98]

From the selected list of reinforcement materials given in Table 2.1, the monoboride and monocarbide of titanium may then be the most appropriate reinforcing choices on account of their compatibility with titanium-based matrices.[99] In particular, both TiB and TiC particles exhibit limited solubility in titanium alloys during processing and service, as indicated in Table 2.1.

Recently, TiB particulate reinforced titanium composites have been fabricated using blended elemental powder metallurgy technology: the matrix and boron source powders (*e.g.* boron powder or TiB_2) were mixed, compacted isostatically and consolidated by sintering in a vacuum furnace at 1300°C for 2-100 hours.[100-101] During consolidation the boron source powders dissolve and react with titanium to form uniformly dispersed TiB platelets in the matrix. Following vacuum sintering, the composites are either hot isostatically pressed at 900°C for 3-4 hours or hot worked and heat treated to maximize the properties of the TiB reinforced titanium-based material.[102] The work of Saito et al. has shown that interaction between the TiB platelets and the titanium alloy matrix is minimal on account of the low solubility of boron in titanium.[101] The resulting TiB-titanium alloy interface boundary revealed good crystallographic coherency and no obvious reaction products.[76,103] A microstructural shortcoming of this composite system is the needle-like morphology of the TiB reinforcement phase which, albeit the higher strength potential (*i.e.* short fiber reinforcement), gives a low ductility.[104] Recent work by Fan et al. has shown that rapid solidification processing of Ti-TiB composites can be used to modify the TiB morphology to nearly equiaxed particulates, which was found to improve the mechanical properties.[105]

Nonetheless, processing of the TiB reinforced titanium composite system is dependent on using the blended elemental powder metallurgy approach, as titanium monoboride reinforcement particles cannot be fabricated. Although the use of elemental powders enables enhanced pressing properties, slow interdiffusion during densification may require high consolidation temperatures and long sintering times to aid diffusion of the alloying elements and achieve homogenization of the matrix alloy.[106-107] Moreover, the inherently low solubility of boron in titanium may augment the processing difficulties further, as sufficient processing times are necessary to complete the chemical reaction between the reinforcement phase and the titanium matrix, so as to produce the TiB platelets.[108] This necessity for long sintering times at elevated processing temperatures may reduce or even countervail the cost benefits of using lower cost elemental powders, as opposed to pre-alloyed powders (as discussed further in the next section).

Titanium carbide has been investigated as a reinforcement phase for titanium-based composite materials because of its good thermodynamic compatibility with matrix alloys and commercial availability in the form of high quality powder particulates. Also, the physical and elastic properties of TiC suggest that it could be promising as a reinforcement phase in titanium composites. TiC has an elastic modulus (460 GPa) more than four times that of titanium (110 GPa), a high hardness, a very high melting temperature (3100°C) and, although its density (4.9 g/cm^3) is slightly higher than that of titanium (4.5 g/cm^3), its coefficient of thermal expansion is within 50% that of titanium and their Poisson's ratios are similar.[109a]

The interfacial reaction between titanium-based matrices and TiC reinforcement particles has been studied in previous works.[26,110] Microstructural investigation of the Ti-TiC interfacial region by optical and scanning electron microscopy techniques has shown no obvious reaction products at the interface between the matrix and reinforcement phases.[110] However, using transmission electron microscopy, a circular dislocation network was found on the periphery of the TiC reinforcement particles by Konitzer and Loretto.[110] Also, their electron diffraction analysis revealed that the lattice parameter of the TiC particle outside the dislocation network corresponded to carbon deficient TiC while that of the reinforcement particle core corresponded to stoichiometric TiC. In their study, chemical analysis by electron-energy loss spectroscopy (EELS) indicated that the carbon deficient TiC annulus has a composition of 33 at.% carbon, corresponding to a Ti:C ratio of 2 (*i.e.* Ti_2C). However, whether the entire carbon deficient annulus corresponds to a composition of Ti_2C remains uncertain. Furthermore, although a difference in lattice parameter has been measured between the two sides of the dislocation wall, the crystal structure of the carbon deficient annulus and TiC particle core was found to remain the same. Should only Ti_2C exist in the interfacial boundary area between the titanium matrix and TiC particles, abrupt changes in composition are expected in this region. However, quantitative analysis of the interfacial chemistry by Gu et al. has revealed a compositional gradient region for carbon between the titanium matrix and TiC particulate center.[111] Referring to the equilibrium carbon-titanium binary phase diagram,[112] as shown in Figure 2.2, these results suggest that a dissolution-type reaction occurs between the matrix and reinforcement particles, forming a continuous carbon deficient region between titanium and TiC. This phase diagram suggests that TiC would dissolve in a titanium matrix until either all the carbon is in solution or there is equilibrium between a saturated solution of carbon in titanium and some remaining TiC, which would then be non-stoichiometric (*i.e.* TiC_x).[113-114] That is, in the carbon-titanium binary system only one intermediate compound, TiC, is present and non-stoichiometric TiC_x varies in composition from 33 to 49 at.%, at room temperature. The existence of another ordered form for this carbide, Ti_2C, remains questionable, as most investigators could not distinguish this structure and little information is available on the stability range of this phase.[115-117]

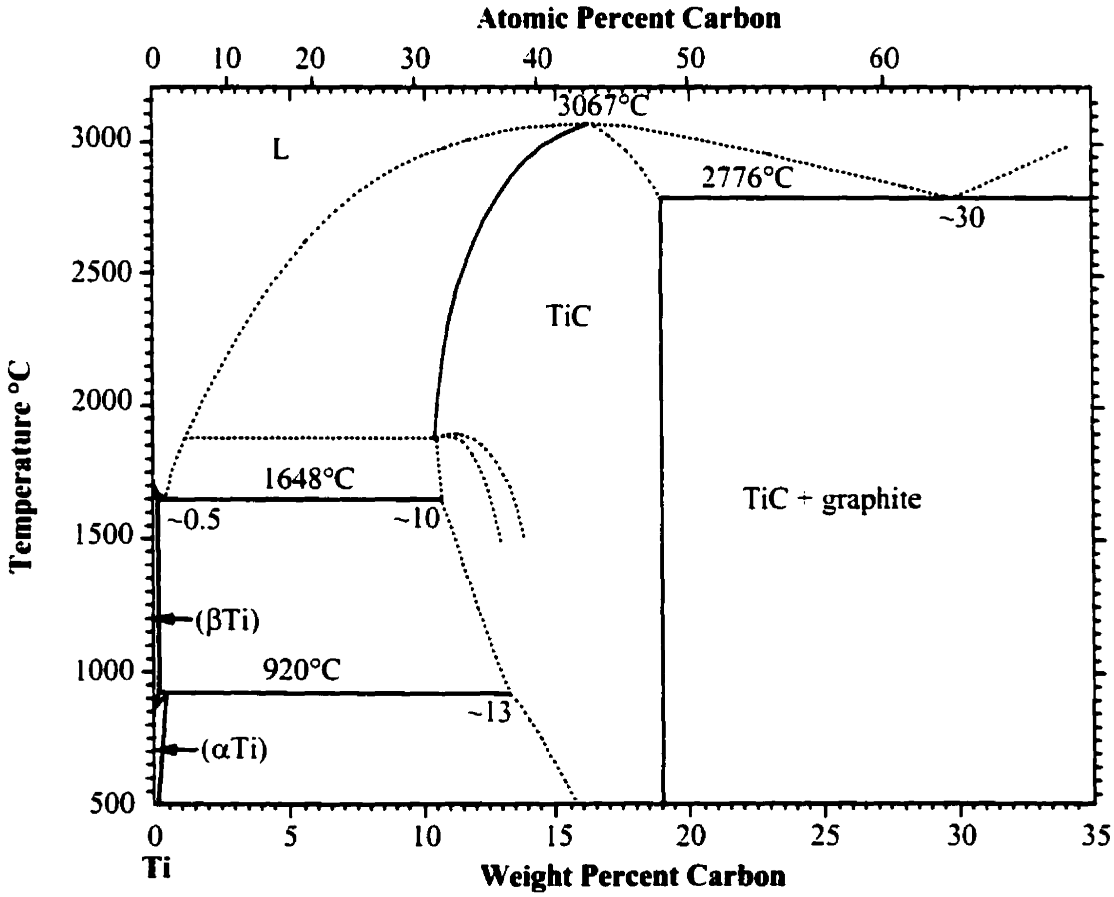

Figure 2.2 Titanium - carbon phase diagram.[112]

Apart from this uncertainty with regard to the chemical composition of the interfacial reaction product(s), previous work on the formation characteristics of the carbon deficient annulus have also been inconclusive.[110-111] The carbon deficient outer annulus in the TiC reinforcement phase may either be generated by the diffusion of carbon from the particles or by diffusion of titanium into the particles, or by interdiffusion of carbon and titanium between the matrix and reinforcement phases. Considering that the formation of a carbon deficient annulus occurs in the TiC particles by carbon dissolution into the surrounding titanium matrix, a maximum of 0.4 wt.% carbon would be present in the α-titanium matrix (or a maximum of 0.2 wt.% carbon in β-titanium above the β-transus temperature), according to Figure 2.2.[118-119] However, this low solubility of carbon in titanium limited detection using electron-energy-loss spectroscopy and energy dispersive x-ray spectroscopy.[110-111] Hu et al. have observed titanium precipitation in non-stoichiometric TiC particles during thermal processing of Ti-TiC composites and thus diffusion of titanium from the matrix into the TiC particles may also be a possible mechanism.[120-121] Moreover, on account of this uncertainty with regard to the diffusion direction and chemical characteristics of the interface region, the kinetics of the interfacial reaction between the titanium matrix and TiC reinforcement particles remain unknown.

Besides the uncertainties in the chemical composition and formation characteristics of the interfacial reaction region, there is a lack of microstructure-property relationships for the Ti-TiC composite system. It has been observed that the small coherent interaction zone (be it Ti_2C or non-stoichiometric TiC) that forms between the TiC reinforcement and the titanium matrix renders good high temperature strength properties.[122] Moreover, the reaction zone thickness in these composites was relatively small, as compared to SiC, B_4C or TiB_2 particulate reinforced titanium composites, which have a large interfacial layer extending deep into the matrix.[123] Hence, excellent bonding[123] between the matrix and TiC particles, as well as good wear resistance[124-126] and high strength and stiffness[127] have been reported for these composites. However, the as-fabricated TiC reinforced Ti-6%Al-4%V composite exhibited a room temperature fracture toughness of 18 MPa·m$^{1/2}$, nearly four times lower than the unreinforced matrix (*i.e.* 77 MPa·m$^{1/2}$).[128-129] Recent work by Liu et al. has indicated that, using a post-thermal annealing treatment to increase the amount of α phase in the matrix, improves the room temperature fracture toughness of this composite to 30 MPa·m$^{1/2}$.[130] Moreover, their work revealed that the fracture toughness is temperature dependent and consists of three regions: a low temperature region (*i.e.* below room temperature), where the fracture toughness increased with temperature; an intermediate temperature region (*i.e.* up to 400°C), where the fracture toughness remained constant at 30 MPa·m$^{1/2}$; and a high temperature region (*i.e.* above 400°C), where the fracture toughness decreased with temperature. The low and high temperature regions were associated with brittle fracture of the matrix and ductile stretching of the matrix, respectively. The intermediate temperature region was found to be a transitional zone, where the fracture mechanism gradually changed from cleavage to ductile failure. Moreover, an improved fatigue crack growth resistance was found in this intermediate temperature region due to extensive microcracking of the TiC reinforcement particles, which promoted fatigue crack closure.[131] However, the overall fatigue properties were found to be lower than the unreinforced matrix alloy either due to the microporosity in TiC particles or residual porosity associated with the TiC particle clusters in the matrix.[110] In addition, studies on the creep behavior of TiC reinforced Ti-6%Al-4%V composite has shown that the creep strain rate is an order of magnitude lower than the unreinforced titanium alloy.[132-133] Further improvement in both the high and low temperature properties may be possible by removing or modifying the deleterious microstructural features through secondary processing. In the following section, the processing techniques utilized for the TiC-Ti composite system are discussed.

2.3 Processing Techniques

Much of the research work on TiC particulate reinforced titanium-based composites has focused on developing a low-cost processing method using liquid- or solid-state techniques. Recent studies have examined producing Ti-TiC composites using a casting approach.[134-137] During casting, the single-crystal TiC particles that form *in situ* during cooling have a dendritic morphology. Although *in situ* formation of the TiC particles has been reported to have the advantage of a *clean* interface (*i.e.* without any interfacial reaction products),[138] the resulting coarse dendritic morphology of the reinforcement phase has been observed to degrade the fracture properties.[134] Refinement of the TiC dendrite colony structure by increasing the cooling rate was reported by Chen et al. to improve the strength and ductility properties of the Ti-TiC composite system.[28] Fine and uniformly distributed TiC particles can also be obtained by melt spinning. However, industrial application of melt spinning may be difficult for composite materials.[139] Rapid solidification,[124,140] gas atomization[139,141] and isothermal forging of cast Ti-TiC[142-143] composites have been successful in modifying the dendritic nature of the reinforcement particles. Recently, *in situ* formation of fine and uniformly dispersed TiC particles in titanium has also been achieved by a combustion-assisted synthesis process which involves conventional melting and casting in association with exothermic chemical reactions.[144-146] However, the greatest difficulty in using a liquid phase fabrication process, specifically in the case of titanium-based composite materials, is related to the high processing temperature requirements which augment reinforcement degradation and necessitate considerable circumspection to maintain melt cleanliness. Hence, processing work on particulate reinforced titanium-based composites has mainly involved solid-state techniques, particularly the use of powder metallurgy.

In the composites processed using powder metallurgy methods, the polycrystalline TiC particles have an equiaxed morphology. The size of the reinforcement particles in the composite material is usually dependent on the mean particle size of the original TiC powder, which is usually greater than 5 μm. Much of the research and developmental work in this field has focused on using blended elemental powder metallurgy technology. The pioneering work by Abkowitz involved incorporating TiC particulates into blended elemental and master-alloy powders.[147-150] The blended matrix and reinforcement powders were cold isostatically pressed to a preform shape, vacuum sintered to a closed porosity and containerless hot isostatically pressed to a full density. Recently, this technique has also been applied to form *in situ* TiC particles in titanium-based matrices by using carbon source powders (*e.g.* graphite, Cr_3C_2) instead of TiC powder.[151] One of the advantages of forming the TiC particulates *in situ* using powder metallurgy processing is that the size can be refined to the point that nanometer size reinforcements are possible using high pressure and high temperature processing conditions.[152] Also, the microporosity associated with polycrystalline TiC particles, which degrades the fracture properties, can be eliminated.

Although the processing temperature requirements for blended elemental powder metallurgy are not as severe as those for liquid-state techniques, long sintering times at temperatures in excess of 1200°C are necessary to achieve homogenization in the matrix phase.[153] These processing conditions have been reported to degrade the mechanical properties, particularly fatigue strength, as compared to pre-alloyed powder metallurgy and ingot metallurgy.[154] This is attributed to the microstructural formation of coarse lamellar colonies and a massive grain boundary α phase during processing.[155-156] In addition, the Hunter sodium process or Kroll magnesium reduction process used to produce the titanium sponge fines results in the presence of residual chloride salts in the titanium powder used in the blended elemental approach. This chloride contamination gives rise to residual porosity and leads to further degradation in the fatigue strength, even with chloride levels as low as 0.016 wt.%.[157-158] Moreover, residual chloride from the titanium sponge fines prevents the achievement of full density, even after secondary processing (*e.g.* hot isostatic pressing, hot working).[159-160] On account of this residual porosity, the size of blended elemental components is limited to the capability of the cold isostatic pressing method; the fabrication of large parts by welding smaller parts is difficult because the porosity causes severe sputtering during welding, leading to a highly porous weld zone.[161]

Recently, a low chloride (*i.e.* less than 0.001 wt.%) titanium powder produced by the hydride-dehydride process has become available and full density processing can be achieved by combining cold and hot isostatic pressing of blended elemental material.[54] It is anticipated that this hydride-dehydride powder will have mechanical properties and welding characteristics similar to that of titanium material produced by ingot metallurgy.[54] As compared to the titanium sponge fines, hydride-dehydride titanium powder is more than twice as expensive,[54] and the processing of this powder using the blended elemental approach still involves relatively high temperatures and long sintering times to homogenize the matrix alloy chemistry. Moreover, secondary processing by hot isostatic pressing is commonly utilized, and although beneficial in attaining full or near-complete density, it is cost intensive and time consuming.

A major barrier for the application of titanium metal matrix composites is related to processing costs and productivity, especially as these materials enter consumer-oriented markets.[162] To minimize processing costs, careful selection of the starting materials and processing techniques is necessary. Moreover, the final microstructure, and hence mechanical properties, is controlled by both these parameters. In the case of TiC reinforced titanium-based composites, the influence of the processing method on interfacial formation remains inconclusive. Nonetheless, it appears that the processing difficulties associated with titanium alloys may be alleviated through the application of near-net shape technologies, such as casting and powder metallurgy processing.[153] Although the casting technique has been successfully applied for titanium alloys, control of the interfacial reaction in titanium-based composites has usually required the lower processing temperature capabilities of the powder metallurgy approach. In terms of microstructural requirements, the powder metallurgy route imparts versatility to the manufacturing of materials through the control of material chemistry, microstructural components (including porosity) and the distribution of phases. Additionally, this process effectively uses automated operations with savings in material, energy and capital costs. In fact, the main drawbacks hindering application of this technique for titanium-based materials are related to the cost, quality and availability of titanium alloy powders.[163-165] Currently, most of the work on powder metallurgy processing of titanium-based composites has involved the blended elemental approach and the use of low-cost titanium sponge fines, from the Hunter or Kroll reduction processes. Considering that the chloride content in these powders produces a final component having inferior properties, more expensive powders, processed by alternate routes to give extra low chlorine contents, are inevitably necessary. Among these techniques, the hydride-dehydride method offers good quality titanium powder at the lowest cost and the potential for mechanical property levels equivalent to those attainable by ingot and cast metallurgy.[54] To reduce the overall cost of the component, a hydride-dehydride pre-alloyed titanium powder may be particularly beneficial; the cost of producing hydride-dehydride powder is the nearly the same for commercial purity titanium or Ti-6%Al-4%V, but application of the pre-alloyed powder reduces the sintering time and temperature requirements as only full densification is of concern.[54] Also, the use of pre-alloyed powders over blended elemental powders, for the matrix phase, is advantageous for titanium, which has a high affinity for oxygen, as alloying reduces its activity.[106]

Work on powder metallurgy processing of pre-alloyed powders has involved using hot isostatic pressing to achieve complete densification and mechanical property levels similar to those obtained by casting techniques and ingot metallurgy.[106] However, use of the hot isostatic pressing technique contributes to the high costs involved in the processing of titanium-based materials. Hence, in this work, the fabrication of the composites was investigated by using two lower cost techniques: the pre-alloyed Ti-6%Al-4%V powder was blended with polycrystalline TiC powder and consolidated by either high temperature sintering or hot working. The ultimate objective is to study the effect of processing on microstructural evolution and interfacial formation for the TiC particle reinforced titanium alloy composite system. Thus, the remaining segment of this chapter is devoted to examining the influence of the consolidation mechanisms and the processing variables on the structural development occurring during densification by (1) high temperature sintering and (2) deformation-assisted sintering.

2.3.1 Consolidation of Powders at High Temperature

In general, the production of a solid component from powder constituents using powder metallurgy processing involves powder compaction and consolidation. The compaction stage entails containing and pressing the loose powder mass to form engineered shapes of close dimensional tolerance and adequate green density for subsequent handling. It involves both rearrangement and deformation of the particles, resulting in the development of inter-particle bonds through cold-welding.[167-168] Powder compaction can simply be performed using axial pressurization. However, isostatic pressing is advantageous in producing a homogeneous density distribution in the green (*i.e.* unconsolidated) compact. Although powder compaction is the primary stage in shaping (*e.g.* dimensional control) and imparting specific properties (*e.g.* moderate strength and density, internal uniformity and integrity), it is insufficient in providing desirable properties for engineering applications and, thus, consolidation is of greater importance in determining the properties of the final product.[169]

Consolidation of a loose powder mass or porous compact by a thermally activated material transport mechanism that decreases the specific surface area of the particle by the formation and growth of particle contacts, shrinkage of the pore volume and change in pore geometry, is termed sintering.[170] During sintering, atomic transfer mechanisms result in interparticle bonding of the powder compact that is being heated at elevated temperatures (*i.e.* 0.6 to 0.8 T_m) in a controlled atmosphere (*e.g.* vacuum or inert gas). As sintering progresses, an increase in interparticle bonding and a change in the amount and morphology of the porosity improve the mechanical properties of the material. The various structural changes that transpire during sintering (*e.g.* neck growth, pore channel closure, pore rounding, pore shrinkage, etc.) depend on the occurrence of material transport within the powder compact. For sintering to progress, a net decrease in free energy of the system must occur. In a powder mass there is excess energy associated with the free surface of each particle. A decrease in the surface area by increasing the interparticle contact area (*i.e.* replacement of higher energy solid-vapor interfaces with lower energy solid-solid boundaries) provides the energy or driving force for sintering. Moreover, the greater the amount of surface area per unit volume in the original material, the greater the driving force for sintering (*e.g.* higher energy available from fine, irregular particles than from coarser spherical powders). Yet, this excess surface energy may not be large,[168] and a heat source is required to activate and maintain mass flow for sintering to occur at a reasonable rate.

To define the nature of the driving force, the thermodynamic situation at the beginning of sintering can be described using a two-sphere model, as shown in Figure 2.3, with sintering contacts and curved surfaces. In these contact regions, the concave neck surface is subjected to a stress (σ) during sintering according to the following equation:[171]

$$\sigma = \gamma\left(\frac{1}{R_1} + \frac{1}{R_2}\right) \tag{2.1}$$

where γ is the surface tension and R_1 and R_2 are as defined in Figure 2.3. At the start of sintering, during neck formation, the length of the sintered neck between the two particles (R_1) is much greater than the radius of curvature of the neck (R_2). Hence the tensile stress that develops is approximately[171]

$$\sigma = \frac{\gamma}{R_2} \tag{2.2}$$

and is directed outwards from the neck, as shown in Figure 2.3. This stress acts on the surface of the solid to pull the outer edge of the neck into the porosity. As sintering progresses, neck growth occurs and this driving force diminishes because the size of the sintered neck region, R_1, increases.

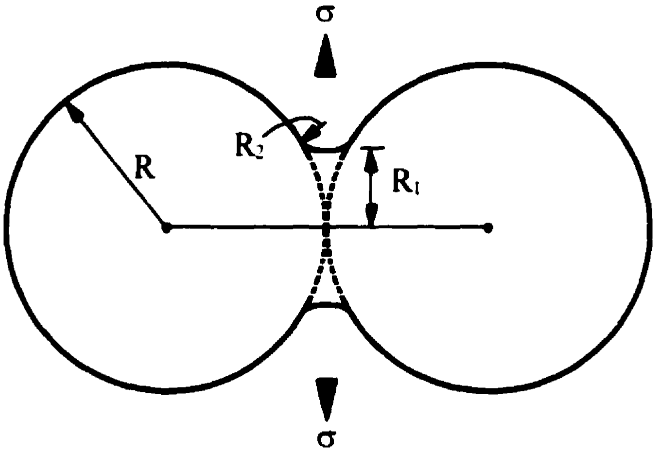

Figure 2.3 Initial stage of sintering showing development of the neck region in between two spherical particles.[171]

As a result of the stress in the neck region, the equilibrium vapor pressure above the neck will be slightly greater than that over the particle surface remote from the neck. The vapor pressure can then be related to the surface tension and curvature of the neck geometry, shown in Figure 2.3, according to[171]

$$\frac{p-p_o}{p_o}=\frac{\gamma V}{RT}\left(\frac{1}{R_1}+\frac{1}{R_2}\right)\cong\frac{\gamma V}{RT}\frac{1}{R_2} \tag{2.3}$$

where p is the vapor pressure over the curved surface, p_o is the vapor pressure over a flat surface, V is the molar volume of the solid, R is the gas constant and R_1 is much greater than R_2. Due to this difference in the vapor pressure, material transport by evaporation from some parts of the particle surface and simultaneous condensation at the neck can result in interparticle neck growth.

A similar dependence of the vacancy concentration on surface curvature exists according to[171]

$$\frac{C-C_o}{C_o}=\frac{\gamma V}{RT}\left(\frac{1}{R_1}+\frac{1}{R_2}\right)\cong\frac{\gamma V}{RT}\frac{1}{R_2} \tag{2.4}$$

where C is the vacancy concentration near the neck region and C_o is the vacancy concentration in the interior of the solid. The vacancy concentration gradient that exists between the neck and the remainder of the particle can result in material transport towards the neck through a surface or volume diffusion mechanism.

When sintering has proceeded to a situation where a spherical pore is isolated within the solid, the stress acting to reduce the pore surface by reducing the pore size is given by[171]

$$\sigma = -\frac{2\gamma}{r} \tag{2.5}$$

where r is the radius of the pore as shown in Figure 2.4. Pore shrinkage is possible if the pressure of the gas inside the pore is less than this stress. Thus the driving force for the latter stage of sintering can be thought of as a compressive stress in the solid surrounding the pore.

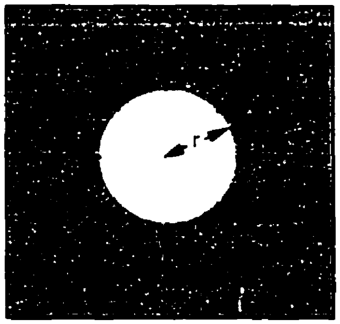

Figure 2.4 Stresses around an isolated pore in a solid.[171]

The driving force for sintering thus lies in the elimination of these stresses, removal of excess vacancies and equalization of the vapor pressure by material transport into the neck region. The mechanisms for material transfer can be grouped into *surface transfer* and *bulk transfer*, as shown in Figure 2.5.[172] Surface transfer mechanisms, which provide for neck growth by moving mass from surface sources, neither change the interparticle spacing nor improve densification. Surface diffusion (SD), evaporation-condensation (E-C) and, to a lesser extent, volume diffusion (VD) are responsible for surface transfer controlled sintering. Alternatively, bulk transfer controlled sintering involves densification as the mass originates from the particle interior and deposits at the neck region. Bulk transfer mechanisms involve lattice volume diffusion (VD), grain boundary diffusion (GB) and plastic flow (PF).

Surface Transfer

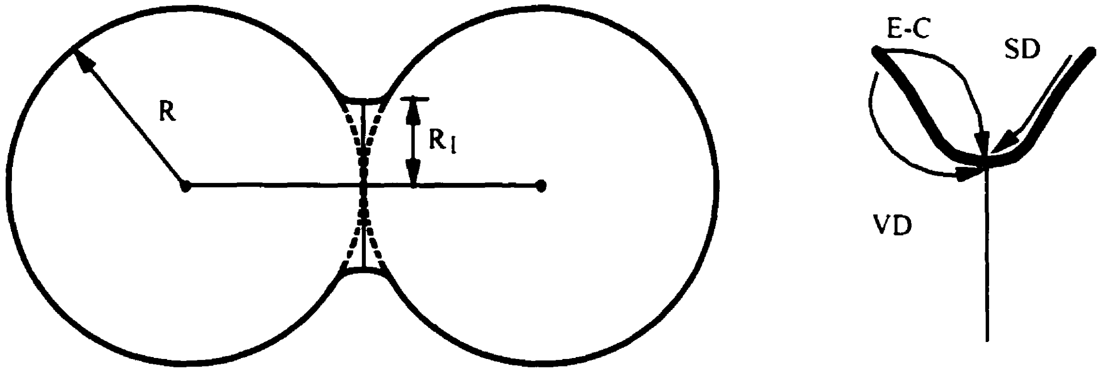

Bulk Transfer

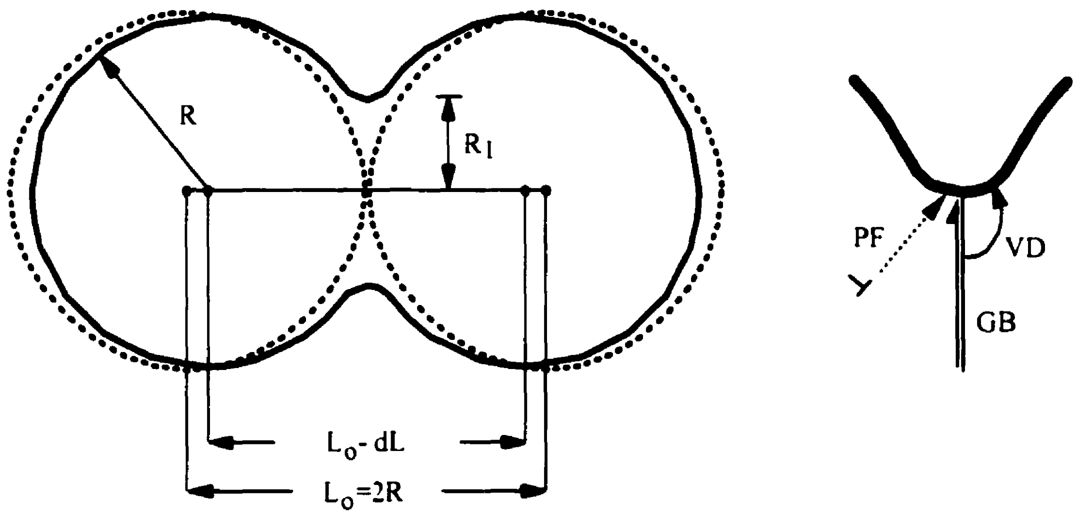

Figure 2.5 Surface transfer and bulk transfer mechanisms as applied to a two-particle sintering model. (The arrows indicate the movement of atoms and the concomitant motion of vacancies is in the opposite direction.)[172]

Surface diffusion involves the movement of atoms along solid-vapor interfaces. On account of the inherent difference in curvature and vacancy concentration in the region of the neck, atomic motion from convex particle surfaces to the neck region can occur and lead to neck growth. Also, smoothing of the surface roughness and pore rounding are possible by this mechanism. Pore shrinkage and elimination by surface diffusion does not occur due to the lack of long range surface diffusion from the outer to inner regions of the sintering component. Although surface diffusion can occur throughout consolidation, the dominance of this mechanism has been determined for the early stages of sintering, especially for fine powders, for which the specific surface is high.[173]

In some systems, the vapor-pressure difference between the neck region and the particle surface can lead to material transport into the neck by evaporation-condensation. The neck growth and pore rounding, which can result from this mechanism, occur by the rearrangement of material and no change in the pore volume or densification is possible. Moreover, material transport by this mechanism occurs for materials having a high vapor pressure and, with the exception of zinc and cadmium, vapor pressure differences in metals are too low for evaporation-condensation to take place at normal sintering temperatures.[173]

For metallic systems, the dominating sintering mechanism is associated with vacancy diffusion. The flow of vacancies from regions of high concentration in the neck to lower ones in the solid particles leads to the diffusion of atoms into the neck area. For this process to cause appreciable material transport, the vacancy gradient must be maintained and the vacancies moving away from the neck area must be eliminated at some suitable sink. If the vacancies emanating from the concave neck area diffuse along grain boundaries or lattice dislocations to convex particle surfaces, the pore itself acts as a sink and no reduction in the total porosity occurs. Only neck growth, change in pore morphology and pore coarsening are possible by this surface transfer volume diffusion mechanism.[169] Alternatively, vacancies can diffuse from the neck into the interior of the particle by means of lattice dislocations and grain boundaries (*i.e.* bulk transfer lattice volume diffusion). Essentially, vacancies move through the lattice from the neck region to grain boundaries existing within the interior of the particle, where there is a lower concentration of vacancies. The vacancies may move along the grain boundary network in the sintering material and reach its external surface, thereby improving densification.[169] For pores existing at grain boundaries, the movement of vacancies directly on to grain boundaries which are in contact with the neck surface and other pore surfaces is possible (*i.e.* grain boundary diffusion mechanism). Basically, grain boundary formation occurs between adjacent powder particles, and the vacancies existing in these contact areas may move along the grain boundaries to external surfaces, thus enabling pore shrinkage.[173]

The role of plastic flow as a sintering mechanism during consolidated is rather controversial. Reed and German consider plastic flow to be effective only if mechanical pressure is applied because the stresses which are encountered during sintering alone are insufficient to generate new dislocations.[172,174] However, during sintering of metals and ionic crystals, some investigators have observed the generation of dislocations in the neck area; dislocation densities of greater than 10^9 cm^{-2} were observed and, although their geometric arrangement was time dependent, the dislocations remained present after prolonged sintering times.[171] It is believed that dislocation-controlled creep generates plastic processes at the neck region and consists of two stages: (1) generation of the dislocation by a shear stress followed by its movement on the slip plane along a slip direction and its ultimate cessation at some obstacle in the lattice; (2) climb of the lead dislocation, in the pile-up of dislocations, over the obstacle and off the slip system, thus allowing a new dislocation to be generated at the source of the stress. The driving force for this material transport mechanism is the presence of shear stresses. Thümmler[171], Oberacker[171] and Hirschhorn[173] state that the stresses in the neck region and around isolated pores can lead to neck growth, pore rounding, and pore shrinkage by the plastic flow mechanism if these are greater than those necessary for dislocation generation and movement. At elevated temperatures, the stresses necessary for the formation and movement of dislocations are small, and for sintering systems that exhibit a large curvature in the neck region, a small pore radius and high surface tension, the presence of plastic flow as a sintering mechanism is possible.[171,173,175]

The importance of the various sintering mechanisms depends on the material and processing variables, including material, powder size, particle morphology, temperature, and sintering stage. To determine which mechanism dominates for a given system, mathematical correlations have been derived to describe isothermal powder sintering using neck-growth models, which can be extrapolated to center-to-center particle approach models, for mechanisms involving shrinkage. Assuming monosized spheres initially in point contact, neck growth rate by a single mechanism has been represented by[172]

$$\left(\frac{R_l}{R}\right)^{n} = \frac{Bt}{R^{m}} \tag{2.6}$$

where R_l is the length of the sintered neck between the two particles (Fig. 2.3), R is the particle radius, t is the isothermal sintering time and B is a collection of material and geometric constants. The exponents n and m are dependent on the mechanism and particle size, respectively. Values for these are given in Table 2.2 for the various sintering mechanisms.[176-186]

In the case of bulk transport processes, neck growth is accompanied by a change in the interparticle spacing as sintering progresses. The approach of the particle centers has been related to the neck size as follows:[172]

$$\frac{\Delta L}{L_0} = \left(\frac{R_1}{2R}\right)^2 = \left(\frac{Bt}{2^{2n} R^m}\right)^n \tag{2.7}$$

Table 2.2 - Values for the variables in the initial sintering stage equation[172,187]

Mechanism	n	m	B
Plastic Flow	1	1	$\frac{9\pi\gamma b D_v}{kT}$
Evaporation-Condensation	$\frac{2}{3}$	1	$\frac{3P\gamma}{\rho^2}\left(\frac{\pi}{2}\right)^{1/2}\left(\frac{M}{kT}\right)^{3/2}$
Volume (Lattice) Diffusion	$\frac{2}{5}$	3	$\frac{8D_v\gamma\Omega}{kT}$
Grain Boundary Diffusion	$\frac{2}{6}$	4	$\frac{20\delta D_B\gamma\Omega}{kT}$
Surface Diffusion	$\frac{2}{7}$	4	$\frac{56D_s\gamma\Omega^{4/3}}{kT}$

γ = surface energy
b = Burgers vector
k = Boltzmann's constant
T = absolute temperature
ρ = theoretical density
δ = grain boundary width

D_v = volume diffusivity
D_b = grain boundary diffusivity
D_s = surface diffusivity
P = vapor pressure
M = molecular weight
Ω = atomic volume of vacancies

where the shrinkage, $\Delta L/L_0$ can be determined by measuring the change in length of the compact and dividing by the original length. Determination of the sintering mechanism by the measurement of shrinkage, for bulk transport processes, is relatively simple as compared to the measurement of individual neck sizes. Having measured the shrinkage values for a range of times during isothermal sintering, a log shrinkage-log time plot yields the sintering mechanism from the slope. (It is noteworthy to mention that the particle size exponent, m, can be determined by a similar linear shrinkage analysis using various narrow particle size distributions.)

Although for each distinct material system a primary sintering mechanism exists, consolidation is often viewed to occur by all the material transport mechanisms with each contributing to neck growth and/or densification. Sintering diagrams have been constructed by Ashby[188] to identify, at a given temperature, particle size and neck size, the dominant sintering mechanism and indicate the sintering rate that all the mechanisms, acting together produce. The diagrams are based on the sintering models and diffusion data, and have been formulated to aid visualizing the effects of changing various material and processing conditions on consolidation.

There are numerous shortcomings to these models and even more so for the sintering diagrams.[189] As mentioned previously, sintering is not a single mechanism process and for most metallic systems, surface diffusion, lattice volume diffusion and grain boundary diffusion have been found to occur simultaneously. Moreover, sintering does not occur isothermally and considerable consolidation is possible during heating to the sintering temperature depending on the heating rate.[175] As such, lower heating rates have been determined to give higher densities at equal isothermal sintering temperatures due to the longer holding time intervals per temperature.[190] Furthermore, the models are based on monosized spherical particles. In real powder systems, particle size, roughness and morphology can deviate substantially from those used to derive the mathematical models. In practice, powders of irregular morphology are used and, in the majority of cases, pressed into the shape of the component before sintering. This produces asymmetric particle packing and irregular contact geometry in the green compact. Thus neck formation during sintering is unsymmetrical and it can induce particle rearrangement to occur concurrently with center-to-center particle approach.[191] Alternatively, the presence of an oxide film on the surface of the particles can inhibit (and even stop) material transport in the contact area during sintering of real powder systems.[192]

However, these relationships do provide insight on the variables that must be controlled during processing. Equation 2.6 in combination with Table 2.2 indicates that, for all the sintering mechanisms, the particle size of the powder has a major effect on the sintering rate (*i.e.* roughly proportional to the inverse of the particle size). Also the sintering temperature has a double influence for most of the mechanisms, as the diffusion coefficient is also a function of temperature. Although not apparent in equation 2.6, particle size distribution is also critical because single-sized particles are difficult to pack efficiently and form compacts with large pores and a high percentage porosity.[172]

The above analysis of the sintering mechanisms was derived for the initial stage of sintering, in which the sharp curvature gradients located near the interparticle neck provide the initial driving force for consolidation to occur. In this stage, the particle contacts are transformed to bonded bridges or necks between adjacent particles, as illustrated in Figure 2.6. Surface smoothing of the particles and rounding of interconnected, open (*i.e.* connected to the external surface) pores occur. Although the powder particles remain discrete during the initial stage, grain boundaries often begin forming between two adjacent particles in planar contact. The particle centers approach only slightly and the total shrinkage in this stage is usually between 3% to 10%. With prolonged sintering, the open and fully interconnected pore structure becomes smoothed, eliminating the major curvature gradients, as depicted in Figure 2.6. This leads to the intermediate stage of sintering in which the pores have a cylindrical structure and the single particles begin to loose their identity. Considerable shrinkage occurs in this stage, as the shrinkage of open pores occurs rapidly through the intersecting grain boundaries which run from pore to pore. In the latter portion of the intermediate stage, slow grain growth frequently occurs. This can lead to the movement of pores or isolation of pores within the grain boundary. This replaces the coherent network of interconnected pores with closed pore channels, which leads to the final stage of sintering. During this stage, the cylindrical pores collapse and become spherical pores that are not as effective in slowing grain growth. Frequently, the microstructure exhibits pores separated from the grain boundaries (*i.e.* isolated pores) which are difficult to eliminate. As mentioned above, the densification in this stage depends on the pressure inside the pore being less than that due to the surface tension (*i.e.* equation 2.5). Shrinkage of isolated pores has been determined to be a slow process and prolonged sintering times in the final stage can lead to substantial microstructural coarsening of the grains and pores.[172]

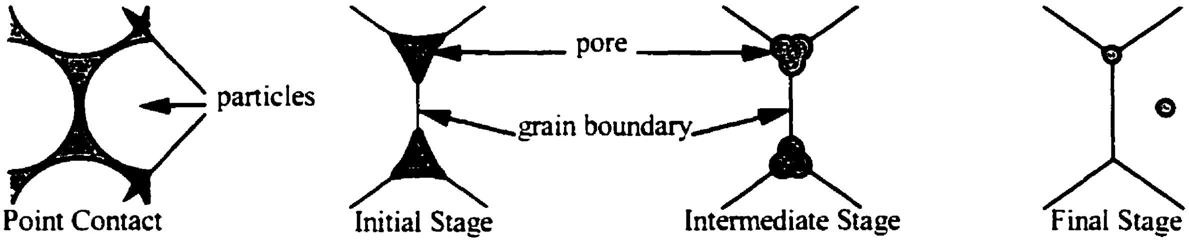

Figure 2.6 The development of interparticle bonding during sintering.[193,172]

To define the sintering rate in the intermediate stage, Coble[194] constructed a model consisting of cylindrical pores situated along the edges of tetrakaidecahedron grains. However, the pore structure is highly convoluted, especially at the beginning of the intermediate sintering stage, and even as sintering progresses the pore morphology deviates from being cylindrical. Beere[195] formulated a closer approach to the complex pore geometry for the intermediate stage by assuming six interconnecting corner units of tetrahedral symmetry arranged to form an enclosed toroid of porosity, as shown in Figure 2.7. In his model, this toroidal pore structure is arranged around the edges of an idealized tetrakaidecahedron grain. With either model, the system of interconnected pores is stable provided that the volume of porosity remains above a particular threshold value (approximately 8% porosity), below which the connected structure (cylindrical or toroidal) collapses and the porosity segments (approaching spherical in morphology) retreat to grain corners. Regardless, both models give rather complicated expressions for the densification rate and the assumptions involved in their derivation render considerable uncertainty when quantitatively determining the effect of processing parameters on consolidation of non-ideal systems. Nonetheless, experimental work using the models for spherical copper powders indicates that the densification rate is dependent on the grain size, initial density, temperature and time. The effect of temperature was found to be dominant for both the intermediate and final stages, as the diffusion coefficient, grain growth and pore motion are dependent on temperature.[172] Also, both a fine initial particle size and a narrow particle size distribution have been found to enhance the densification rate owing to a low grain boundary mobility.[172]

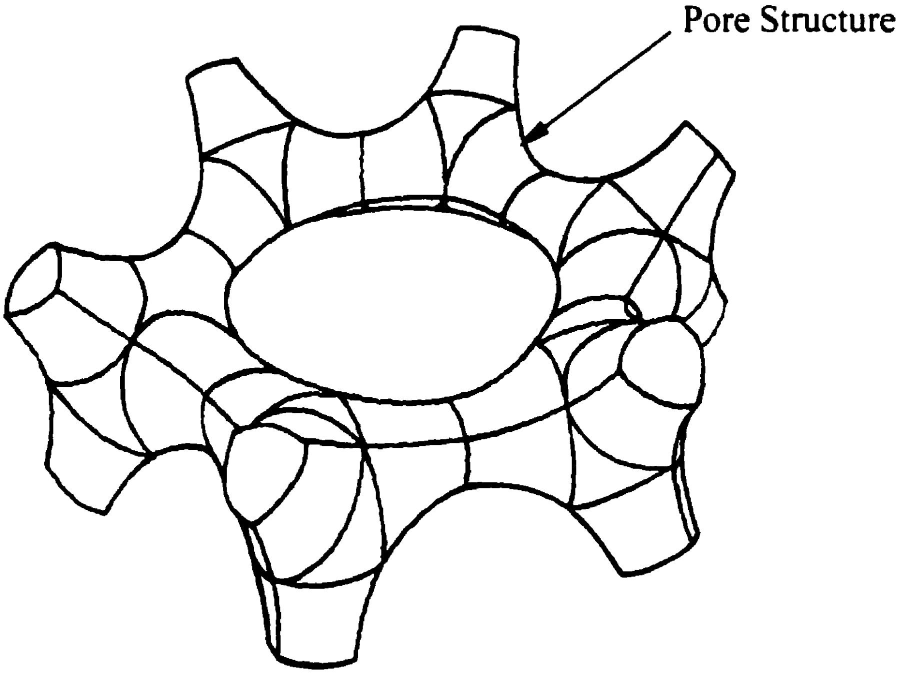

Figure 2.7 An arrangement of six interconnecting corner units of tetrahedral symmetry distorted slightly to fit round the edges of a tetrakaidecahedron grain.[195]

Therefore, microstructural variation in the sintering of powder materials is mainly related to the morphological evolution of the porosity, which occurs through material transport, by one or more of the sintering mechanisms mentioned. The characteristics of the starting powder (*e.g.* particle size, shape, distribution, blended or pre-alloyed) and the processing conditions (*e.g.* heating rate, temperature, holding time) influence the sintering rate and control the final microstructure in the sintered component. Apart from residual porosity, the as-sintered microstructure is usually similar or equivalent to that of wrought or annealed materials. The grain size is dependent on the initial powder size and on the extent of grain growth during the intermediate and final sintering stages.

In the case of the Ti-6%Al-4%V alloy, a lamellar morphology of α plates separated by inter-plate β is expected. For composite materials, the presence of the reinforcement phase may also contribute towards improving densification during consolidation by controlling grain growth during the latter sintering stages (*i.e.* prolongation of the intermediate sintering stage relies on the pores remaining attached to the grain boundaries to support continued densification[196]). However even with prolonged sintering, elimination of the residual pores has been found to be difficult, and in the case of the titanium-based composites, considerable interaction of matrix and reinforcement phases, during extended holding at elevated temperatures, may even deteriorate the overall material properties.

2.3.2 Deformation-Assisted Consolidation of Powders

The intrinsic ability of metals and alloys to be worked into various shapes forms the traditional basis for the use of plastic deformation processes. The importance of deformation processing in modern technology is attributed to the ability to control the microstructure and mechanical properties via the temperature, strain and strain rate. In the case of metals and alloys produced by conventional P/M processing methods (compaction and sintering), residual porosity, which deteriorates the mechanical and physical properties of the structure, can be removed by deformation processing.

The fundamentals of deformation-assisted sintering (also called hot-pressing) are closely related to those described previously for pressureless sintering. Essentially, deformation processing can be considered as a sintering process, where the internal driving forces of the system, defined by equations 2.1 to 2.5, are enhanced by the external stresses due to loading of the compact. Thus in deformation-assisted sintering, the applied pressure acting on the compact is transmitted to the single particle contacts, as depicted in

Figure 2.3, and superimposed on the existing tensile stress on the curved region (*e.g.* equation 2.1), thereby increasing the contact stress. Similarly, for the latter stages of sintering, both the stress described in equation 2.5, as well as the applied stress reduce the surface of the isolated spherical pores.

The way in which external loading contributes to the existing stresses in the particle contact regions or on isolated spherical pores depends on the nature of the applied stress, the compact geometry, and the microstructural condition of the material system. In general, however, the total contact and pore surface stresses are greatly increased by the application of an external pressure. As such, the dominating material transport mechanisms relevant to deformation-assisted sintering are different from those discussed previously for pressureless sintering. The important hot deformation processing mechanisms for solid-state systems are plastic yielding, power-law creep, diffusional creep and grain boundary sliding. Deformation mechanism diagrams have been developed by Ashby[197] to indicate the relative importance of the various mechanisms for different stress-temperature combinations, and are illustrated in Figure 2.8.

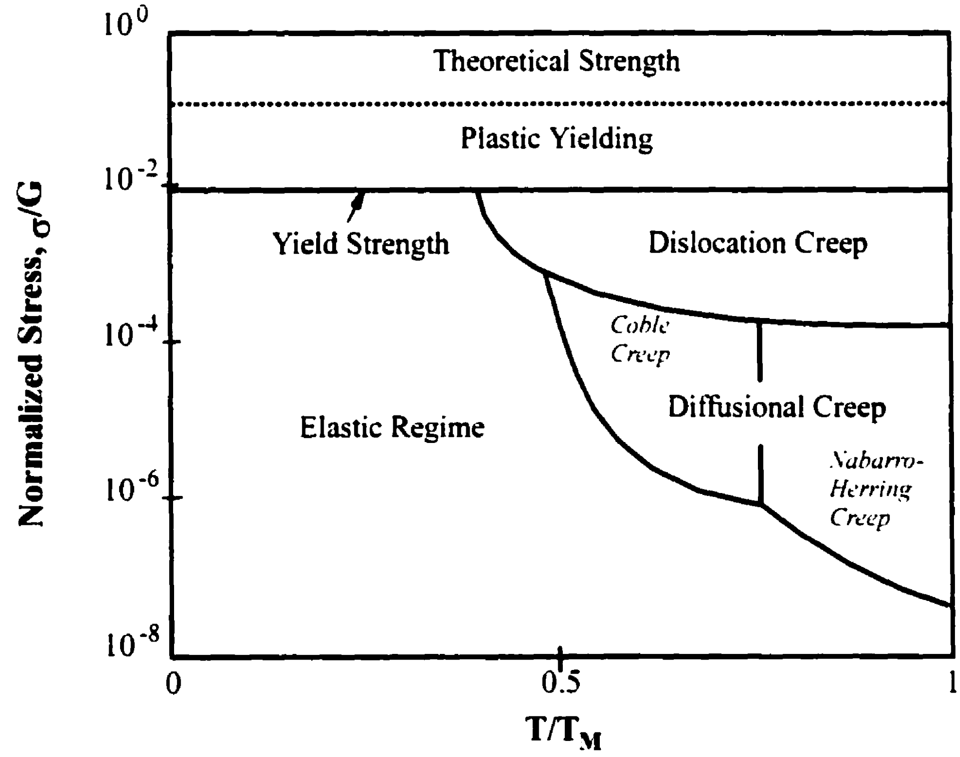

Figure 2.8 Simplified map showing the various deformation mechanisms at different stresses and temperatures.[197]

Plastic yielding or dislocation glide, which involves dislocation movement along slip planes, occurs at stress levels that are high relative to the other deformation mechanisms shown in Figure 2.8. Hence this mechanism is likely to dominate in the beginning of hot deformation processing when the curvature gradients are large (*i.e.* highest internal stress as defined by equation 2.1). Under the influence of an external stress, the powder compact begins to yield if the total stress in the contact region or on the pore surface exceeds the yield strength of the material. Yielding proceeds until contact flattening and/or work hardening establishes a balance between the contact stress and the deformation resistance of the material.[198] Subsequently, dislocation or power-law creep occurs by dislocation glide aided by vacancy diffusion (*i.e.* dislocation climb),[199] as described in the paragraph on plastic flow as a mechanism for sintering alone. The difference for deformation-assisted sintering is that the total stress in the contact region and around isolated spherical pores incorporates the external stress. Thus, during deformation processing, material transport by this mechanism occurs even for material systems not exhibiting favorable characteristics for plastic flow during sintering alone. With the progression of densification, the stress resulting from curvature differences reduces substantially, as explained in the sintering section. In the presence of a constant external pressure, as the curvature stress is reduced, the rate of dislocation creep diminishes and diffusional creep commences to dominate. Diffusional creep results from stress-induced vacancy gradients which induce vacancy flow from the grain boundaries in tension to those in compression, as shown in Figure 2.9.[199-200] At high processing temperatures, relative to the melting temperature of the material, diffusion occurs through the crystal lattice and is referred to as Nabarro - Herring creep. At lower processing temperatures, lattice diffusion is slower and grain boundary diffusion or Coble creep dominates. Finally, it has been shown that grain boundary sliding, which is the relative movement of adjacent grains, must accompany diffusional flow mechanisms to maintain grain continuity.[201]

For each of the deformation mechanisms, equations for the rate of densification have been developed by modeling the solid-state pressure sintering process as a random arrangement of densely packed monosized spherical particles under an external hydrostatic force.[202] However, as demonstrated for sintering, the applicability of such equations for real powder systems is limited by the assumptions of such micro-mechanical models. Nonetheless, their formulation indicates the variables affecting deformation-assisted densification. In general, hot working is relatively ineffective at temperatures below half of the melting temperature (T_M), regardless of the deformation mechanism. From Figure 2.8, it is observed that at temperatures below $0.5 \cdot T_M$, only plastic yielding is a possible deformation mechanism and high pressures are necessary to achieve densification. The influence of temperature on plastic yielding is related to the temperature dependence of flow stress. The rate of densification by dislocation creep increases exponentially with temperature and progressively with pressure, depending on the power-law creep exponent of the material.[198,202] Both plastic yielding and dislocation creep have been determined to be independent of the particle size of the powder and grain size. However, diffusional creep densification is strongly influenced by the grain size or particle size of the compact, with the densification rate inversely proportional to the square or cube of the grain diameter for Nabarro-Herring creep or Coble creep, respectively.[203-204] Also diffusional creep densification rates linearly increase with pressure and exponentially with temperature.[202] In most practical deformation processing systems involving low strain rates (*e.g.* axial or isostatic hot pressing), diffusional creep has been determined to be the dominant densification mechanism, especially in the final part of the process.[198] Hence, densification by this mechanism during hot working can be greatly enhanced by small particle or grain sizes.

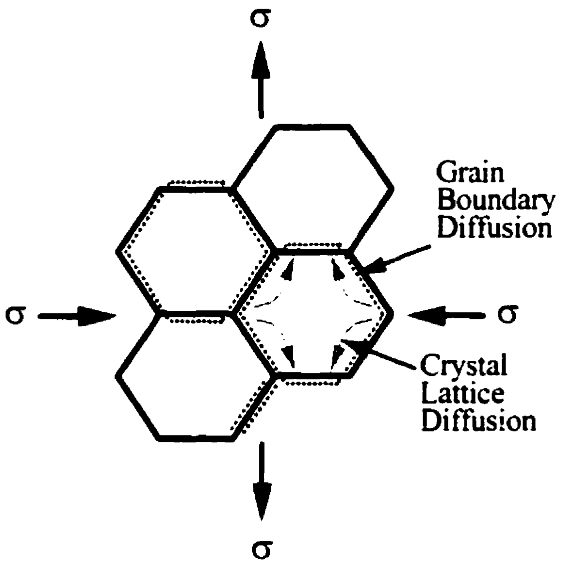

Figure 2.9 Diffusional creep as a mechanism for hot deformation processing.[199]

Besides modeling the consolidation behavior of powders by means of mechanistic techniques (*i.e.* plastic flow, power law creep, diffusional flow), continuum methods exist to model the densification response of sintering powder particulates. In general, the mechanistic models are closely related to microstructural evolution of the material during consolidation.[205-206] Alternatively, continuum models are based on the development of a plasticity theory for porous (compressible) powder metallurgy materials. In general, formulation of a plasticity theory considers the yielding and flow behavior of a densifying powder during deformation.[207-208] To understand the densification behavior of a porous material, deformation of an element of material containing a void, as illustrated in Figure 2.4, can be considered. The pressure required for plastic deformation of a solid material containing a void is given by[209]

$$P = 2\sigma_o \ln \frac{r_o}{r_i} \qquad (2.8)$$

where σ_o is the flow stress of the material, r_o is the outside radius (equivalent to the mean space between the voids), and r_i is the void radius. This analysis indicates that voids of large diameter require less pressure for densification than small voids. As the void diameter approaches zero, the pressure required for densification becomes unbound. Hence in a pure hydrostatic stress state, as shown in Figure 2.10, the equal pressure in all directions is not as conducive to complete densification, since infinite pressures are required to eliminate fine spherical pores.[209] If, however, the net stress state consists of a small difference in the vertical and horizontal stresses, the void will become flattened as opposite sides of the pores come closer together, such that the shape of the pores change from spherical to ellipsoidal on collapse, as illustrated in Figure 2.10. This is typical of re-pressing type deformation, where extensive flow of material in the lateral direction is constrained by die walls.[209] During high temperature processing, atomic movement (by diffusional and dislocation creep) across the collapsed pore interfaces can result in porosity removal and chemical bonding.[210] Extensive unconstrained expansion of the material in the lateral direction during compression occurs in upset forging operations as depicted in Figure 2.10. Here the presence of the shear stress generates a relative motion between opposite sides of the collapsed pore, which can cause mechanical rupture of the oxide film on the metal surface bounded by the pore. This, along with intimate surface contact due to sliding, is expected to result in a sound metallurgical bond across the collapsed pore interfaces.[209] Hence, for high temperature deformation processing of porous materials, higher densification rates are expected of forging or axial hot pressing operations as compared to hot isostatic pressing.

The fundamental mechanical responses of a porous material (densification, plastic flow and fracture) during plastic forming processes can be determined through compression testing of cylindrical specimens. Plastic deformation of powder materials is similar to that of conventionally produced fully dense materials, but there are additional complications due to the substantial volume fraction of voids. In particular, these voids must be eliminated during deformation to obtain a sound metallurgical structure. However, the voids are sites of weakness at which ductile fractures may initiate during deformation. A feature which distinguishes the deformation behavior of a powder material from that of a fully dense solid is that porous materials undergo a permanent volume change due to densification during deformation. A further consequence of porous material densification during deformation is reflected in the Poisson's ratio, which is a measure of the lateral flow behavior of a material. For a solid material, the Poisson's ratio for plastic compressive deformation is 0.5 since the volume of material remains constant during deformation. During compressive deformation of powder preforms, flow of material into the pores decreases the volume and changes the Poisson's ratio with densification. Hence the classical plasticity theory cannot be used for plasticity analysis of porous materials.

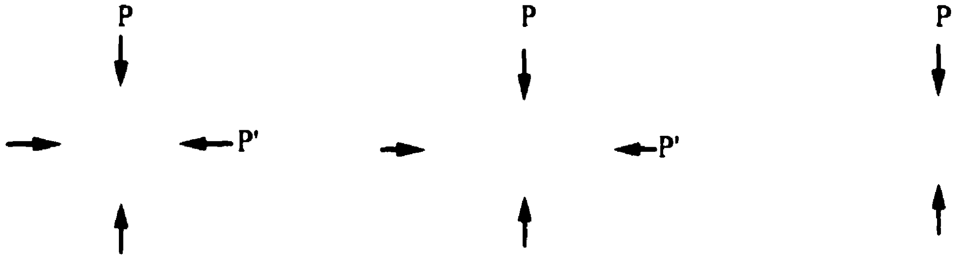

Hydrostatic Pressure   Repressing (no lateral flow)   True Forging (lateral flow)

Figure 2.10 Schematic diagram depicting the mechanical response of a porous material to deformation.

To determine the flow behavior of porous materials, the dependence of the Poisson's ratio on the relative density of the porous compact must be determined. From frictionless compression tests on various metal powder preforms Kuhn et al. have determined the following empirical relationship between Poisson's ratio (ν) and instantaneous relative density (ρ):[211]

$$\nu = 0.5\rho^{n} \tag{2.9}$$

The best fit to the experimental data is attained with the exponent n = 1.92 for room temperature deformation and n = 2.0 for hot deformation, with the slight difference in the exponent being attributed to work hardening.[209]

In general, the Poisson's ratio provides an insight into the relative competition between material deformation and densification under a given applied stress. It is, however, important to note that the material itself is still considered to be incompressible ($\nu = 0.5$) and that the Poisson's ratio describes only the macroscopic behavior of the porous material viewed as a continuum. The significance of Poisson's ratio for providing a measure of the densification and deformation strain has been described by Dutton et al. under conditions of uniaxial compression as follows:[212]

$$\varepsilon_p = (1 - 2\nu)\varepsilon_a \tag{2.10}$$

where ε_p is the densification strain and ε_a is the axial strain. As full density is approached, $\nu \rightarrow 0.5$, the deformation strain (ε_d) in the material approaches the axial strain (ε_a) and the densification strain (ε_p) drops to zero (*i.e.* $\varepsilon_a = \varepsilon_d + \varepsilon_p$). Thus the deformation strain in the matrix of a porous metallic material is related by

$$\varepsilon_d = 2\nu\varepsilon_a \tag{2.11}$$

For composite materials containing rigid incompressible particulates, the deformation strain of a densifying matrix phase has been determined to be also a function of the reinforcement volume fraction (V_f) according to[213]

$$\varepsilon_d = \frac{2\nu\varepsilon_a}{(1 - V_f)} \tag{2.12}$$

To quantify the influence of the relative density on the stress component of the flow behavior, a stress-intensification factor (ϕ) has been defined as the ratio of the cross-sectional area of the porous sample, A_p, to the actual load-bearing area, A_m. A number of theoretical approaches have been developed to estimate the variation of ϕ with relative density (Table 2.3). Coble's[214] relation is based solely on the average effective load bearing capacity of a porous material while Scherer[215-216] proposed a model using a cylindrical lattice array of open-pore materials such as gels. Beere[195,217] considered a more complicated pore-grain boundary geometry model and the work of Vieira and Brook[218] indicated that Beere's results fit an exponential relationship between ϕ and relative density. Some investigators have curve fitted experimental data using power law relationships between ϕ and relative density.[219-221] Models incorporating the effect of initial density on particle compaction during densification have been proposed for uniaxial compression[222] and hot isostatic pressing.[223-226] Besides the diversity in functional relationship between stress-intensification factor and relative density, most of the models used for predicting ϕ

divide the densification process into two or more stages, each characterized by a different pore geometry. This leads to discontinuities in the corrected-effective stress of the matrix material at the boundary limits, which are not observed experimentally.

Table 2.3 - Models proposed for the stress-intensification factor

Stress-Intensification Factor	Model	Density Range
(2.13) $\phi = \frac{1}{\rho}$	Coble: Random distribution of isolated pores	$\rho > 0.90$[214]
(2.14) $\phi = \frac{(3-2\rho)}{\rho}$	Scherer: Cylindrical lattice network of continuous porous material	$\rho < 1.0$[215-216]
(2.15) $\phi = \exp(a(1-\rho)$	Vieira & Brook: Pore-grain boundary geometry	$\rho < 1.0$[195,217-218]
(2.16) $\phi = \frac{1}{\rho^n}$	Curve fitting experimental data Shima & Oyane: $n = 5/2$[219] Dutton et al.: $n = 3.56$[220]	$\rho < 1.0$
(2.17) $\phi = \left\{\frac{1}{(2\rho^2-1)}\right\}^{\frac{1}{2}}$	Doraivelu et al.: Curve fitting experimental data[207,221]	$0.7 < \rho < 1.0$
(2.18) $\phi = \frac{(1-\rho_o)}{(\rho-\rho_o)}$	Lee & Kim: Curve fitting experimental data Uniaxial compression	$\rho < 1.0$[222]
(2.19) $\phi = \frac{(1-\rho_o)}{\rho^2(\rho-\rho_o)}$	Helle et al.: Mono-sized spherical powder Hot isostatic pressing	$\rho < 0.9$[224]
(2.20) $\phi = \frac{(1-\rho_o)^2}{\rho(\rho-\rho_o)^2}$	Helle et al.: Mono-sized spherical powder, including neck growth due to interparticle diffusion Hot isostatic pressing	$\rho < 0.9$[224]

a = depends on pore shape, coordination number and the morphology and size distribution of the powder[227-229]

ρ_o = initial relative density

ρ = instantaneous relative density

ϕ = stress-intensification factor

Figure 2.11, a plot of ϕ versus relative density, illustrates the differences in the stress-intensification factors calculated from the various models. Large differences in ϕ values are observed at low densities, and above a relative density of 0.85, the ϕ results for all geometries are approximately similar. The random pore distribution model proposed by Coble has the lowest values and is thus best applicable for relative densities above 0.90. The ϕ values for both the cylindrical lattice model and the empirical fit of Shima and Oyane range from approximately 3.0 at low densities to the required 1.0 at full density. Alternatively, the mono-size sphere models give quite high stress-intensification (> 100.0) for low relative densities but decrease rapidly with increasing ρ.

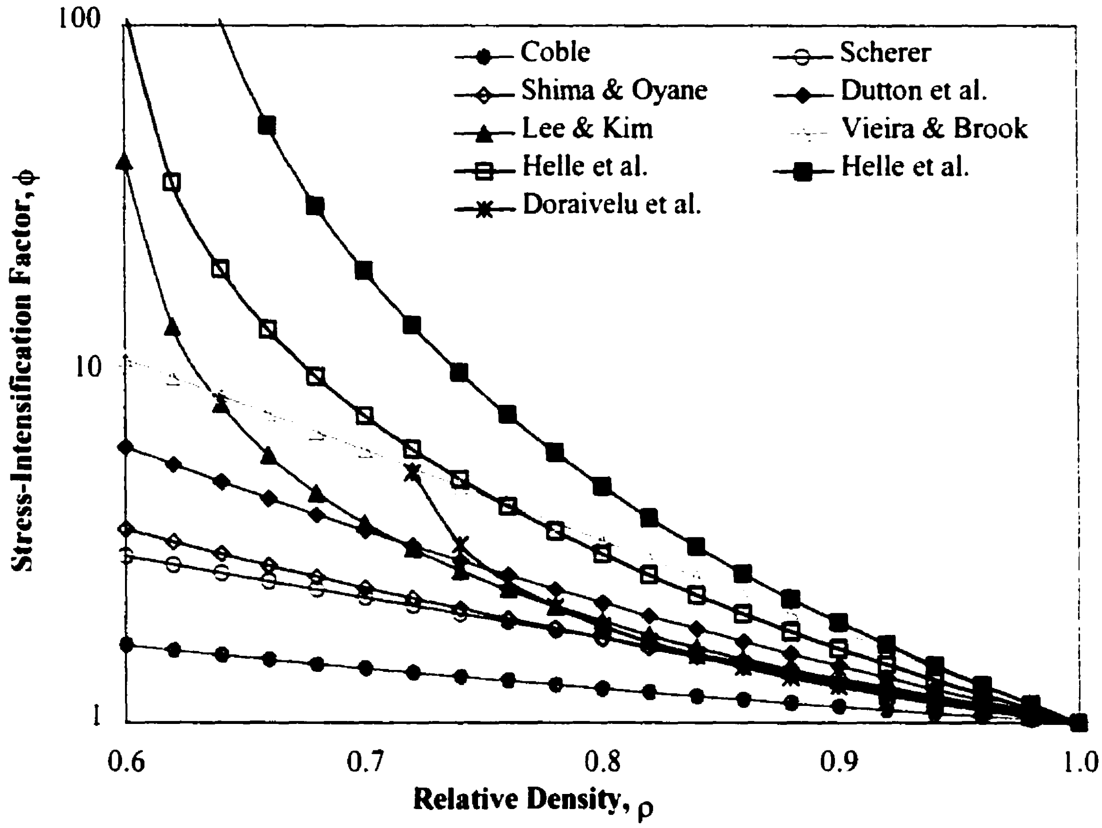

Figure 2.11 Stress-intensification factor (ϕ) as a function of relative density for various powder geometries or empirical correlations.

Selection of the appropriate relationship for the variation in stress-intensification factor with relative density is highly dependent on the powder morphology, size distribution, green density, and processing condition. In the vacuum hot pressing work of Taylor et al.[230] on mono-sized titanium and 90% titanium-10% TiC powders placed in a molybdenum die, the stress-intensification factor relation formulated for hot isostatic pressing by Helle et al.[224] (equation 2.19) was used to correct the applied pressure measurements. For conditions of hot pressing without lateral constraint (*i.e.* frictionless uniaxial compression testing), the stress-intensification relationship formulated by Lee and Kim[222] (equation 2.18) can conceivably correct the applied stress of densifying powder materials for relative densities less than 0.90.[231] However, the high stress-intensification factor (~ 40) at low relative densities for Lee and Kim's relationship was too extreme of a correction and the correlation developed by Shima and Oyane provided the most suitable correction factor for the titanium-based composites in this work. For relative densities above 0.90, the random pore distribution model proposed by Coble[214] (equation 2.13) can be applied to determine the effective stress, however, caution must be exercised to fit both models at the boundary of $\rho = 0.90$ to avoid or minimize the discontinuity resulting from changing the geometric model.

Besides densification, deformation processing can simultaneously develop the final microstructure and dimensions of a powder metallurgy component. As determined previously, a portion of the axially applied strain (ε_a) is stored in the material as a deformation strain (ε_d) which increases as densification progresses and converges to ε_a when full density is reached. At elevated temperatures, the accumulated deformation strain energy (in the form of excess point defects and dislocations) in the material may be reduced by two main restoration processes: recovery and recrystallization. Generally, recovery is considered to be a precursor to nucleation and growth of recrystallization. It has been observed that the initial 20% of softening is recovery and the remaining is recrystallization. Recovery is generally due to dislocation annihilation and/or rearrangement into lower energy configurations (such as sub-grains). Recrystallization is dislocation annihilation via grain boundary movement, which 'sweeps out' the dislocation density. Grain boundary migration is initiated by the nucleation of dislocation free nuclei, which then begin to grow in the deformed material if the temperature is high enough, and gradually consume the whole of the deformed matrix.[232]

In metals and alloys, the hot deformation structure develops with increasing strain from tangled dislocations to sub-grains. Microstructural inhomogeneities, such as micro-bands, transition bands and shear bands are present, although at a lower frequency with increasing deformation temperature. That is the deformation microstructure becomes more homogeneous with increasing deformation temperature.[233] Introducing particles into a metal matrix affects the deformation pattern and leads to differences in the stress and strain distribution at both the local and macroscopic level. These effects are reflected in the dislocation structure and internal stress state. Besides being introduced by mechanical deformation, both dislocations and internal stresses may be formed by a difference in the coefficient of thermal expansion between the matrix and the reinforcement.[233]

The local effect of particles is to increase the dislocation density at a given strain due to the formation of "geometrically necessary" dislocations (*i.e.* dislocations generated at the particle due to non-uniform deformation). For small particles (*i.e.* 0.01 to 0.1 μm – dispersion strengthened composites) the geometrically necessary dislocations are normally present as Orowan loops or tangles at the particles.[233] At the large particles (*i.e.* 0.1 to

100 μm – particle reinforced composites), these dislocations give rise to the formation of deformation zones[233] of high dislocation density adjacent to the particles (Fig. 2.12). The actual characteristics of such zones depend on various material and processing parameters. One parameter of particular importance is the volume fraction of the reinforcement particle.[233] For volume fractions in the range of 0.1 to 0.3, deformation zones will overlap. Such zones have a complex microstructure characterized by the presence of small sub-grains and dislocation boundaries with a large misorientation across them.

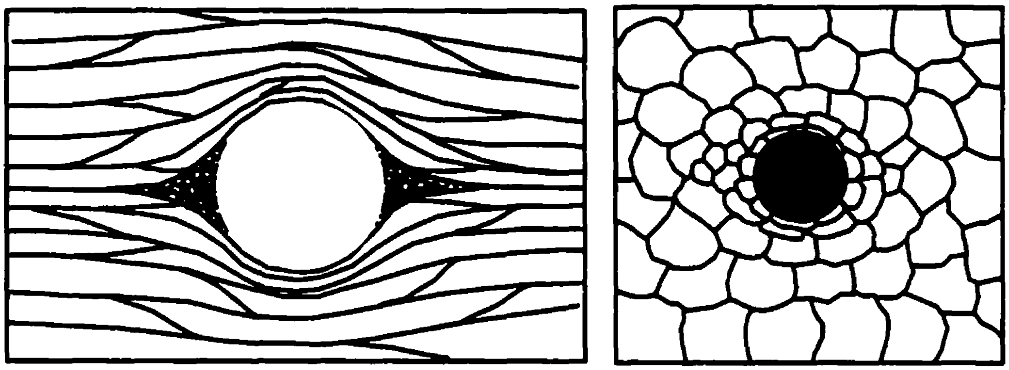

Figure 2.12 Schematic diagram showing possible sub-grain structures that form around large particles during deformation

In composites, the effect of reinforcement particles during deformation is not limited to the formation of geometrically necessary dislocations and local inhomogeneities. Particles also affect the overall deformation pattern and thereby influence the macroscopic deformation microstructure.[233] Thus, particles in composites can accelerate microstructural evolution compared to that of a single phase material. Such an effect may be enhanced with an increasing number of particles, but saturates at medium and large strains. Another macroscopic effect of particles appears to be a homogenization of the deformation microstructure, thus reducing the frequency of microstructural heterogeneities such as micro-bands and transition bands. The presence of large particles may, however, cause plastic instabilities such as shear bands. Small particles may homogenize the slip pattern and, as a result, the distribution of dislocations may be more uniform than for a material without particles.

As mentioned previously, recovery in single-phase materials leads to a decrease in the mobile dislocation density, and to sub-grain growth by coalescence and migration of sub-grain boundaries. Such growth may occur in the matrix, particularly at deformation inhomogeneities. The non-uniform distribution of dislocations and internal stresses in the presence of large particles, not only enhances the *overall* sub-grain growth, but also introduces inhomogeneous growth. A high sub-grain growth rate is therefore characteristic of deformation inhomogeneities at the reinforcement, especially where the particles are present in clusters. The effect of small particles is mainly to retard sub-grain growth, through pinning of dislocations and sub-grain boundaries.

In particulate reinforced composites, recrystallization nuclei may form preferentially at the deformation inhomogeneities in the matrix phase as well as at deformation zones around large particles. Nucleation sites tend to be regions of high dislocation density, such as original grain boundaries, high angle grain boundaries formed during deformation and shear bands. Of particular importance is enhanced nucleation at particle clusters, where the stored energy of the dislocation configurations can become high and where the lattice rotations can approach that of grain boundaries. The effectiveness of such nucleation sites depends on the reinforcement shape, which dictates the characteristics of the deformation zone. For instance, angular particles are stronger nucleation sites than spherical particles, due to the larger concentrations of strain in the vicinity of sharp corners. An increase in the reinforcement size enhances the effectiveness of the particle as a recrystallization nucleation site. However, for a particular volume fraction of reinforcement, the number of potential nucleation sites decreases with increasing particle size.

Thus, deformation processing of powder materials essentially involves the progressive elimination of porosity with densification as well as the development of the matrix microstructure. Previous work on the mechanical and deformation behavior of composites has concentrated mostly on the effect of fiber and whisker reinforcements on the development of microstructures and properties. Where the effect of particle reinforcements have been considered, the matrix material was almost exclusively a single-phase aluminium alloy. In these materials, consolidation by hot deformation processing was successful in reducing the temperatures and times required for densification. Hence, the present work is aimed at studying the effectiveness of hot deformation processing (as compared to sintering) in improving the microstructural characteristics (particularly the interfacial region) and mechanical properties of TiC particulate reinforced Ti-6%Al-4%V composites produced by powder metallurgy. Additionally, the influence of TiC particles on the densification, microstructure and mechanical behavior of a two-phase titanium alloy will be investigated.

2.4 Mechanical Properties

The mechanical properties of a composite material depend on the properties of its constituents, their distribution and physical and chemical interactions. The most accurate way to determine such properties is by experimental methods, however, these can be time consuming and expensive. Hence a number of investigators have developed models to predict the mechanical properties of the composite. Although these models can, in some cases, predict accurately the influence of the various microstructural constituents on the mechanical properties, the large number of microstructural variables associated with composites has lead to substantial discrepancy between the predicted and experimentally determined properties. However, formulation of these mathematical models does provide a basis for understanding the manner in which the various constituents influence the mechanical properties. Specifically, the factors that influence the composite properties include the presence of residual porosity, the reinforcement volume fraction, the metal-ceramic interface and matrix microstructure.

2.3.1 Residual Porosity

For the fabrication of structural components using powder metallurgy techniques, the dependence of various properties on the amount and nature of the residual porosity in the consolidated material is of great concern. In general, porosity has a large effect on the static and dynamic properties of powder metallurgy materials. Strength tends to be one of the least sensitive monitors of porosity. Ductility is slightly more sensitive, with impact, fracture and fatigue behavior having the greatest sensitivities to porosity.[172] In the assessment of static properties (*e.g.* strength and ductility) under the loading environment of a standard tensile test, the bond integrity developed by the collapse of pores during densification is measured.[209] For the powder properties in such testing to be equivalent to those of corresponding cast or wrought materials, particle bonding during consolidation need only be achieved by diffusion, without the need for shear and lateral flow of the material. Sensitivity to porosity increases for dynamic properties (*e.g.* impact and fatigue) because these require the development of a sound metallurgical bond through considerable shear and lateral flow as well as diffusion.[209] The improvement in dynamic properties with lateral flow is related to the break-up of the oxide layer that surrounds each particle surface. Moreover, it has been found that micro-porosity around particle boundaries will persist in the absence of lateral flow, thus contributing to a poorer microstructural integrity and, thus, dynamic properties.[209]

For evaluating the influence of porosity in a powder metallurgy material, the strength and ductility are usually inspected first to see if these correlate satisfactorily with that of corresponding cast or wrought compositions. For a particular powder metallurgy processing procedure should the static properties obtained appear acceptable, the dynamic properties are then considered for investigation. In this work, the strength and ductility after synthesis of the composite materials will be assessed and compared to those in the literature, and as such only the variation of these properties with porosity are considered.

To understand the role of porosity during loading, one can first consider a typical ductile wrought material being stressed gradually in tension. As the load increases, the material initially undergoes recoverable elastic deformation and eventually a critical stress level (*i.e.* yield stress) is reached at which point the material begins to deform plastically. During plastic deformation, small voids or cracks are formed in the material and these grow and coalesce until the reduced cross-sectional area of the material can no longer support the applied load and fracture occurs. Essentially, the presence of residual porosity in powder metallurgy materials reduces the effective cross-sectional area resisting the stress as soon as the load is applied.[173] An added complexity to this situation is pore morphology. Around any geometrical discontinuity, a stress distribution exists with the maximum stress concentrated in the vicinity of the surface of the defect. The stress concentration is minimum for spherical pores and increases, as the void becomes sharper and narrower.[173] The presence of voids thus signifies that the solid material experiences a greater stress than indicated by the applied load and external dimensions of the specimen. These stresses are significant enough to induce plastic deformation, pore growth and fracture at lower applied loads than expected of the material system.[173]

Any quantitative formulation for the dependence of strength on porosity must consider the amount of porosity, pore size, pore morphology (angularity and regularity of the pores), distance between pores and connectivity of pores. Due to the complexity and variability of porosity in real sintered materials, most of the work has concentrated on relating the strength to the total amount of pores only. At low relative densities (< 85%), the size of the interparticle sinter bonds appears to be the main determinant for the yield and tensile strengths, which are observed to increase linearly with decreasing amount of porosity. At higher densities, the pore size, morphology, spacing and volume fraction are the primary factors influencing the strength properties. Such considerations of strength dependence on porosity have lead to the formulation of semi-empirical relations such as[172,173]

$$\sigma = k\sigma_o(1-P)^m \qquad (2.21)$$

Or

$$\sigma = \sigma_o \exp\{-kP\} \tag{2.22}$$

where σ is the yield or tensile strength of the porous material, σ_o is the yield or tensile strength of the pore-free material, k is a material and processing constant (highly dependent on particle size and temperature), P is the fractional porosity and m is the density exponent. Typically k has been found to lie between 2 and 10, often 4, whilst m ranges between 3 and 6, being influenced by notch effects, which are dependent on pore size and shape.[172,173]

For ductility, an additional sensitivity to pore shape and spacing has been observed. Smooth pores at large spacings are reported to be less detrimental than fine, closely spaced pores.[173] The negative effect of porosity on ductility is attributed to strain concentration, uneven cross section, and their role as crack initiation sites. With more than 15% porosity, the ductility is small and gives less than 5% total elongation. Also, ductility shows a greater scatter from specimen to specimen than strength and reflects the greater defect sensitivity of ductility. For sintered powder metallurgy materials, the influence of porosity on ductility has been approximated as[173]

$$\frac{e_p}{e_w} = \frac{(1+P)^{3/2}}{\sqrt{1+CP}} \tag{2.23}$$

where e_p and e_w are the percent elongations of the porous and wrought materials, respectively, P is fractional porosity and C is an empirical constant that represents the sensitivity of the ductility to the presence of pores.

2.4.2 Reinforcement Phase

For most metal matrix composites, the reinforcement is harder and stiffer than the matrix and the matrix transfers some of the applied stress to the reinforcement phase, which bears a fraction of the load. The use of particulates rather than fibers lowers the maximum volume fraction of reinforcement that can be uniformly distributed in the matrix. This tends to lower the increases in elastic modulus and strength that can be achieved by incorporating discontinuous reinforcements in a metallic matrix. The simplest equations to predict the strength or elastic modulus are based on the rule of mixture which predict that the properties should fall between an upper linear bound represented by[109b]

$$E_c = E_m V_m + E_p V_p \quad \text{or} \quad \sigma_c = \sigma_m V_m + \sigma_p V_p \tag{2.24}$$

and a lower bound,

$$E_c = \frac{E_m E_p}{V_m E_p + V_p E_m} \quad \text{or} \quad \sigma_c = \frac{\sigma_m \sigma_p}{V_m \sigma_p + V_p \sigma_m} \tag{2.25}$$

where E is the elastic modulus, σ is the yield or tensile strength and V is volume fraction, while the subscripts c, m and p represent composite, matrix and particles, respectively.

The rule of mixtures expression considerably overestimates the properties and has been found to be most appropriate for continuous reinforcements. For discontinuously reinforced aluminium composites, the elastic modulus may be better approximated by

$$E_{DRA} = \frac{E_m V_m + E_p V_p}{(V_m + V_p)} \tag{2.26}$$

at the upper linear bound and by

$$E_{DRA} = \frac{E_m V_m + E_p (V_p + 1)}{E_p V_m + E_m (V_p + 1)} \tag{2.27}$$

at the nonlinear lower bound.[22] A limitation of this expression is that it assumes a spherical geometry for the reinforcement particles. The Halpin-Tsai equation incorporates the effect of particulate geometry according to

$$E_c = \frac{E_m (1 + 2sqV_p)}{1 - qV_p} \tag{2.28}$$

where

$$q = \frac{E_m \; E_p - 1}{E_p \; E_m + 2s} \tag{2.29}$$

and s is the aspect ratio.[20] Modeling predictions for strength, however, are slightly more difficult mainly due to the number of failure modes that can cause composite fracture (particle, matrix or interface) and the very local nature of failure initiation. By considering the strengthening mechanisms, which may operate in particle reinforced composites, the strength behavior has been estimated as[20]

$$\sigma_c = V_p \sigma_m \frac{s}{4} + V_m \sigma_m \tag{2.30}$$

where σ_m is the yield stress of the matrix. This equation for the composite strength is based on continuum shear lag models for particles with an aspect ratio below that necessary for full reinforcement loading (s < 5). Nardone and Prewo have modified the above equation to include the effect of loading at the ends of the reinforcement as follows[20]

$$\sigma_c = V_p\sigma_m\left(\frac{s}{2}+1\right)+V_m\sigma_m \tag{2.31}$$

The greatest difficulty with this continuum approach for modeling the strength behavior is that it disregards the influence of particles on the micromechanics of deformation, such as the very high work hardening at low strains and modifications in the microstructure, such as grain size and dislocation density.

The major limitation in the mechanical properties of composites is the ductility, which decreases rapidly with the addition of reinforcing particles. Recent work indicates that composite failure is commonly associated with particle cracking and void formation in the matrix within clusters of particles.[20] Particle fracture is more prevalent in coarser particles, and this may be explained by two points of view. The larger the particle the more it will be loaded by conventional fiber loading and end loading mechanisms. Coarser ceramic reinforcements also have a higher probability of containing fracture initiating defects. Failure associated with particle clusters has been attributed to higher concentration in these regions. Although formulating a mathematical expression for the ductility of composites would be a complex function of the fracture processes, the general criteria maximizing the ductility for a particular reinforcement volume fraction include uniform particle distribution, a fine (< 10 μm) uniform particle size distribution, a good interfacial bond and a ductile matrix.[20]

2.4.3 Interface Characteristics

The interface between any two phases can be defined as the bounding surface where a discontinuity of some sort occurs. The discontinuity may be sharp or gradual. The interface is essentially a region through which material parameters, such as concentration of an element, crystal structure, elastic modulus, density and coefficient of thermal expansion, change.[4] The presence of an interface is significant for mechanical properties because the applied load acting on the matrix is transferred to the reinforcement via this phase. Thus the strength, stiffness and fracture behavior of the composite depend strongly on the characteristics of this phase. Generally, a strong interfacial bond makes the composite more rigid but brittle, while a weak bond decreases the strength and stiffness, but enhances the ductility.[4] To understand the influence of the interfacial phase on mechanical property development, the interfacial strength is commonly measured for fiber reinforced composites using single fiber pull-out tests, while for discontinuous reinforcements Vickers micro-indentation testing can be used. Difficulty exists in incorporating the effect of interfacial strength on mechanical properties primarily because the characteristics of the interface are specific to each reinforcement-matrix combination as well as processing conditions.

2.4.4 Matrix Microstructure

Recapitulating, Ti-6%Al-4%V is a two phase alloy for which the additions of vanadium and aluminium stabilize the α and β phases, respectively. The amount and morphology of the phases present at room temperature depend on the processing path, and various different microstructures can be produced. Thermally produced microstructures by slow cooling have a lamellar morphology of α separated by thin layers of β. Faster cooling rates refine the size of this lamellar structure. Thermomechanical processing is need to transform lamellar α to an equiaxed morphology. Such processing can also be used to produce a mixture of equiaxed and lamellar structures, referred to as a bimodal or duplex microstructure.

Literature on the mechanical properties of titanium alloys abounds and many papers concerning the dependency of strength, ductility, fracture toughness, fatigue properties, etc. on the microstructure are available. The relationship between some of the microstructural features at room temperature and the mechanical properties of Ti-6%Al-4%V are given in Tables 2.4 and 2.5.[47]

2.4.5 Ti-6%Al-4%V/TiC$_p$ Properties

TiC particulate reinforced Ti-6%Al-4%V composites are being manufactured commercially by Dynamet Technology Inc. using the cold and hot isostatic pressing (CHIP) technique.[27.14-150] The process consists of blending elemental and pre-alloyed powders, cold isostatic pressing to a preform shape, vacuum sintering to attain closed porosity in the component, followed by containerless hot isostatic pressing to full density. The tensile properties of the unreinforced alloy and TiC reinforced composites processed by this technique are shown in Table 2.6. Examining these properties, it appears that the TiC-titanium alloy system achieves a considerable improvement in the strength behavior with a slight deterioration of the fracture-related properties.

Table 2.4 - Microstructure-property relationship for Ti-6%Al-4%V

Feature	Enhances	Degrades
Equiaxed α	Ductility Fatigue Initiation Resistance	Fracture Toughness Fatigue Crack Growth Resistance
Lamellar α	Fatigue Crack Growth Resistance Fracture Toughness	Strength Ductility Fatigue Initiation Resistance
Elongated α	Fracture Toughness Fatigue Crack Growth Resistance	Ductility Fatigue Initiation Resistance
Bimodal α	Strength Ductility Fatigue Initiation Resistance	Fatigue Crack Growth Resistance Fracture Toughness
Grain Boundary α	Fracture Toughness Fatigue Crack Growth Resistance	Ductility Fatigue Initiation Resistance

Table 2.5 - Mechanical properties for Ti-6%Al-4%V microstructures

Microstructure	Yield Strength (MPa)	Ultimate Tensile Strength (MPa)	Percent Elongation (%)	Reduction in Area (%)
Lamellar (α+β)				
As-cast	834	917	4	13
Cast and HIP	813	884	8	13
Anneal – coarse	860	956	8.8	21.5
Anneal - fine	1056	1278	11.5	20
Equiaxed α	950-1030	980-1404	15-22	26-59

Table 2.6 - Mechanical properties for TiC particle reinforced Ti-6%Al-4%V composites produced by powder metallurgy techniques (CIP and HIP process)[27,147-150]

Property	Ti-6Al-4V	Ti-6Al-4V/10%TiC$_p$	Ti-6Al-4V/20%TiC$_p$
Density (g/cm^3)	4.42	4.45	4.48
Yield Strength (MPa)	862	965	1034
Tensile strength (MPa)	896	999	1055
Elastic Modulus (GPa)	113	133	144
Fracture Toughness (MPa·m^{½})	55	44	32
Hardness (HRC)	34	40	44

CHAPTER 3

OBJECTIVES

The technical challenge facing the development of titanium-based composites originates from the high reactivity of titanium with most reinforcing phases, as well as high processing temperature requirements. With regard to the previous research work on the processing and characterization of TiC particulate reinforced titanium matrix composites, the considerable uncertainty encompassing the composition and formation of the interfacial reaction region has hindered the establishment of microstructure-property relationships for this material system. Hence the main objectives of the present work were,

- To process the TiC particulate reinforced Ti-6%Al-4%V composites by using two powder metallurgy processing techniques: elevated temperature pressureless sintering and hot deformation-assisted sintering.

- To investigate the influence of processing parameters (*e.g.* hold time, temperature, strain and strain rate, as applicable) on the densification behavior, matrix microstructure and interfacial development using various microscopic techniques.

- To examine the compositional characteristics of the various phases present in the microstructure (*e.g.* alpha and beta phases of the titanium alloy matrix, TiC reinforcement phase and interfacial phase) using neutron diffractometry.

- To study the influence of incorporating TiC reinforcement particles on the densification behavior and microstructural development of the titanium alloy during high temperature consolidation with or without deformation.

- To assess the tensile mechanical properties of the composites using data from shear punch testing. (To employ the shear punch testing technique for discontinuously reinforced composites, the punch load-displacement data must be correlated to the deformation features prior to formulating an empirical relationship between the mechanical properties from shear punch testing and tensile testing.)

- To establish the interdependence of microstructure and mechanical properties for the TiC-titanium alloy system.

- To compare the two powder metallurgy processing routes based on the evolution in densification behavior, matrix microstructure, interfacial phase and mechanical properties.

CHAPTER 4

EXPERIMENTAL TECHNIQUES

The as-received materials were processed and characterized according to the experimental procedure flow chart illustrated in Figure 4.1. The remainder of this chapter will describe in detail the techniques associated with each component of this flow chart.

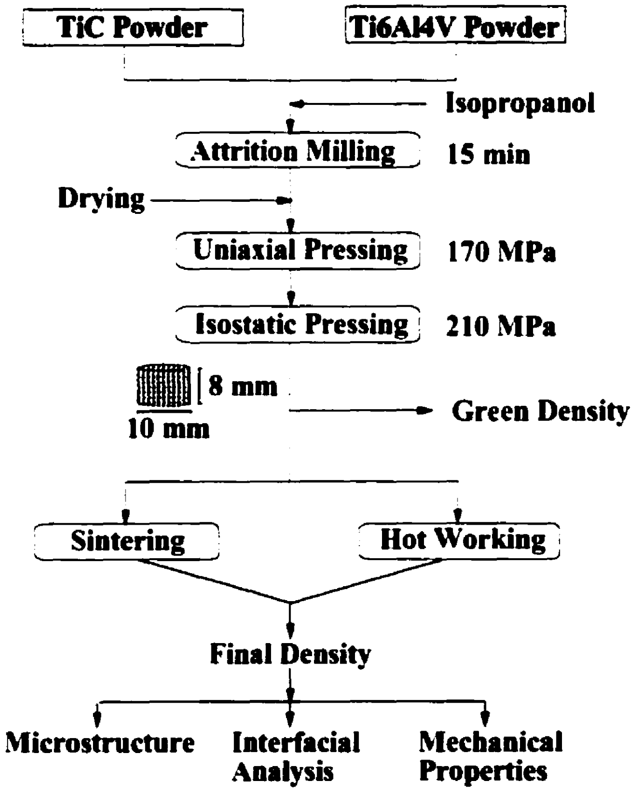

Figure 4.1 Flow diagram showing the experimental procedure.

4.1 Material Characterization

Commercial Ti-6%Al-4%V master alloy powder, having a density of 4.43 g·cm^{-3}, was supplied by *Micron Metals Inc.* (Salt Lake City, Utah). The chemical composition and appearance of the Ti-6%Al-4%V as-received powder are given in Table 4.1 and Figure 4.2, respectively. The Ti-6%Al-4%V powder had an angular morphology which is characteristic of the hydride-dehydride process used to manufacture this powder.

Table 4.1 - Chemical composition of Ti-6%Al-4%V powder

	Al	V	O_2	C	N_2	H_2	Cl_2	Na	Ti
Composition (wt.%)	6.0	4.0	0.24	0.06	0.3	0.03	0.01	0.005	Balance

TiC powder, of density of 4.93 g·cm^{-3}, was supplied by *Kennametal Inc. Macro Division* (Port Coquitlam, British Columbia). The chemical composition and appearance of the TiC as-received powder are given in Table 4.2 and Figure 4.3, respectively. The TiC particles were both angular and facetted in appearance due to the milling process used to reduce the particle size after fabricating the powder by the carbothermic reaction process.

Table 4.2 - Chemical composition of TiC powder

	Free Carbon	Total Carbon	N_2	O_2	Fe	Ti
Composition (wt.%)	0.11	19.77	0.10	0.21	0.26	Balance

The as-received powders of Ti-6%Al-4%V and TiC were analyzed for average particle size and particle size distribution by means of screening and sedimentation techniques. A dry sieve analysis was performed by using 38, 53, 75 and 106 μm opening screens. Powder characterization using a *Micromeritics 5000D* sedigraph was performed by mixing a small quantity (1 to 2 g) of powder with water to yield a dilute suspension which was allowed to settle for a predetermined time. During sieving, the Ti-6%Al-4%V powder passed through the 75 μm screen and remained on the 38 μm screen. From the sedigraph (Fig. 4.4), the Ti-6%Al-4%V was determined to have a particle size distribution of 55 μm to 75 μm (d_{25} to d_{75})[1] with a mean particle size (d_{50}) of 65 μm. The TiC powder had a particle size distribution of less than 30 μm with a mean particle size (d_{50}) of 15 μm, as shown in Figure 4.4.

---

[1] d_{25} is the particle size at a cumulative weight percent passing of 25 as indicated by the lines on Figure 4.4.

Figure 4.2 SEM micrograph of the as-received Ti-6%Al-4%V pre-alloyed powder used for the matrix phase.

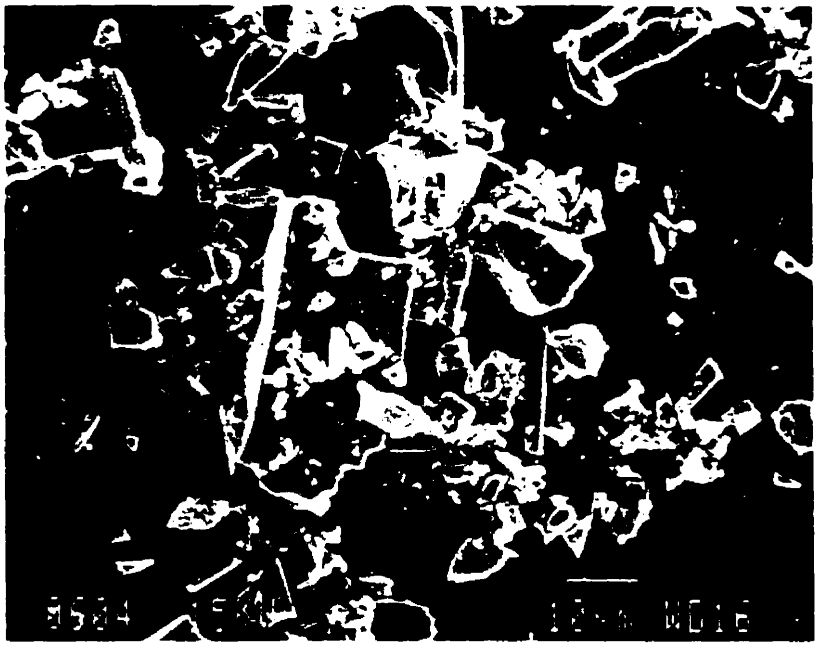

Figure 4.3 SEM micrograph of the as-received TiC powder used for the reinforcing phase.

Essentially, the pre-alloyed hydride-dehydride Ti-6%Al-4%V powder was chosen to have a narrow particle size distribution, while a relatively broad particle distribution and finer mean particle size was selected for the TiC particles. The difference in the particle size distribution and powder size were chosen to aid dispersion of the reinforcement phase in the matrix and improve the packing density by increasing the number of initial contact points in the compacted preform.

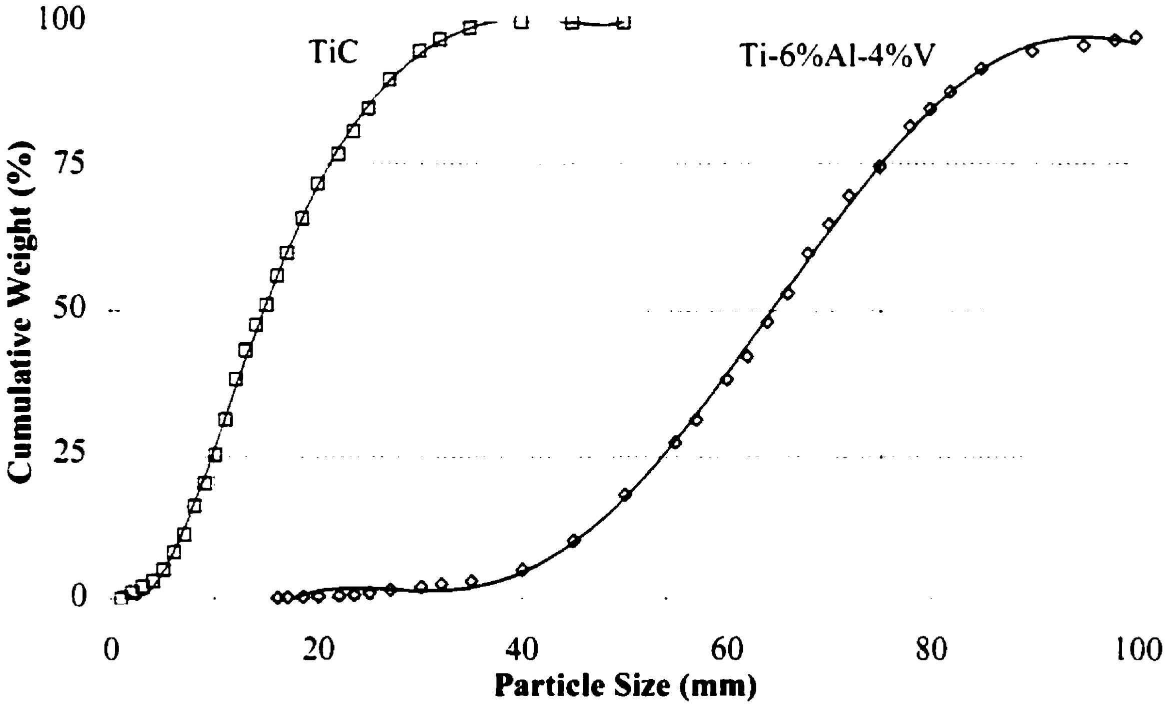

Figure 4.4 Sedigraph analysis of the as-received TiC and Ti-6%Al-4%V powders.

4.2 Powder Processing

4.2.1 Powder Blending

The Ti-6%Al-4%V powder was mixed with proportions of 5, 10, 15 and 20 volume percent TiC powder. The pre-mixed compositions were then wet attrition milled for 15 minutes[89] with alumina (99.7% pure) grinding balls and isopropyl alcohol (solid:liquid ratio of 1:5 by weight) in a 4L Teflon cylindrical container (Fig. 4.5). The

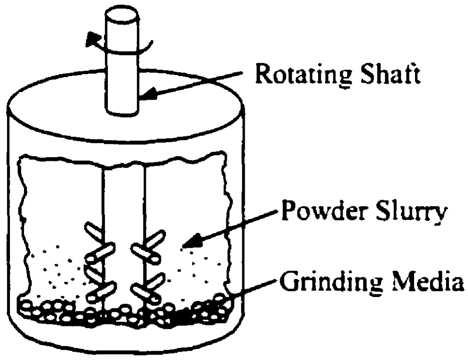

Figure 4.5 Diagram of an attrition mill.

alumina grinding balls, 3.7 mm in diameter, were added in a proportion of five times the weight of the Ti-6%Al-4%V/TiC mixture. Agitation was achieved by a series of Teflon stirrers mounted to an axial Teflon shaft rotating at 200 rpm. Sieving the mixture through a 212 μm screen enabled separation of the powder slurry from the alumina grinding media. The powder slurry was then decanted for an hour to separate the solid mixture from the liquid solvent. The wet solid mixture was placed in a conventional oven at 100°C to remove remaining traces of isopropyl alcohol (about 12 hours).

4.2.2 Compact Processing

Powder compaction was performed using uniaxial pressing followed by cold isostatic pressing to achieve good dimensional control and uniform density distribution in the green compacts. During uniaxial pressing, the blended powder mixtures were pressed in a rigid steel die at a pressure of 172.5 MPa (25,000 psi). This pressure, transmitted by a single action punch, achieved sufficient green strength for handling the compacts prior to isostatic pressing. Pressures substantially higher or lower than 172.5 MPa, caused cracking or crumbling, respectively, during ejection of the compact from the die. To minimize density gradients during uniaxial pressing, the cylindrical compacts were designed to be roughly 11 mm in diameter and 6 mm in height. (Also, these dimensions were chosen in consideration of the load capacity of the deformation equipment[234], as described later.)

These uniaxially pressed green compacts were placed in flexible rubber molds and then vacuum sealed. Cold isostatic pressing of the molds was performed by immersing them in the fluid chamber (emulsified mixture of water and oil) of the steel cylindrical pressure vessel of an *Autoclave Engineers IP3*-isostatic press. A hydrostatic pressure of 207 MPa (30,000 psi) was applied uniformly from all sides of the mold to the center of the compact, thereby removing the density gradients from uniaxial pressing. Upon release of the pressure the compacts were removed from the mold and placed in a vacuum chamber until sintering.

4.3 Sintering

Prior to sintering the green density of each compact was calculated by measuring the dry weight and dimensions. The green compacts were then placed on a boron nitride setter and sintered in a graphite-element resistance furnace, as shown in Figure 4.6. The furnace chamber (30 x 30 x 40 cm^3) was insulated from the water-cooled steel exterior by graphite fiber insulation. The graphite-elements were connected to a 50 kV·A power supply. The furnace was equipped with a rotary pump which maintained the vacuum at less than 30 Pa during heating and 5 Pa during holding at the fixed temperature. The furnace temperature was regulated by a digital controller connected to a type C (W-5% Re versus W-26% Re) close ended thermocouple, located at the center of the furnace. An accuracy of ± 2 °C between the temperatures of the specimen and the center of the furnace was ascertained regularly by calibration. This was performed by heating pure metal powders (*e.g.* of nickel or copper) to just below the melting temperature and then comparing the temperature reading with the melting point of the powder.

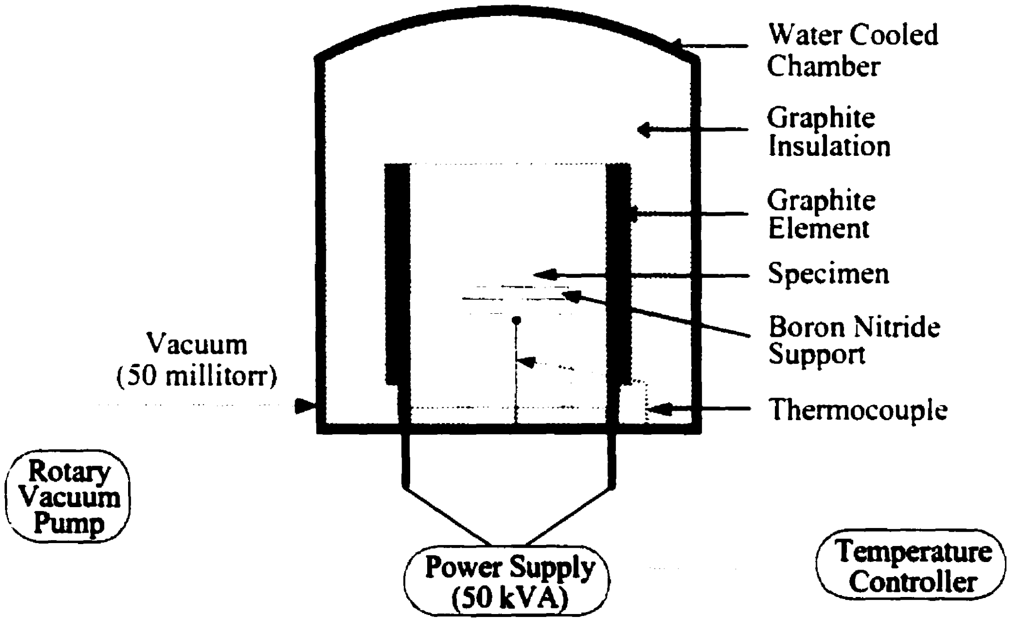

Figure 4.6 Schematic diagram of the graphite-element resistance furnace.

The thermal cycle during sintering is illustrated in Figure 4.7. The specimens were heated at the maximum rate of 20 °C/min to the desired temperature (*i.e.* 1100°C, 1300°C and 1500°C), maintained at that temperature for the required hold time (½, 1, 2 and 4 hours) and then furnace cooled.

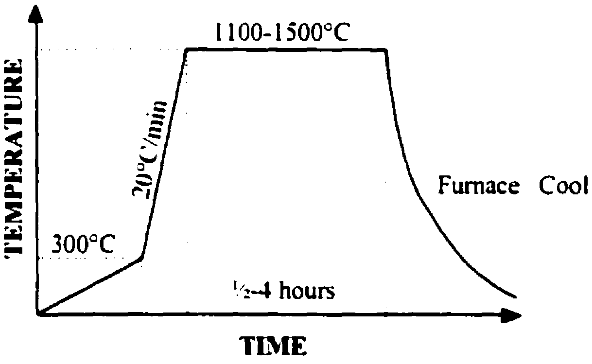

Figure 4.7 Thermal cycle for sintering.

4.3.1 Mass Loss Evaluation During Sintering

To investigate the weight loss occurring in the sintering atmosphere, the set-up illustrated in Figure 4.8 was utilized. A custom-built vertical tube furnace, having an open-ended 6 cm diameter mullite ($Al_6Si_2O_{13}$) tube was fitted on the bottom end with a rotary vacuum system capable of maintaining a 5 Pa vacuum. The top end was attached to a glass tube of a similar diameter, leading to a Thermo-Gravimetric Analyzer, or TGA (Cahn D-100). The furnace temperature was controlled with a type B (Pt-6% Rh vs. Pt-30% Rh) thermocouple located on the outside of the mullite tube. An accuracy of ± 2°C between the actual and measured furnace temperatures was ascertained by calibration with pure metal powders.

A green compact was placed on top of a boron nitride bed contained in an alumina crucible. Whilst the furnace was opened, the crucible was suspended from the TGA arm using a molybdenum (T_m = 2610°C) wire long enough to reach the hot zone of the furnace. The hot zone was ascertained to be roughly 23 cm in length. The furnace was then closed and evacuated to a vacuum of 5 Pa. The TGA was tared and the furnace was heated to a temperature of 1500°C. The change in weight experienced by the sintering compact during heating was monitored through the TGA, which collected data every 10 seconds and stored these in a personal computer. (Weight changes in the specimen were calibrated by removing changes during sintering due to the crucible, boron nitride bed and molybdenum wire.)

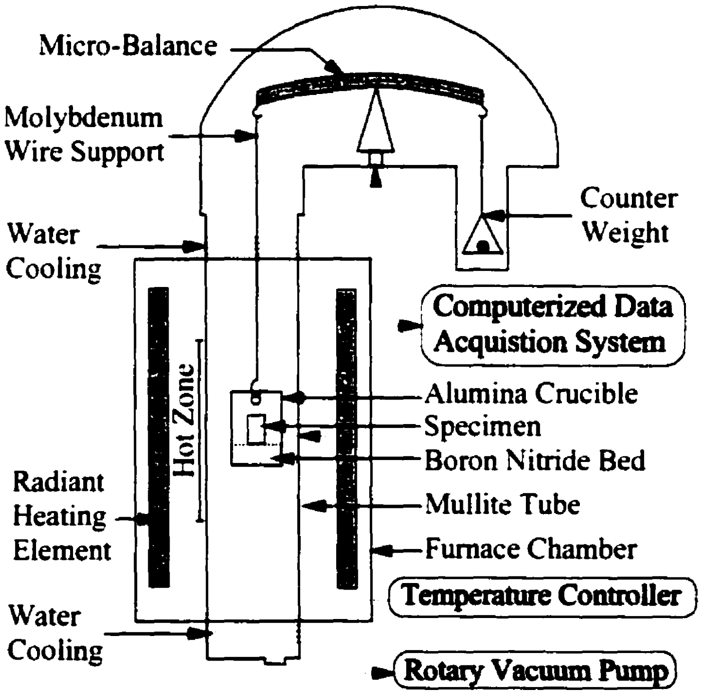

Figure 4.8 Schematic diagram of the set-up used for mass loss analysis during sintering.

4.4 Hot Working

All high temperature deformation-assisted sintering experiments were performed on a computerized Materials Testing System (*MTS 810*), adapted for hot compression tests, as shown in Figure 4.9. The equipment consisted of a load frame rated for a maximum load of 25 kN, a hydraulic power supply and closed loop servohydraulic and computerized outer loop systems. The high temperatures were attained with a Research Incorporated radiant furnace (16 kW power rating), interfaced with a Micristar digital programmer and controller. After the completion of each deformation test, the load and displacement data were transferred to a personal computer for analysis. The compression anvils were made of TZM alloy (molybdenum-based alloy containing a dispersion of 0.5% Ti and 0.08% Zr oxides) which have high strength and creep resistance properties at elevated temperatures.

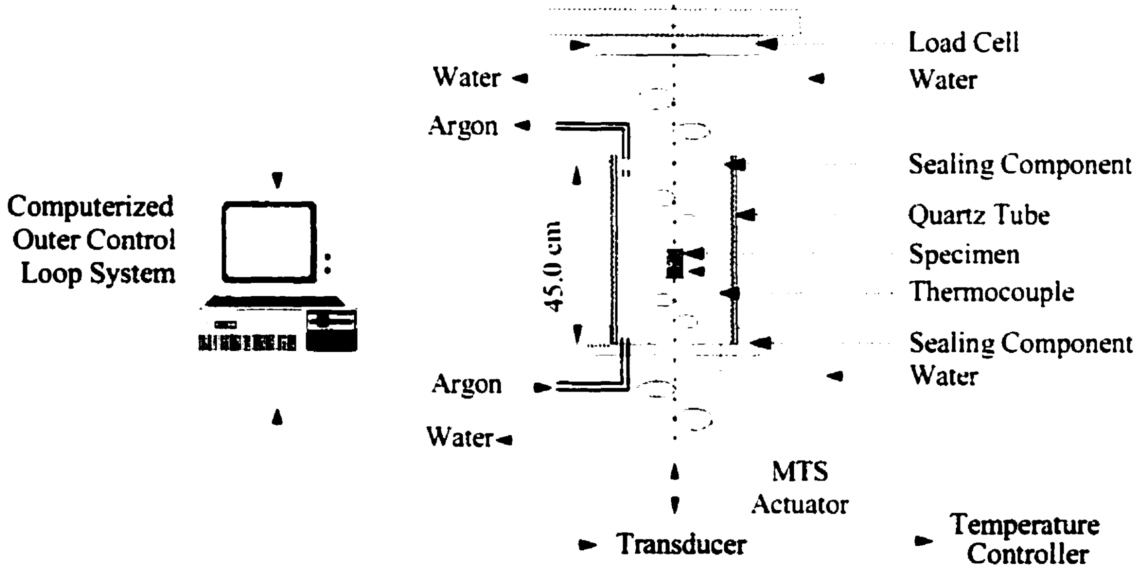

Figure 4.9 Schematic diagram of the compression testing equipment.

The thermal cycle and deformation schedule of a single hit deformation test are shown in Figure 4.10. The compression specimen was placed between the upper and lower compression anvils. Boron nitride and thin sheets of mica were used to reduce the friction between the smooth faces of the specimen and compression anvils.

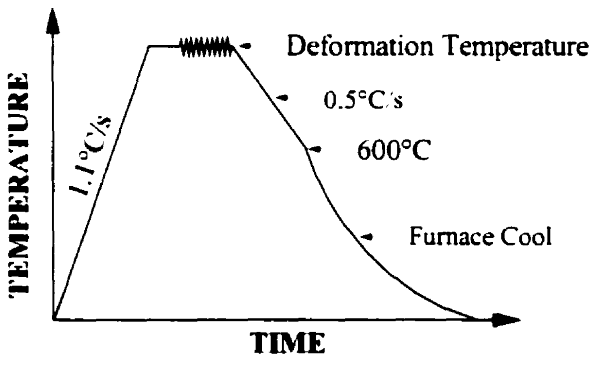

Figure 4.10 The heating and deformation schedule.

To minimize oxidation, the specimen and anvils were enclosed by a quartz tube sealed with O-rings in which a high purity argon atmosphere was maintained. The temperature was measured and controlled by a type K (chromel-alumel) closed ended thermocouple in contact with the specimen. The accuracy of the temperature measurement was checked periodically by placing a second thermocouple in contact with another region of the specimen. The maximum temperature difference in the specimen was within ± 3°C. The heat required for high temperature compression testing was generated by four tungsten filament lamps of the water-cooled radiant furnace, which was mounted on the columns of the MTS load frame. The heat from the filaments was reflected to the furnace center (where the specimen is located) by four mirror-finished elliptically shaped aluminium reflectors. Each specimen was heated, at a constant rate of $1.11°C \cdot s^{-1}$, to the deformation temperature, and held for 5 minutes to homogenize the temperature in the specimen. The specimen was deformed isothermally at a constant strain rate in the range of 5×10^{-4} to $5 \times 10^{-2}\ s^{-1}$ up to a total strain of 80%. Deformation temperatures were selected above and below the nominal β transus (~ 988°C for Ti-6%Al-4%V), ranging from 850°C to 1200°C. The specimen was then furnace cooled to 600°C at a constant rate of $0.5°C \cdot s^{-1}$ to ensure uniform transformation conditions for all test schedules.

4.5 Densification Investigation

4.5.1 Archimedes Technique for Density Measurement

The density of the sintered or deformed Ti-6%Al-4%V-TiC composites was measured as described in ASTM standard C373-72[235]. This density measurement method depends on Archimedes' principle, where the difference in the wet weight of the composite specimen in air compared to the weight suspended in water is a measure of the volume. The procedure involved first measuring the dry weight (D) of the specimen. Then the specimen was boiled in distilled water for 5 hours and soaked in this water for an additional 24 hours. The wet suspended weight in water (S) and the wet weight in air (M) were measured. The following equations were then used to determine the bulk density (ρ_B) and percent relative density (RD):

$$V_B = \frac{M-S}{\rho_{water}} \tag{4.1}$$

$$\rho_B = \frac{D}{V_B} = \frac{D}{M-S} \tag{4.2}$$

$$\mathrm{RD}(\%) = \frac{\rho_B}{\rho_{th}} \times 100\% \tag{4.3}$$

where ρ_{th} and V_B are the theoretical density of the composite (as calculated by the rule of mixtures using the reinforcement volume fraction and the theoretical density of each phase) and the bulk volume (cm^3), respectively.

4.5.2 Image Analysis Technique for Density Measurement

Image analysis is a technique that processes an image to extract quantitative information related to the amount, size and distribution of phases (*e.g.* pores, TiC particles). To extract such quantitative information, the specimens were prepared for optical metallography (as described in the next section) and examined using the *Leco L2002* image analysis system. Each optical image was transformed into a binary digitized image constructed of successive gray levels ranging from numerical values of 0 to 255 (*i.e.* black to white). The quantity of the phase of interest (*e.g.* percent porosity, TiC volume fraction) was then measured by area percent (ratio of the total area of detected phase to the image frame area). Besides density measurement, image analysis was also used to provide information on the pore size. The pore size was measured using two techniques: one based on a feret average calculation and the other by an equivalent spherical diameter measurement. The feret calculation is an average of straight-line measurements made between two parallel tangents at various angles in 8 different directions (0, 22.5, 45, 67.5, 90, 112.5, 135, and 157.5°). The equivalent spherical diameter estimation is based on measuring the area of the feature and then equating this area to an equivalent spherical feature of this diameter. All measurements were averages based on 400 fields per specimen (180 and 220 fields in the longitudinal and transverse directions, respectively), with the fields preset on an automatic stage facility.

4.6 Microstructural Investigation

4.6.1 Metallographic Preparation

The procedures required for preparation of composite materials for microscopic examination can deviate substantially from the conventional techniques that exist for most engineering alloys. The main concerns for composites include pull-out or fracture of friable reinforcement or interface phases, excessive surface deformation (leading to closure or smearing of pores or microcracks), edge-rounding around the pores or reinforcement phase and scratching of the soft matrix phase by the hard reinforcement phase. The techniques developed for the titanium composites minimize the previously mentioned specimen preparation problems and achieve reproducible results.

Initially, the consolidated composites were cut longitudinally into two halves using a *Leco CM-15* slow speed diamond cut-off wheel operated with an oil coolant to protect the specimens from over-heating. A low concentration diamond wafering blade (*Extec Technologies*, Enfield, PA) was selected to minimize surface deformation which in composite materials may result in debonding and microcracking. After sectioning, one half of each specimen was mounted in a low-shrinkage thermosetting powder (silica fiber filled) using a *Leco PR-10* mounting press at a temperature of 125 °C and 28 MPa pressure. As opposed to the phenolic thermosetting powder, which is filled with wood, the silica fiber filled powder achieves superior edge retention and planarity in the specimen. This is due to the higher hardness of the silica filler, which approaches that of the composite materials. The techniques developed for metallographic preparation of the TiC particulate reinforced titanium matrix composites are summarized in Table 4.3. All metallographic preparations were performed on the *Leco VP-150 VARI/POL* automatic grinding/polishing machine equipped with a *Leco AP-50* pressure application unit.

Table 4.3 - Metallographic preparation technique for titanium composites

Stage	***Surface***	***Lubricant***	***Time***	***Force***	***Speed***
Planar Grinding	15 μm diamond abrasive disk	distilled water	Until Plane	2 kg/sample	240 RPM
Rough Polishing	non-woven, perforated fiber pad	6 μm diamond suspension	3 min.	2 kg/sample	150 RPM
	non-woven, fiber resin pad	1 μm diamond suspension	3 min.	2 kg/sample	150 RPM
Final Polishing	chemical-resistant, porous pad	0.06 μm colloidal silica	1 min.	1 kg/sample	120 RPM
Etching	For analysis of porosity, specimens were not etched. For phase and grain boundary contrast, specimens were immersed for 10 to 20 seconds in a solution of 6 ml HNO_3, 3 ml HF and 100 ml H_2O (Kroll's Reagent).[236]				
Remarks	Etchant stains on the microstructure were removed by swabbing the sample for 10 seconds with a solution consisting of 1 ml HF, 2 ml HNO_3, 50 ml H_2O_2 and 47 ml H_2O. Samples were cleaned ultrasonically in ethanol after each stage to minimize contamination during subsequent stages.[236]				

4.6.2 Microscopic Examination

As described previously, optical image analysis (*Leco L2002*) was used on polished specimens to examine the evolution of porosity with changing consolidation conditions. A *Neophot 21* optical microscope was used for photographing all polished and etched specimens. Higher resolution investigation of the microstructural consitituents was performed on a *JEOL JSM-840A* scanning electron microscope (SEM). The microscope was operated in secondary electron (SE) and backscattered electron (BE) mode at an accelerating voltage of 15 keV. The SEM was equipped with an X-ray detector (*TN-96-606ES/518*) and two Tracor Northern systems: (i) the *TN5402* X-ray analysis system enabled chemical analysis and (ii) the *TN8500* Advanced imaging system enabled X-ray mapping and quantified image analysis.

4.7 Interfacial Analysis

4.7.1 Low Voltage Field Emission Gun SEM (LV FEGSEM)

To resolve the interfacial reaction between the titanium alloy matrix and TiC particles, an *Hitachi S-4500* cold field emission gun SEM having a through-the-lens (TTL) objective lens (Fig. 4.11) was used in low voltage operation (1 to 3 keV). Essentially the fine tip of the cold field emission electron source (Fig. 4.12) coupled with the TTL detection system achieved much higher resolution than that of a conventional SEM, it being comparable to that of a transmission electron microscope (TEM). The LV FEGSEM was equipped with an energy dispersive X-ray spectrometer for chemical compositional analysis of the interfacial region.

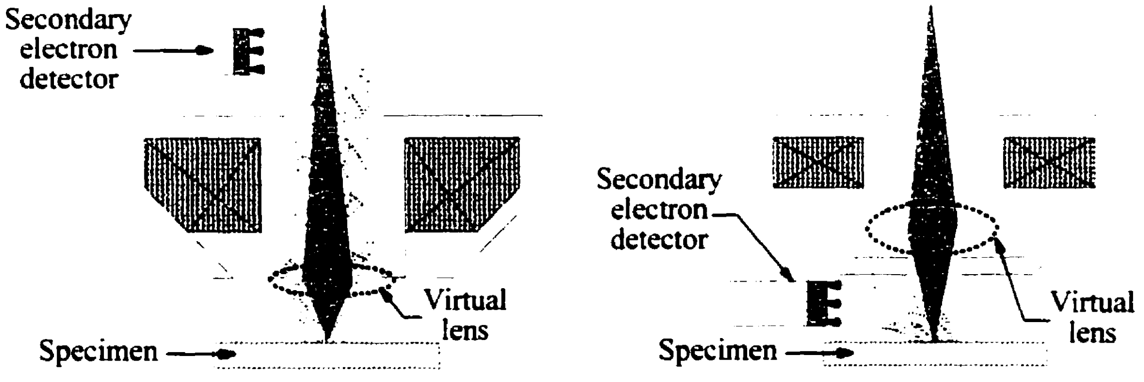

TTL objective lens

Conventional objective lens

Figure 4.11 Schematic diagram comparing the TTL objective lens to the conventional objective lens of a SEM.

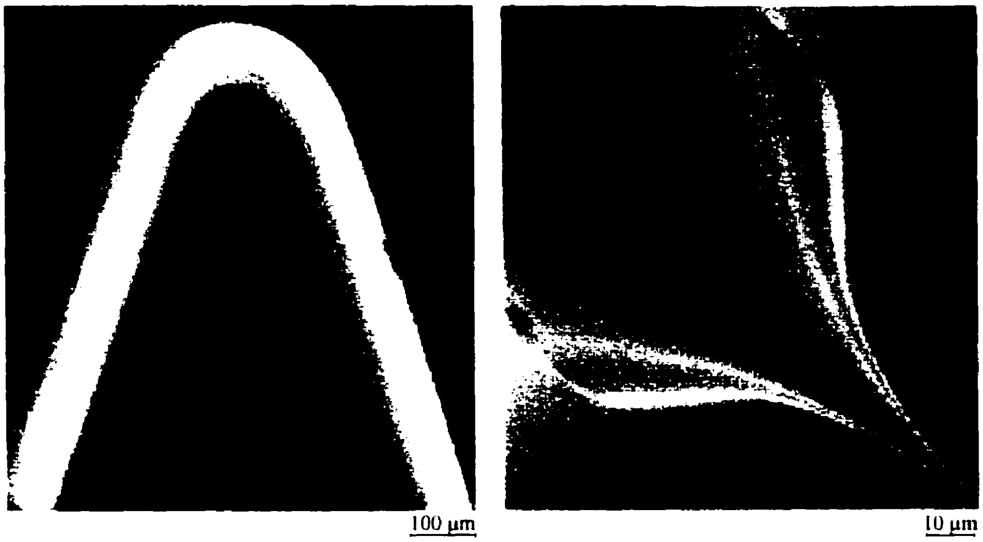

tungsten wire filament oriented single crystal tungsten

Figure 4.12 Comparison of the electron sources illustrating the much finer tip radius (~100 nm) of the field emission source relative to the V-shaped hairpin tip (~100 µm) of a typical filament in a common SEM.

4.7.2 Electron Probe Micro-Analysis

Interfacial reaction investigation was also performed using a *Jeol-8900 Superprobe* Electron Probe Micro Analyzer (EPMA) equipped with wavelength dispersive spectroscopes (WDS) for quantitative compositional analysis. Normalizing the EPMA signal, using a TiC standard, enabled direct measurement of the quantity of carbon along a line analysis from the TiC particles to the Ti-6%Al-4%V matrix. Along this line, measurements for carbon, titanium, aluminium and vanadium were obtained every 2.5 µm at an accelerating voltage of 15 keV and probe current of 12 nA. The size of the electron beam was 1 µm and the x-ray volume generated from the surface of the specimen was estimated to be 2.5 µm in size using a Monte Carlo algorithm written by David C. Joy for the *Hitachi PhiRoZ2W Software.*[237] The error in this quantitative analysis for carbon was estimated to be approximately ±1%.

4.7.3 Neutron Diffractometry

To determine the growth kinetics of the interfacial reaction, the lattice parameter variations during consolidation at elevated temperatures were monitored *in situ* with the *DUALSPEC* neutron powder diffractometer at the *NRU* reactor of *AECL* (Atomic Energy of Canada Limited), Chalk River Laboratories (Fig. 4.13). The diffractometer was equipped with a graphite-element vacuum (~ 1E-4 torr) furnace capable of reaching temperatures as high as 1350°C. The furnace programming and data acquisition system were fully computerized, allowing accurate temperature control and rapid data collection. A unique feature of the diffractometer is an 800-channel position-sensitive detector that spans 80° in scattering angle, 2θ. The wavelength, λ, of the neutron beam was calibrated by measuring the diffraction pattern of a standard powder of alumina, obtained from the National Institute of Standards and Technology.

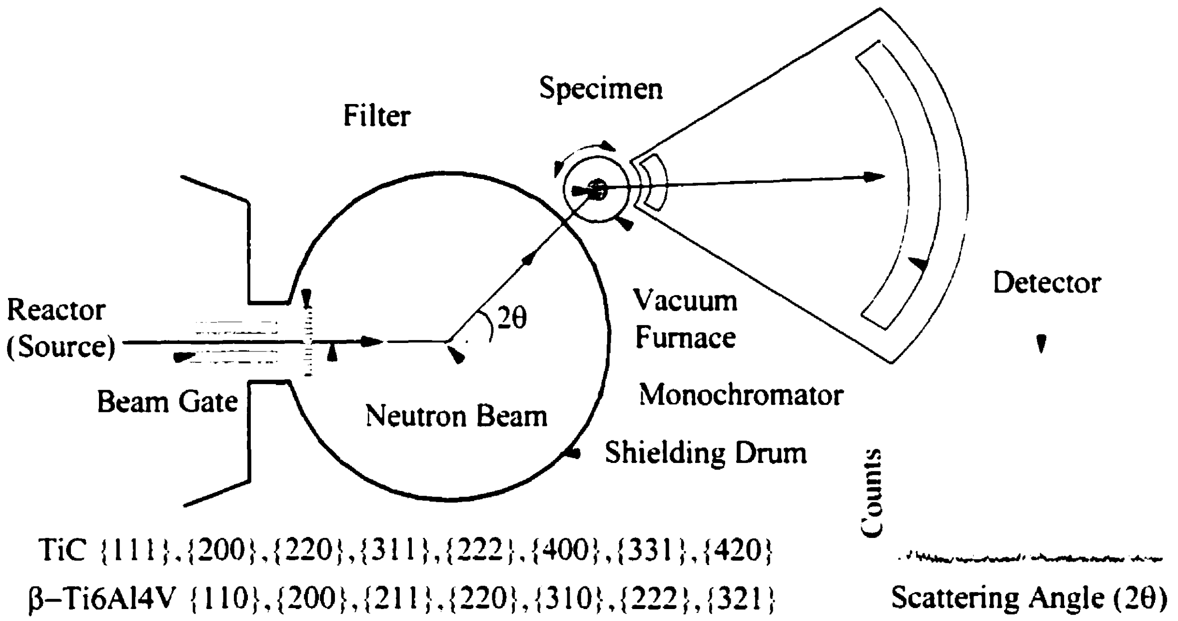

Figure 4.13 Schematic diagram of the neutron powder diffractometer set-up at AECL.

Sintering of the titanium composites at temperatures in the range of 1000°C to 1350°C for long hold times was performed *in situ* while periodically collecting diffraction pattern data. Also, composites formed by deformation-assisted sintering were raised above the beta transus temperature and held at that temperature to observe the extent of chemical reaction after deformation processing. During either processing technique, changes in the diffraction pattern (*i.e.* scattering angle and intensity of the diffraction peaks) occurred with time at temperature. Hence, these neutron diffraction measurements enabled real-time evaluation of the chemical reaction at the particle-matrix interface. Diffraction peaks from the various phases in the composite material were analyzed to obtain the mean scattering angles and integrated intensities at the beginning and after certain hold times. For identification of any phase, the crystallographic interplanar spacings, d_{hkl}, of that phase were determined by measuring the scattering angle, $2\theta_{hkl}$, of the diffraction peaks and substituting into Bragg's law. The lattice parameter, a, of each phase was then corrected for systematic errors in diffraction angle measurements by using the $\cos^2\theta$ extrapolation method to $\theta = 90°$.[238]

4.8 Mechanical Property Measurement

The effect of sintering conditions on the room temperature mechanical properties can be investigated by increasing the specimen size so as to produce standard tensile specimens. Unfortunately fabrication of such specimens can be expensive and difficult. In the case of investigating the effect of deformation-assisted sintering on mechanical properties, small specimen test techniques were necessary, as the specimens tested in compression were too small for conventional mechanical property measurement.

The numerous small-specimen testing methods that have been considered in the literature[239-241] have ranged from a simple scale down of some standard specimen geometry (such as miniature tensile and fatigue samples) to developing methods that utilized a pre-existing, small volume specimen. The corresponding analyses encompassed simple empirical correlations between miniature and standard specimen property data, as well as finite element analyses of small specimen deformation. The development of these methodologies for miniaturized specimens has evolved to minimize the effect of the dimensions and shape of the specimen on the deformation characteristics. Existing engineering standards for property testing incorporate size requirements so as to ensure that measured values are not influenced by grain size and structure, surface conditions, and state of strain. Therefore, in using sub-size specimens, the testing technique had to be developed to account for the effect of the reduction in specimen dimension, such that material properties could be accurately predicted from miniature specimen data. Table 4.4 lists some of the more promising miniature specimen tests, the corresponding specimen volume, the type of analysis undertaken, and the type of property information obtained.

Amongst the various existing techniques, two test methods, the hardness test and shear punch test, are particularly attractive due to the small average specimen volume subjected to deformation and therefore high sensitivity to microstructure. Although hardness testing utilizes a small specimen volume, the test is essentially nondestructive (*i.e.* the material undergoes local deformation only) and the data can be empirically related to the tensile strength of the test material. Alternatively, mechanical property measurement using shear punch testing includes both strength and ductility information since the test material is deformed to failure. Furthermore, the nature and ease of analysis of the raw data and properties is comparable to that performed on data obtained by conventional tensile testing. In the following sections, the use of these two test techniques for extracting mechanical property information is described.

Table 4.4 - Small specimen testing techniques and characteristics

Test	*Average Specimen Volume (mm^3)*	*Nature of Raw Data*	*Type of Properties*	*Nature of Analysis*
Tensile	15	Load-Displacement	$\sigma = f(\varepsilon)$	Direct
Pressurized Tube	350	Diameter-Time	Creep Rate, Rupture Time	Direct Direct
Microhardness				
Diamond Pyramid	<1.7	Load/Area	Strength,	Empirical
Ball	1.7	Load/Area	$\sigma = f(\varepsilon)$	Semi-empirical
Punch				
Ball	1.7	Load-Displacement	Ductility, Strength, $\sigma = f(\varepsilon)$	Analytical Semi-empirical Analytical
Shear	2.5	Load-Displacement	Strength, Ductility	Empirical
Bend	10	Load-Displacement	Strength	Analytical
Fracture	370	Load-Crack Growth	Fracture Toughness	Direct
Impact	200	Load-Time-Temp.	Energy-Absorbed, Strength	Direct Analytical
Fatigue				
S-N	1000	Load-Cycles	S-N	Direct
FCP	245	Crack Length-Cycles	Crack-Growth-ΔK	Direct

4.8.1 Hardness Testing

Using loads in the range of 50-100 g on the *Leco M-400-G2* Vickers Microhardness Tester, the hardness of the TiC reinforcement particles and Ti-6%Al-4%V matrix was determined to examine the effect of processing. The Vickers microhardness value (kg·mm^{-2}) was calculated from scalar measurements of the dimensions of pyramid indentation using a built in microprocessor. On average, at least 25 microhardness readings were taken of each phase to minimize sampling errors.

Hardness assessment of the bulk material was performed by Rockwell K hardness testing by penetrating a 1/8" (3.2 mm) spherical ball indenter into the specimen using a 150 kg load. Prior to testing, a calibration was performed using two standard blocks, one having a hardness of 61.2 ± 0.2 HRK (25.6 ± 0.1 HRC) and the other being 99.8 ± 0.2 HRK

(62.5 ± 0.1 HRC). On average at least 10 readings were obtained for each consolidation condition. Also, the distance between neighboring indentation edges was at least five indent diameters apart in order to minimize the effect of adjacent indentations.

4.8.2 Shear Punch Testing

Shear punch testing was used to complement hardness testing and improve on some of its disadvantages, in particular the high sensitivity to local changes in the microstructure because of smaller sampling volumes and the inability to fracture the specimen. The shear punch apparatus (Fig. 4.14) consisted of an upper and lower housing. The upper housing contained a punch, and the lower one held a die. The material selected for both the punch and die was A2 air hardened tool steel (58 RC). The central axes of the punch and die were exactly aligned in the upper and lower housing. The housings were fitted to the upper and lower rams of the servohydraulic materials testing system load frame (MTS 810 as described previously). The specimen was placed between the die and a washer. The latter prevented the specimen from moving during punching. A flat tip punch was forced through the specimen, and the action of the punch against the die sheared a circular disk from the specimen, completing the test. The punch apparatus can be constructed for any punch sizes (*i.e.* 6.25, 3, or 1 mm) and a 3 mm diameter was selected. By performing the punch operation in a materials testing system load frame, which was equipped with a load cell and displacement transducer, the force on the punch could be monitored as a function of lower housing travel. The specimens were punched under a constant punch displacement rate of 0.667 mm/min.

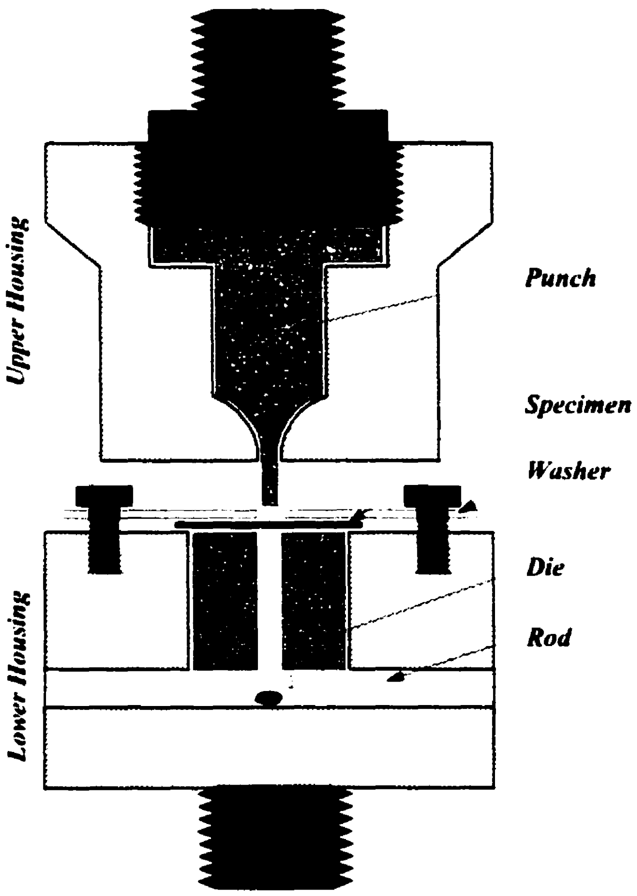

Figure 4.14 Diagram of shear punch apparatus.

CHAPTER 5

METHOD DEVELOPMENT: SHEAR PUNCH TESTING

5.1 Introduction

The development of the shear punch-and-die mechanical testing configuration was initially driven by the demand to assess the effects of irradiation on the mechanical properties from a volume of material small enough to fit into irradiation test assemblies. The miniature sampling feasibility, coupled with previous successes with using shear punch testing for common engineering alloys,[239-240] prompted the present investigation to determine the applicability of this testing technique to discontinuously reinforced composites. The development of this technique would be particularly advantageous for composites due to the simple sample geometry and small sampling volume required for shear punch testing. Presently, the assessment of mechanical property data by means of standard tensile testing is associated with high fabrication costs due to the greater machining difficulty of composite materials as compared to common engineering alloys (*i.e.* greater wear on machining tools, longer machining or grinding time, etc.). Also, tensile testing of composites, and brittle materials in general, is complicated by the need for perfect alignment of the specimen during testing and a specimen surface free of flaws or machining grooves. Hence the ability to evaluate the mechanical properties of composites in a relatively inexpensive and simple manner would contribute immensely to the research and development of these materials.

The shear punch test is based on blanking a circular disk from a fixed sheet specimen. In the case of traditional engineering alloys, a close correlation between tensile shear punch data and tensile test data has been identified, thus permitting a means of evaluating the flow properties when only a small amount of material is available[241-242]. In employing shear punch testing for discontinuously reinforced composites, the punch load-displacement data must be examined to identify the critical regions of the flow curve associated with deformation of the material, i.e. elasticity followed by yielding, work hardening, ultimate tensile strength and fracture. The load-displacement curves generated in shear could then be compared to the conventional tensile curves in order to calibrate the former method and develop the strength and ductility correlations for the composite materials.

5.2 Experimental Procedures

Empirical correlations for composites were generated by calibrating the data from shear punch tests with standard tensile tests[243] using the range of materials with and without reinforcement as shown below:

5.2.1 Materials

(1) Steel (1022, 1045, 1050, 3405, 3406, and 3407)

(2) Copper alloys (annealed copper, 70/30 annealed brass and 70/30 cold worked brass)

(3) Cobalt-chromium-molybdenum ASTM F1537 alloy

(4) Squeeze cast A356 aluminium in both as-fabricated and T6 condition

(5) Squeeze cast A356 aluminium reinforced with Saffil Al_2O_3 (5, 10, and 15 vol.%) short fiber composites in both as-fabricated and T6 condition

(6) 6061 aluminium reinforced with Al_2O_3 (10, 15 and 20 vol.%) in the T6 condition

(7) Mill annealed Ti-6%Al-4%V

(8) Ti-6%Al-4%V produced by powder metallurgy processing using pre-alloyed powder

(9) Ti-6%Al-4%V reinforced with TiC (5, 10, 15, and 20 vol.%) and produced by powder metallurgy processing using pre-alloyed powder

The various steel compositions were supplied by *Stelco Incorporated* (Hamilton, ON, Canada). The copper alloys were provided by *Drummond McCall* (Montreal, QC, Canada). Both the as-received copper (99.9% pure) and cold rolled 70/30 brass were annealed at a temperature of 525°C for 20 minutes. The Co-Cr-Mo alloy was supplied by *Wright Medical Technologies* (Arlington, TN, USA). The A356 Al based short fiber reinforced composites, containing up to 15 vol.% Saffil short alumina fiber, were fabricated at McGill University by the squeeze casting technique in which preforms containing up to 15 vol.% Saffil Al_2O_3 fiber were infiltrated by the liquid A356 melt under pressures ranging from 20 to 60 MPa.[244-245] The 10, 15 and 20 vol.% Al_2O_3 particle reinforced 6061 Al composites, produced by liquid mixing, were supplied by *Alcan Corporation* (Kingston Laboratories, ON, Canada). The mill annealed $\alpha+\beta$ titanium alloy was supplied by *RMI* (MI, USA). The titanium alloy composites, containing up to 20 vol.% of TiC reinforcement particles, were fabricated using the powder metallurgy technique of powder blending, cold pressing and sintering, as described previously in this work.

5.2.2 Shear Punch Specimen Preparation

To obtain the final geometrical size required of the shear punch specimens, the various materials were sliced into blanks of roughly 1 mm thickness using a *Leco CM-15* slow speed diamond cut-off saw (Fig. 5.1). The surfaces of each slice were then mechanically ground on successively finer silicon carbide grinding paper (220, 320, 400 and 600-grit) followed by rough polishing with 6 μm and 1 μm diamond suspensions (water-based) to a final thickness of roughly 0.35 mm ± 0.03 mm.

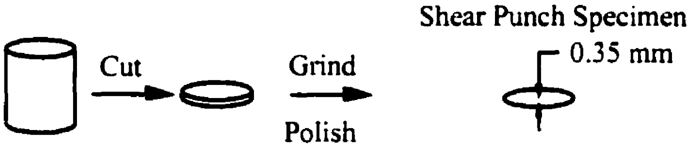

Figure 5.1 Schematic diagram showing specimen preparation for shear punch testing.

5.3 Applicability of the Shear Punch Test for Composites

The general behavior of a specimen during shear punch testing is illustrated by the load-displacement curve shown in Figure 5.2. The curve has features similar to a load displacement curve produced in a uniaxial tension test: an initial linear region, followed by a departure from linearity, a non-linear increase in load with displacement, a maximum in the load, and a decreasing load with displacement to the point of failure.

The stages of deformation of the specimen pertaining to these features were revealed by stopping the test at various stages during deformation, and examining the specimen. An example of part of this analysis is shown in Figure 5.2 in which Ti-6%Al-4%V/TiC specimens were sectioned perpendicular to the punched surface to determine the degree of penetration at various points on the load displacement curve, and etched to reveal the microstructure. For all the materials tested, the point of initial departure from linearity corresponded to permanent penetration of the punch into the specimen, as shown in Figure 5.2 a. Further deformation proceeds in an annular region approximately coincident with the clearance between the punch and the die hole, as indicated by Figure 5.2 b. In the region between initial penetration and the load maximum, the material strain hardens in response to the decreasing specimen thickness in the annular (shear) deformation zone. Immediately after the maximum load, fracture begins to occur, as illustrated by Figure 5.2 c. The specimen thickness decreases considerably in the plastic deformation region with increasing punch displacement until failure occurs, as depicted in Figure 5.2 d.

The volume of material undergoing plastic deformation in the region between initial penetration and maximum load can be estimated using the tolerance (approximately 25.4 μm) between the punch and die as follows

$$\begin{aligned} \text{Plastic Zone} &\cong V_{\text{annulus}} \cong V_2 - V_1 \cong \pi t\left(\frac{d+c}{2}\right)^2 - \pi t\left(\frac{d}{2}\right)^2 \\ &\cong \pi\cdot 0.36\cdot\left(\frac{3+0.0254}{2}\right)^2 - \pi\cdot 0.36\cdot\left(\frac{3}{2}\right)^2 \cong 4 \times 10^{-2}\ \text{mm}^3 \end{aligned} \tag{5.1}$$

where t is the thickness of the punched disk,
d is the diameter of the punch, and
c is the tolerance between the punch and die

This volume of 4×10^{-2} mm^3 is considerably greater than the plastic zone associated with microhardness testing (~4×10^{-4} mm^3).[241] Thus the sensitivity errors associated with small sampling volumes in microhardness testing are reduced using the shear punch testing technique.

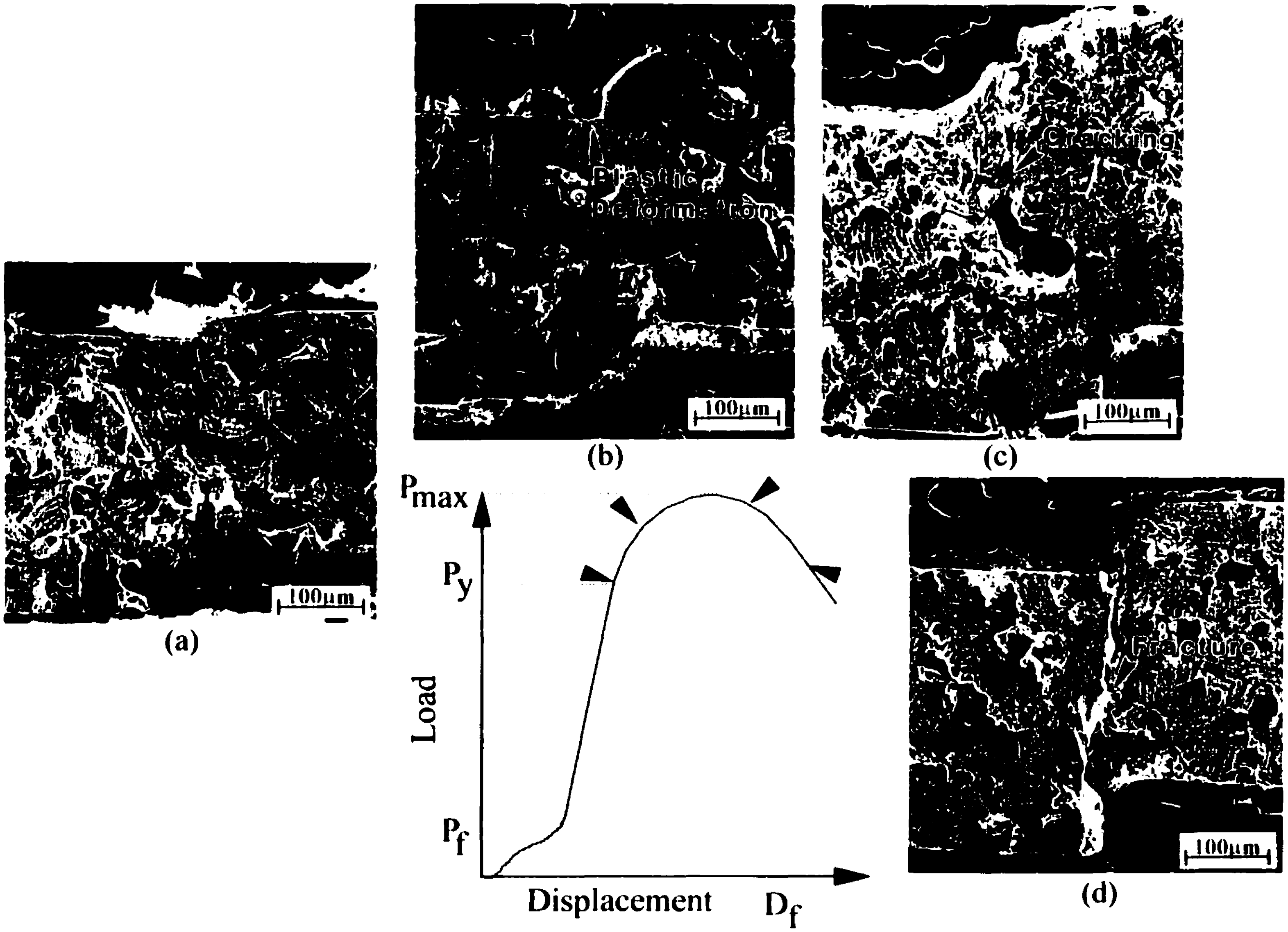

(a) (b) (c) (d)

Figure 5.2 Typical load-displacement curve of a shear punch test and SEM micrographs of a Ti-6%Al-4%V/TiC composite specimen cross-section, depicting the extent of deformation at several points of displacement. P_f, P_y, P_{max}, are the friction, yield and maximum loads and D_f is the displacement at fracture.

To determine the stress state in this annular process zone, a number of slip line fields have been calculated in previous work.[241] The stress state was established to be primarily one of shear with tension and bending contributions also occurring. For engineering alloys, there was also evidence of a strong hydrostatic state of tension in the annular process zone during the final phases of plastic deformation. Thus failure occurs in a similar manner to that in tension testing for these materials. Fractography (*i.e.* a view of the edge of a punched and fractured disk), as illustrated in Figure 5.3 a, reveals essentially two regions: a smooth zone caused by the penetration of the punch, followed by fracture. The size of the smooth zone depends on the material and is apparently a function of the ductility of the material. The fracture surface region of the disk reveals details related to the nature of the failure in the material. In the case of the metals, fracture occurred by a ductile-dimple mode, as shown in Figure 5.3 b for mill annealed Ti-6%Al-4%V. Essentially, microvoids nucleate in the annular process region, and under continued straining these grow and coalesce until one or more cracks are generated and cause failure by rapid propagation through the remaining material.

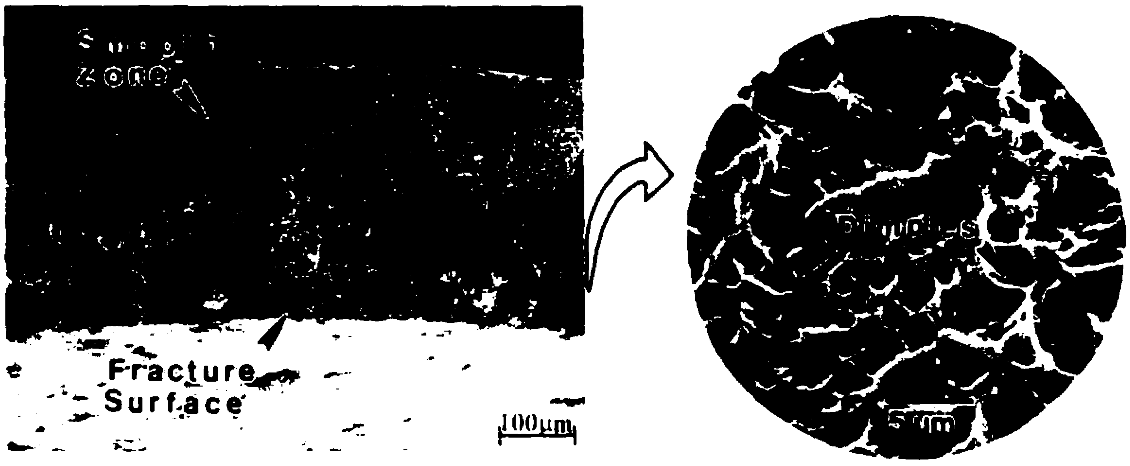

(a) (b)

Figure 5.3 SEM fractograph of a shear punched disk of Ti-6%Al-4%V showing ductile failure in the remaining ligament. (Specimen was punched from the top.)

By maintaining a constant specimen thickness, the shear load-displacement behavior of the various materials can be compared to some extent, as shown in Figure 5.4. During shear punch testing, all materials tested exhibited the general load-displacement behavior as illustrated in Figure 5.2. For the materials tested, the observed load-displacement curves appear to correspond with the tensile results; the mechanical properties of aluminium-based composites were the lowest, followed by the copper, titanium and steel-based materials.

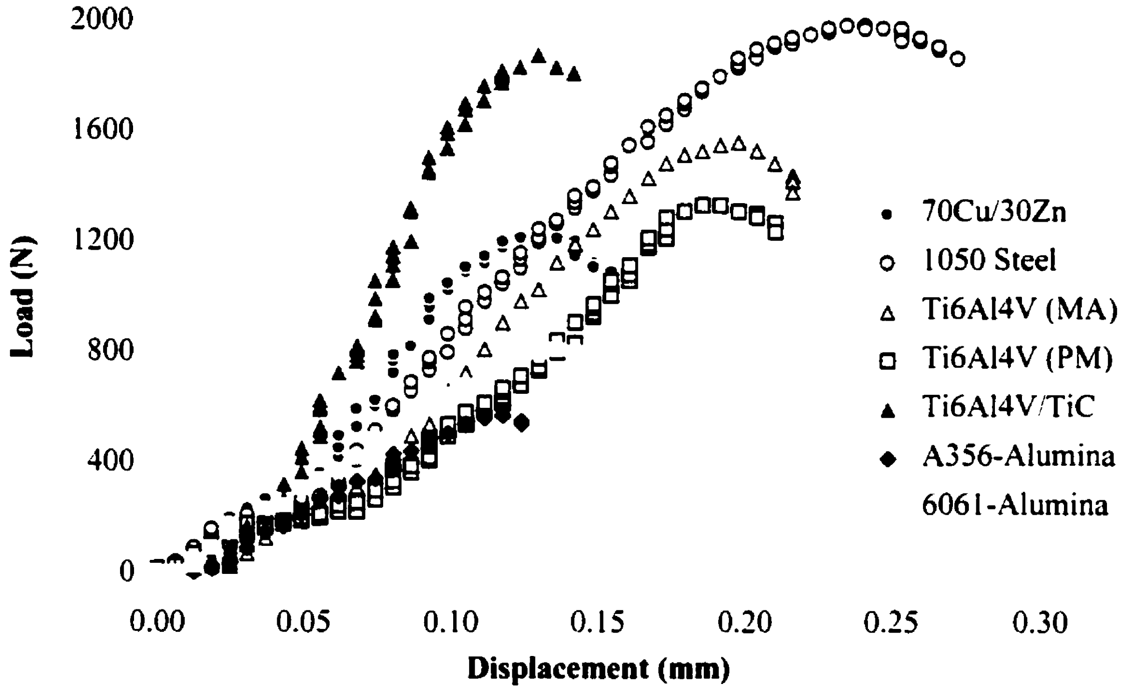

Figure 5.4 Load-displacement curves in a shear punch test for various materials.

Previous work on shear punch testing of various alloys has established that the deformation and failure processes, which occur during shear punching, are analogous to those that occur in uniaxial tension. It was thus the purpose of this work to concentrate on the deformation and failure behavior during shear punch testing of discontinuously reinforced materials (*i.e.* Al_2O_3 particle reinforced 6061 Al, Saffil fiber reinforced A356 and TiC particle reinforced Ti-6%Al-4%V).

As shown previously, deformation and failure processes can be investigated by sectioning the specimen to analyze the penetration of the punch at various points on the load-displacement curve (Fig 5.2 a-d). Alternatively, the degree of penetration can be monitored through the development of the fracture surfaces on the side opposite to the punch. Surface observation of the Al_2O_3 particle reinforced 6061 Al alloy composite at the point of permanent penetration (Fig. 5.5 a), load maximum (Fig. 5.5 b) and fracture (Fig. 5.5 c) indicates that the characteristics of the shear punch flow curve are similar to those observed in tension. That is, the point of deviation from linearity corresponds to permanent penetration of the shear punch and beyond the load maximum failure begins to occur. Final fracture (Fig. 5.5 c) in the Al_2O_3 particle reinforced 6061 Al composite appears to occur by a combination of ductile failure in the matrix (*i.e.* by void nucleation, growth and coalescence) and fracture or debonding of the reinforcement particle (depending on the strength and nature of the interfacial region).

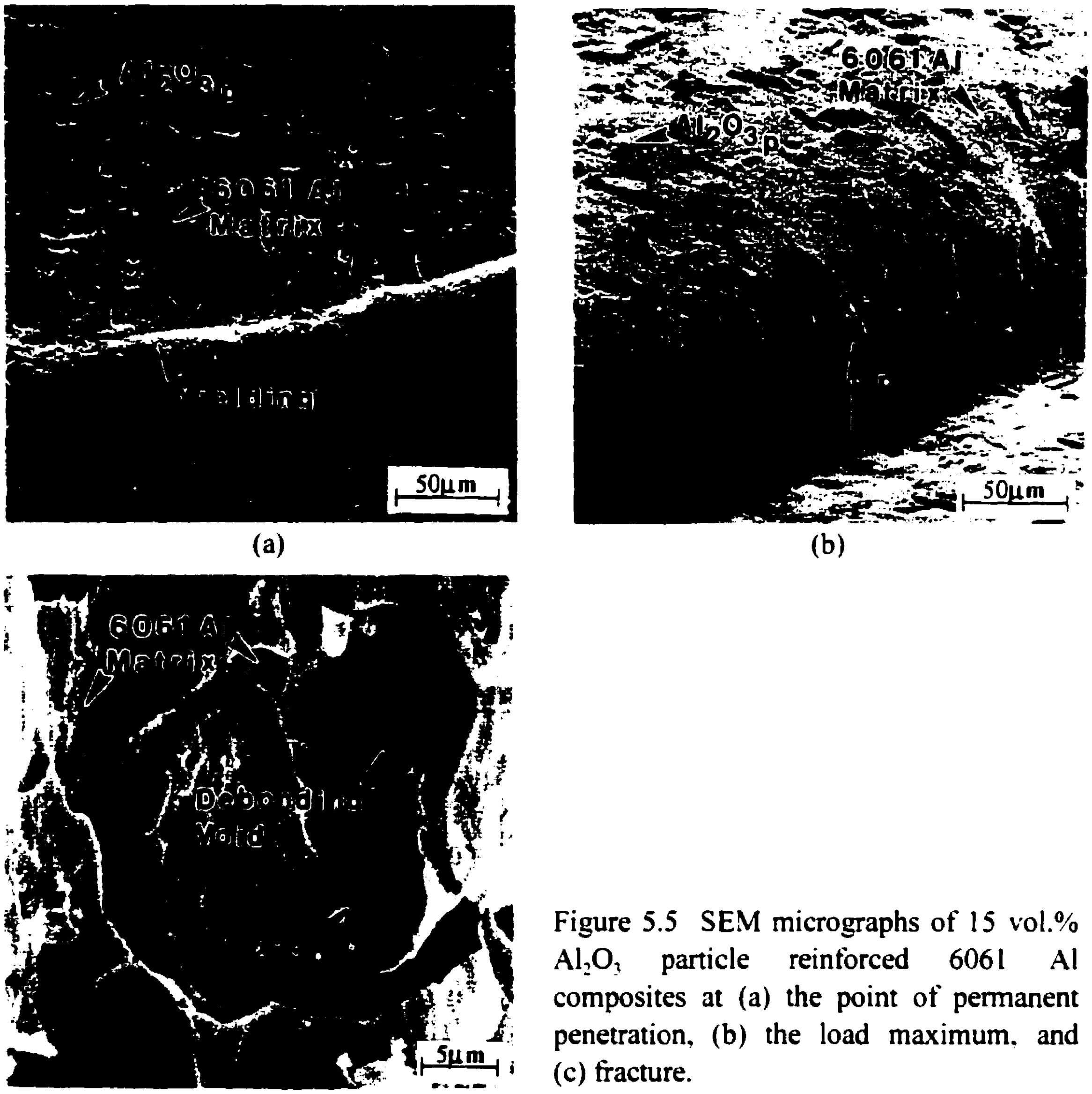

(a)

(b)

(c)

Figure 5.5 SEM micrographs of 15 vol.% Al_2O_3 particle reinforced 6061 Al composites at (a) the point of permanent penetration, (b) the load maximum, and (c) fracture.

Similar deformation characteristics were observed for the Saffil Al_2O_3 short fiber reinforced A356 composites (Fig. 5.6). Again, the point of deviation from linearity corresponded to permanent penetration of the punch (Fig. 5.6 a). However, it appears that at the load maximum (Fig. 5.6 b) failure processes have commenced, as indicated by the formation of two surfaces. This corresponds well to the flow curve observations, which reveal failure just beyond the load maximum (Fig. 5.4). For the A356 composites, the fracture surface reveals randomly oriented fibers intimately bonded with the matrix (Fig. 5.6 c). Due to the strong fiber-matrix bonding, little fiber pullout was observed, and residual matrix and/or interface material was apparent on the fibers.

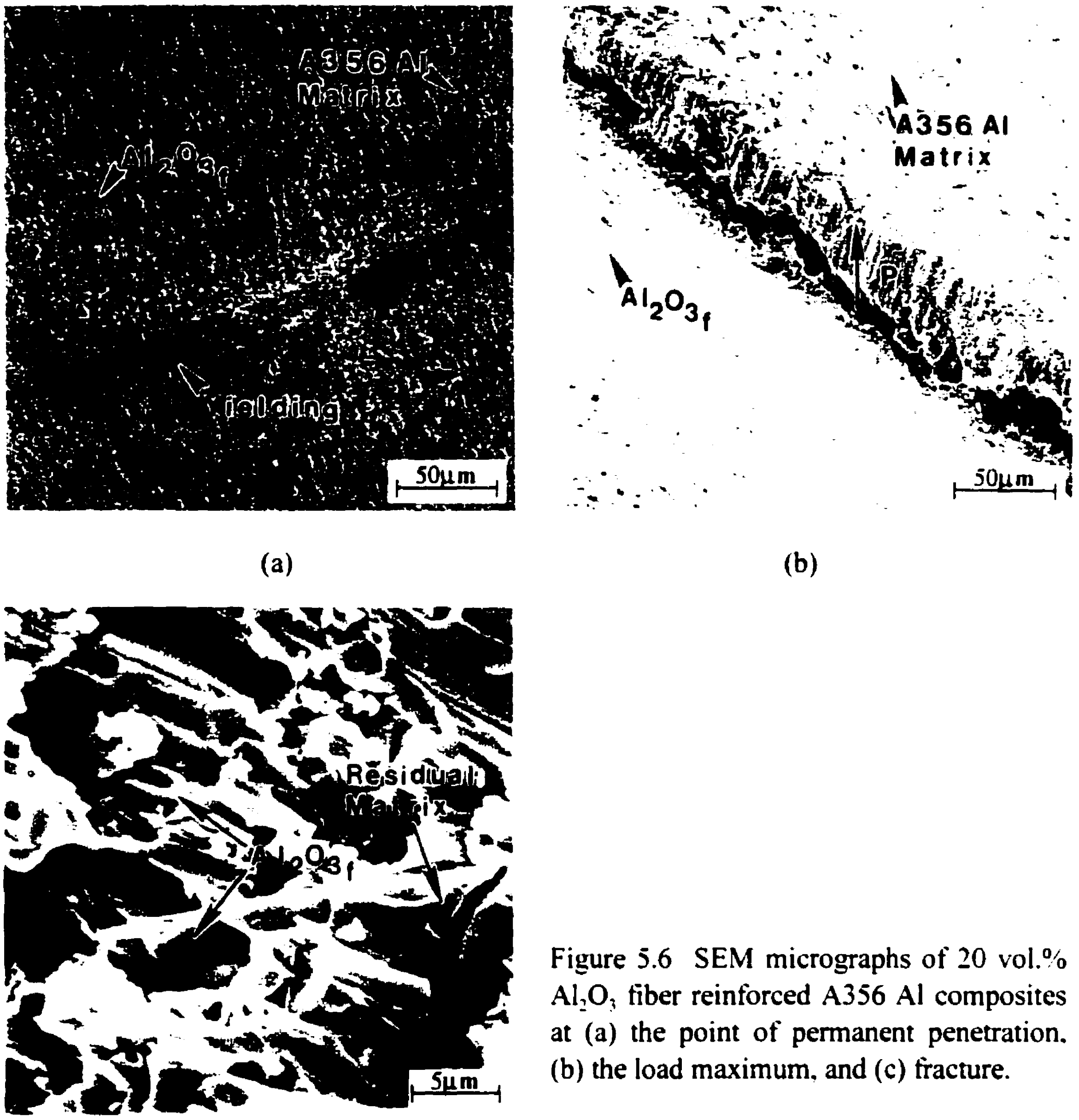

(a)

(b)

(c)

Figure 5.6 SEM micrographs of 20 vol.% Al_2O_3 fiber reinforced A356 Al composites at (a) the point of permanent penetration, (b) the load maximum, and (c) fracture.

Deformation and fracture characteristics of the TiC particle reinforced Ti-6%Al-4%V alloy composites produced by powder metallurgy processing are shown in Figure 5.7. The deformation behavior (Fig. 5.7 a and 5.7 b) is again similar to that observed for the other composites. However, fracture in these composites appears to occur by a mixture of ductile and brittle failure in the matrix, and debonding or fracture of the TiC reinforcement particles (Fig. 5.7 c). The latter has been determined to be influenced by the presence and size of the pores in the as-received reinforcement. No interfacial reaction products were apparent on the debonded TiC reinforcement particles.

The viability of shear punch testing for determining tensile mechanical property information relies on the degree of correspondence of the deformation features and load-displacement data with those obtained in uniaxial tension. The fracture surfaces in uniaxial tension for Ti-6%Al-4%V, Al_2O_3 particle reinforced 6061 Al, Saffil Al_2O_3 short fiber reinforced A356 and TiC particle reinforced Ti-6%Al-4%V, shown in Figure 5.8, closely correspond to shear punch fracture surface observations (Fig. 5.9). It was thus reasonable to perform a data correlation analysis to calibrate the load-displacement results in shear punch testing to that in uniaxial tension.

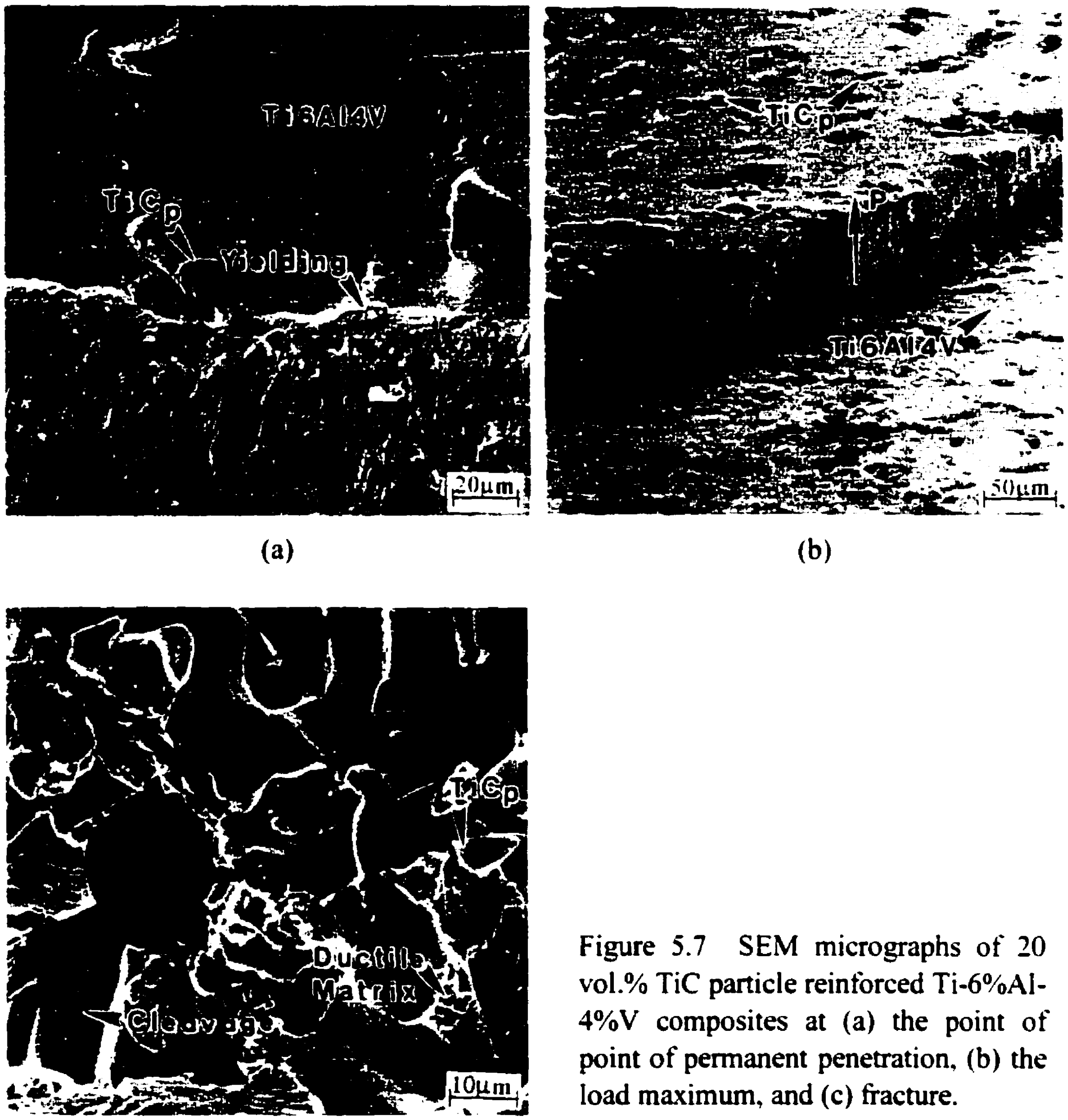

(a) (b)

(c)

Figure 5.7 SEM micrographs of 20 vol.% TiC particle reinforced Ti-6%Al-4%V composites at (a) the point of point of permanent penetration, (b) the load maximum, and (c) fracture.

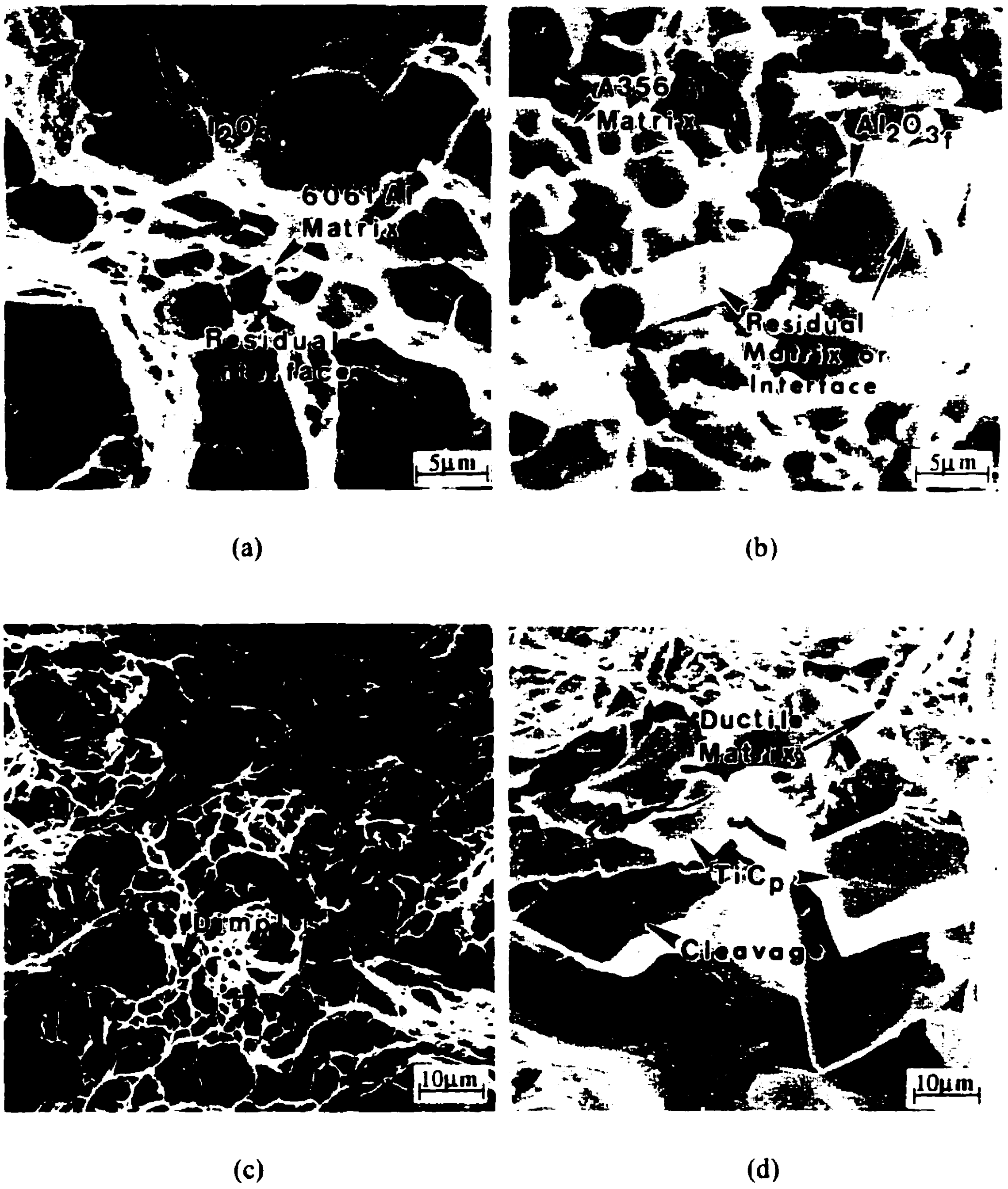

(a) (b)

(c) (d)

Figure 5.8 SEM micrographs of the fracture surface in uniaxial tension for (a) 15 vol.% Al_2O_3 particle reinforced 6061 aluminium, (b) 20 vol.% Saffil Al_2O_3 fiber reinforced A356 alloy, (c) Ti-6%Al-4%V and (d) 20 vol.% TiC particle reinforced Ti-6%Al-4%V alloy.

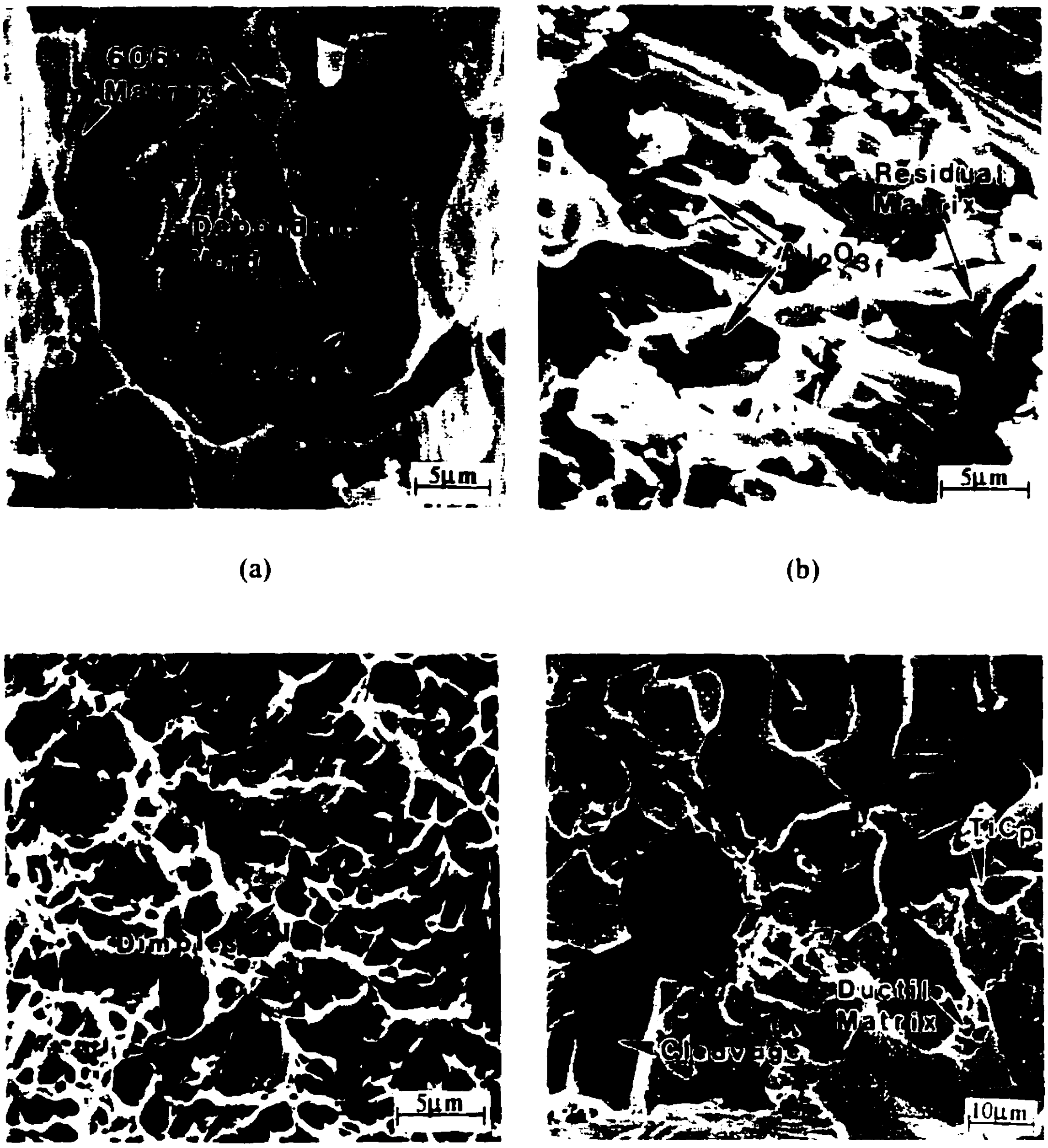

(a) (b)

(c) (d)

Figure 5.9 SEM micrographs of the fracture surface in shear punch testing for (a) 15 vol.% Al_2O_3 particle reinforced 6061 aluminium, (b) 20 vol.% Saffil Al_2O_3 fiber reinforced A356 alloy, (c) Ti-6%Al-4%V and (d) 20 vol.% TiC particle reinforced Ti-6%Al-4%V alloy.

5.4 Data Correlations for Composite Materials

In order to calibrate shear-punch data with the standard tensile data, a series of shear punch and uniaxial tension tests were performed at room temperature. In general, at least six shear punch tests and three to five tensile tests were performed for each material. For metallic materials, round tension test specimens were designed according to ASTM standard E 8M-94a.[243] For the powder metallurgy materials, standard round tension test specimens were machined to have the dimensions illustrated in Figure 5.10.[243]

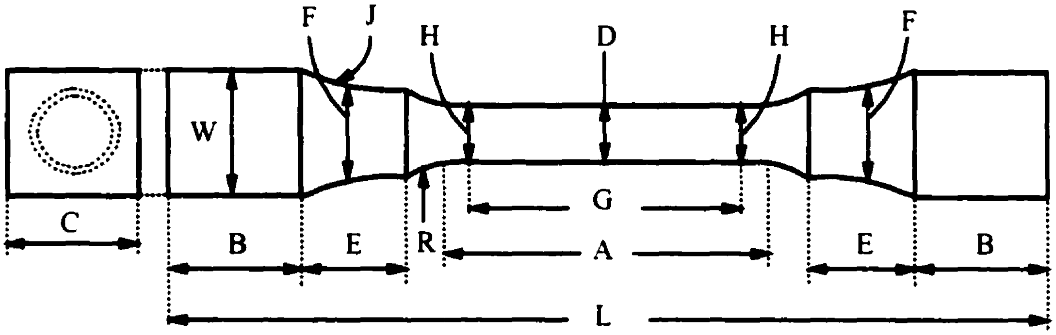

Figure 5.10 Schematic configuration of the tensile test specimen.

where G = Gage length, 25.45 ± 0.03 mm,
D = Diameter at center of reduced section, 4.75 ± 0.03 mm,
H = Diameter at ends of gage length, 4.85 ± 0.03 mm,
R = Radius of fillet, 6.35 ± 0.03 mm,
A = Length of reduced section, 47.65 ± 0.03 mm,
L = Overall length of tensile specimen, 75 mm,
B = Length of end section, 7.85 ± 0.03 mm,
C = Thickness of sintered compact, 10.0 ± 0.03 mm
W = Die cavity width, 10.0 ± 0.03 mm,
F = Diameter of shoulder, 6.35 ± 0.03 mm,
J = End fillet radius, 1.3 ± 0.03 mm

It was found that the load at departure from linearity, P_y, correlates well with the uniaxial yield stress and that the load maximum, P_{max}, correlates with the ultimate tensile strength, according to the following empirical equation:[241]

$$\sigma_{eff} = \frac{P - P_f}{2\pi rt} = C\sigma \tag{5.2}$$

where P is either the yield or maximum load from the shear load-displacement curve, σ is the corresponding yield or maximum stress in tension, σ_{eff} is the effective yield (P_y) or ultimate stress (P_{max}) in shear punch testing, P_f is the friction load, r is the punch radius, t is the specimen thickness, and C is the correlation coefficient. P_f, P_y, and P_{max} can be determined from the load-displacement curve as shown in Figure 5.2. The friction between the various contacting surfaces (*e.g.* specimen and punch or specimen and die) gives rise to the friction load, P_f.

By applying the above correlation, it was found that, for the yield data (Fig. 5.11), $C = 0.55$, and for the maximum load data (Fig. 5.12), $C = 0.65$. The 95% confidence interval on the predicted σ for a given P is ±9% of σ_y for yield and ±7% of σ_{uts} for ultimate tensile strength. The uncertainty is somewhat larger for the yield strength predictions as opposed to the maximum load because of the greater difficulty associated with determining P_y. For instance, to obtain a distinguishable point of deviation from linearity, it is essential that the initial punch penetration of the specimen be uniform around the circumference. The yield point is thus particularly sensitive to proper alignment of the punch and die.

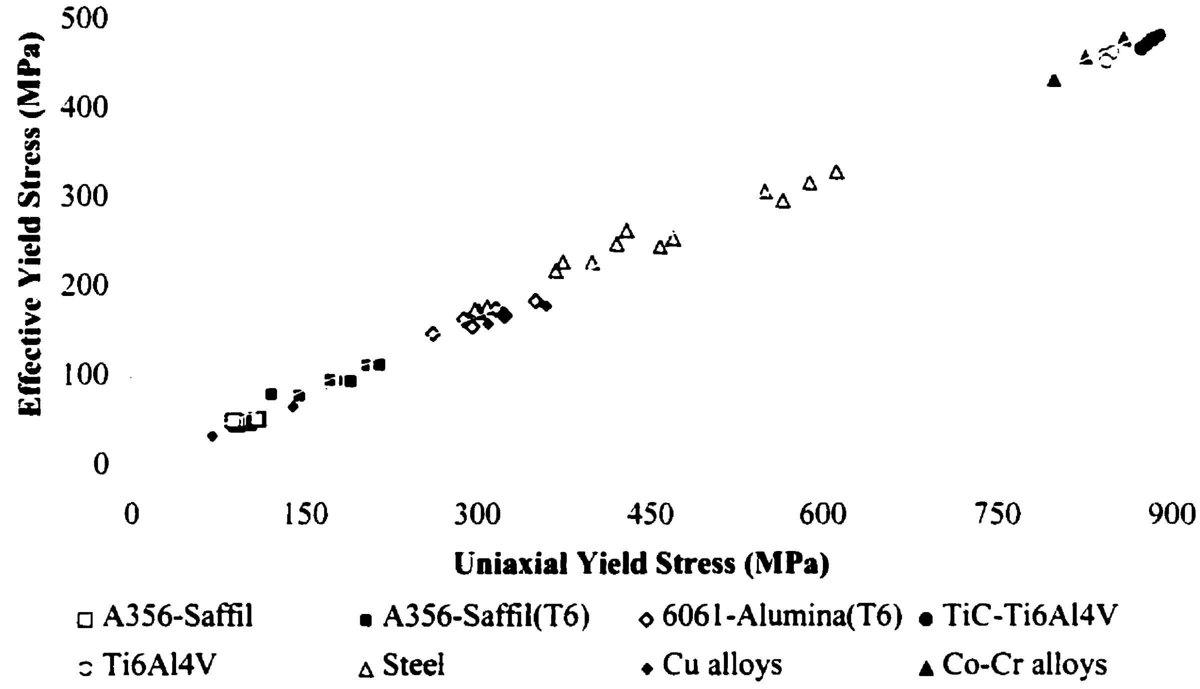

Figure 5.11 Comparison of the shear yield data with yield strength from uniaxial tensile data. The solid line is the regression line for the yield data.

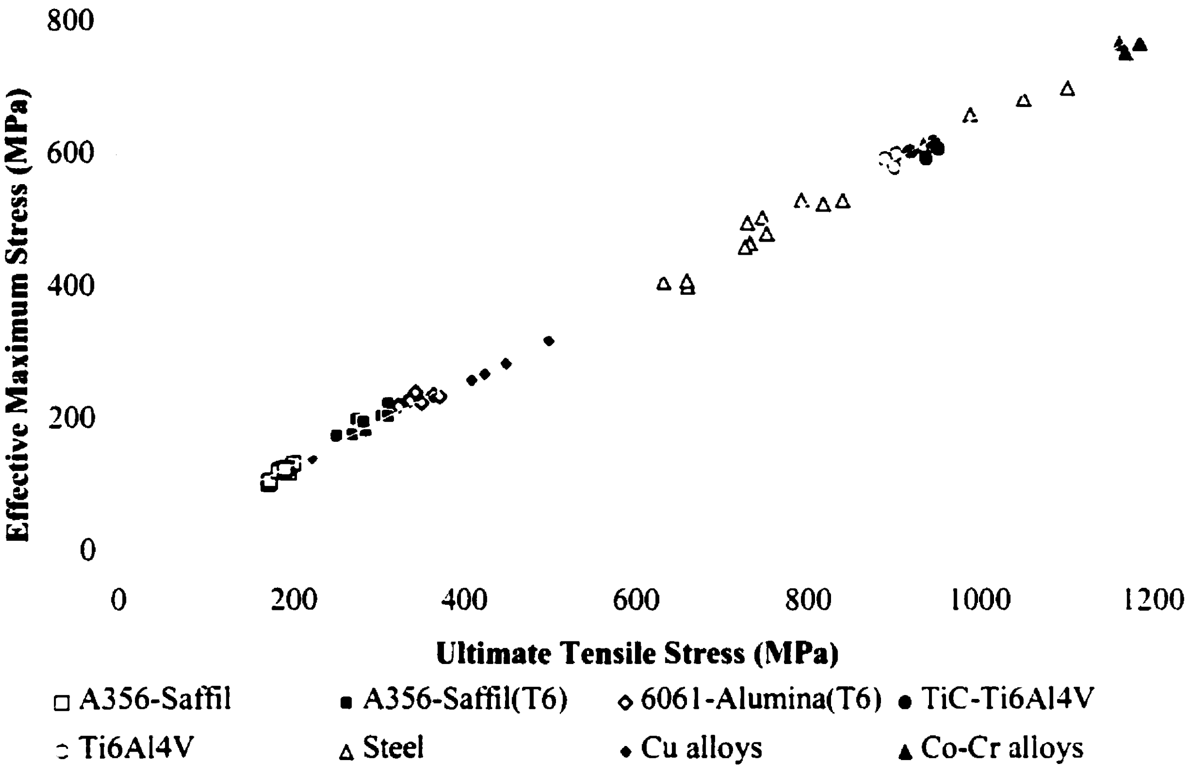

Figure 5.12 Comparison of the ultimate tensile strength determined by the shear punch and uniaxial tensile testing. The solid line is the regression line for the maximum load data.

Shear punch data have also been used to determine the ductility of materials by correlating the ratio D_f / t from shear punch tests with either the reduction in area[241] or total percent elongation.[242] For the materials tested, the latter correlation best fits the shear punch data as illustrated in Figure 5.13. This linear relationship is intuitively satisfying in that D_f should be zero for completely brittle material and D_f should be equal to the specimen thickness for completely ductile materials. The 95% confidence interval on the percent elongation for a given D_f/t is ± 3% of the elongation.

There have also been attempts to use shear punch test data to determine the work-hardening behavior of traditional engineering alloys. However, significant scatter in the data has resulted in a high error of ± 40% and low predictability for the work-hardening exponent in these materials. In the case of the discontinuously reinforced composites, the scatter in the data for the work-hardening exponent was found to be even greater on account of the smaller uniform plastic deformation region in these materials. Thus a correlation for the work-hardening exponent was not developed in this work for the discontinuously reinforced composites.

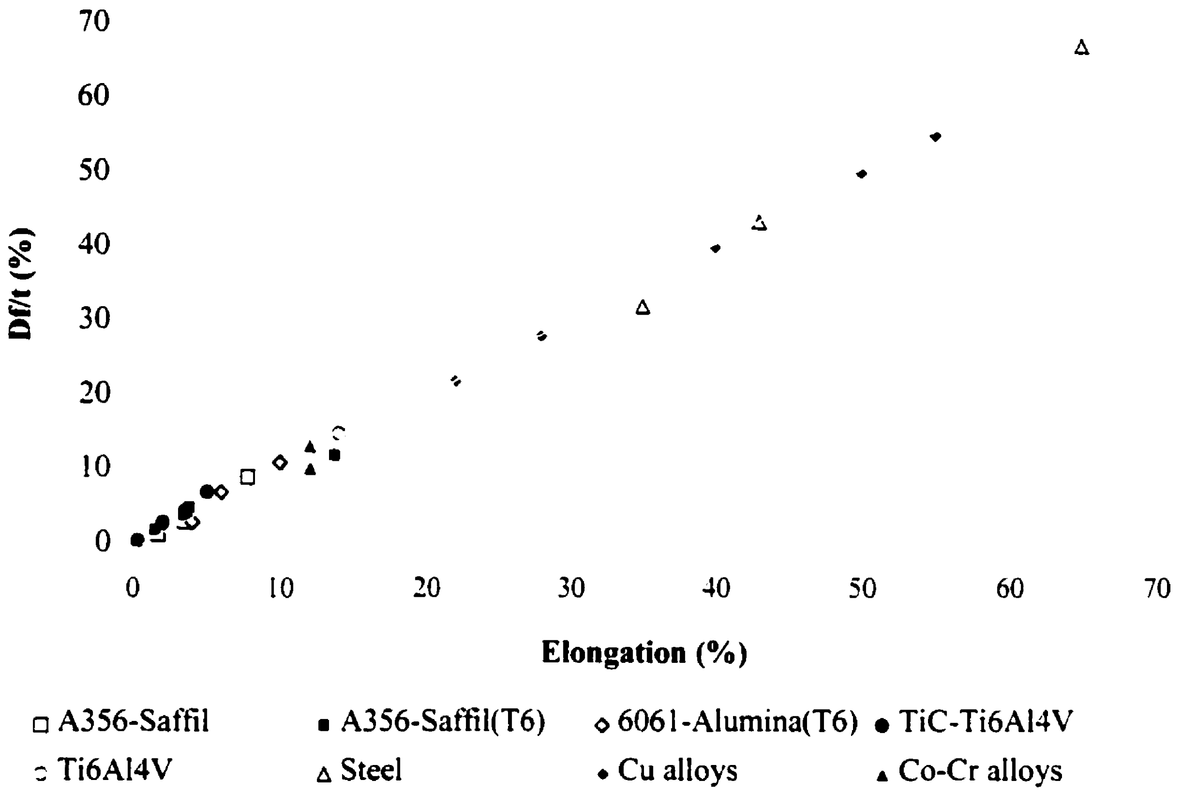

Figure 5.13 Comparison of D_f/t with percent elongation measured in uniaxial tension. The solid line is the regression line for the ductility data.

5.5 Mechanical Property Evaluation

The shear punch test approach has been shown to be a viable alternative to tensile testing for evaluating the mechanical properties of composite materials. As compared to tensile testing, the small sample volume and simple specimen geometry characteristics of the shear punch testing technique are particularly advantageous in the case of composites as there are high costs associated with both the fabrication and machining of these materials. In addition, evaluation of the mechanical properties after certain processing conditions (*e.g.* deformation-assisted sintering) is not possible by the standard tensile test. In such cases, microhardness testing has often been used to estimate the properties. However, a limitation of the microhardness testing is that the specimen is not deformed to failure and thus only the deformation characteristics can be obtained (*e.g.* yield strength). Also, the volume of material deformed is two orders in magnitude smaller than that in shear punch testing (4 x 10^{-2} mm^3). Hence the test is very sensitive to the specimen surface condition (*i.e.* parallel top and bottom surfaces and specimen surface finish) and microstructure.

Given that empirical correlations between the standard tensile data and the shear punch data have been developed for determining the strength and ductility characteristics for discontinuously reinforced composite systems, the shear punch test, once calibrated, can provide a rapid and cost-effective means of assessing the mechanical properties from a relatively small sample volume.

CHAPTER 6

PROCESSING BY SINTERING

This investigation concerns the P/M processing and characterization of TiC particulate reinforced Ti-6%Al-4%V composites. As mentioned in the literature survey, no extensive work has been performed on the low cost fabrication of these composites. Much of the consolidation work to date has involved hot isostatic pressing to full densification and as such has incurred high processing costs. Thus, an objective of this present work to develop a processing route that achieves low temperature consolidation to near-complete densification while offering flexibility for microstructural modification at low processing costs. Ultimately, an assessment of the mechanical properties of this composite system will determine the feasibility of using this material for demanding applications (*i.e.* properties beyond those achievable of conventional metallic materials). In this chapter, composites processed by sintering alone will be characterized for densification, microstructure and mechanical properties.

6.1 Powder Processing

The as-received powder of Ti-6%Al-4%V was blended thoroughly with various proportions of TiC powder. Selection of the mixing time required a preliminary examination of the grinding conditions that would achieve maximum removal of the oxide layer on the Ti-6%Al-4%V powder and a uniform dispersion of the TiC particles. This investigation first involved attrition milling the Ti-6%Al-4%V powder in isopropanol for 15, 30 and 60 minutes. It was found that milling for more than 15 minutes caused work hardening and flaking of the Ti-6%Al-4%V powder as illustrated in Figure 6.1. Using a *STRÖHLEIN ON-mat 822* analyzer, the oxygen content of the as-received Ti-6%Al-4%V powder was determined to be 0.25 wt.%, which is similar to the oxygen level specified by *Micron Metals Inc.* (as reported in Table 4.1). After attrition milling the Ti-6%Al-4%V powder for 15, 30 and 60 minutes, the oxygen content was found to be 0.19 wt.%, 0.15 wt.% and 0.17 wt.% ± 0.04 wt.%, respectively. Although the milling results indicated the lowest oxygen content for 30 minutes grinding, flaking and working hardening of the Ti-6%Al-4%V particles led to poorer packing during compaction of the powder milled at times greater than 15 minutes. Moreover, the compressibility of the powder attrition milled for 15 minutes was similar to that of the as-received Ti-6%Al-4%V powder. Nonetheless, milling for 15 minutes was found to improve the sinterability of the material in previous work.[89] For determining the conditions for uniform dispersion of the TiC particles, the two powders were attrition milled in isopropanol for 15 and 30 minutes. The blended powder mixtures were then observed and, as illustrated in Figure 6.2, no significant improvement in TiC dispersion was observed. Hence the attrition milling conditions were fixed at 15 minutes grinding in isopropanol for all compositional mixtures.

The blended powder mixtures were then compacted in two stages, uniaxially and isostatically. The pressures applied during uniaxial and isostatic pressing enabled rearrangement of the powder, particle contacting and plastic deformation of the metal powders. The pressures selected for compaction (*i.e.* 172.5 MPa and 207 MPa for uniaxial and isostatic pressing, respectively) were sufficient to obtain adequate green strength for handling the compacts without causing cracking or crumbling of the green compacts during processing.

Uniaxial pressing was advantageous in providing good dimensional control for shaping of the component. However, axial pressurization alone causes nonuniformity in the density distribution leading to differential shrinkage during sintering, and possibly warpage, distortion, or cracking of the component. By subsequently applying cold isostatic pressing to axially shaped components, good dimensional control and uniform density distribution was possible.

For compaction, a broad particle size distribution would be beneficial, since finer particles can be accommodated between adjacent coarser particles, giving high green densities.[187] Also, finer particles are more difficult to compact, since large pores collapse under lower pressures than fine pores. In processing the Ti-6%Al-4%V-TiC composites, the large particle size and narrow size distribution of the Ti-6%Al-4%V powder was found to be beneficial because the finer TiC particles occupied the void spaces between the larger

Ti-6%Al-4%V particles in contact. Hence the difference in particle sizes and size distributions of the two powders improved the packing conditions, as illustrated by the increase in green density with increasing volume fraction of TiC particles (Fig. 6.3). The percent porosity of the compacted composites ranged from 33 to 38%. However, due to the broad TiC particle size distribution local agglomeration was found to occur due to several TiC particles fitting in each void spacing, as illustrated in Figure 6.4a.

(a) (b)

(c) (d)

Figure 6.1 Effect of attrition milling time on the Ti-6%Al-4%V powder: (a) as-received, (b) after 15 minutes, (c) after 30 minutes and (d) after 60 minutes.

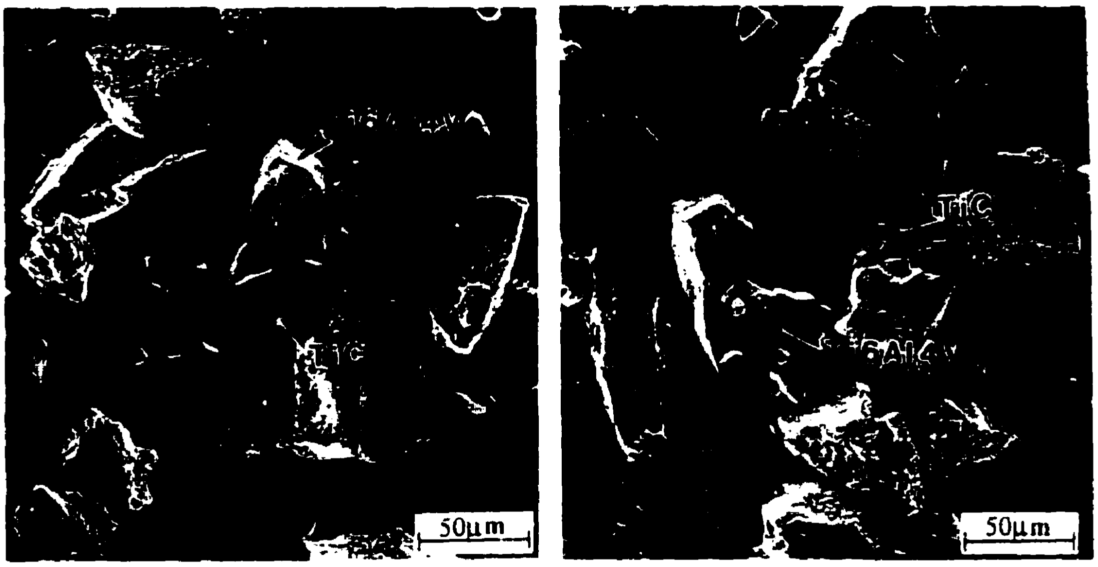

(a) (b)

Figure 6.2 Effect of milling time on TiC dispersion in Ti-6%Al-4%V powder: (a) 15 minutes and (b) 30 minutes.

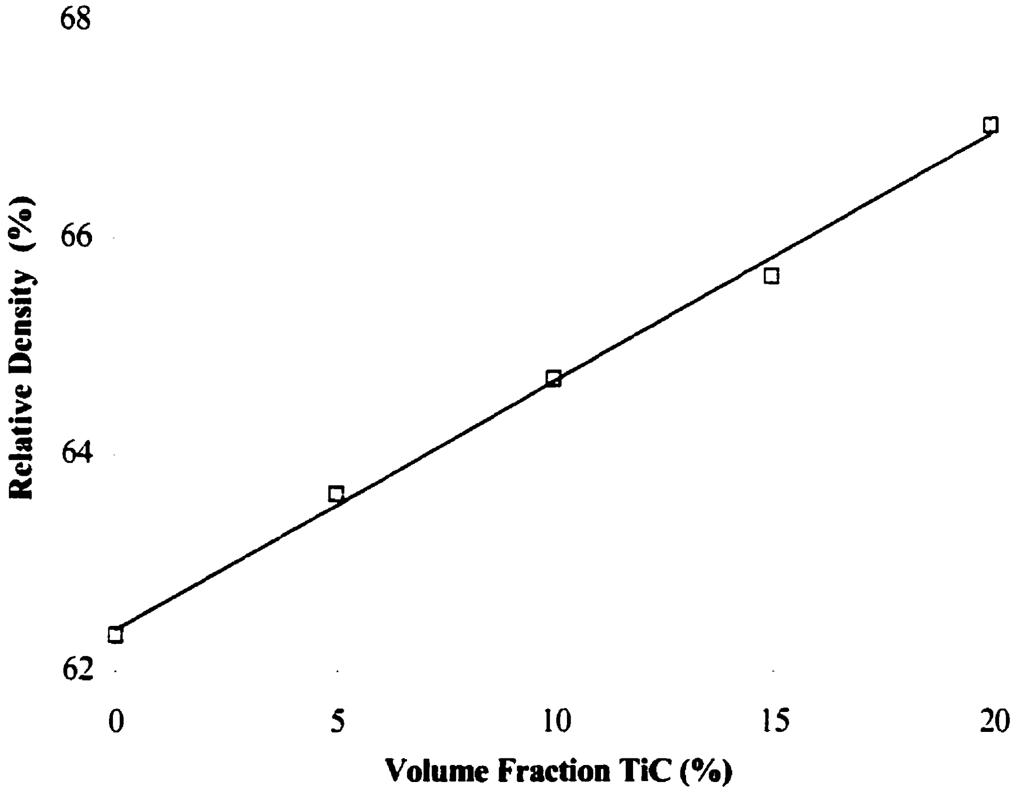

Figure 6.3 Green density of the Ti-6%Al-4%V-TiC composites after uniaxial and isostatic compaction.

The effect of particle shape on compaction is difficult to predict concisely. An irregular powder shape usually gives lower apparent density and hinders the achievement of a high pressed density. However, an irregular powder can also lead to a higher green strength because of mechanical interlocking.[187] In the case of the Ti-6%Al-4%V-TiC composites, the angular shapes of both powders resulted in some bridging during compaction, producing large or irregularly shaped pores as illustrated in Figure 6.4b.

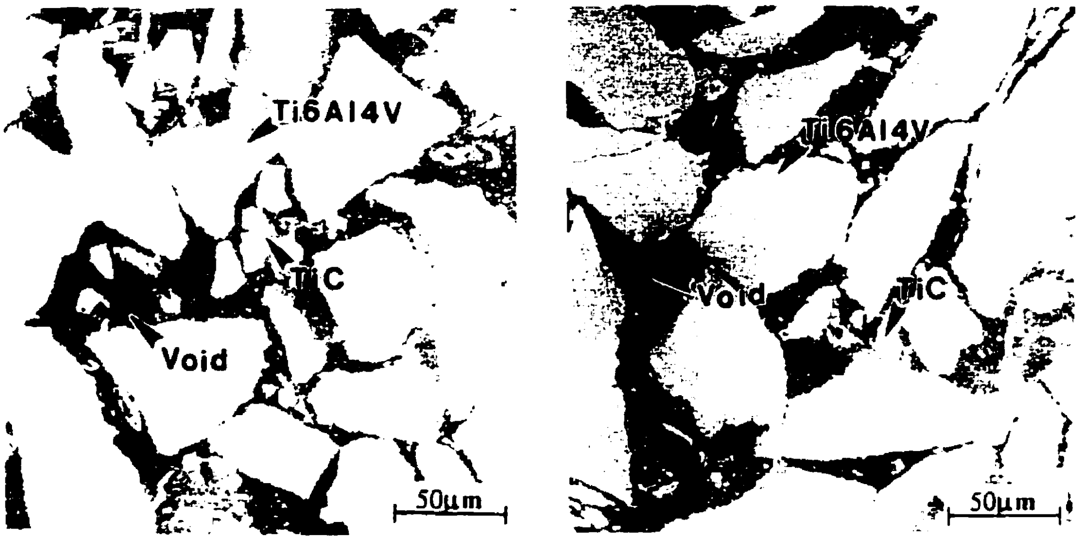

(a) (b)

Figure 6.4 (a) Local clustering of the TiC reinforcement particles in the void spaces of the contacting Ti-6%Al-4%V matrix particles and (b) regions of large irregularly shaped pores after compaction due to angular morphology of the as-received powders of Ti-6%Al-4%V and TiC.

6.2 Sintering

6.2.1 Densification Behavior

The compacted specimens were then sintered at temperatures of 1100°C, 1300°C and 1500°C for times of 0.5, 1, 2 or 4 hours. The relative density was determined for all sintering conditions using the Archimedes' method and optical image analysis techniques. Figure 6.5a illustrates the effect of the isothermal sintering temperature and hold time on densification, as determined by the Archimedes' method, of the composites containing TiC particles in volume fractions ranging from 0 to 20%. Microstructural investigation of the percent porosity by image analysis techniques, Figure 6.5b, indicates similar trends for the effects of sintering temperature, hold time and TiC volume fraction on densification.

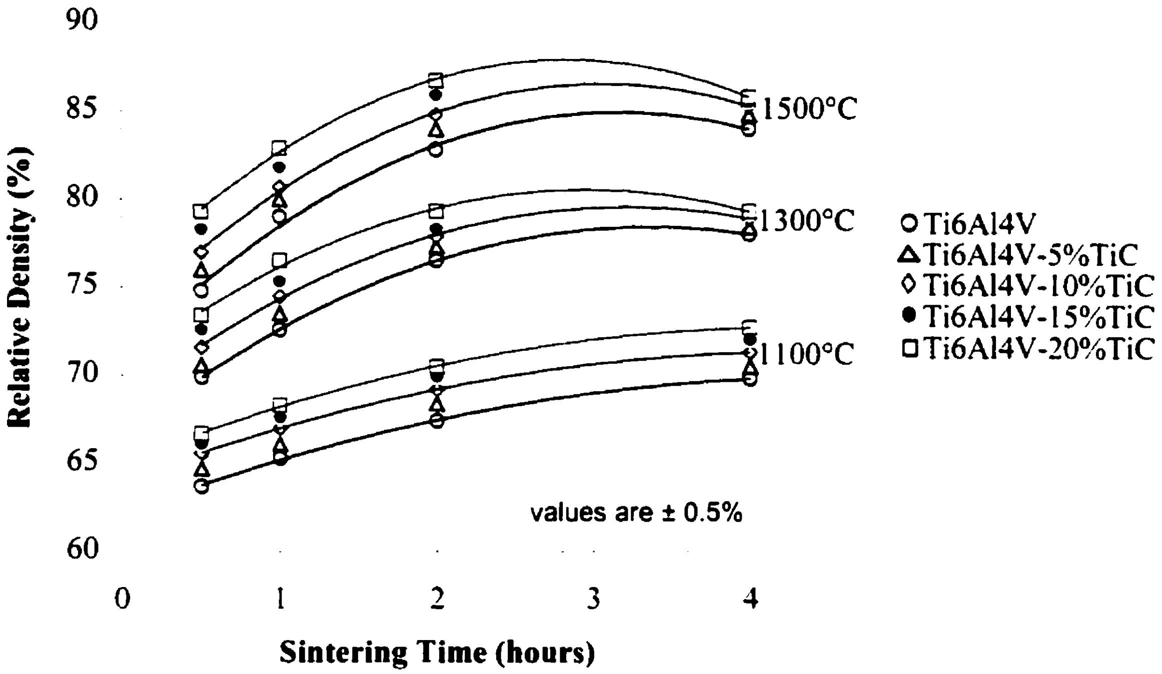

(a) Archimedes method

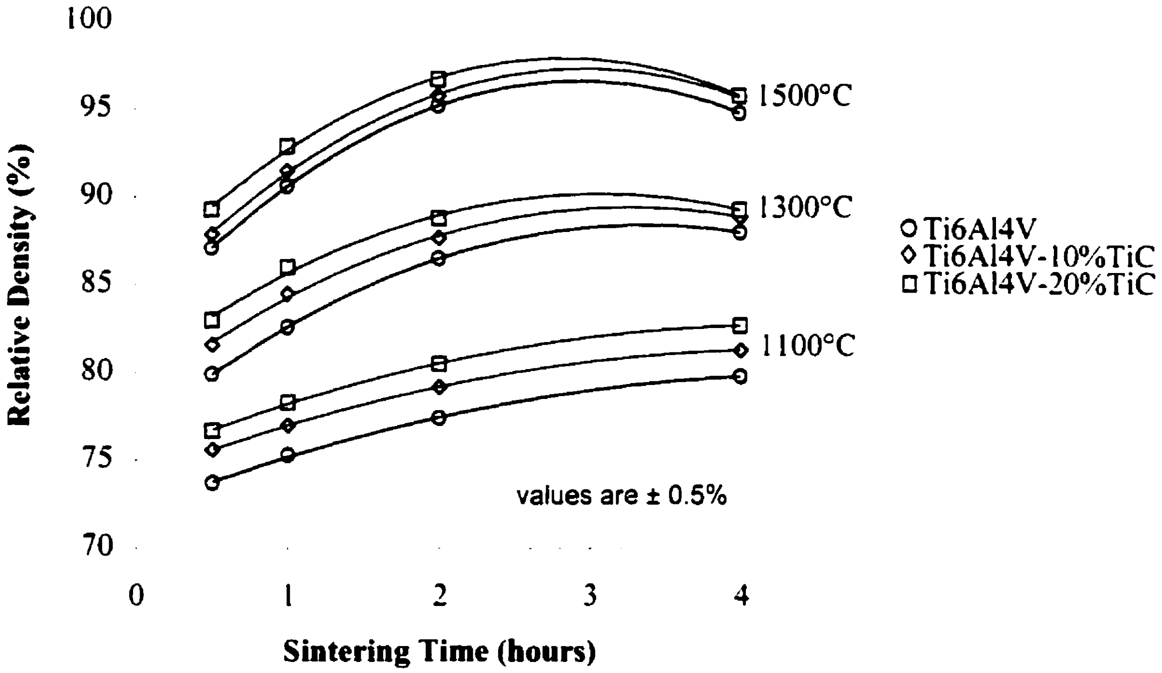

(b) Image analysis

Figure 6.5 Relative density as a function of the sintering time at different temperatures for Ti-6%Al-4%V composites containing up to 20 vol.% TiC. (Each point in these plots is the average density of four specimens sintered under the same conditions.)

Both techniques used to determine the densification behavior indicated that, for all the titanium alloy composites, an increase in sintering temperature resulted in a decrease in percent porosity, regardless of the hold time. Previous work on TiC particle reinforced titanium composites has shown that the density increases until approximately 1500°C after which de-sintering and pore coarsening occur.[89] The temperature at which these phenomena become significant depends on the melting point of the material. The overall effect of adding aluminium and vanadium on the melting point of pure titanium (about 1670°C) is negligible[246] (*i.e.* 6% aluminium in titanium increases the liquidus temperature to roughly 1720 C, while 4% vanadium in titanium decreases the liquidus temperature to roughly 1650°C). Hence the de-sintering effect was observed to begin at 1550°C for all compositions of TiC in the Ti-6%Al-4%V composites. The consolidation of the titanium-based composites was thus investigated up to 1500°C as further increases in sintering temperature would not generate any densification improvements.

For these low green density composites, the sensitivity of the densification process to increases in the hold time seems to vary depending on the sintering temperature. At extremely low temperature (1100 °C), slow diffusion kinetics limit densification, and the density keeps increasing with time. At intermediate temperatures (1300°C and 1500°C), the influence of time on the densification appears to indicate that the greatest reduction in porosity occurs in the initial sintering period. This is because an increase in the holding time is not as effective as an increase in temperature for improved densification and is attributed to the exponential relationship between the diffusion coefficient and temperature, as mentioned in the literature review section (*i.e.* equation 2.7). Thus, it appears that the composites sintered at 1300°C are leveling off at a relative density far below 100%. In fact, given sufficient time, it would be theoretically possible at 1300°C for the composites to achieve full densification. Regarding sintering at 1500°C, there is a rapid increase in density until approximately 2 hours holding, beyond which de-sintering commences. This is consistent with previous work on TiC particulate reinforced titanium composites[89] which indicated that de-sintering begins at a holding time of 2 hours for sintering temperatures above 1350°C and drops to 0.5 hours at a sintering temperature of 1600°C.

This phenomenon of de-sintering or decrease in density at prolonged holding times for the high sintering temperatures has been observed by other investigators[87,89,167,247] but little attempt has been made to determine the nature of its occurrence. It is possible that this de-sintering results, as it does in the sintering of ceramic materials, from a decomposition reaction. (Many of the constituents in ceramic materials are in the form of silicates, carbonates or hydrated compounds; these decompose during firing to form the ceramic oxide and gaseous oxides and/or H_2O.) In the present titanium composite system, the density increases during sintering with material being transported by volume diffusion of atoms (accompanied by the counter-diffusion of vacancies). However, for bonding to occur, the surface oxide on the titanium particles must first be reduced. Since the sintering environment of the graphite-element vacuum furnace is likely to have residual CO/CO_2 gas (*e.g.* from the reaction of residual oxygen in the furnace chamber with the graphite element), the titanium surface oxide may react with the CO to generate CO_2. Hence throughout consolidation, evolution of this CO_2 gas would reduce the increase in density obtainable from volume diffusion of material to the neck region. During prolonged sintering, particularly at the elevated temperatures, the decrease in density occurs as a result of the evolution of CO_2 gas. That is, during the intermediate and final stages of sintering, the driving force for porosity removal is markedly reduced as compared to the initial stage, as is to be discussed further in the next section. Thus, the decrease in density occurring from the CO_2 gas evolution outweighs the density increase by vacancy removal and could result in de-sintering.

Besides the effect of time or temperature, an increase in the volume fraction of the TiC particles tended to increase the density. This can be attributed to the higher green density as well as the finer pore size of the titanium alloy composites containing 20 vol.% TiC particles. That is, the TiC reinforcement particles improve the packing density by being accommodated in the void spaces between adjacent Ti-6%Al-4%V particles. This in turn increases the number of point contacts and reduces the size of the void spaces to be eliminated during elevated-temperature sintering, thus improving densification.

A comparison of Figure 6.5 (a) to Figure 6.5 (b) indicates that the bulk density of the composites determined by image analysis techniques were on average 10% higher than those calculated by the Archimedes' method. This was due to a highly porous surface layer approximately 150 to 200 μm in depth as shown in Figure 6.6. During optical image analysis testing for percent porosity, this surface layer region was not included in the measurements. As such, the percent porosity values from image analysis represent the bulk density of the material since the thin surface layer is likely to be removed during final finishing of the component.

Occurrence of this surface layer was investigated by elevated temperature sintering in a radiant tube furnace equipped with a microbalance for measuring changes in weight (refer to section 4.3.1). Essentially, the specimens were heated in a vacuum and by monitoring the weight change with increasing temperature, it would be possible to assess the reactions occurring during sintering. Regrettably, the vacuum sintering environment of the lanthanum-chromite element radiant furnace differed slightly from that of the graphite-element resistance furnace because of the differences in the heating element materials (*i.e.* inert versus carbon). As such, this investigation could not be extended to resolve the phenomenon of desintering as observed previously.

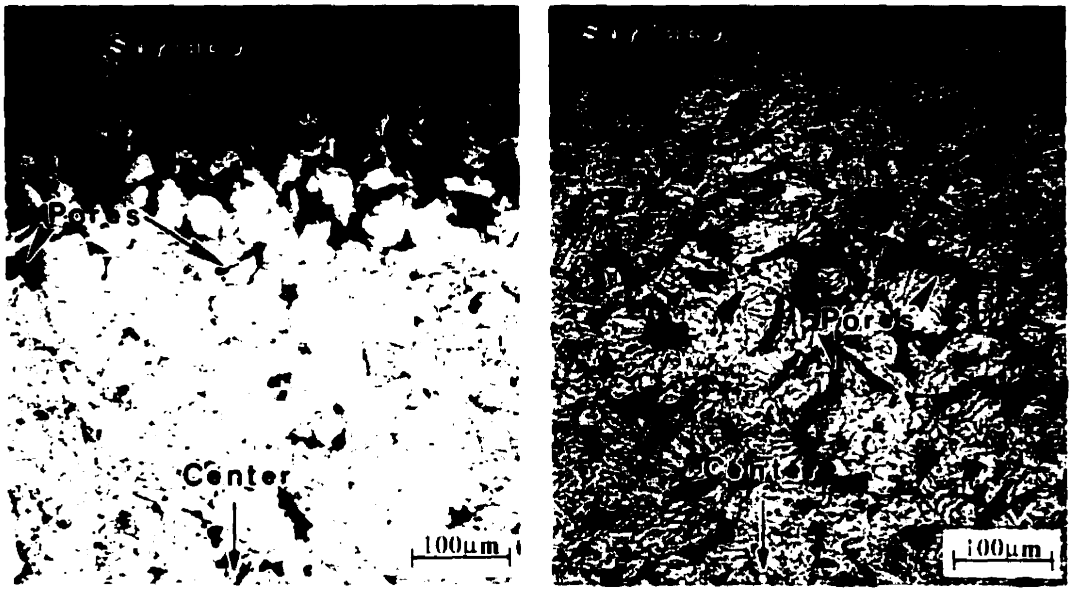

(a) (b)

Figure 6.6 Optical micrograph of a typical porous surface (a) Ti-6%Al-4%V alloy and (b) Ti-6%Al-4%V/TiC composite.

Figure 6.7 illustrates the change in weight as a function of sintering temperature for the titanium alloy and composites. It is observed that there is initially a loss in weight up to a temperature of roughly 550°C for all materials tested. This weight loss is attributed to the evaporation of water, initially, followed by burn out of residual isopropanol from attrition milling. Interestingly, the initial weight loss was greatest for the unreinforced titanium alloy for which the total surface area per unit volume was the lowest. The addition of TiC increases the total surface area per unit volume such that the quantity of entrained moisture and isopropanol in the composite should be higher. Thus the lower weight loss observed for the composites is most probably a result of the higher surface hydrophobicity of the TiC as compared to TiO_2. (A 70.7° contact angle for water on a TiO_2 surface suggests that the oxide of titanium is wetted.[248a] This occurrence has been manipulated in the production of ferrous cermets. Essentially during sintering of iron-TiC, carbon is removed from the TiC surface through the formation of CO_2. The removal of carbon to form a carbon deficient TiC surface was observed to improve wettability.[248b] Moreover, extensive work on the properties of coal has demonstrated that coal is naturally hydrophobic.[248c] Hence, a greater hydrophobicity for TiC as compared to TiO_2 is likely and has resulted in lower adsorption of moisture and isopropanol for the present composite system.)

Between 550°C and 800°C, the weight remains fairly constant for all the materials. Beyond 800°C, the titanium-based materials begin to gain weight, most likely due to oxidation. The oxidation rate was observed to be the greatest for the unreinforced titanium alloy and it decreased with increasing volume fraction of TiC particles. It is thus possible that this oxidation during heating generates a high residual porosity in the region of the specimen surface. That is, the individual particles of the titanium alloy in the vicinity of the surface are highly oxidized. In general, oxidation interferes with the material transport mechanisms for densification, and as such poorer sintering between the oxidized particles occurs (*e.g.* due to higher melting temperature of oxide and also its larger diffusion path). This supports the results obtained, since the greatest weight change occurred for the unreinforced titanium alloy and it was found to have the thickest surface reaction region, as illustrated in Figure 6.6 a.

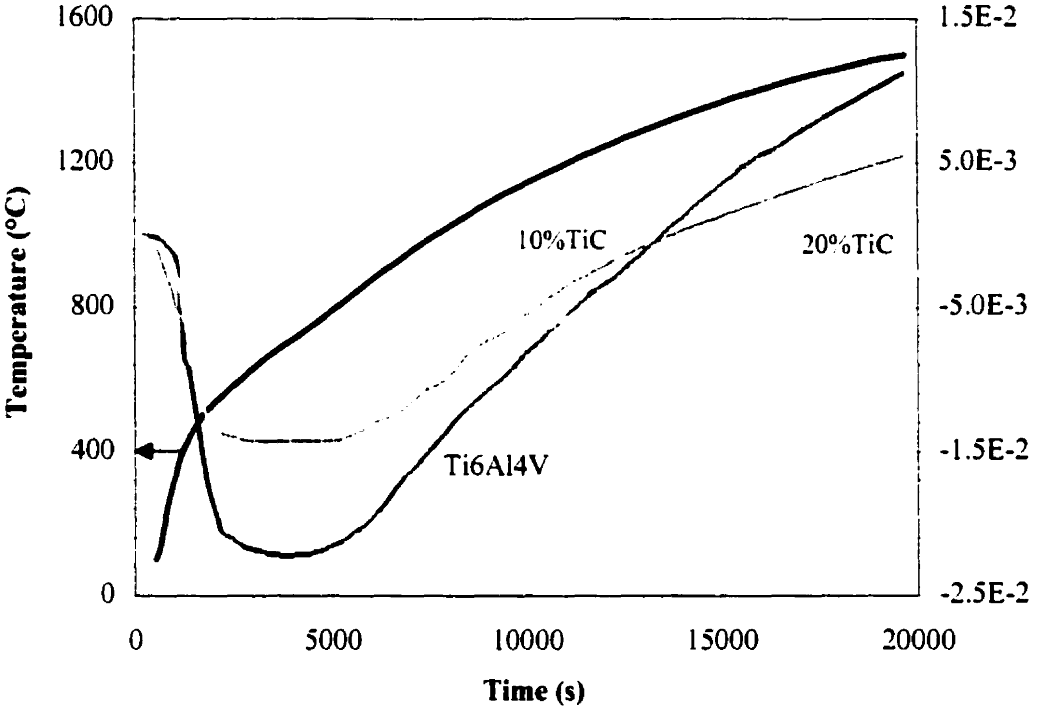

Figure 6.7 Weight changes of the various materials with increasing sintering temperature.

6.2.2 Sintering Mechanisms

During sintering the material transport processes can create a change in the interparticle spacing as neck growth occurs. Hence, if the particle centers are brought closer together during sintering, shrinkage occurs, which is the case for all the sintering mechanisms with the exceptions of surface diffusion and evaporation-condensation, as mentioned in the literature review. Monitoring the sintering process with the linear shrinkage data is important not only for the manufacturing of precision components but also for determining the sintering mechanism.

The shrinkage behavior of the titanium composites during sintering is illustrated in Figure 6.8. The linear shrinkage, $\Delta L/L_o$, was determined by measuring the length change of the sintered disk and dividing this by the initial length. Both the temperature and time dependencies illustrated in this plot are typical of sintering powder materials. The highest amount of shrinkage was observed for the titanium alloy sintered at 1500°C for 4 hours. As, expected, there was a slight decrease in the percent shrinkage with increasing TiC volume fraction due to the higher green density and finer pore size as before. It should be mentioned that the non-uniform shrinkage during sintering was minimal on account of the removal of the density gradients during isostatic pressing of the green compacts. However, if the compact is fabricated by uniaxial pressing alone, density gradients in the compacted powder can lead to warpage and non-uniform shapes.

Solid-state sintering involves material transport by diffusion through the movement of atoms or vacancies through lattice dislocations or along a surface or grain boundary. As mentioned previously, surface diffusion does not result in shrinkage. Hence the observed shrinkage is due to volume diffusion either along grain boundaries or through lattice dislocations. The general form of the neck growth model for determining the material transport mechanism is defined as (*i.e.* equation 2.7 in the literature review):

$$\frac{\Delta L}{L_o} = \left(\frac{Bt}{2^{2n} R^{m}} \right)^{n} \tag{6.1}$$

For isothermal sintering, the slope of the log-log shrinkage-time plot (Fig. 6.9) gives the mechanism characteristic exponent, *n*. For the materials sintered at 1100°C, the exponent was determined to be 0.22 which is lower than that predicted by the model for volume diffusion along grain boundaries (*i.e.* 0.4 from Table 2.2). This deviation is inevitably due to the over simplifications used to derive the material transport model.[176] Primarily, the assumptions of equal size spherical particles and ideal packing are not appropriate in the present work, as the particle morphology was angular and, for the composites, the size distribution was bimodal. Hence the real powder system, having a distribution in particle size and a non-homogeneous powder geometry, can attain a fewer number of contact points per particle (*i.e.* coordination number) as well as contact flattening during compaction (*i.e.* smaller neck size). Also, materials can sinter by a process involving several modes of mass flow. With the progression of sintering, the coordination number increases, and the dominant sintering mechanism can vary considerably. Previous work has considered the error associated with using the simplified model to predict the mechanism characteristic exponents for volume diffusion. The exponent was found to vary with the coordination number and neck size, and for real systems a decrease in these two parameters could diminish the exponent by 20%.[175,190-191]

For the composites sintered at temperatures above 1100°C, as illustrated in Figure 6.9, there appears to be a decrease in the densification rate beyond 2 hours hold time. The mathematical model, given by equation 6.1, is derived on the basis of neck growth for the initial stage of sintering. Decrease in the densification rate at a sintering temperature of 1300°C after 2 hours holding time then suggests that the material has progressed into the intermediate densification stage. At this point, the driving force shifts from that for interparticle neck growth (curvature gradients) to that for grain boundary and pore structure formation (interfacial energy). That is, the driving force for sintering (*i.e.* reduction in the surface energy of the system) is initially expended for interparticle neck growth as manifested by the decreased surface curvatures of the particles. In the intermediate stage, the surface energy available as a driving force is reduced since the curvature gradients associated with the pores (between the sintering particles), that are now cylindrical, decrease. Furthermore, since at every sintering interface there is a subsequent creation of a grain boundary, which is associated with a grain boundary energy, the net driving force is reduced and the associated linear shrinkage in the intermediate stage can decrease substantially as compared to the initial sintering stage.

At 1500°C, the data seem to indicate that beyond 1 hour of sintering the shrinkage rate has decreased. Thus the shrinkage values at 1 and 2 hours holding time at 1500°C deviate from the regression line having a slope of 0.22. This suggests that sintering at this point is no longer in the initial stage of densification. Beyond 2 hours holding at this sintering temperature, the linear shrinkage appears to remain constant, indicating little if any densification. With shrinkage of the pore structure, the cylindrical pores of the intermediate stage have been found to become unstable at approximately 8% total porosity (*e.g.* for the monosized-spherical particle model) and collapse into spherical pores which are characteristic of the final stage of sintering. In this work, the percent total porosity in the sintered materials was determined to be less than 8% (Fig. 6.5b) beyond a holding time of 1 hour at 1500°C. This suggests that for an isothermal temperature of 1500°C, sintering is in the intermediate densification stage for a hold time of between 1 hour and 2 hours. Around 2 hours holding time at 1500°C, the driving force for sintering decreases further and this is characteristic of the final stage of sintering in which isolated, spherical pores shrink by a slower volume diffusion process.

The activation energy for shrinkage can be obtained from an Arrhenius plot of the logarithm of shrinkage versus the inverse of the absolute temperature (Fig. 6.10). The slope of this plot enables calculation of the activation energy for diffusion. Table 6.1 gives these calculated activation energies for the titanium alloy and composites.

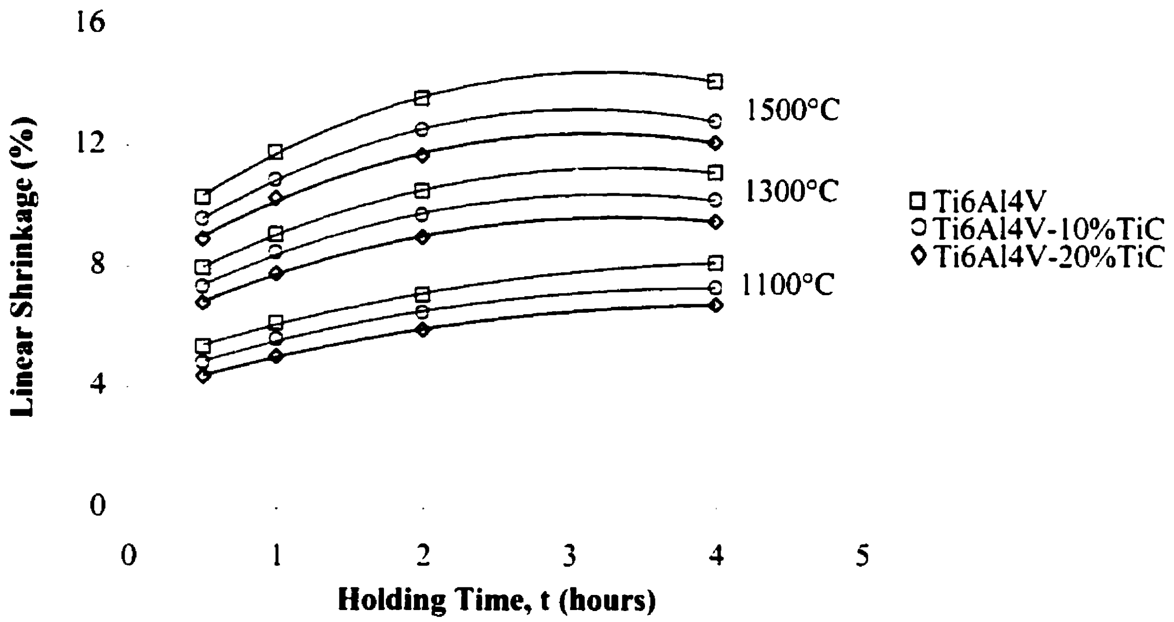

Figure 6.8 Shrinkage behavior of the titanium composite materials during sintering.

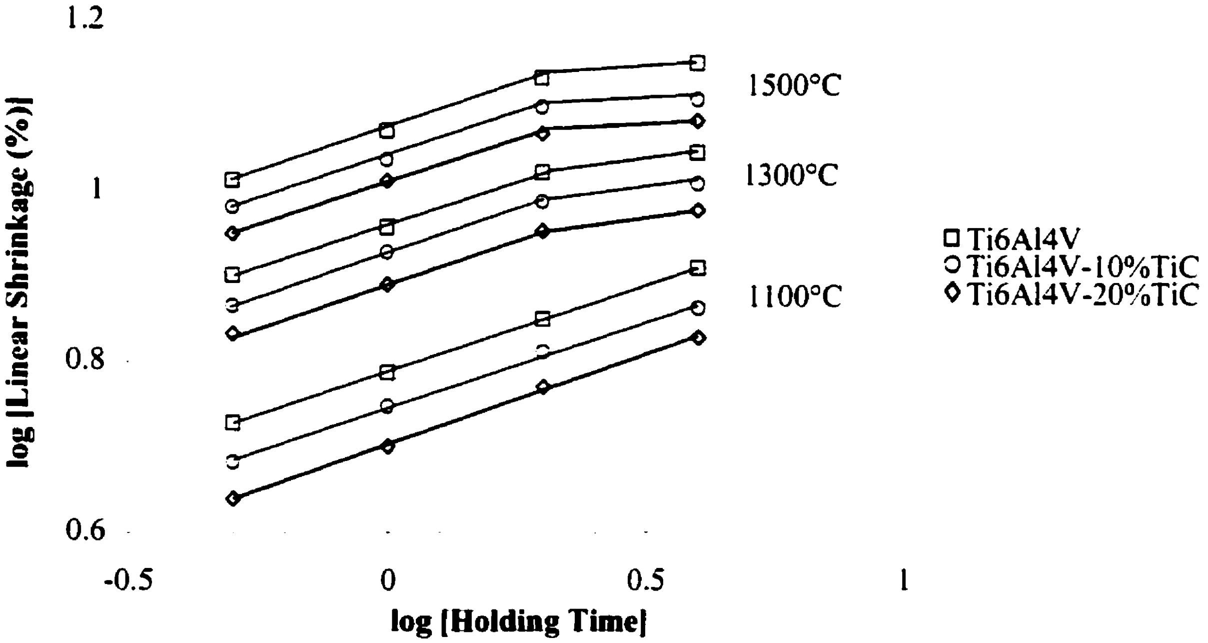

Figure 6.9 Log-Log plot of the shrinkage-time behavior of the titanium composite materials during sintering.

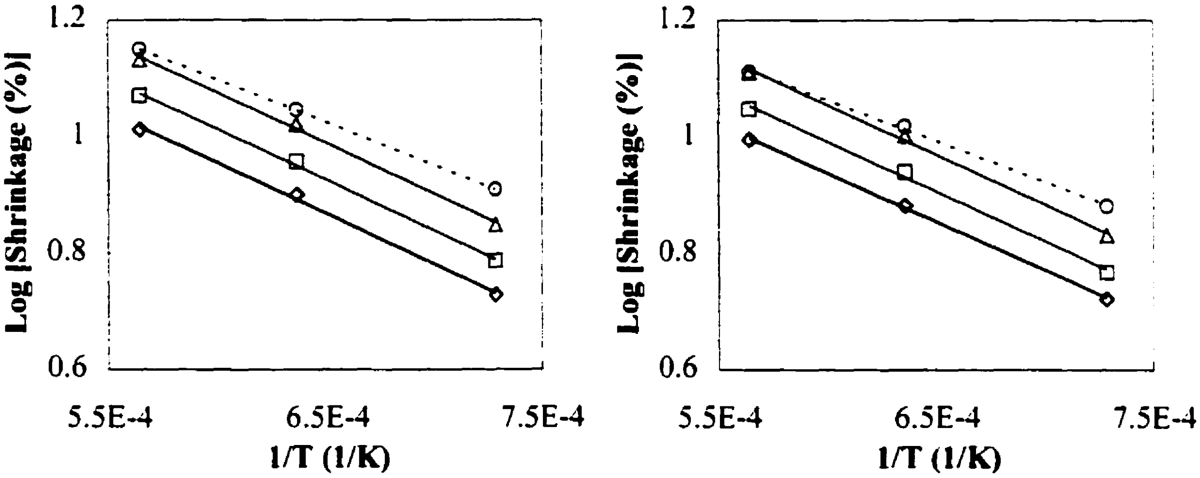

Ti-6%Al-4%V alloy Ti-6%Al-4%V - 5 vol.% TiC_p

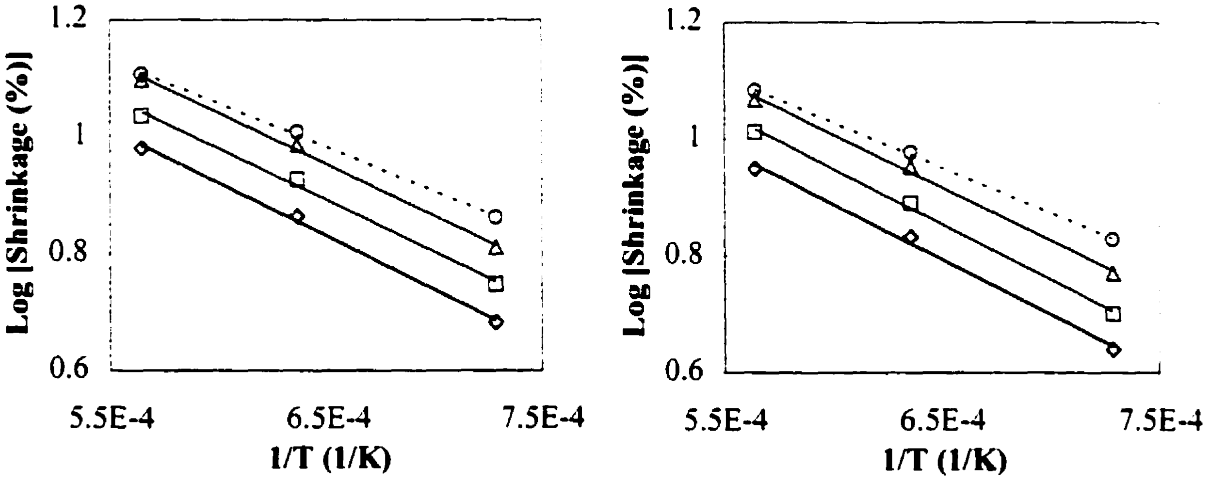

Ti-6%Al-4%V - 10 vol.% TiC_p Ti-6%Al-4%V - 20 vol.% TiC_p

◇ ½ hour □ 1 hour △ 2 hours ○ 4 hours

Figure 6.10 Arrhenius plots of the isothermal shrinkage measurements for determining the diffusion activation energy.

Table 6.1 - Activation Energy for Volume Diffusion

Material	Activation Energy, Q ($kJ \cdot mol^{-1}$)
Ti-6%Al-4%V	322
Ti-6%Al-4%V/5 vol.% TiC	325
Ti-6%Al-4%V/10 vol.% TiC	328
Ti-6%Al-4%V/15 vol.% TiC	331
Ti-6%Al-4%V/20 vol.% TiC	335

The activation energies calculated for the materials ranged between 322 to 335 kJ·mol^{-1}. There was a slight increase in activation energy with increasing TiC volume fraction, but this change was roughly the same as the error associated with each value (± 10 kJ·mol^{-1}). Hence, no significant difference in the activation energy for the composites as compared to the titanium alloy was found. However, the activation energies determined agree reasonably well with the apparent activation energy for titanium diffusion in a titanium alloy containing 4 wt.% vanadium, which is approximately 290 kJ·mol^{-1}.[249-251]

To determine the activation energies for the various materials from the Arrhenius plots, the data for 4 hours holding time were discarded, as Figure 6.10 illustrates that the slope for this condition deviates substantially from that obtained for the other sintering times. This deviation at 4 hours holding time is inherently due to the progression from the initial stage of sintering at 1100°C to the intermediate stage at 1300°C and to the final stage at 1500°C. Hence the data values for the higher temperatures are influenced by the change in driving force. As observed previously with the shrinkage-time plot, Figure 6.9, there is a decrease in the driving force at 1300°C for holding times beyond 2 hours, indicating the onset of the intermediate stage. In the same plot, the slope at 1500°C, beyond 2 hours holding, is almost horizontal and the data values for lower holding times were found to deviate from the regression line having a slope characteristic of the initial sintering stage. Consequently, at the higher sintering temperature of 1500°C, there is rapid progression from the initial sintering stage, at approximately ½ hour holding time, to the intermediate sintering stage, roughly in the region between 1 and 2 hours. Beyond 2 hours holding, the material is likely to be in the final sintering stage. These microstructural observations, related to nature and evolution of the pore structure, as speculated from Figures 6.9 and 6.10, can be established through microscopic characterization of the change in microstructure with sintering, as described in the next section.

6.3 Microstructural Characterization

6.3.1 Optical Microscopy

Selected optical micrographs of the polished specimens are presented in Figure 6.11. These composites, containing 10 vol.% TiC particles, were sintered at temperatures in the range of 1100 to 1500°C for 4 hours. At low temperatures (Fig. 6.11a), the microstructure reveals finer TiC particles that may be attributed to the inadequate bond strength between the particles and matrix, which resulted in pullout of the larger reinforcement particles. The amount of pullout at this temperature, measured by image analysis techniques, was found to vary between 3 to 6% depending on the TiC volume fraction. Furthermore, substantial porosity can be found in the vicinity of the remaining particles and along the forming grain boundaries. The pore structure is open and interconnected and the pore morphology is not very smooth due to the existence of relatively sharp curvature gradients near the interparticle neck region, as illustrated in Figure 6.12. This pore structure is typical of the initial sintering stage, as predicted by the log-log shrinkage-time behavior for isothermal sintering at 1100°C (Fig. 6.9).

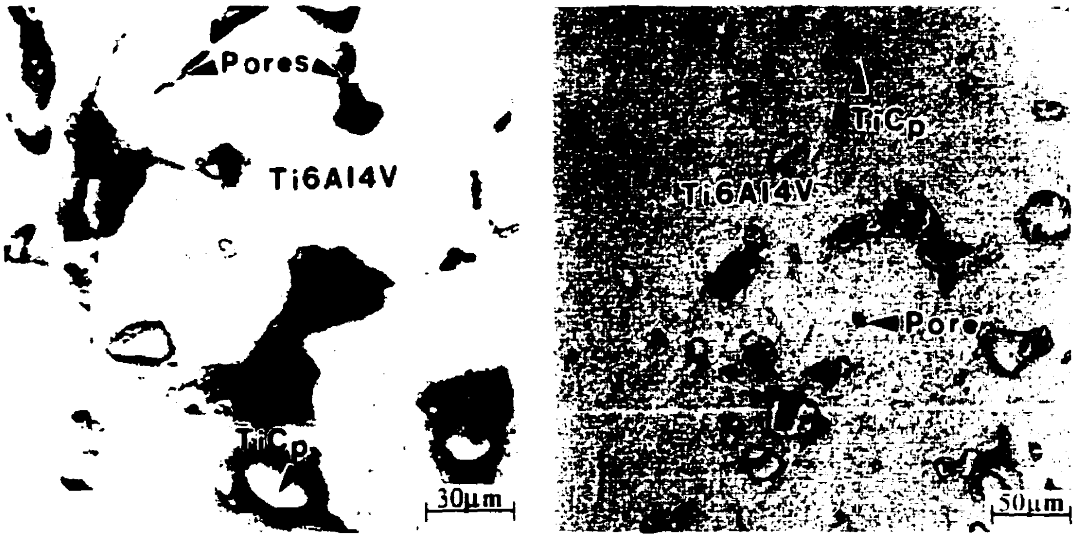

(a) 1100°C (b) 1300°C

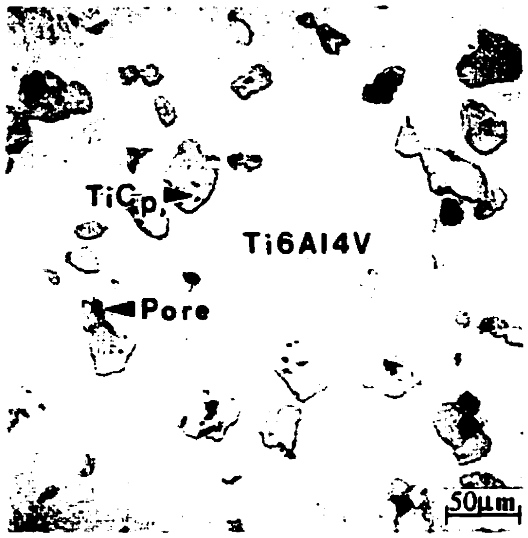

(c) 1500°C

Figure 6.11 Optical micrographs of unetched 10 vol.% TiC_p reinforced Ti-6%Al-4%V composites sintered for 4 hours.

Improvement in the diffusion kinetics at 1300°C resulted in substantial pore shrinkage and progression into the intermediate sintering stage (Fig. 6.11b) before 4 hours holding time. This supports the shrinkage-time plot results (Fig 6.9), which indicated a decrease in the densification rate for 2 hours sintering at a temperature of 1300°C. The microstructure reveals good bonding between the matrix and reinforcement, since little if any particle pullout was revealed by image analysis techniques. Numerous cylindrically shaped pores can be observed in the vicinity of the TiC particles with a few smaller pores appearing to spheroidize into a closed structure. In general, this stage was characterized by a relatively smooth pore structure which remained, on the whole, interconnected; however there were much smaller changes in curvature between particles (Fig. 6.13).

With further increases in the sintering temperature, the cylindrical pores of the intermediate stage at 1300°C collapsed to form spherically shaped pores at 1500°C for 4 hours holding time (Fig. 6.11c). This progression into the final stages of sintering agrees with the shrinkage results for 4 hours holding at 1500°C. The pores are mostly spherical in shape and isolated in the vicinity of the TiC particles. In addition, there appears to be some growth of TiC particles at 1500°C, as evidenced by the greater reinforcement size as compared to that of the as-received TiC powder size (less than 32 μm).

Figure 6.12 SEM micrograph of etched 10 vol.% TiC_p reinforced Ti-6%Al-4%V sintered at 1100°C for 4 hours showing an interconnected pore structure with sharp curvature gradients. (The α and β phases of the matrix are also indicated.)

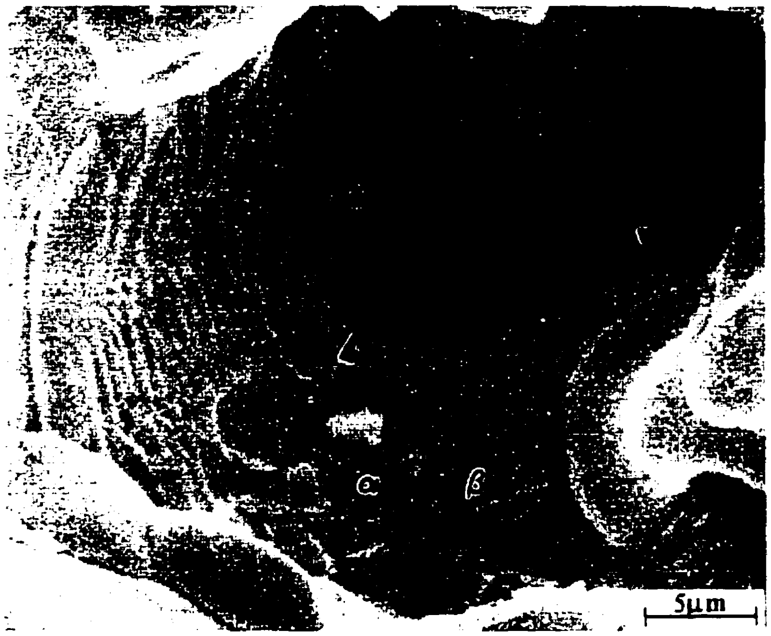

Figure 6.13 SEM micrograph of etched 10 vol.% TiC_p reinforced Ti-6%Al-4%V sintered at 1300°C for 4 hours showing a smooth interconnected pore structure.

The change in matrix microstructure with increasing sintering temperature is depicted in Figure 6.14 for Ti-6%Al-4%V. Micrographs of etched specimens were selected to simultaneously show the effect of sintering on the evolution of the pore and grain boundary structure. At 1100°C (Fig. 6.14a), the closely spaced pores are located at the grain boundaries as an irregular network of connected channels (*i.e.* initial sintering stage). Progression into the intermediate sintering stage at 1300°C (Fig. 6.14b) produced a smoother interconnected pore structure, but the pore size increased as void coalescence and matrix microstructure coarsening commenced. Since pore coarsening is due to shrinkage of other pores, the number of pores decreased. Sintering at 1500°C (Fig. 6.14c) results in the spheroidization of the pores into a closed structure. However, substantial microstructural coarsening of the matrix has occurred (hence a lower magnification was used) and the pores are now isolated from the grain boundaries. Further improvement in densification may be more difficult because continued densification by void dissolution relies on the presence of pores remaining at the grain boundaries. After breakaway from the grain boundary, the pore must diffuse vacancies to a distant grain boundary to continue shrinking. This is a slower process as evidenced by the lower densification rate in Figure 6.9 for the final sintering stage. Moreover, the densification behavior, Figure 6.5, indicates that there is de-sintering at 1500°C for a holding time of 4 hours. This de-sintering is accompanied by substantial microstructural coarsening particularly at the elevated temperatures and prolonged sintering times. Hence further increases in the sintering temperature or time will augment pore coarsening and cause the mean pore size to increase, ultimately leading to a marked decrease in density as observed with previous work on Ti-TiC composites.[89]

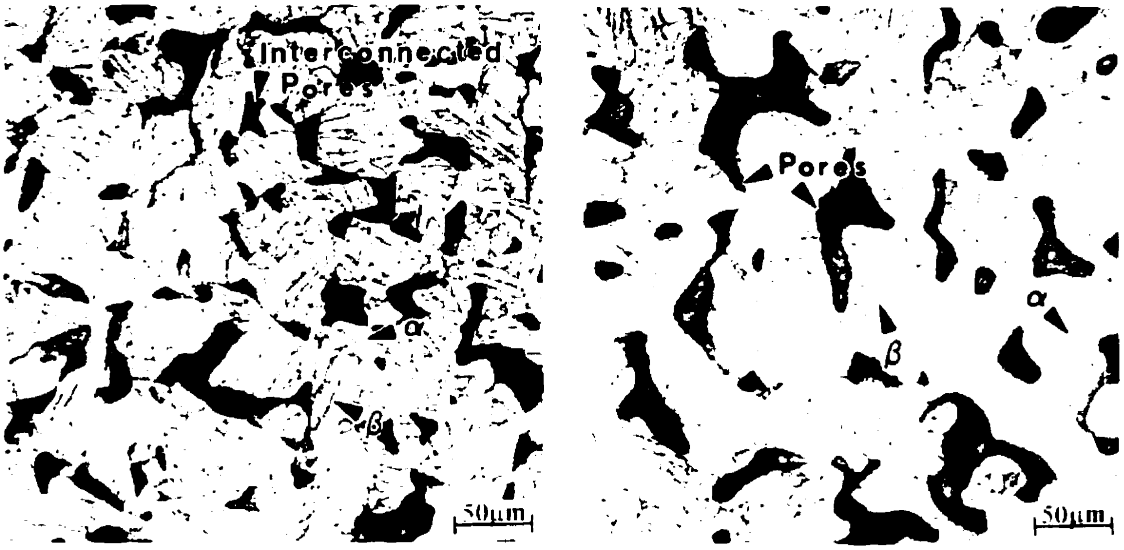

(a) 1100°C (b) 1300°C

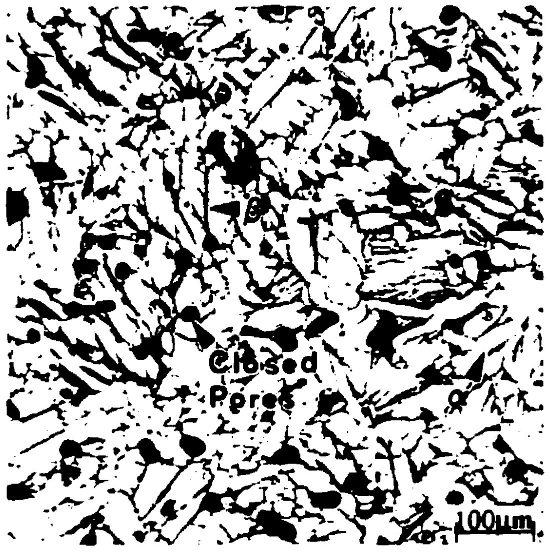

(c) 1500°C

Figure 6.14 Optical micrographs of etched Ti-6%Al-4%V sintered for 4 hours.

The evolution of the matrix microstructure during sintering (Fig. 6.14) is essentially coarsening of the lamellar arrangement of plate-like α (light regions). The reinforcement particles modify this lamellar arrangement by controlling the rate of grain growth and constraining the growth of the lamellar α + β structure, as indicated by the finer plates of α (Figs. 6.15a and 6.15b). Consequently, the presence of the TiC reduces the porosity in two ways: (1) by increasing the green density and decreasing the size of the void spaces prior to sintering and (2) by preventing grain growth, thereby reducing pore break-away from the grain boundary. The particles also have a homogenizing effect on the refinement of the lamellar structure as indicated by the matrix phase of the 20 vol.% TiC composites that shows a similar α-plate size regardless of the temperature (Fig. 6.15b and 6.15c). In fact, this grain size was observed at 1100 and 1300°C, irrespective of the TiC volume fraction. At 1500°C, at least 20 vol.% TiC is required before a fine lamellar structure is obtained.

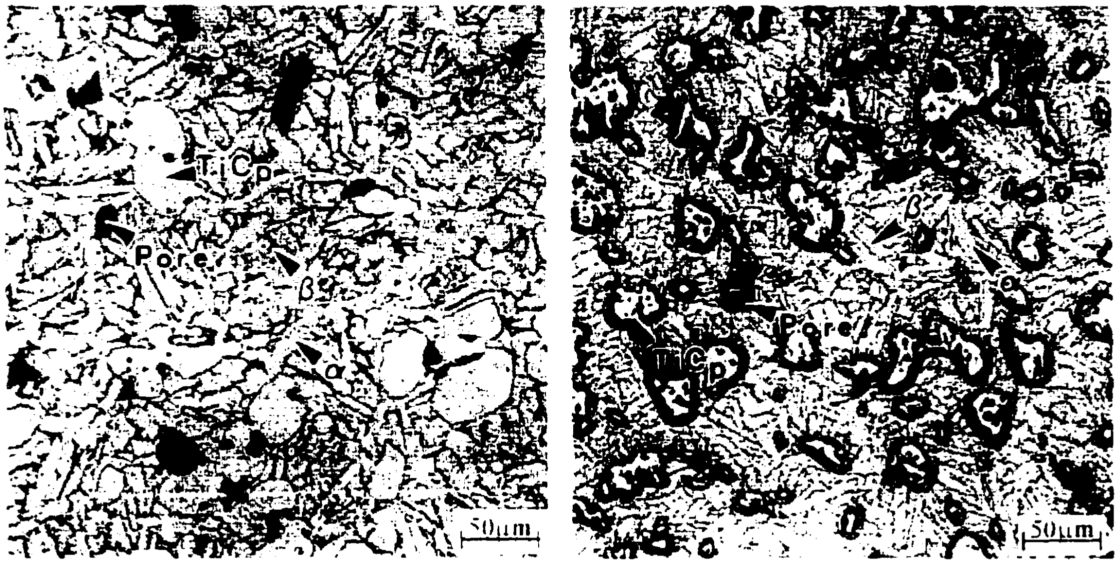

(a) 15 vol.% TiC, 1500°C

(b) 20 vol.% TiC, 1500°C

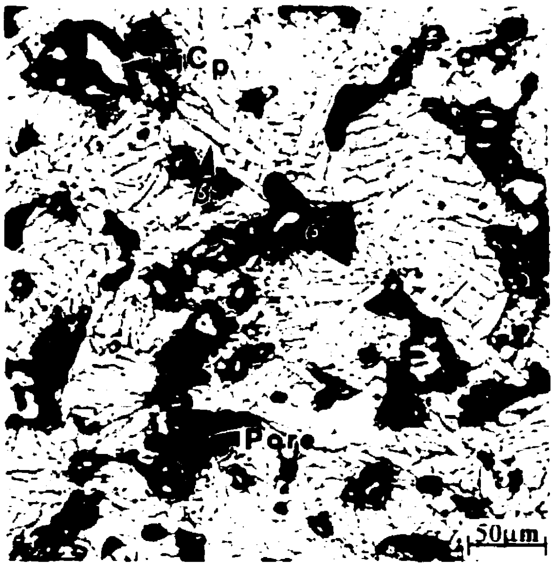

(c) 20 vol.% TiC, 1300°C

Figure 6.15 Optical micrographs showing the effect of particles in preventing coarsening of the lamellar matrix.

6.3.2 Scanning Electron Microscopy

The microstructure of the composites was analyzed at a higher resolution using secondary electron imaging (Fig. 6.16a) and backscattered electron imaging (Fig. 6.16b) on a *JEOL JSM-840A* SEM. As observed previously using optical microscopy, the matrix of the etched composite material basically consisted of a lamellar arrangement of α plates separated by interplate β and no other phases were apparent. Also, for all the TiC compositions and processing conditions investigated in this work, no obvious interfacial reaction region between the Ti-6%Al-4%V matrix and TiC particles was observed at this resolution. Some of the reinforcement particles were found to contain regions of micro-porosity, the volume fraction of which appeared to be greater in the larger particles, as shown in Figure 6.17a and 6.17b. However, these micro-pores were also visible in the many of the individual particles of the as-received TiC powder prior to incorporation into the composite material, as illustrated in Figure 6.17c and 6.17d. This suggests that the pores arise from the carbothermic reaction process used to synthesize the TiC powder.

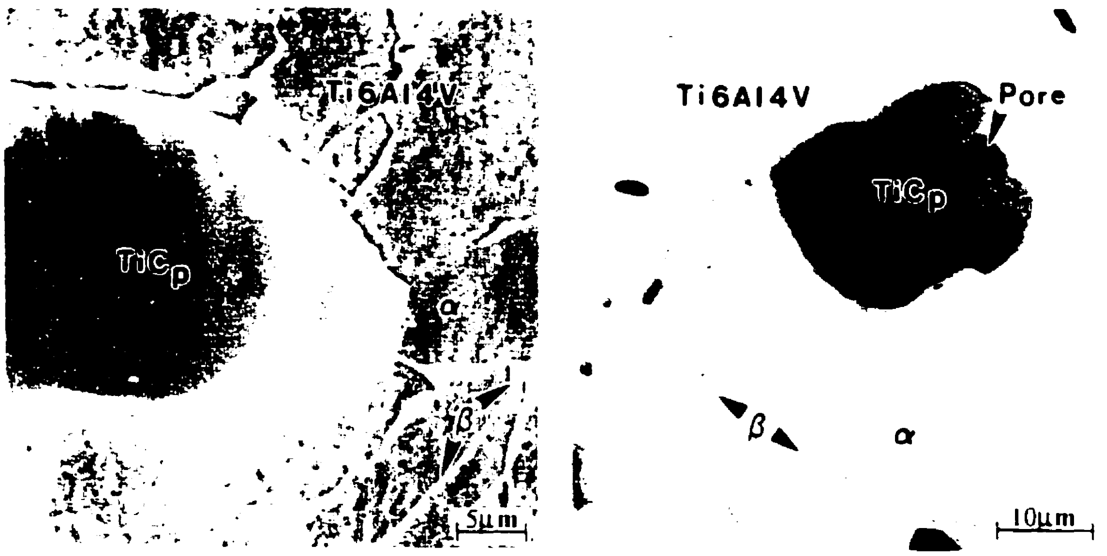

(a) (b)

Figure 6.16 SEM micrographs of etched Ti-6%Al-4%V/20 vol.% TiC_p composites sintered at 1300°C for 4 hours: (a) secondary electron imaging and (b) backscattered electron imaging.

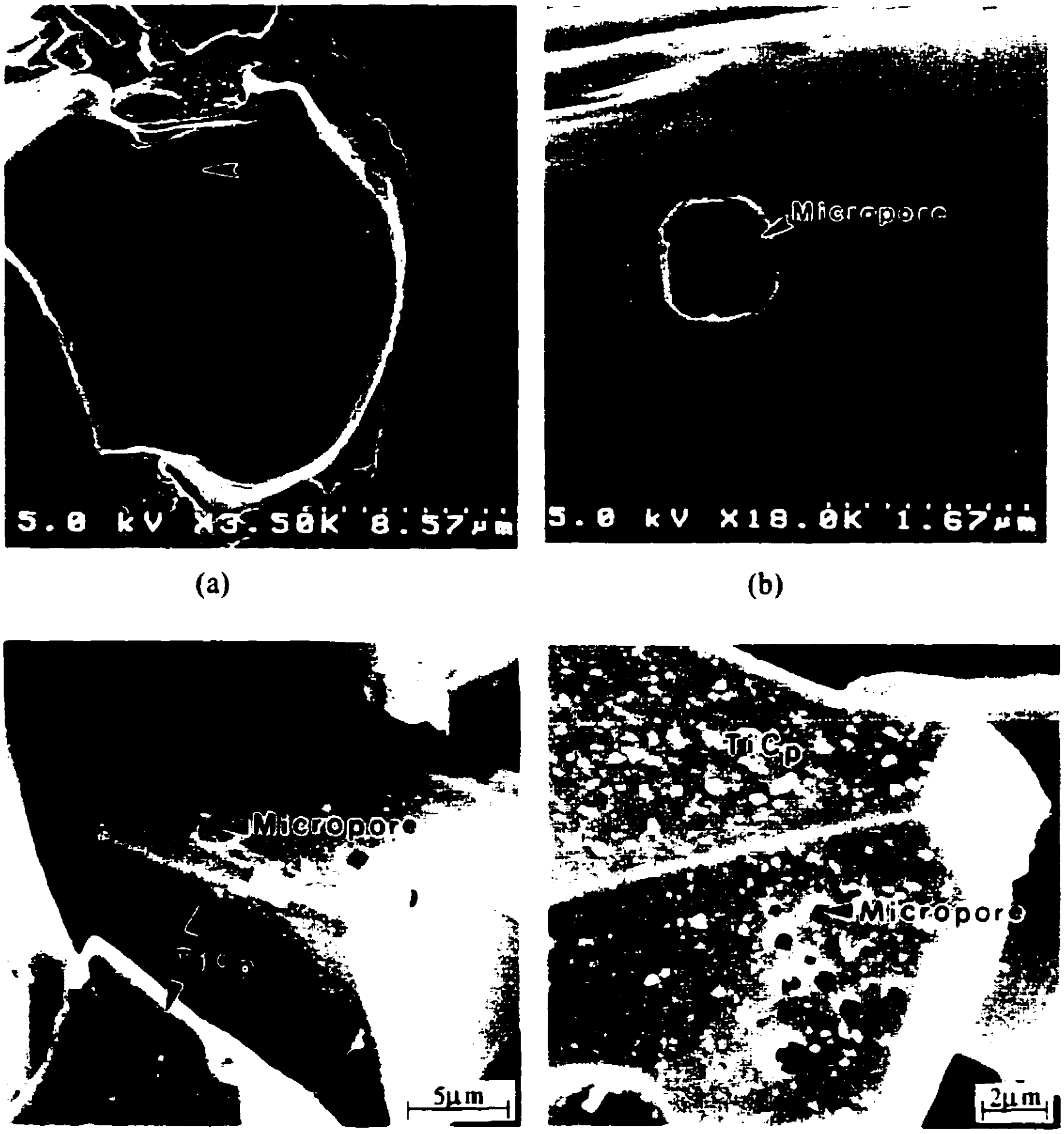

(a) (b)

(c) (d)

Figure 6.17 SEM micrographs showing the micro-porosity present in (a) TiC reinforcement particles in the Ti-6%Al-4%V composites. A magnified view of this microporosity is presented in (b). The microporosity in the TiC reinforcement particles of the composite material originates from powder processing, as evidenced by the micropores in numerous individual particles of the as-received TiC powder. Individual micropores (c) as well as pore clusters (d) were observed in the starting TiC powder particles.

6.4 Interfacial Analysis

6.4.1 Low Voltage Field Emission Gun SEM

Scanning electron microscopy work of previous investigators has not revealed any interfacial phase region in TiC particulate reinforced titanium composites. However, it appears that the main limitation preventing the observation of the interfacial phase in these composites is related to the resolution of the detection equipment used for surface analysis of specimens, as illustrated in Figure 6.18 using an *Hitachi S-4500* cold field emission gun SEM. Here the improved resolution of the upper through-the-lens detector enabled low voltage imaging for differentiation of the interfacial phase between the TiC particles and the Ti-6%Al-4%V matrix.

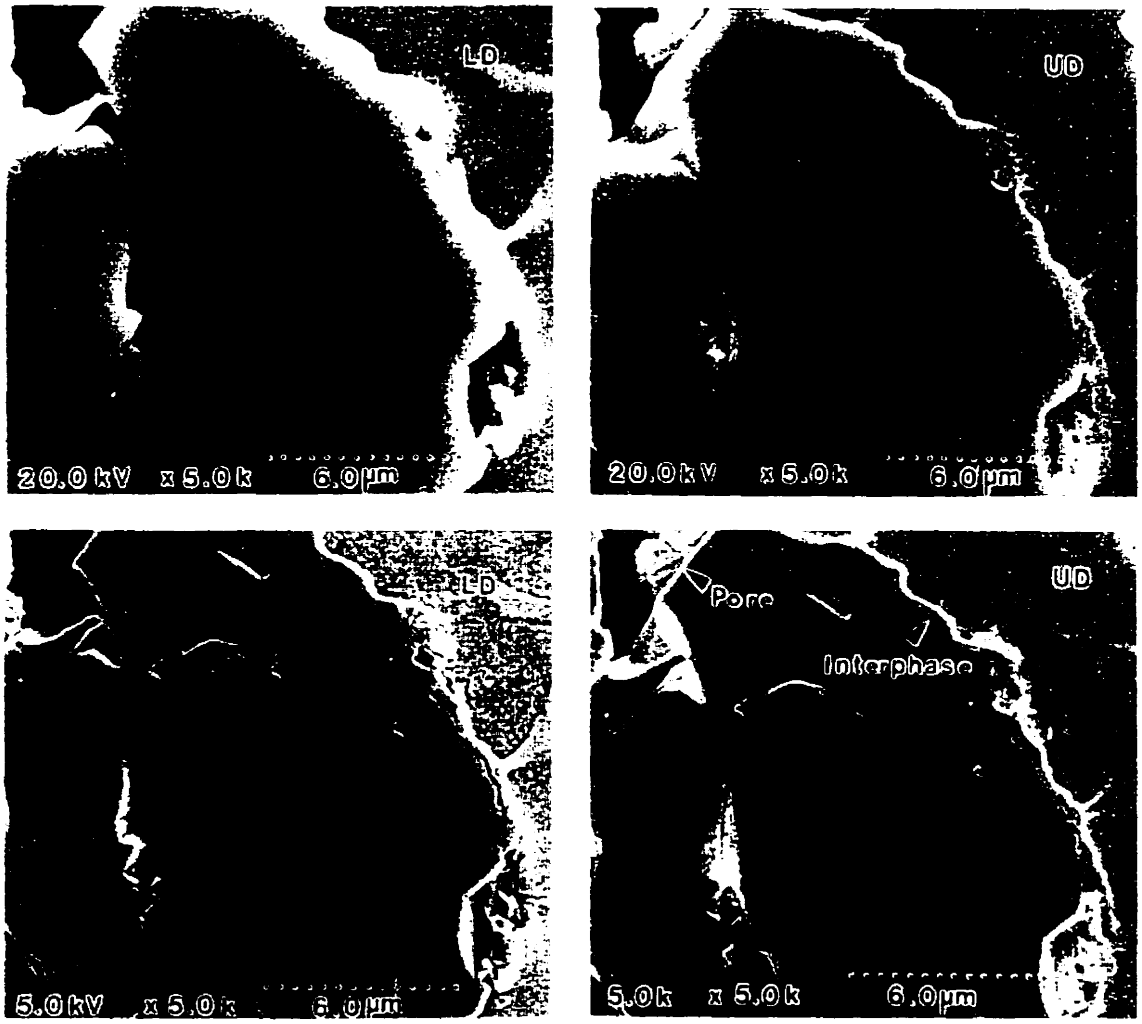

Figure 6.18 Secondary electron images of Ti-6%Al-4%V/20 vol.% TiC_p composites sintered at 1100°C for 1 hour (LD = conventional lower detector. UD = Hitachi upper detector).

The effect of processing variables on the formation and growth of this interface was thus investigated using this low voltage imaging technique. For the composites sintered at 1100°C, a layer having a lighter phase contrast than TiC was revealed on the periphery of the particles (Fig. 6.19a). An increase in the temperature to 1300°C increased the thickness of this boundary layer from approximately 0.6 µm at 1100°C to 3 µm at 1300°C, as shown in Figure 6.19b. Interestingly, a similar analysis for the composites sintered at 1500°C, failed to reveal a boundary layer of lighter phase contrast around the particles (Fig. 6.19c).

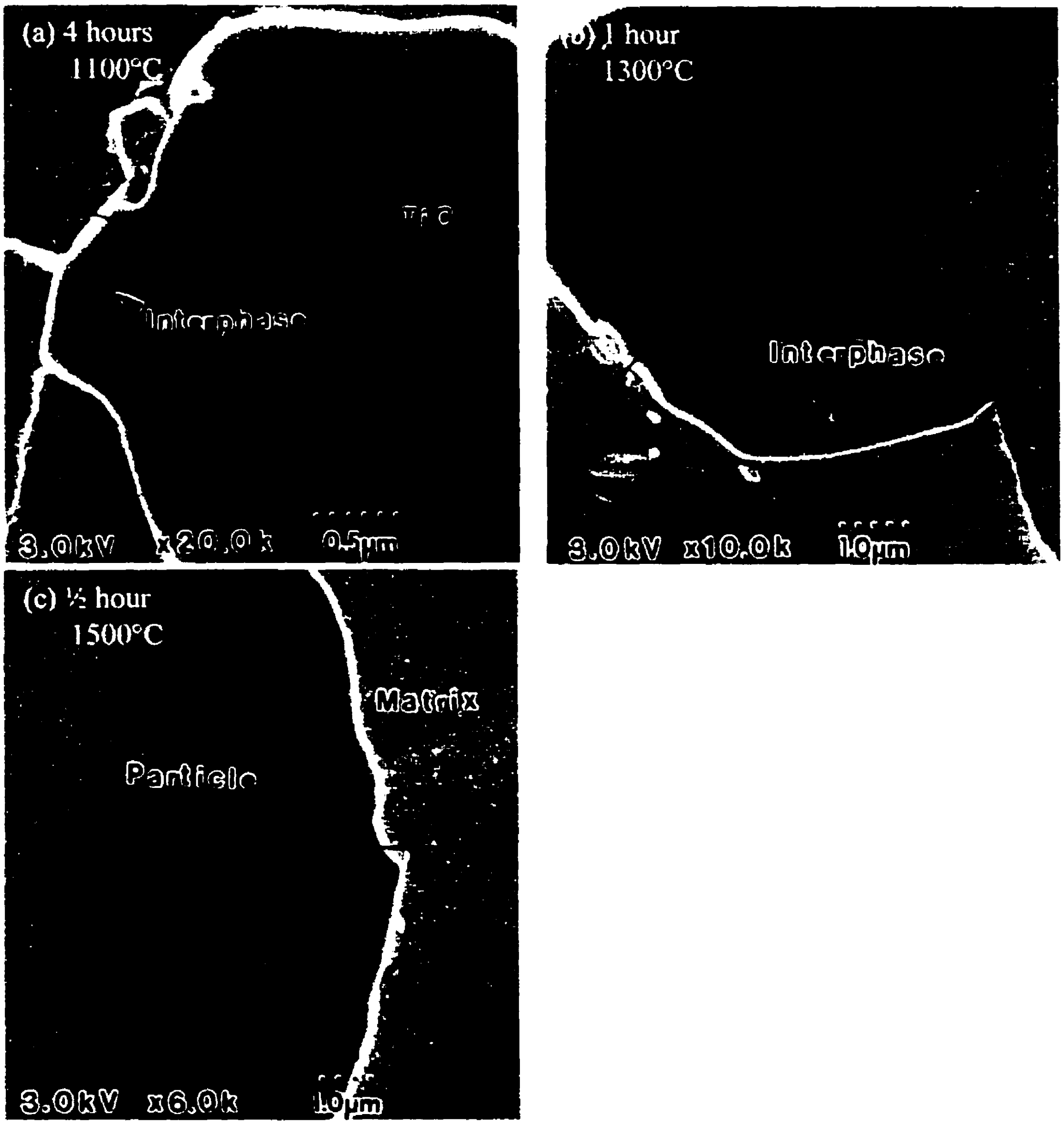

Figure 6.19 Interfacial reaction analysis using low voltage imaging on a field emission gun scanning electron microscope equipped with a through-the-lens detector for Ti-6%Al-4%V/20 vol.% TiC_p composites sintered for (a) 4 hours at 1100°C, (b) 1 hour at 1300°C and (c) ½ hour at 1500°C.

Chemical compositional analysis for carbon was performed at 3 keV along a line from the TiC particles to the Ti-6%Al-4%V matrix using energy dispersive X-ray spectroscopy. For the composites sintered at 1100°C and 1300°C the chemical analysis indicated that this boundary region had a lower carbon content than the adjoining region toward the center of the particle (Figs. 6.20a and 6.20b, respectively). For the composites sintered at 1500°C a homogeneous carbon content across the entire particle (Fig. 6.20c) was measured. However, it would be difficult to determine precisely the composition of this boundary layer region by this technique, as carbon contamination from the beam at these low accelerating voltages was very rapid. Nonetheless, it is observed that for the composites sintered at 1100°C, the carbon content of the reinforcement centers (region A in Fig. 6.20a) is approximately twice that of the boundary layer, region B in Figure 6.20a. In comparison, a similar carbon count analysis (*i.e.* same accelerating voltage and count time) for the composites sintered at 1300°C gave a slightly lower amount of carbon for the particle center, as illustrated by region A in Figure 6.20b (as compared with region A of Fig. 6.20a). However, the boundary layer carbon content, region B in Figure 6.20b, remained at approximately the same carbon counts. For the composites sintered at 1500°C, the carbon content in the entire particle, region A in Figure 6.20c, remained similar to that obtained for region B in Figures 6.20a and 6.20b. This suggests that the entire particle has transformed and its composition is similar to the boundary layer phase observed for the lower sintering temperatures. This analysis thus suggests that the TiC particles react with the titanium alloy matrix, forming an interfacial phase that grows with increasing processing temperature. At 1500°C the growth rate appears to be extremely rapid and the entire TiC particle appears to have transformed within a half-hour of sintering.

6.4.2 Electron Probe Micro-Analysis

To complement the results from the low voltage chemical analysis, electron probe micro-analysis measurements for carbon, titanium, aluminium and vanadium, were taken every 2.5 μm along an electron probe line path from the TiC particles to the Ti-6%Al-4%V matrix, as shown in Figure 6.21. Of these, carbon analyses for the as-consolidated composites indicated that temperatures higher than 1300°C resulted in extensive carbon loss from the particles, as illustrated in Figure 6.22. The carbon in the particles essentially decreases from the stoichiometric 20 wt.% at a sintering temperature of 1100°C to as low as 12 wt.% at 1500°C. That is, at a processing temperature of 1100°C, the carbon composition of the TiC particles remained similar to that of the as-received TiC powder. Increasing the temperature enhanced carbon loss from the particles such that at 1500°C, the reinforcement has a carbon concentration of 12 wt.%, which corresponds to that of Ti_2C.

Thus, both the electron probe results and the low voltage chemical compositional analysis work suggest the gradual transformation of TiC to Ti_2C. This phase is not shown on the Ti-C phase diagram because there exists some uncertainty related to its stability (see literature review) and thus dashed lines appear in the equilibrium phase diagram (Fig. 2.2).[112]

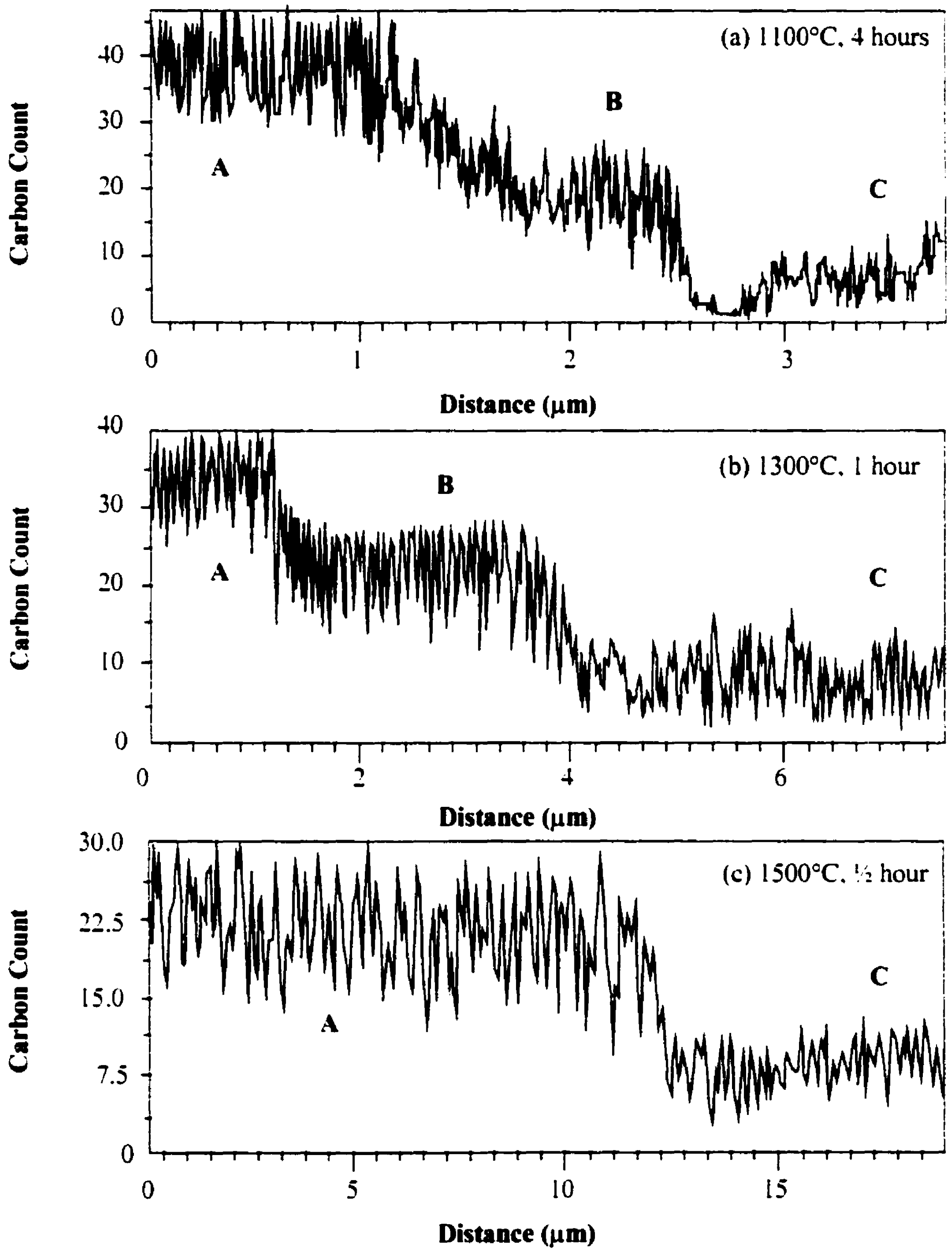

Figure 6.20 Chemical compositional analysis at 3 keV for carbon for interfacial analysis in Ti-6%Al-4%V/20 vol.% TiC_p composites (as shown in Figure 6.19).

The carbon concentration in the Ti-6%Al-4%V matrix was determined to be in the range of 0.3 wt.% to 0.6 wt.% for the composites sintered at 1100°C to 1500°C. From the Ti-C phase diagram, Figure 2.2, the solubility limit of carbon in α-titanium is 0.4 wt.%. Errors associated with concentration analyses of light elements using wavelength or energy dispersive spectroscopy can be quite high (*e.g.* 1 wt.%). In the case of carbon, contamination from the electron beam increases with detection time, thereby increasing the measurement error further. Hence, the carbon concentration values obtained for the Ti-6%Al-4%V matrix, in the composites processed at various conditions, agree reasonably with that expected from the solubility limit using the phase diagram. Moreover, there appears to be a negligible influence of the enhanced carbon loss on the carbon concentration of the matrix with increasing processing temperature. This supports the concept of stable phase formation at the interface between the TiC particles and Ti-6%Al-4%V matrix, as evidenced in the FEGSEM for the composites processed at 1100°C and by the growth of the TiC particles in the composites sintered at 1500°C. However, characterizing the nature of the chemical reaction products would be difficult using this technique as the x-ray volume generated from the electron beam diameter is the same order of magnitude as the region over which there is a reduction in carbon, as illustrated in Figure 6.23.

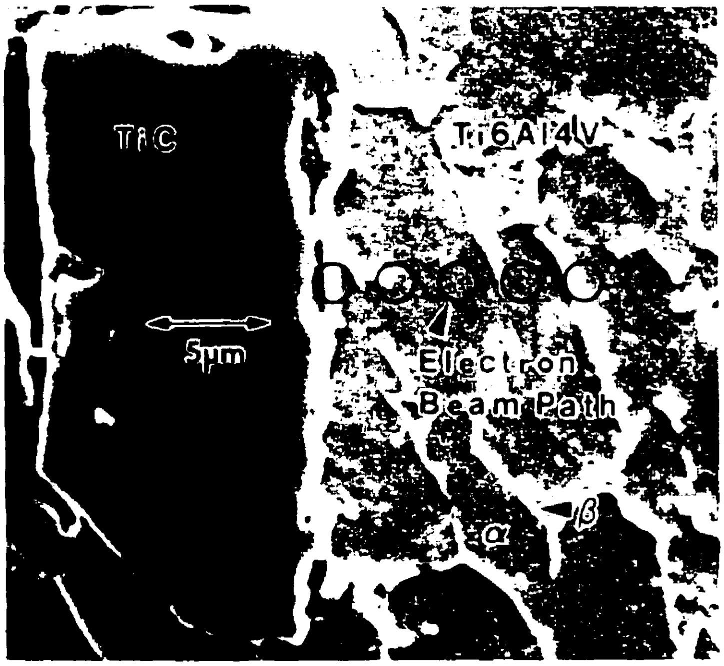

Figure 6.21 SEM micrograph showing the electron probe path taken from a TiC reinforcement particle to the Ti-6%Al-4%V matrix for a 10 vol.% TiC$_p$ reinforced Ti-6%Al-4%V composite sintered for 4 hours at 1300°C.

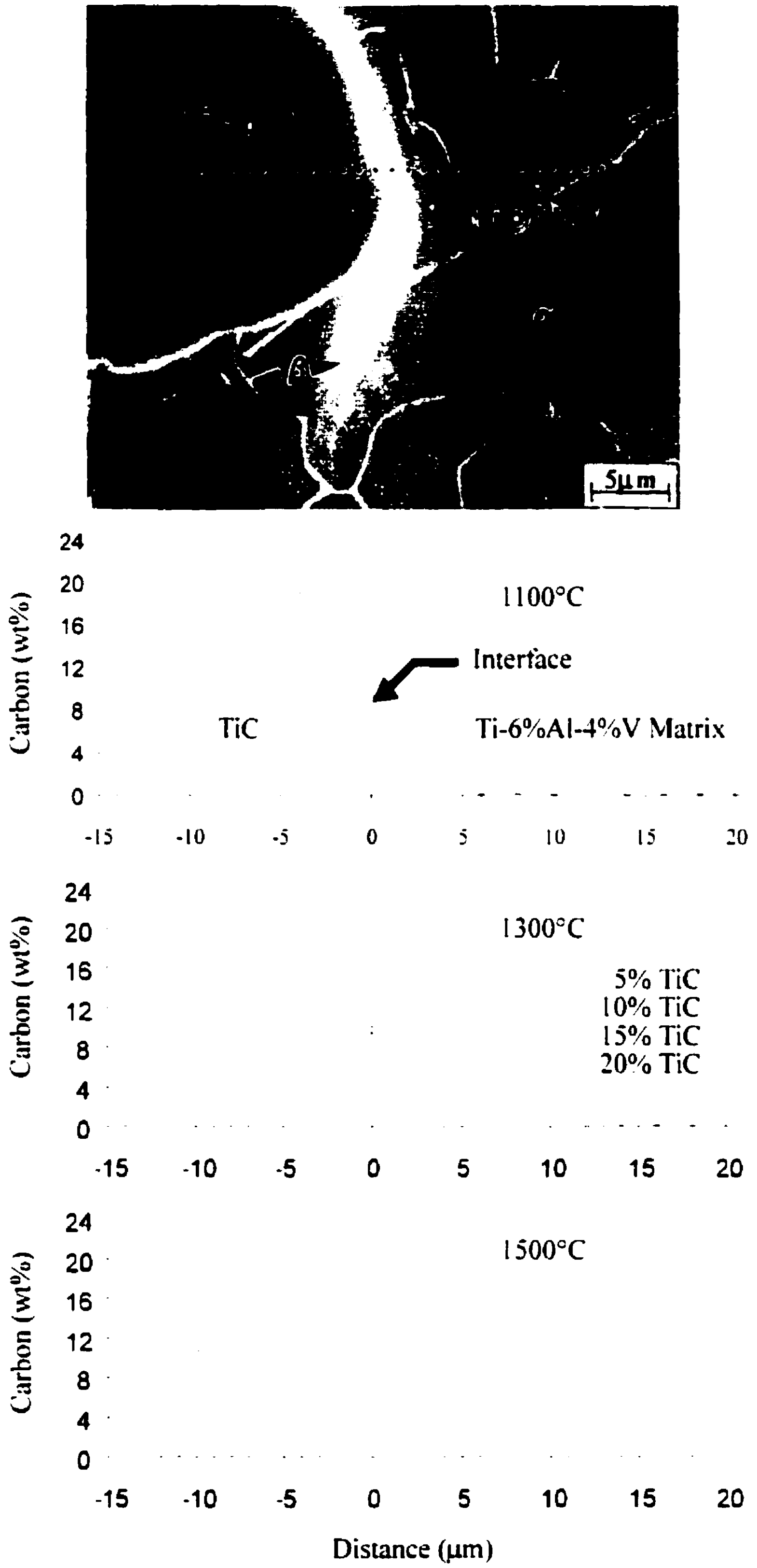

Figure 6.22 EPMA of carbon from the reinforcement to the matrix for the composites sintered for 4 hours at 1100°C, 1300°C and 1500°C.

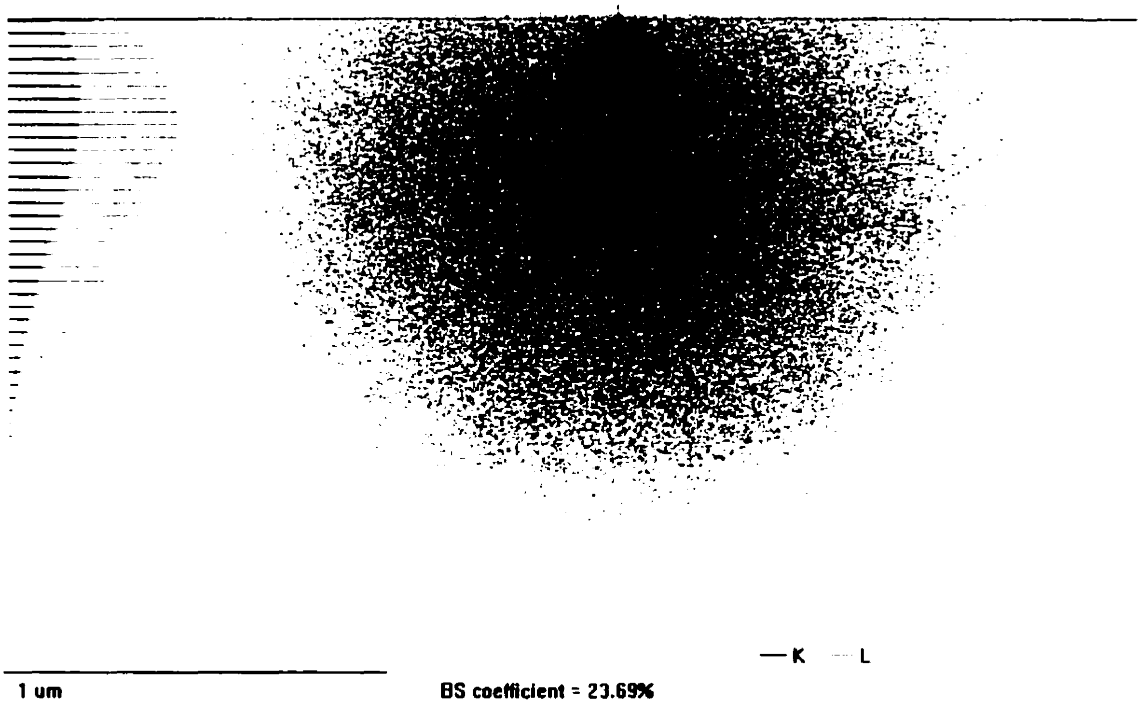

Figure 6.23 Monte Carlo simulation of the x-ray volume generated from a 1 μm beam on the TiC_p reinforced Ti-6%Al-4%V composite at an accelerating voltage of 10 keV and a probe current of 1×10^{-8} A.

6.4.3 Neutron Diffraction Examination

Neutron diffractometery was used to investigate and characterize the phase changes occurring during elevated temperature sintering of the titanium alloy matrix with the TiC reinforcement particles. Initially, the variation in the lattice parameter and coefficient of linear thermal expansion with temperature were examined individually for both Ti-6%Al-4%V and TiC. Although this information is well documented for the latter phase, in the case of the titanium alloy little if any information is available for the high temperature body centered cubic β phase. More specifically, the lattice parameter measurements for the β phase have been obtained by attempting to retain this high temperature phase through quenching. Additionally, only a few values for the coefficient of linear thermal expansion of Ti-6%Al-4%V exist for temperatures above the β-transus. Accordingly, the variation in these parameters with temperature was examined, especially the lattice parameter of β-Ti-6%Al-4%V, since a change in this value during processing of the composite materials may give some insight related to the nature of the reaction between the reinforcement and matrix phases.

The lattice parameter values for the beta phase of the Ti-6%Al-4%V alloy and TiC are plotted as a function of temperature in Figure 6.24. The relationship for the dependency of the lattice parameter on temperature, in the range of 1000°C to 1350°C, for the two phases was determined by fitting the data and is shown on the respective plots.

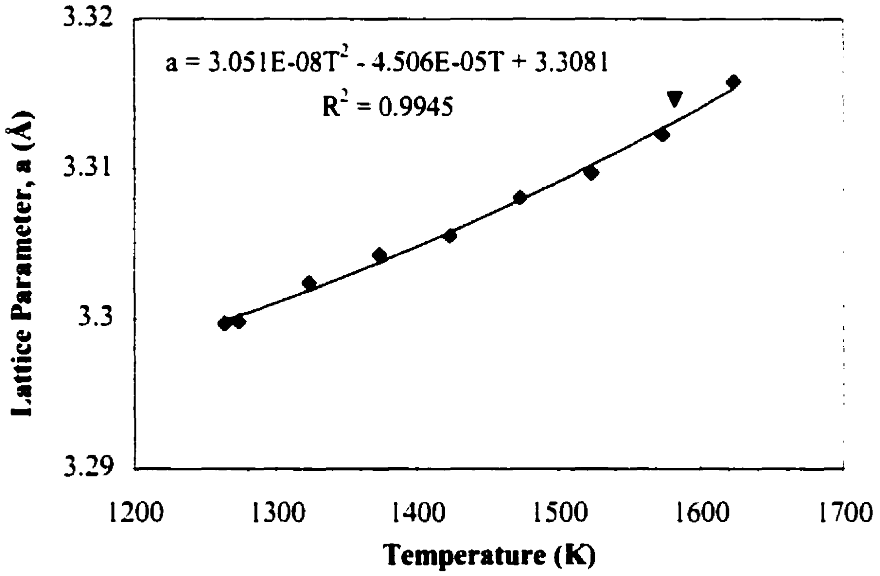

(a) β-Ti-6%Al-4%V

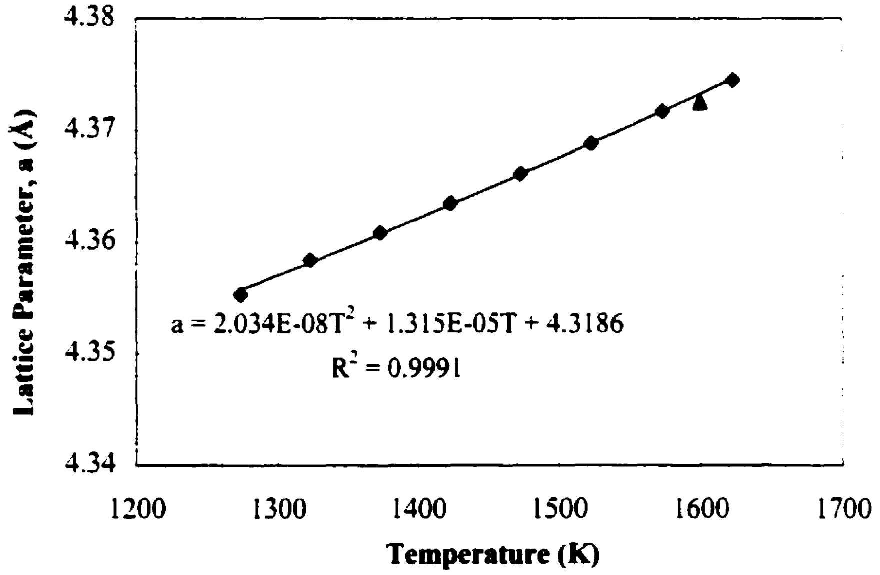

(b) TiC

Figure 6.24 Lattice parameter measurements at various temperatures.

In the composites, a reaction between the TiC reinforcement and the β-Ti-6%Al-4%V matrix during sintering would result in a change in these lattice parameters determined for either phase constituents at the various temperatures. Hence at any isothermal sintering temperature, a change in the lattice parameter with holding time can be used to monitor the reaction between the TiC particles and the β-Ti-6%Al-4%V matrix. Such values are given in Table 6.2.

Table 6.2 - Lattice Parameter Values for β-Ti-6%Al-4%V and TiC

Temperature (°C)	Lattice Parameter Ti-6%Al-4%V alloy (Å)	Lattice Parameter TiC ceramic (Å)
990	3.2997	-
1000	3.2998	4.3553
1050	3.3024	4.3584
1100	3.3043	4.3609
1150	3.3055	4.3635
1200	3.3081	4.3661
1250	3.3098	4.3688
1300	3.3123	4.3717
1350	3.3184	4.3745

In general, the lattice parameter of a given phase is related to temperature by the following equation,

$$a_2 = a_1 + \alpha a_1 (T_2 - T_1) \qquad (6.2)$$

where a_1 and a_2 are the lattice parameters at temperatures T_1 and T_2, respectively and α is the coefficient of linear thermal expansion (CTE). Although this equation appears to suggest that lattice expansion is a linear function of temperature, the CTE also varies with temperature and, for most solids, is not necessarily linear. In the case of TiC, α can be calculated with an accuracy of ± 7% from the following equation:[252]

$$\alpha = 5.710x10^{-4} + 2.348x10^{-7}T + 7.236x10^{-12}T^2 \qquad (6.3)$$

The lattice parameter values obtained for TiC by applying these equations are given in Table 6.3 and are in agreement with the present results. In the case of the Ti-6%Al-4%V alloy, thermal expansion coefficients have been tabulated in the literature up to 1426°C, and are given in Table 6.4.[253] Plotting the lattice parameter data as a function of the temperature in the range of 1000°C and 1350°C (Fig. 6.25), the thermal expansion coefficients (tangents along the curve) for the β phase of the Ti-6%Al-4%V were calculated, as given in Table 6.4. There appears to be good agreement with the values obtained for the CTE of the β phase of Ti-6%Al-4%V as compared to those reported for this alloy.[253]

Table 6.3 - Comparison of Lattice Parameter Values for TiC

Temperature (°C)	**Experimental Lattice Parameter of TiC (Å)**	**Literature Lattice Parameter of TiC (Å)**
1000	4.3553	4.3557
1050	4.3584	4.3582
1100	4.3609	4.3607
1150	4.3635	4.3633
1200	4.3661	4.3659
1250	4.3688	4.3686
1300	4.3717	4.3714
1350	4.3745	4.3742

Table 6.4 - Coefficients of Thermal Expansion for Ti-6%Al-4%V

Temperature (K)	**Literature $\alpha \times 10^{-6}$ (K^{-1})[253]**	**Experimental $\alpha \times 10^{-6}$ (K^{-1})**
1255	8.54-10.99	-
1263	-	9.8
1273	-	10.0
1323	-	10.9
1366	9.88-12.39	-
1373	-	11.8
1400	-	12.4
1423	-	12.7
1473	-	13.6
1477	13.99	-
1523	-	14.5
1573	-	15.4
1588	15.63	-
1600	-	15.9

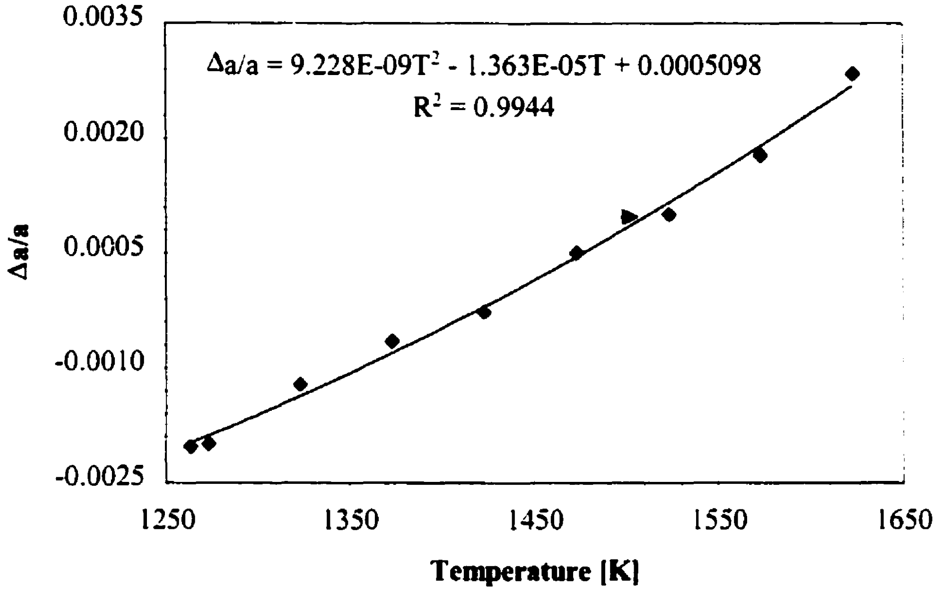

Figure 6.25 Δa/a versus temperature plot for coefficient of thermal expansion measurement.

The β-transus temperature of Ti-6%Al-4%V has been found to vary between 955°C to 1010°C, depending on the alloy composition and interstitial impurities, particularly oxygen content, as depicted in Figure 6.26.[254-255] For the Ti-6%Al-4%V prealloyed powder that was vacuum sintered, the intensity of the diffraction peaks obtained from the neutron scattering studies was analyzed to obtain the volume fractions of α and β in the temperature range of 990°C to 1350°C. The *General Structure Analysis System* (GSAS) program from *Atomic Energy of Canada Limited* (Chalk River Laboratories, Ontario) was used to process and analyze the diffraction data to give the structural parameters of the α and β phases. Volume fraction analysis was performed by determining the integrated intensity of all the diffraction peaks corresponding to both α and β. The volume fraction of α is then the ratio of the total integrated intensity for α to that for α and β. From the plot of α volume fraction as a function of temperature, Figure 6.27, the β-transus temperature for the P/M Ti-6%Al-4%V alloy appears to be 1017°C. Using Figure 6.26 from the literature, the oxygen content corresponding to this β-transus temperature for the P/M sintered Ti-6%Al-4%V alloy would be approximately 0.28 wt.%. Typically, the oxygen content in wrought Ti-6%Al-4%V can vary between 0.08 wt.% to approximately 0.2 wt.%.[254] However, the oxygen content in titanium-based P/M products is usually specified to be 0.3 wt.% maximum.[256] In P/M processing, the oxygen content of the final product depends on the composition of the starting powder material and on the furnace environment used during consolidating. In the present work, the oxygen content in the as-received titanium alloy powder was 0.24 wt.% (Table 4.1). Attrition milling for 15 minutes removed the accumulated oxide layer and the oxygen content of the powder was analyzed to be 0.19 wt.%, prior to elevated temperature consolidation. The increase in oxygen from this level to approximately 0.3 wt.% is then attributed to the reaction of the Ti-6%Al-4%V alloy with residual oxygen present in the vacuum environment during sintering.[256]

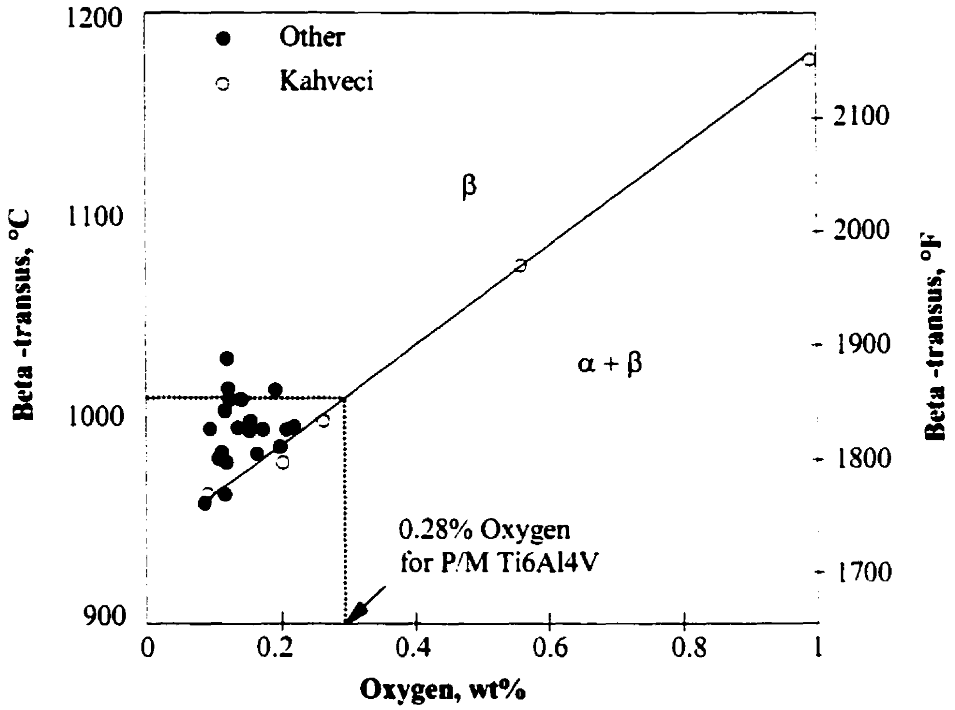

Figure 6.26 Beta-transus temperature versus oxygen content for Ti-6%Al-4%V.[254-255]

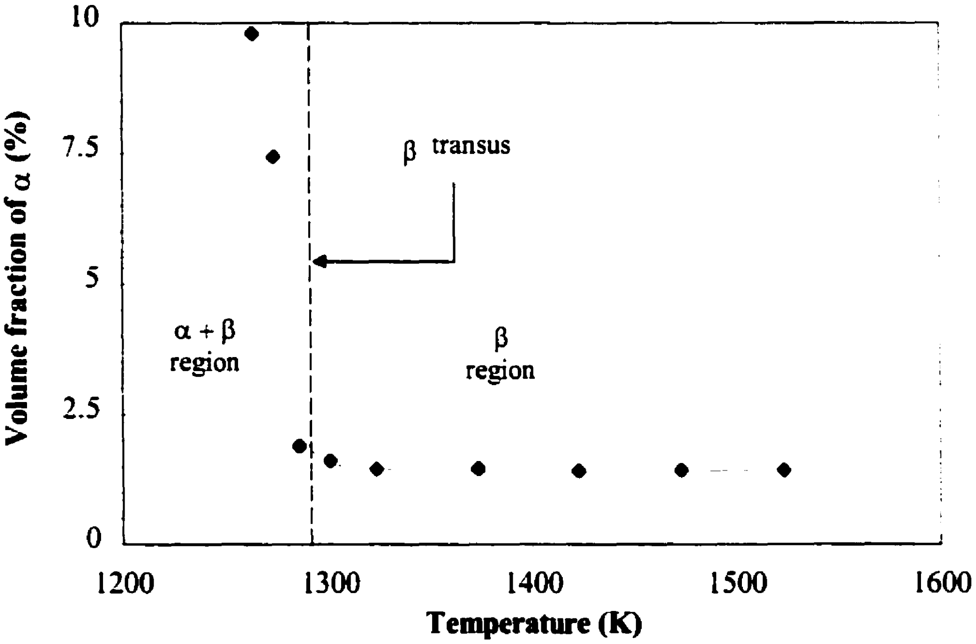

Figure 6.27 β-transus temperature determination.

To investigate the nature of the interfacial reaction between the matrix and reinforcement phases, consolidation of the TiC_p reinforced Ti-6%Al-4%V composites was studied *in situ* at elevated temperatures on a neutron powder diffractometer. This was performed by monitoring the changes in the TiC and β-titanium neutron diffraction patterns in the titanium-based composite material with consolidation time at a particular sintering temperature. Figure 6.28 illustrates the evolution in the neutron diffraction pattern of the two phase constituents at a sintering temperature of 1100°C after sintering for 20 hours.

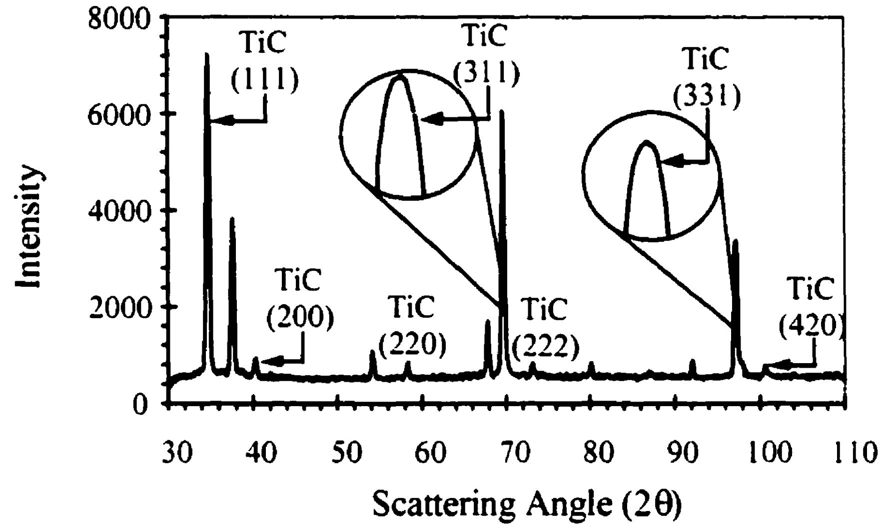

(a) start of consolidation at 1100°C

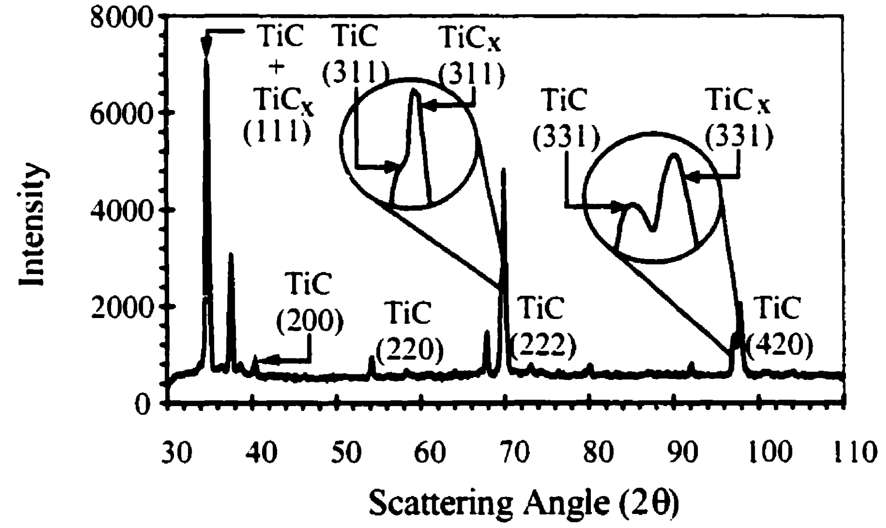

(b) after 20 hours of consolidation at 1100°C

Figure 6.28 Variation in the diffraction peaks of the TiC and β-titanium phases for the 20 vol.% TiC_p reinforced Ti-6%Al-4%V composite. (Unlabeled peaks are the β phase of the Ti-6%Al-4%V alloy.)

The main evolution in the diffraction pattern appears to be the gradual reduction in the intensity of the TiC diffraction peaks. With the progression of sintering, the emergence of two distinctive peaks at higher scattering angles was clearly evident near the original (311) and (331) TiC peaks. As changes in the lattice parameter values are reflected more easily at higher scattering angles, the appearance and growth of these new peaks suggests the formation of a new phase(s), which, in this case, would be the interfacial reaction product(s). Additionally, the mean scattering angle of the (111) peak of TiC was observed to shift to slightly higher angles and increase in width with increasing holding time at temperature. This shift is explained by the growth of a neighboring peak that cannot be resolved. Moreover, increasing the temperature to 1300°C resulted in a similar evolution of the neutron diffraction pattern with holding time for the composites, as shown in Figure 6.29.

At higher sintering temperatures, the appearance and growth of these new peaks at the higher scattering angle occurs more rapidly. This supports the suggestion that the appearance of these new peaks is a result of sintering. That is, higher sintering temperatures have resulted in considerable reaction of the TiC reinforcement phase with the Ti-6%Al-4%V matrix, as evidenced by the previous observations of carbon loss from the TiC particles, enhanced consolidation and coarsening of the TiC particle. Thus, the increased growth kinetics of these news peaks is not unusual if they occur directly on account of sintering.

The maximum temperature attainable for the sintering furnace facilities attached to the neutron powder diffractometer was 1350°C. Hence, the composites sintered at 1500°C were analyzed in the neutron diffractometer by re-heating above the β-transus temperature of the Ti-6%Al-4%V alloy to characterize the various phase constituents of the composites. The reason for acquiring the diffraction pattern in the single-phase beta region (*i.e.* 1100°C), as opposed to room temperature analysis, is to eliminate the hexagonal closed-packed (hcp) alpha-titanium peaks, which would considerably increase the difficulty of analyzing the spectra. Interfacial reaction rates between the titanium alloy matrix and TiC particles at 1100°C have been observed to be quite slow, as illustrated in Figure 6.28. Thus, re-heating to a temperature slightly above the beta transus and holding for 20 minutes to obtain the diffraction pattern had very little influence on the as-sintered condition of the composites.

The diffraction pattern of the composites sintered at 1500°C for ½, 1, 2 or 4 hours did not reveal the appearance of a peak doublet at the higher angles, as illustrated in Figure 6.30. Since lower temperature sintering revealed the appearance of new peaks after prolonged holding times, it is possible that the TiC particles in the β-Ti-6%Al-4%V matrix remain unreacted after 4 hours of sintering at 1500°C. However, the lattice parameter calculated for the reinforcement phase did not correspond to that of TiC. Hence, sintering at 1500°C results in rapid transformation (*i.e.* within ½ hour) of the TiC reinforcement particles due to extensive carbon loss during sintering at 1500°C.

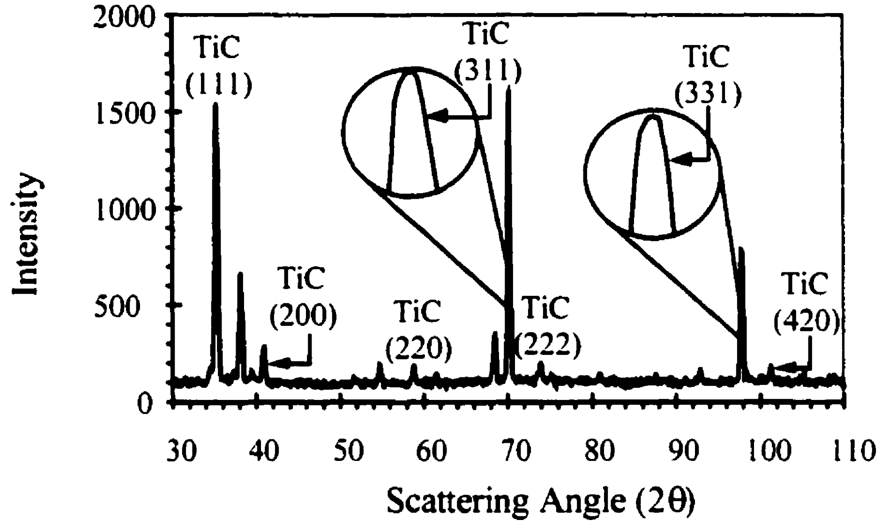

(a) start of consolidation at 1300°C

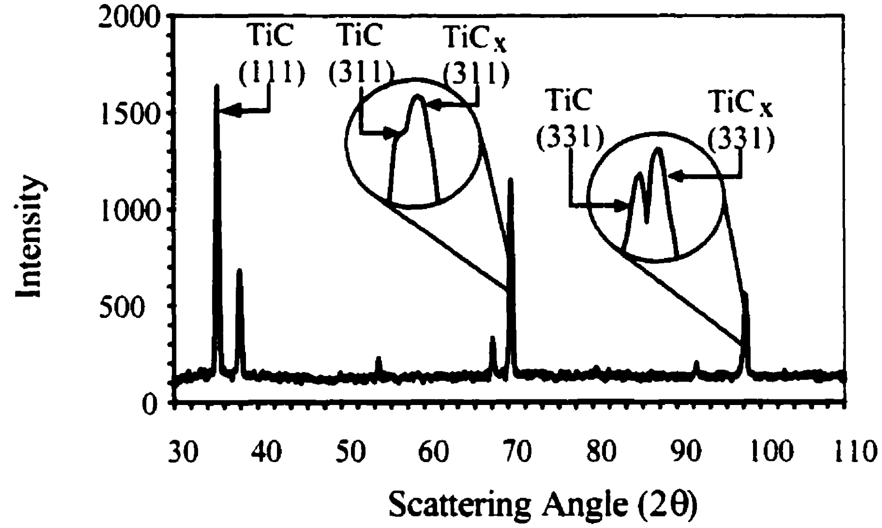

(b) after 8 hours of consolidation at 1300°C

Figure 6.29 Variation in the diffraction peaks of the TiC and β-titanium phases for the 20 vol.% TiC_p reinforced Ti-6%Al-4%V composite. (Unlabeled peaks are the β phase of the Ti-6%Al-4%V alloy.)

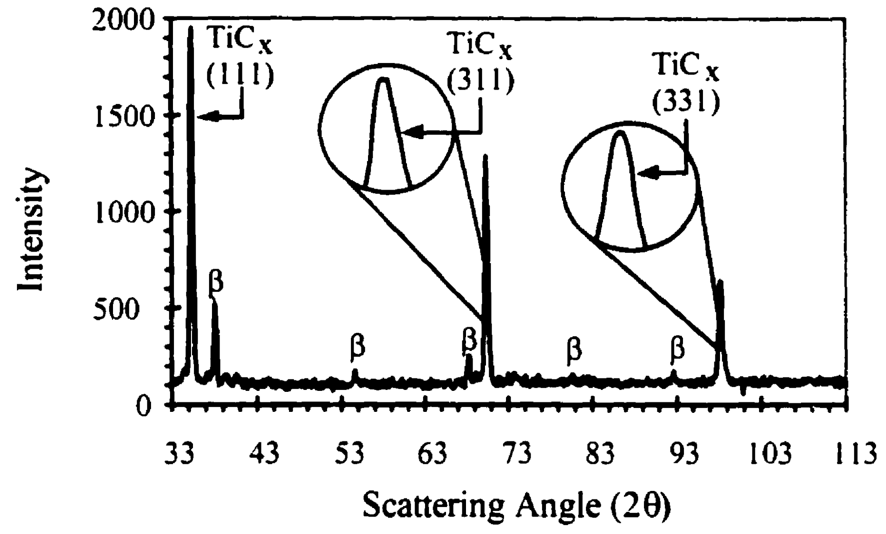

Figure 6.30 Diffraction pattern of the TiC and β-titanium phases for the 20 vol.% TiC_p reinforced Ti-6%Al-4%V composite sintered at 1500°C for ½, 1, 2 or 4 hours holding and reheated to 1100°C for analysis by neutron diffraction. (The peaks labeled β represent the beta phase of the Ti-6%Al-4%V alloy.)

To calculate the lattice parameter for identification of the various phases, the scattering angle of the diffraction peaks was measured. From these measurements of the diffraction peak angles, the d_{hkl} values were calculated using Bragg's law (where the wavelength of the neutron beam, λ, was 1.5008 Å). For each phase, the lattice spacing of each plane, a, was then determined from the d_{hkl} values from the equation for cubic crystal symmetry. These measured values of a were plotted against $\cos^2\theta$ to obtain the *true* value of the lattice parameter, a_0, by extrapolating to $2\theta = 180°$ (*i.e.* correcting for errors in diffraction angle measurements). This technique is described in Appendix III.

Interaction of the Ti-6%Al-4%V matrix with the TiC particles during elevated temperature consolidation appears to occur through lattice and/or grain boundary diffusion as determined from the previous investigation of the sintering mechanism. Considering the diffusivities of the various elements in β-titanium, carbon being an interstitial element has been found to diffuse faster than the other metallic elements, as illustrated in Figure 6.31. However, whereas interstitial elements, such as carbon, nitrogen and oxygen, can diffuse several orders of magnitude faster than many metals, the diffusivity of interstitial atoms in α- or β-titanium is only one to two orders of magnitude larger than the self-diffusivity of titanium.[250] In fact, substantially higher activation energies for the diffusion of interstitials in titanium, as compared to those in other metals, suggests the formation of strong covalent-like bonds between these interstitial atoms and the host titanium atoms.[250] Hence it is possible that the reaction zone in the TiC particles can be generated either by the diffusion of carbon from the reinforcement phase or by the diffusion of titanium into the particles, or by a combination of both.

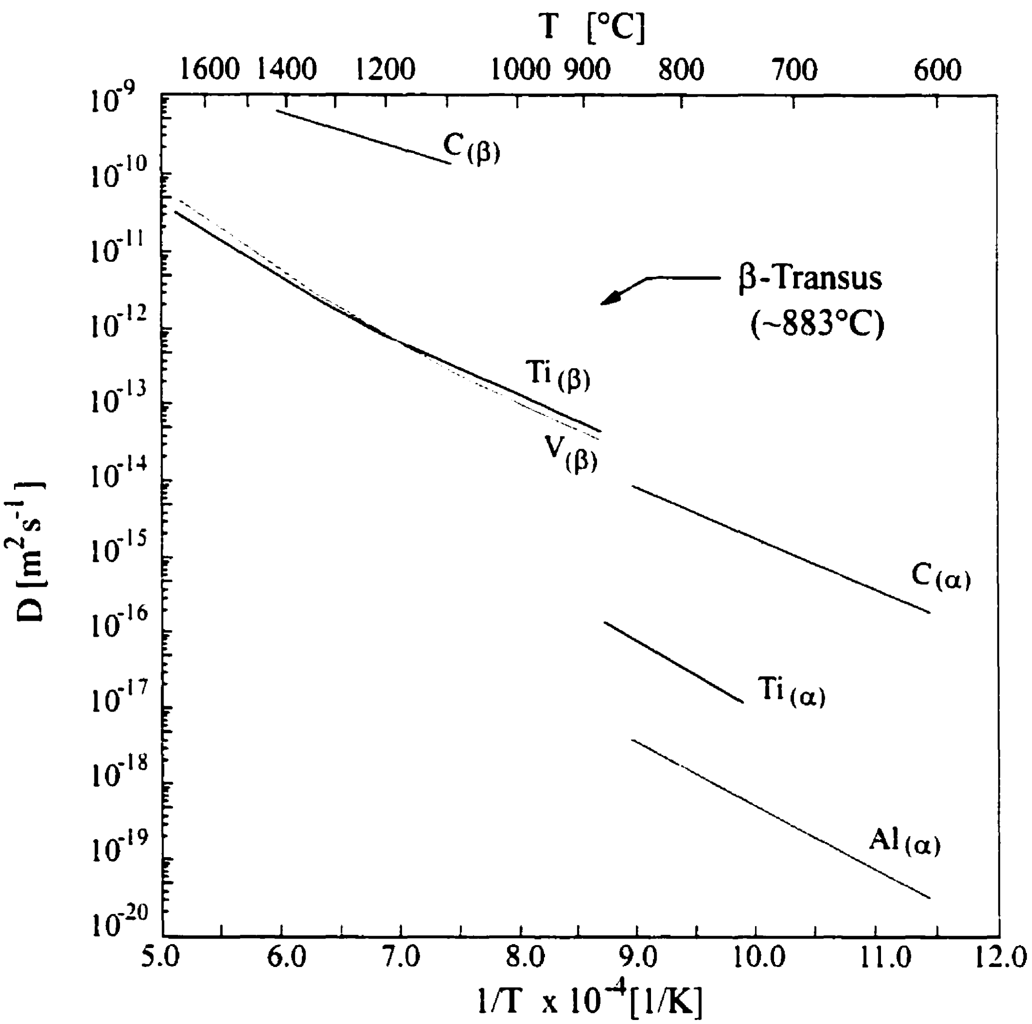

Figure 6.31 Temperature dependence of self and impurity diffusivities in α- and β-titanium. Reproduced using available data summarized in the review by H. Nakajima and M. Koiwa.[250]

Thus, isothermal reaction of TiC with Ti-6%Al-4%V is expected to result initially in an increase in the carbon concentration of the matrix until saturation of the β-Ti-6%Al-4%V occurs (~ 0.2 wt.% for carbon in β-titanium). Generally, a change in composition within a single-phase region of an equilibrium phase diagram produces a change in the lattice parameter (calculated from the scattering angle) of that phase. Hence for the β-Ti-6%Al-4%V phase, a change in composition can be resolved by monitoring the shift in the positions of the neutron diffraction peaks of this phase. A downward shift in the positions of the neutron diffraction peaks for the β-Ti-6%Al-4%V matrix phase was observed with increasing hold time at temperature. For isothermal temperatures in the range of 1100°C to 1350°C, the change in the lattice parameter of the β-Ti-6%Al-4%V phase with holding time was calculated for the composites as illustrated in Figures 6.32 to 6.37. There appears to be an increase in the lattice parameter of the β-Ti-6%Al-4%V phase with hold time regardless of the sintering temperatures. Since the addition of interstitial atoms is always accompanied by an increase in the unit cell volume, for the cubic system, the lattice parameter must increase.[238] In the case of non-cubic systems, one lattice parameter may increase and the other may decrease, as long as these changes result in an overall increase in the unit cell volume. For hcp α-titanium, the lattice parameters for both the a- and c-axes have been found to increase linearly with increasing carbon content.[257]

Figures 6.32 to 6.34 indicate that at lower temperatures the lattice parameter values are initially close to that obtained for unreinforced Ti-6%Al-4%V (Table 6.2). These initial lattice parameter values (*i.e.* intercept values in the regression equations found in Figs. 6.32 to 6.34) then increase with holding time and appear to level off asymptotically. This increase in the lattice parameter with holding time at the isothermal sintering temperatures appears to suggest carbon dissolution into the β-Ti-6%Al-4%V matrix. As the maximum solubility of carbon in pure-titanium is approximately 0.2 wt.% (Fig. 2.2), the significance of the lattice parameter value leveling off with prolonged holding time at the various temperatures is presumably due to carbon saturation of β-Ti-6%Al-4%V.

At higher consolidation temperatures (Figs. 6.35 to 6.37), the initial lattice parameter measured for the β-matrix phase (*i.e.* intercept value from the regression equations found in Figs. 6.35 to 6.37) deviates from that measured for unreinforced Ti-6%Al-4%V (Table 6.2). As with low temperature sintering, there is an increase in these initial lattice parameter values with holding time, although this increase diminishes with increasing temperature. The increase in the initial lattice parameter value of the β-matrix phase for consolidation of the composites at the higher temperatures is most probably due to enhanced diffusion, which promotes rapid carbon dissolution into the β-Ti-6%Al-4%V matrix. Moreover, for the composites consolidated at 1300°C and 1350°C, it is possible that substantial carbon diffusion occurs during heating to the isothermal sintering temperature. Typically, the maximum heating rate, 25°C·min^{-1}, was utilized; however, it appears that carbon diffusion occurs rather rapidly in this high temperature region. The 'carbon saturated' lattice parameter values for the β-Ti-6%Al-4%V matrix phase in the composites are compared to those calculated for the unreinforced Ti-6%Al-4%V alloy at the various isothermal temperatures (Table 6.5).

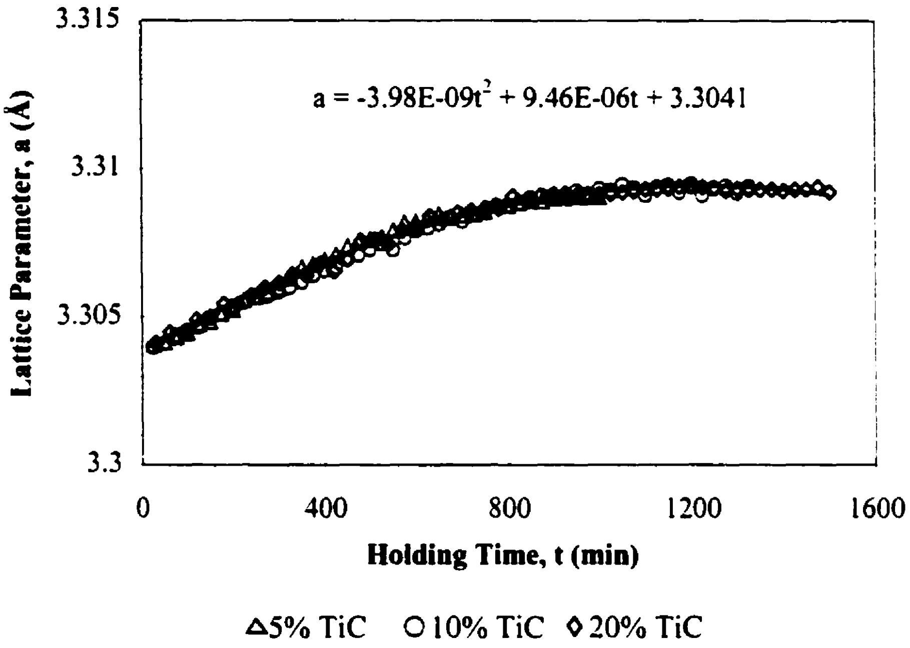

Figure 6.32 Change in the lattice parameter of the β-Ti-6%Al-4%V phase with increasing holding time for the TiC particulate reinforced composites sintered at 1100°C.

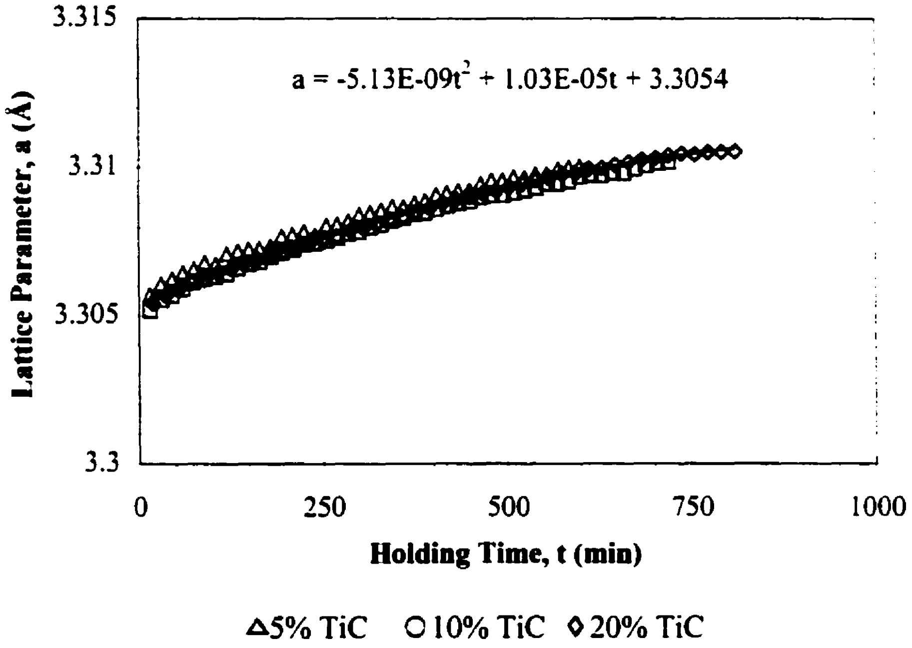

Figure 6.33 Change in the lattice parameter of the β-Ti-6%Al-4%V phase with increasing holding time for the TiC particulate reinforced composites sintered at 1150°C.

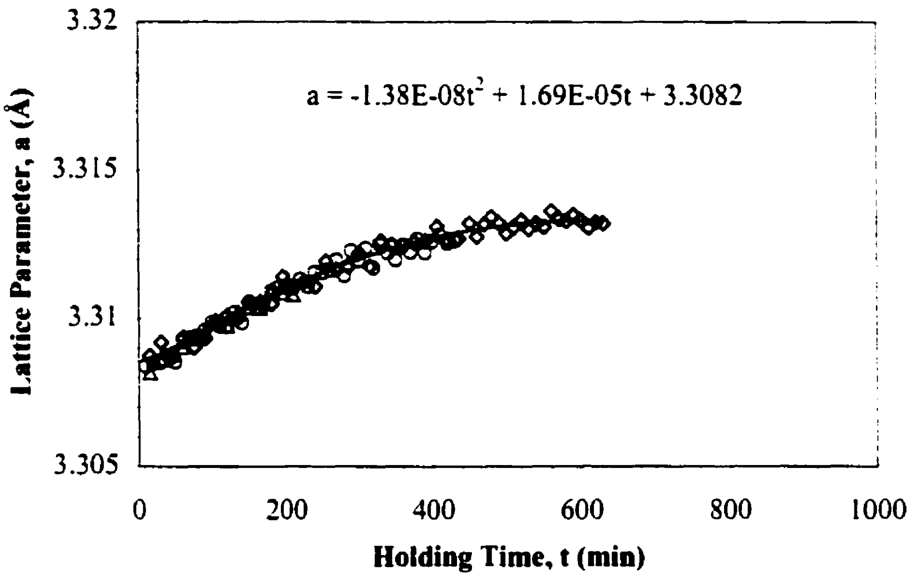

△5% TiC ○10% TiC ◇20% TiC

Figure 6.34 Change in the lattice parameter of the β-Ti-6%Al-4%V phase with increasing holding time for the TiC particulate reinforced composites sintered at 1200°C.

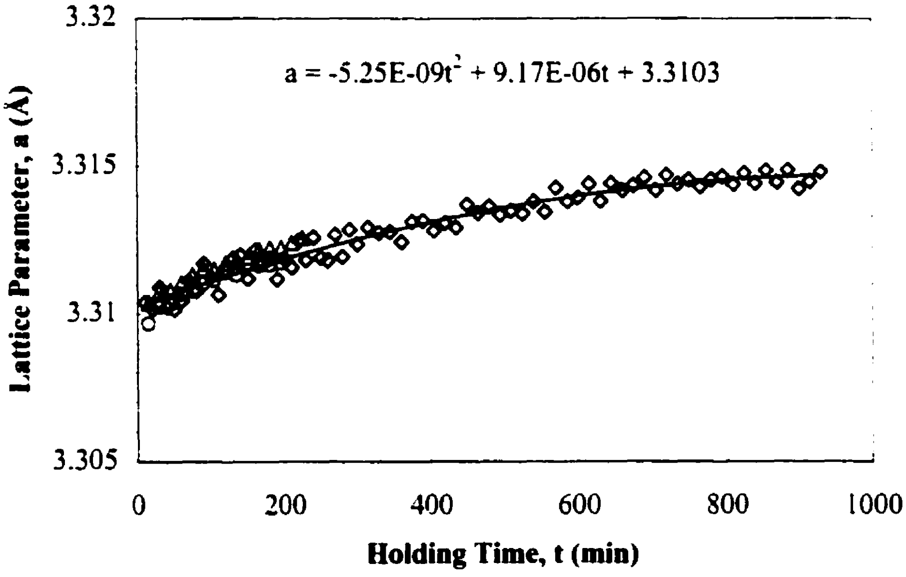

△5% TiC ○10% TiC ◇20% TiC

Figure 6.35 Change in the lattice parameter of the β-Ti-6%Al-4%V phase with increasing holding time for the TiC particulate reinforced composites sintered at 1250°C.

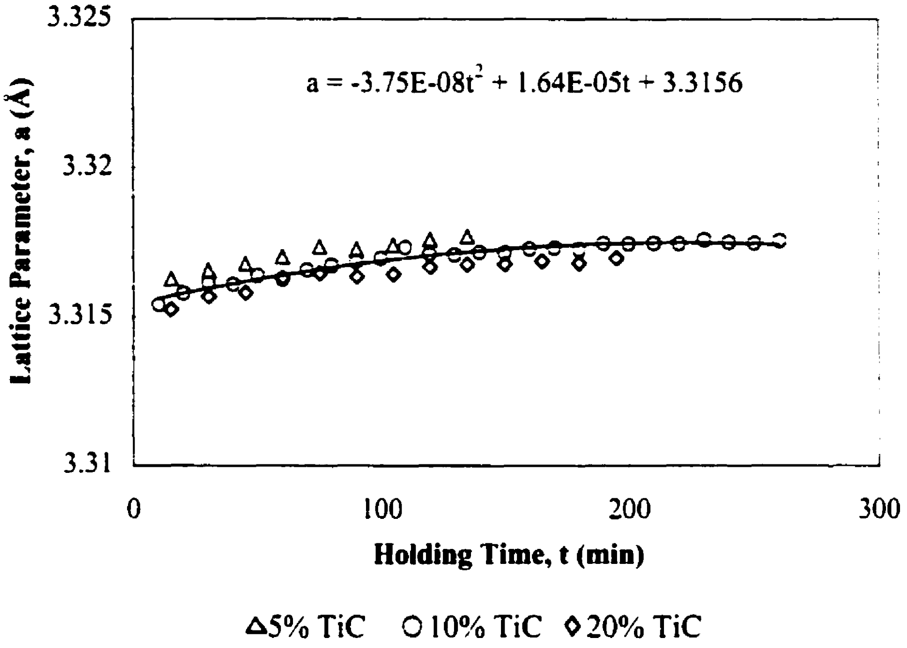

Figure 6.36 Change in the lattice parameter of the β-Ti-6%Al-4%V phase with increasing holding time for the TiC particulate reinforced composites sintered at 1300°C.

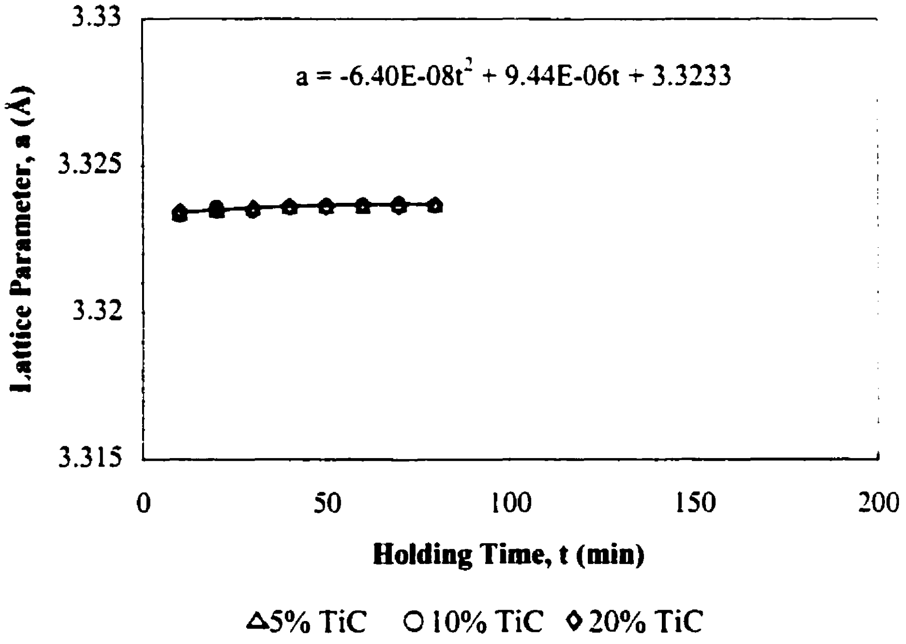

Figure 6.37 Change in the lattice parameter of the β-Ti-6%Al-4%V phase with increasing holding time for the TiC particulate reinforced composites sintered at 1350°C.

Table 6.5 - Lattice Parameter Values for Ti-6%Al-4%V with and without carbon

Temperature (°C)	Lattice Parameter (Å)	
	Ti-6%Al-4%V alloy	Ti-6%Al-4%V matrix with carbon
1100	3.3043	3.3097
1150	3.3055	3.3103
1200	3.3081	3.3134
1250	3.3098	3.3143
1300	3.3123	3.3174
1350	3.3184	3.3236

Besides carbon diffusion in Ti-6%Al-4%V, reaction of the β-matrix with TiC generates an interfacial phase as evidenced by the appearance of distinct peaks in the neutron diffraction patterns. Formation and growth of the interfacial phase would then necessitate a decrease in the amount of the reacting phases, namely β-Ti-6%Al-4%V and TiC. The intensity of the diffraction pattern of a particular phase in a mixture of phases depends on its amount in the mixture. However, the relation between diffraction intensity and concentration is not generally linear and must be corrected for all geometric and sample dependent factors such as absorption, texture, temperature, etc.. The total corrected integrated intensity was calculated for each phase using Gaussian distribution functions (Appendix IV and V). For Ti-6%Al-4%V, the plots of total integrated intensity with holding time at the various isothermal sintering temperatures (Figs. 6.38 to 6.43) reveal a decrease in the intensity with increasing time.

In Figures 6.38 to 6.43, it is observed that the integrated intensity of the β-Ti-6%Al-4%V matrix phase was consistently the lowest for the 20 vol.% TiC reinforced composites. Additionally, there was a progressive increase in the integrated intensity of the β-Ti-6%Al-4%V phase with decreasing TiC volume fraction. This increase is inherently related to the higher proportion of the Ti-6%Al-4%V matrix phase in the composites containing lower volume fractions of TiC particles. This relative comparison remains true if the neutron count time is roughly the same for all materials tested under a particular sintering condition. In addition, for a particular sintering temperature, the mass and density of the starting compact specimens of the various composites must be approximately similar. The plot of green density as a function of TiC volume fraction, Figure 6.3, indicated that for every 5 vol.% increase in TiC there is a 1% increase in the relative density. Considering that this change in the green density is relatively small, the integrated intensity of the β-Ti-6%Al-4%V phase is expected to be the greatest in the 5 vol.% TiC composite as compared to the

10 vol.% TiC and 20 vol.% TiC composites. Alternatively, this effect can also be observed by monitoring the integrated intensity of the TiC phase in the various composite materials, as illustrated in Figures 6.44 to 6.49. That is, for a particular isothermal sintering temperature, the integrated intensity of the TiC phase in the 20 vol.% TiC composite is approximately twice as high as that of the 10 vol.% composites, with the latter in turn being approximately twice as high as the 5 vol.% TiC composite. A similar decrease in the integrated intensity with holding time was observed for the TiC phase. This decrease, then, appears to suggest a decrease in the quantity of TiC with sintering time.

In the analysis of integrated intensity as a function of holding time for the two reacting phases, it was observed that there is a general decrease in the quantity of both the β-Ti-6%Al-4%V and TiC. Previous work on these composites has suggested that reaction of these two phases leads to the formation of a non-stoichiometric interface phase having a composition of TiC_x , where x ranges between 0.5 and 1. Formation of such a non-stoichiometric phase would then be indicated by broadening of the TiC diffraction peaks, especially those located at the high scattering angles. However, as observed in Figures 6.28b and 6.29b, the present neutron diffraction data, that is, the (331) and (311) diffraction peaks of TiC, suggest the formation of a distinct interfacial phase having a fixed stoichiometry and a crystal structure similar to that of TiC, namely face-centered cubic. Moreover the lattice parameter of the TiC phase was found to remain constant with holding time for each isothermal sintering temperature. These neutron diffraction observations are consistent with the FEGSEM work in which the annular boundary layer around the TiC particles was observed to have a fixed composition regardless of the temperature.

The lattice parameter of the interfacial phase was measured for each isothermal sintering temperature, as shown in Figure 6.50. By fitting a polynomial regression function to the experimental data plotted in Figure 6.50, the room temperature lattice parameter value for the interfacial phase was determined by extrapolation to be 4.296 Å ± 0.001 Å. Also a room temperature diffraction pattern was acquired for the 20 vol.% TiC composite processed at 1500°C for 1 hour to directly measure the lattice parameter value of the interfacial phase under ambient conditions. A Reitveld regression analysis using the *General Structure Analysis System* program was performed on the diffraction pattern and the fractional occupancy of carbon in the TiC lattice was varied. A room temperature lattice parameter value for the interfacial phase was determined to be 4.290 Å ± 0.001 Å with a fractional occupancy of carbon of 0.45 ± 0.04. It has been suggested by Goretzki[117] that carbon occupies ordered positions in a supercell with twice the lattice parameter of the basic TiC face centered cubic cell. For simplicity we have assumed a face centered cubic structure with random occupancy of the carbon atoms.

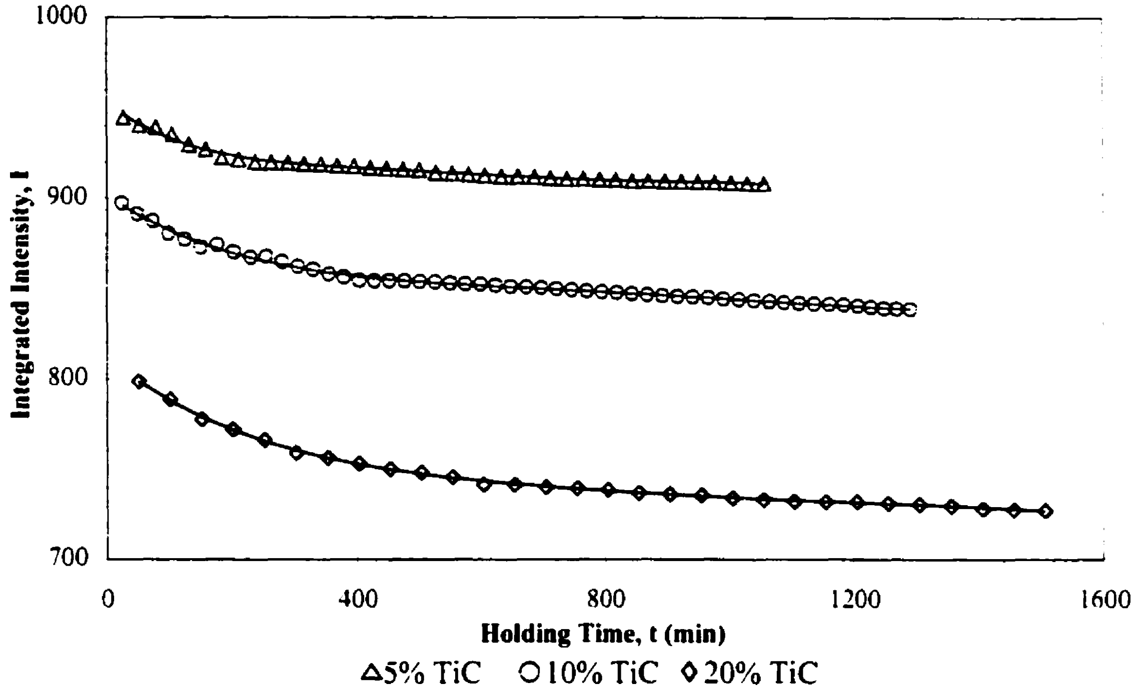

Figure 6.38 Change in the integrated intensity of the β-Ti-6%Al-4%V phase with increasing holding time for the TiC particulate reinforced composites sintered at 1100°C.

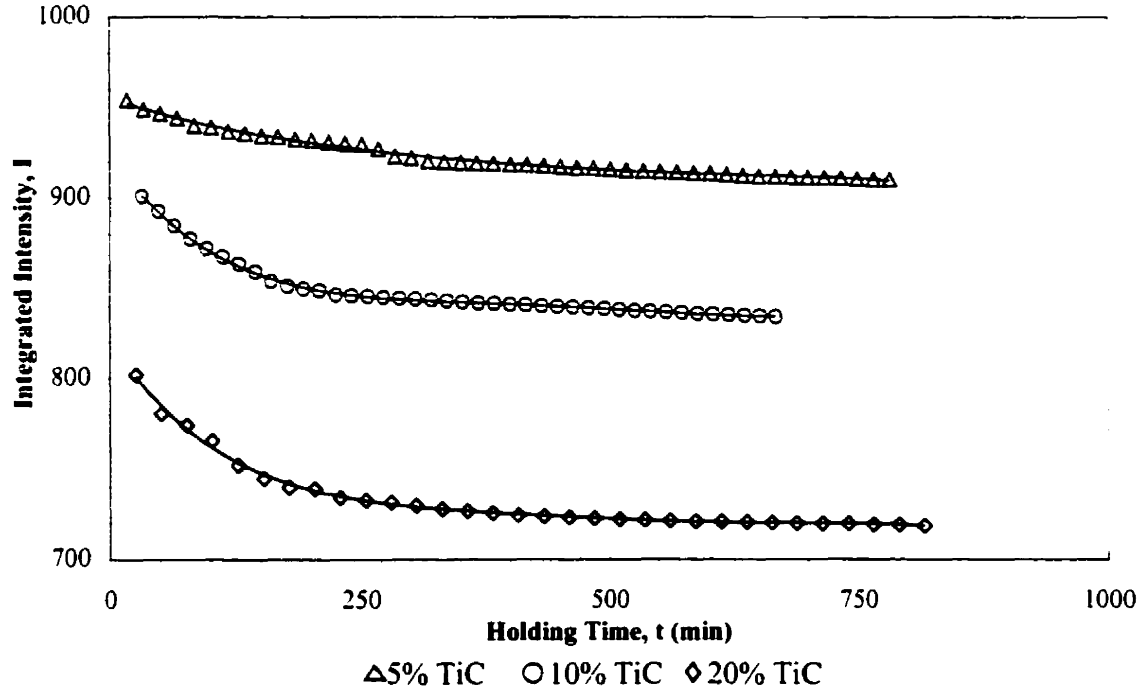

Figure 6.39 Change in the integrated intensity of the β-Ti-6%Al-4%V phase with increasing holding time for the TiC particulate reinforced composites sintered at 1150°C.

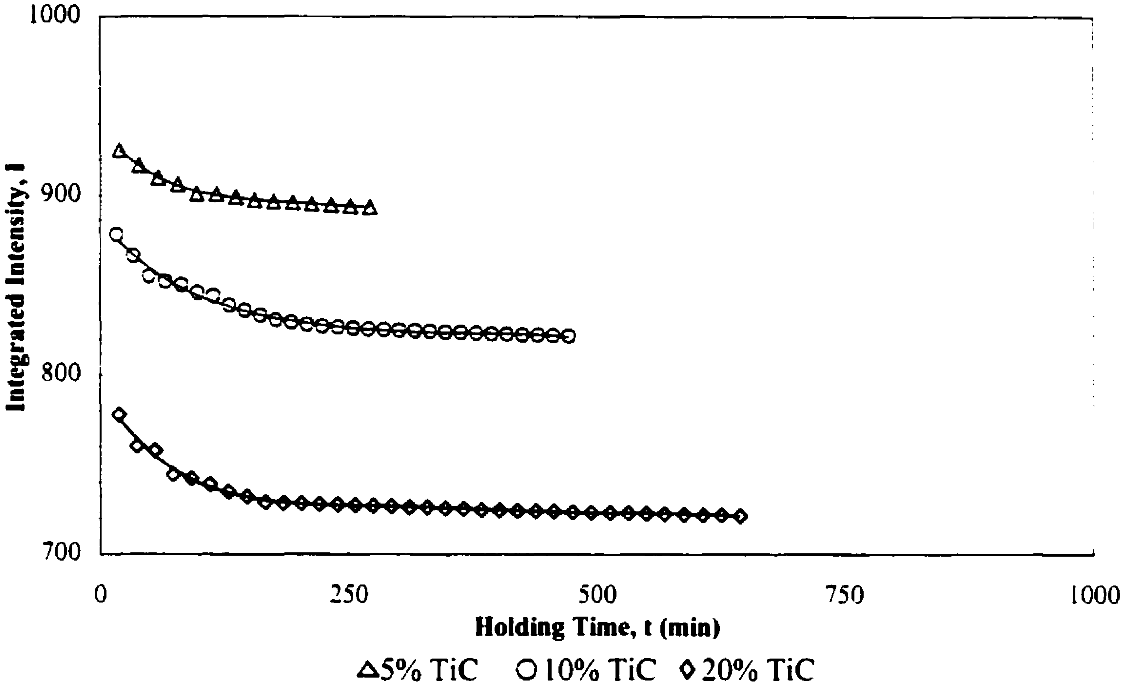

Figure 6.40 Change in the integrated intensity of the β-Ti-6%Al-4%V phase with increasing holding time for the TiC particulate reinforced composites sintering at 1200°C.

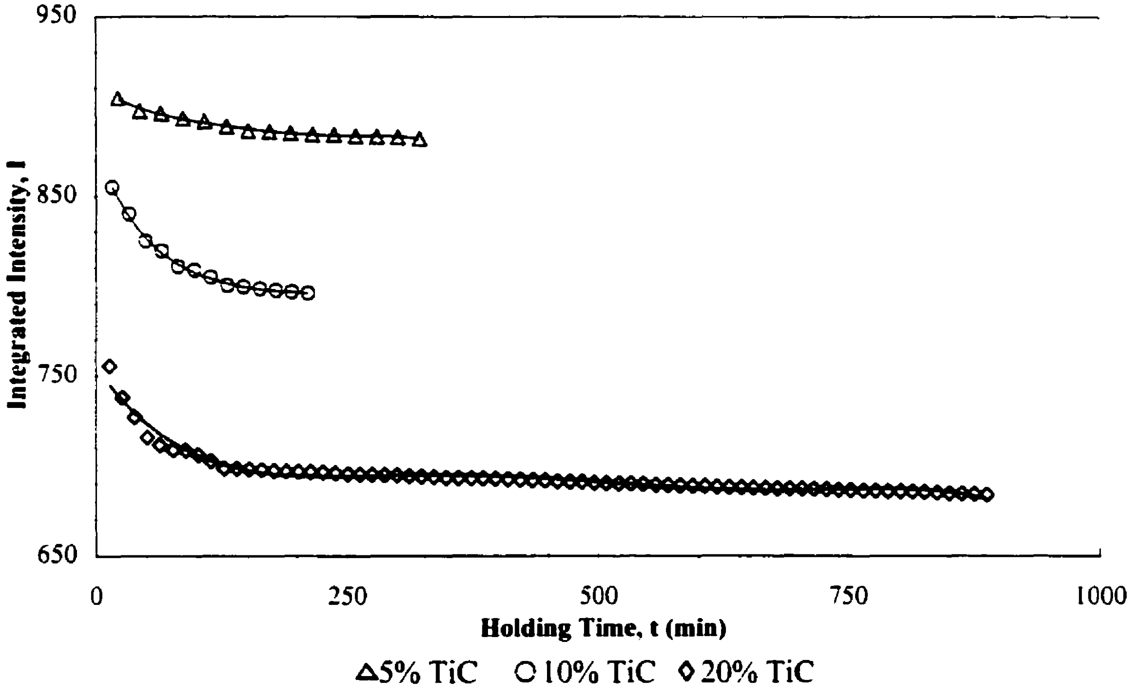

Figure 6.41 Change in the integrated intensity of the β-Ti-6%Al-4%V phase with increasing holding time for the TiC particulate reinforced composites sintered at 1250°C.

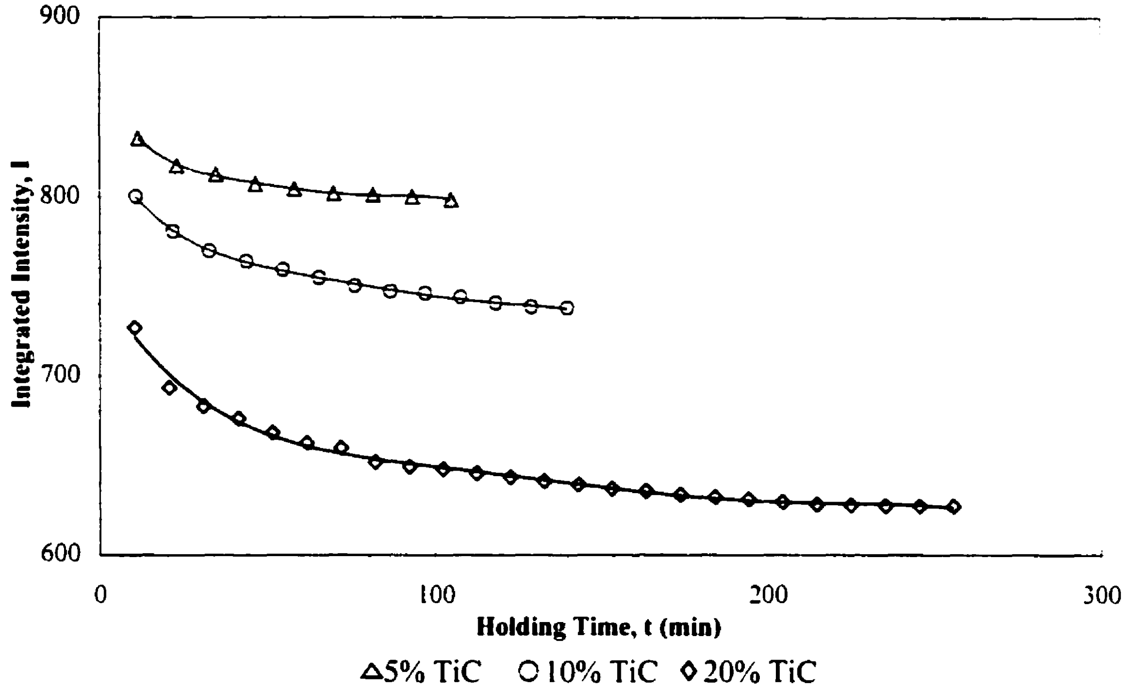

Figure 6.42 Change in the integrated intensity of the β-Ti-6%Al-4%V phase with increasing holding time for the TiC particulate reinforced composites sintered at 1300°C.

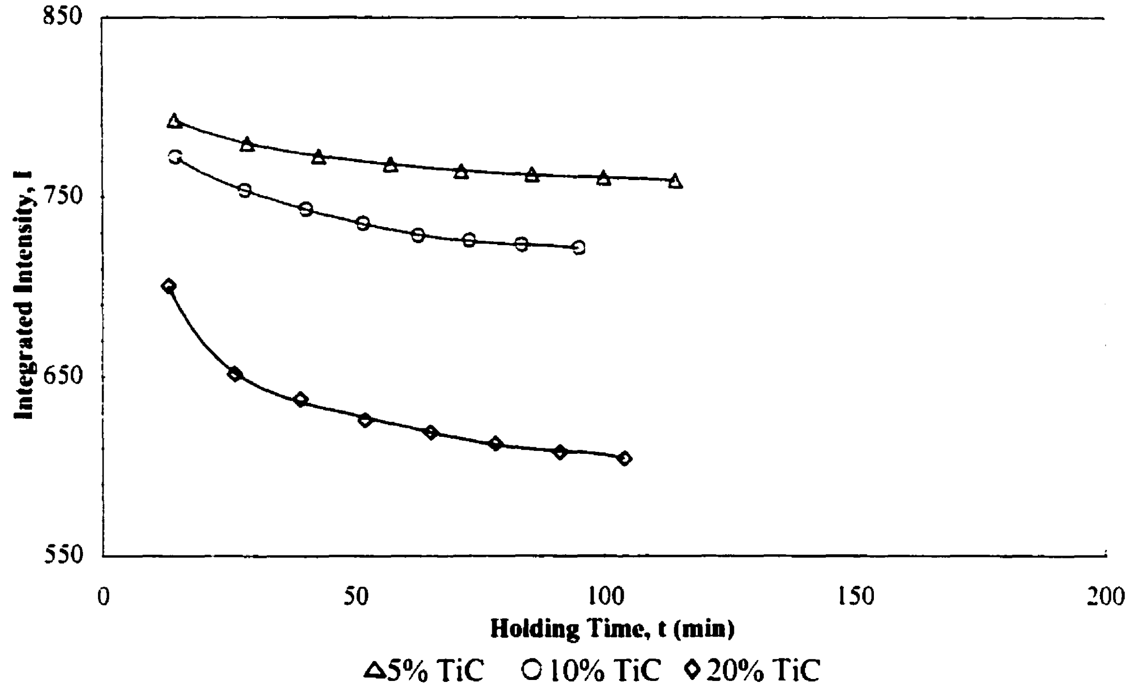

Figure 6.43 Change in the integrated intensity of the β-Ti-6%Al-4%V phase with increasing holding time for the TiC particulate reinforced composites sintered at 1350°C.

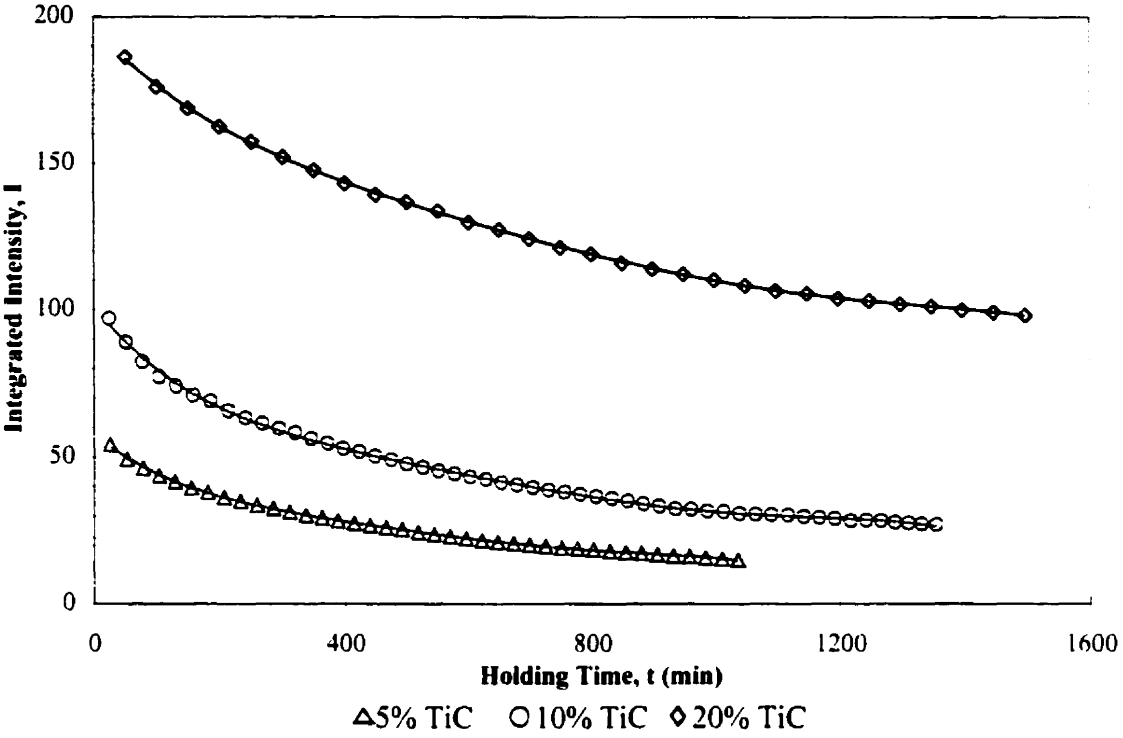

Figure 6.44 Change in the integrated intensity of the TiC phase with increasing holding time for the Ti-6%Al-4%V composites sintered at 1100°C.

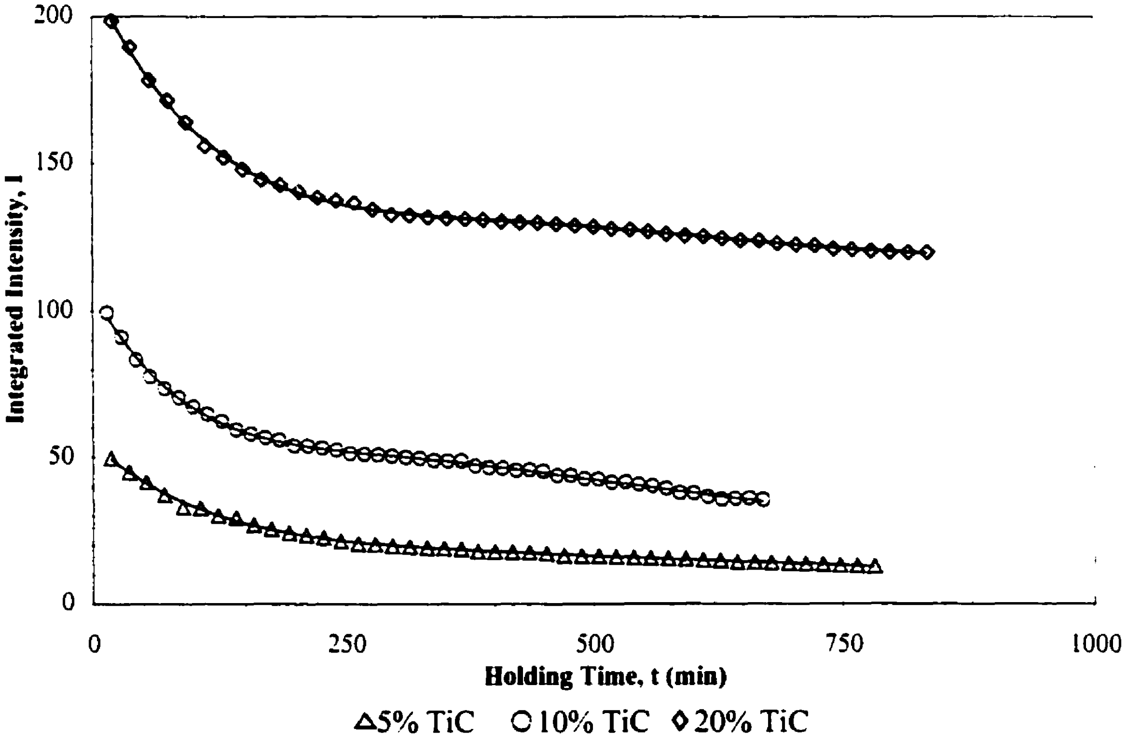

Figure 6.45 Change in the integrated intensity of the TiC phase with increasing holding time for the Ti-6%Al-4%V composites sintered at 1150°C.

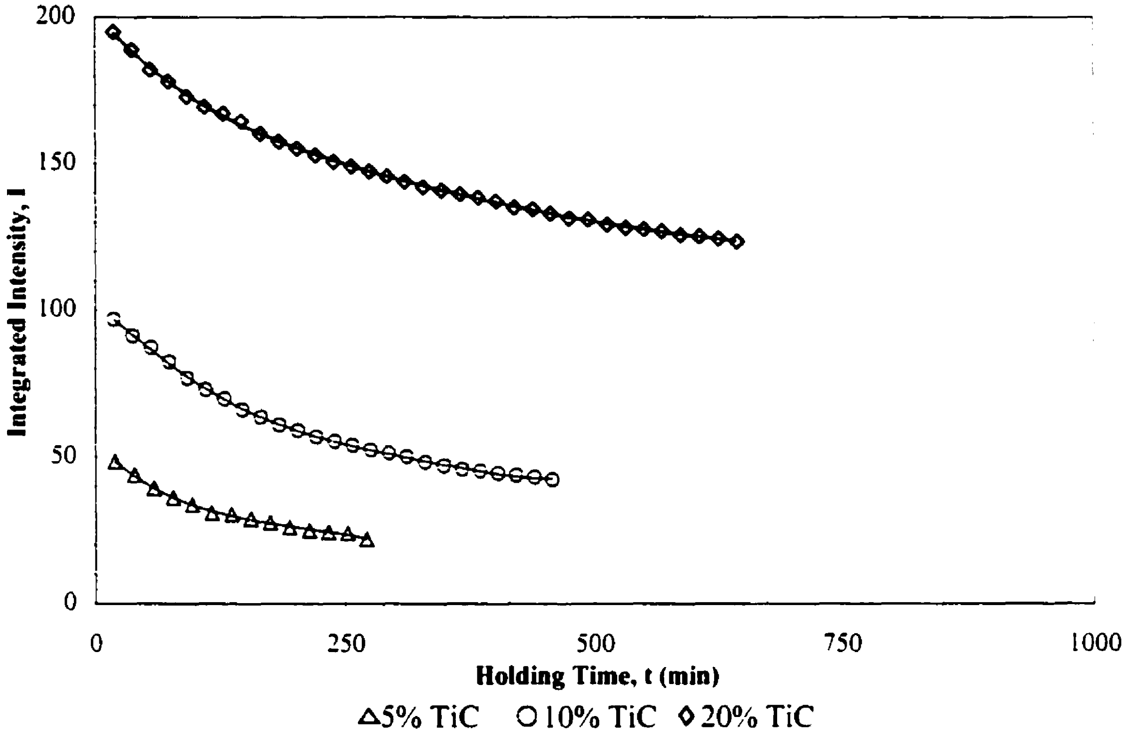

Figure 6.46 Change in the integrated intensity of the TiC phase with increasing holding time for the Ti-6%Al-4%V composites sintered at 1200°C.

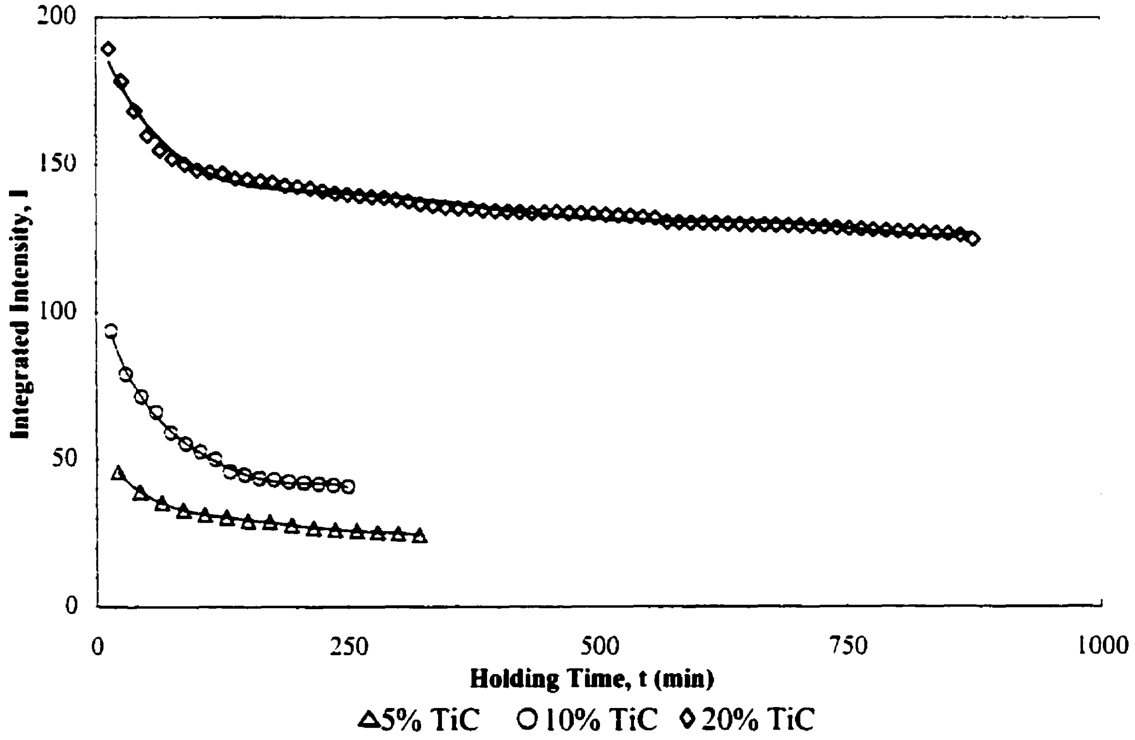

Figure 6.47 Change in the integrated intensity of the TiC phase with increasing holding time for the Ti-6%Al-4%V composites sintered at 1250°C.

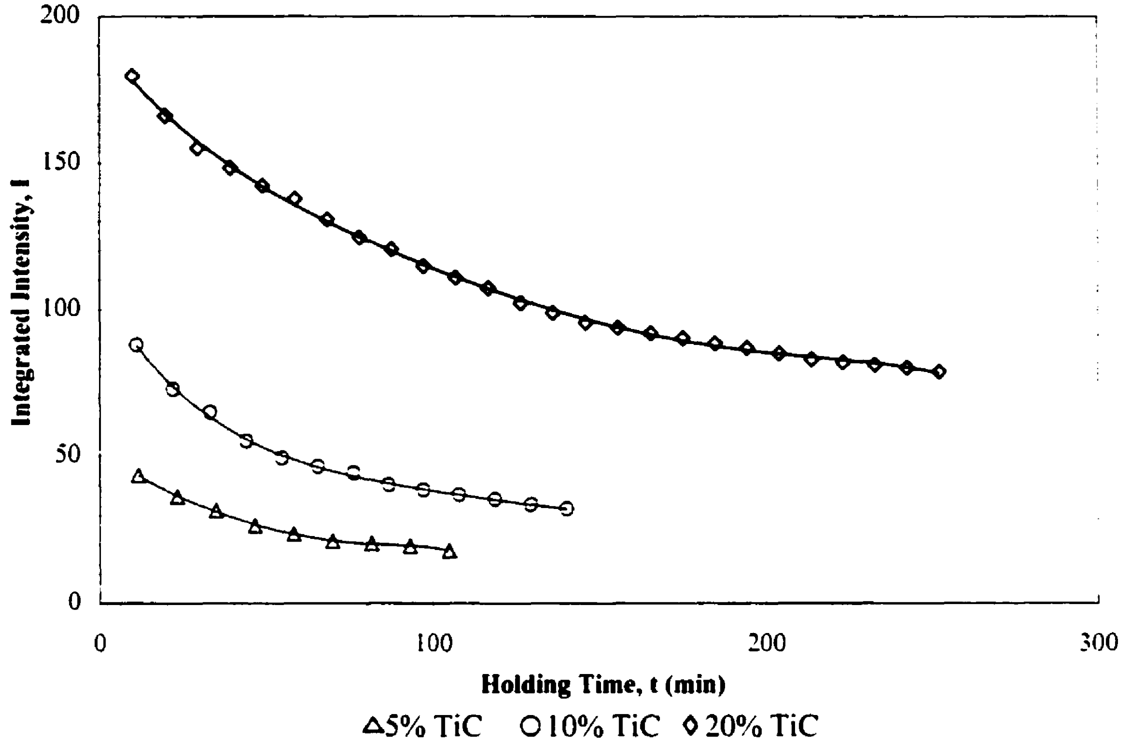

Figure 6.48 Change in the integrated intensity of the TiC phase with increasing holding time for the Ti-6%Al-4%V composites sintered at 1300°C.

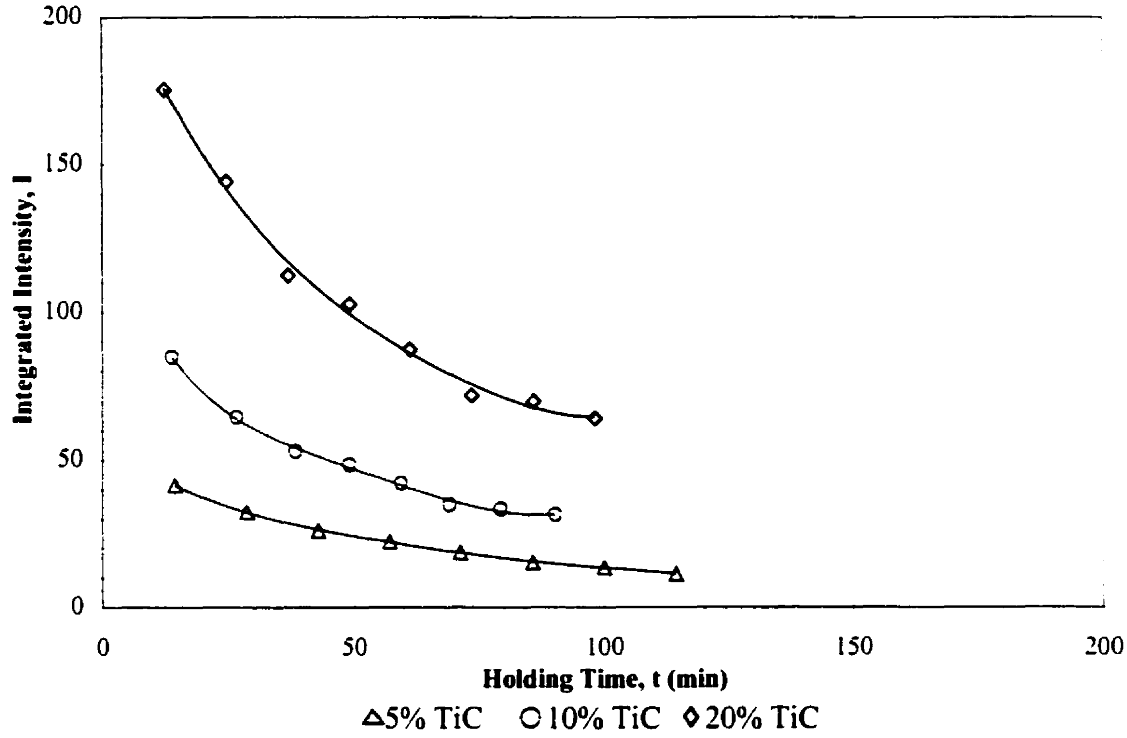

Figure 6.49 Change in the integrated intensity of the TiC phase with increasing holding time for the Ti-6%Al-4%V composites sintered at 1350°C.

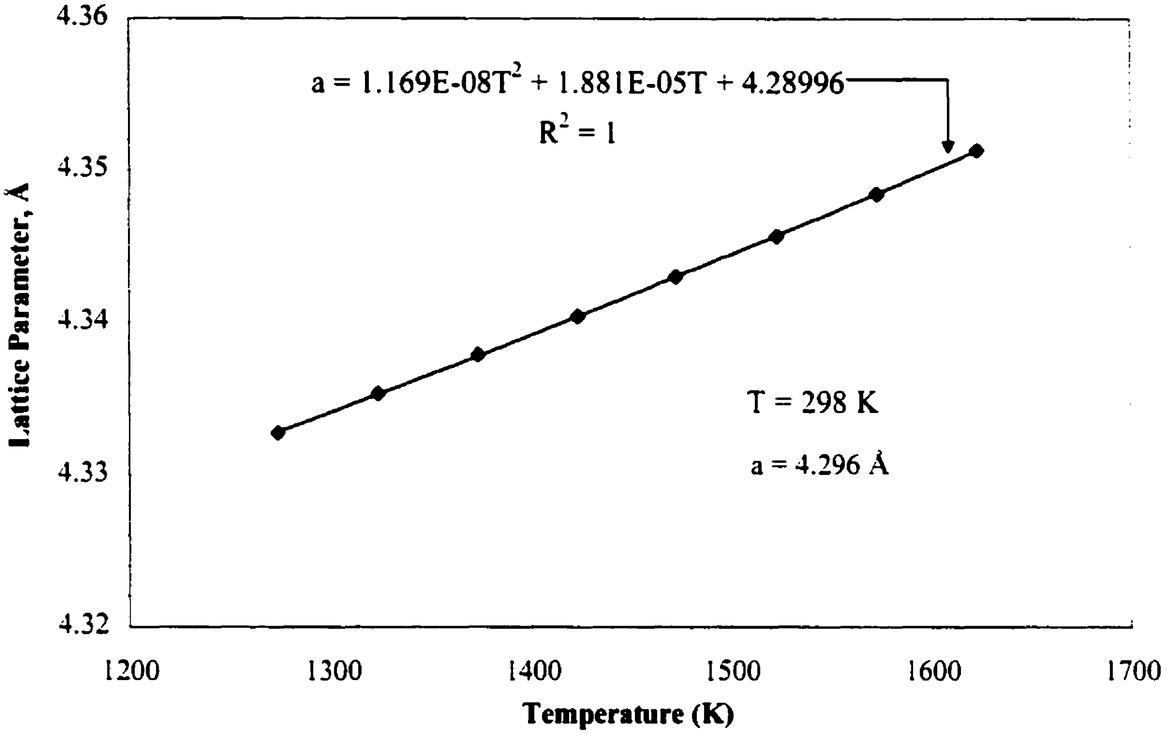

Figure 6.50 Lattice parameter measurements at various temperatures for the TiC_x interfacial phase.

The lattice parameter values obtained suggest a stoichiometry of Ti_2C as shown in Figure 6.51.[257-259] As noted earlier, there has been much uncertainty regarding the existence and stability of stoichiometric Ti_2C. However the present work appears to suggest that stoichiometric Ti_2C exists and is a stable phase. In the TEM work of Konitzer and Loretto,[110] electron energy loss spectra (EELS) of the interface between the Ti-6%Al-4%V matrix and TiC reinforcement revealed an interfacial product having a carbon content of 33 at.% (*i.e.* Ti:C ratio of 2) and a lattice parameter of 4.278 Å. Due to the limitations of the EELS technique, Konitzer and Loretto were unable to detect the presence of carbon in solid solution in the Ti-6%Al-4%V matrix and establish whether the chemical composition of the entire interfacial region was 33 at.%.[110] The present neutron diffraction work coupled with Figure 6.51 indicates that the interfacial reaction product is Ti_2C and that there is carbon diffusion into the Ti-6%Al-4%V matrix that leads to an increase in the lattice parameter of the β phase at the various sintering temperatures in the range of 1100°C to 1350°C, as shown in Figures 6.32 to 6.37.

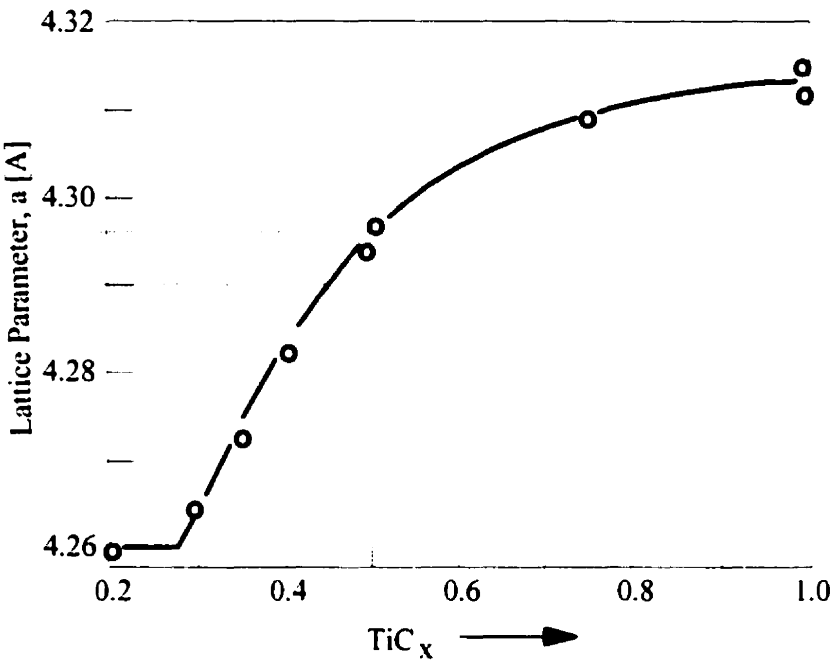

Figure 6.51 Room temperature lattice spacings of the FCC cubic, TiC$_x$ phase as a function of carbon content. Replotted from reference.[257]

The discrepancy in the nature of the interfacial region between the observations of previous investigators[26,86-89,110-121] (a non-stoichiometric TiC$_x$ interface) and the present work (formation of stoichiometric Ti$_2$C) may be explained by the difficulty in discerning Ti$_2$C using x-ray diffraction. In Table 6.6 the room temperature x-ray scattering angles of the (331) diffraction planes of TiC and Ti$_2$C are calculated for CuKα radiation. Considering the equal co-existence of both phases, it is expected that within a 1° range, four (331) x-ray diffraction peaks would be superimposed, two corresponding to TiC and two to Ti$_2$C. Of these, it is observed that the (331) TiC x-ray diffraction peaks from the CuKα1 and CuKα2 radiation are relatively close together in the diffraction pattern, such that these are unlikely to appear as separate peaks. For Ti$_2$C there is a similar closeness in the (331) diffraction scattering angles calculated for the CuKα1 and CuKα2 radiation, effectively superimposing these peaks. Thus, during the formation of the Ti$_2$C phase in the TiC/Ti-6%Al-4%V system at temperatures above the beta-transus, initially the x-ray diffraction pattern is likely to reveal a broad (331) TiC peak corresponding to the superimposed peaks of CuKα1 and CuKα2 radiation. With the formation of Ti$_2$C, the x-ray diffraction pattern would reveal the emergence and growth of another broad peak corresponding to that of the (331) diffraction plane of the Ti$_2$C interface. However, due to the proximity of the (331) peaks of TiC and Ti$_2$C, their superposition is likely to appear as though the original (331) TiC peak broadens with consolidation and shifts preferentially to higher scattering angles (*i.e.* the (331) peak of Ti_2C occurs at a slightly higher scattering angle as compared to that of TiC). It is not surprising that previous work[26,86-89,110-121] on the interfacial reaction region may have concluded that a non-stoichiometric annulus of TiC_x forms between the stoichiometric TiC particles and Ti-6%Al-4%V matrix. In this work the enhanced resolution achieved using neutron diffractometry has enabled the clear distinction between the (331) diffraction peak of TiC and that of Ti_2C.

Table 6.6 - Calculated Scattering Angles for the 331 Planes of TiC and Ti_2C in X-ray Diffraction using a Copper Wavelength Source

Phase	Scattering Angle (2θ)	
	Room Temperature	1100°C
TiC (Cukα1)	102.07	100.70
TiC (Cukα2)	102.42	101.04
Ti_2C (Cukα1)	102.79	101.54
Ti_2C (Cukα2)	103.14	101.89

The evolution of the Ti_2C interfacial product was monitored using the (331) diffraction planes of TiC before and after reaction with the matrix. Whereas, with increasing consolidation temperature and hold time the integrated intensity of both TiC and Ti-6%Al-4%V decreased (Figs. 6.38 to 6.43 and Figs. 6.44 to 6.49, respectively), it was observed that the integrated intensity of Ti_2C increased, as shown in Figures 6.52 to 6.57. The reaction of TiC with Ti-6%Al-4%V to form Ti_2C essentially begins in the contact region between the matrix and ceramic reinforcement. With increasing holding time the intensity of the Ti_2C interface increases, suggesting the gradual transformation of TiC to Ti_2C. The complete transformation of TiC to Ti_2C was evidenced in Figure 6.30 which revealed that, within an ½ hour of sintering the composites at 1500°C, only two phases are apparent, β-Ti-6%Al-4%V and Ti_2C. Thus, for the composites sintered at 1500°C, this substantiates the FEGSEM results that revealed a constant carbon concentration across the reinforcement particle, as well as the EPMA results which indicated a carbon concentration of 10-12 wt.% (*i.e.* corresponding to Ti_2C) for the reinforcement phase.

Quantitative volume fraction analysis for Ti_2C was performed to determine the transformation kinetics of the interfacial reaction region with holding time at the various isothermal temperatures. Variation in the interface volume fraction with holding time is plotted for the various isothermal sintering temperatures, as shown in Figures 6.58 to 6.63.

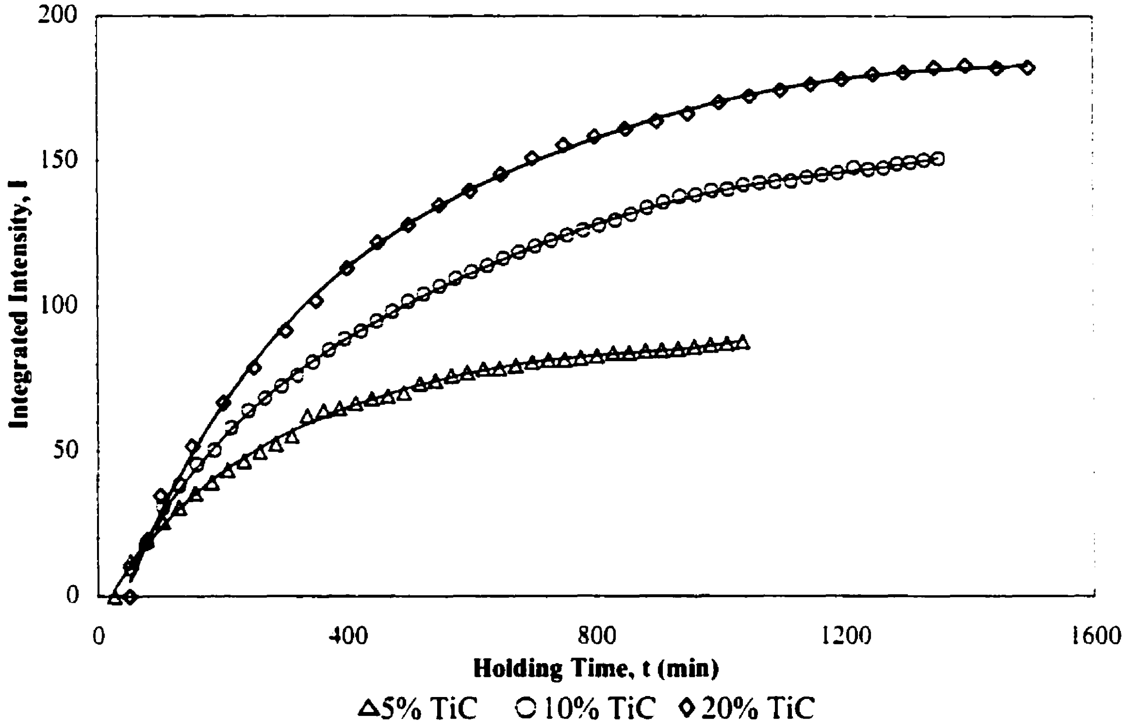

Figure 6.52 Change in the integrated intensity of the Ti_2C phase with increasing holding time for the Ti-6%Al-4%V composites sintered at 1100°C.

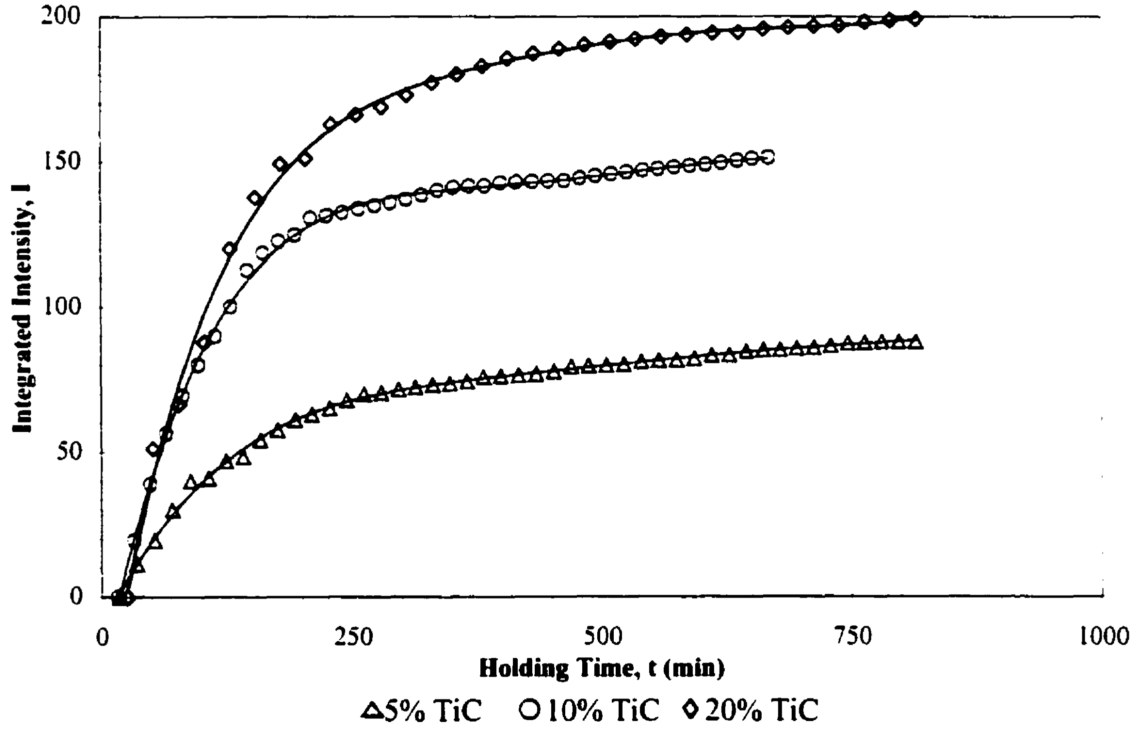

Figure 6.53 Change in the integrated intensity of the Ti_2C phase with increasing holding time for the Ti-6%Al-4%V composites sintered at 1150°C.

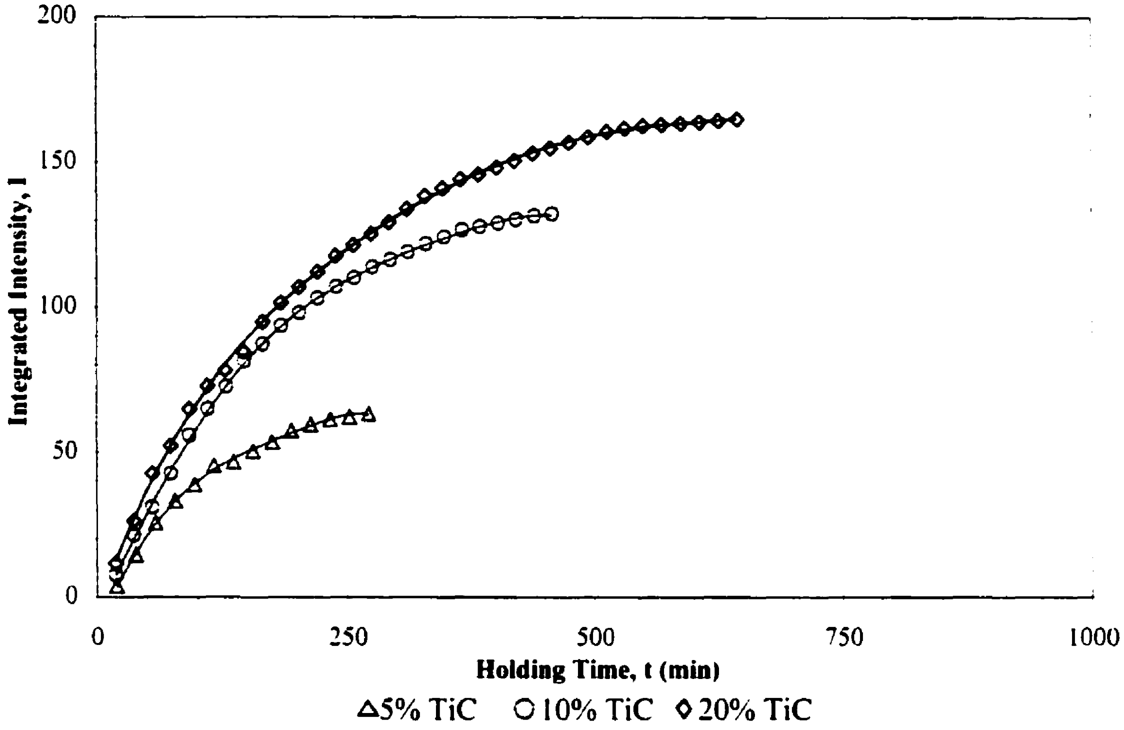

Figure 6.54 Change in the integrated intensity of the Ti_2C phase with increasing holding time for the Ti-6%Al-4%V composites sintered at 1200°C.

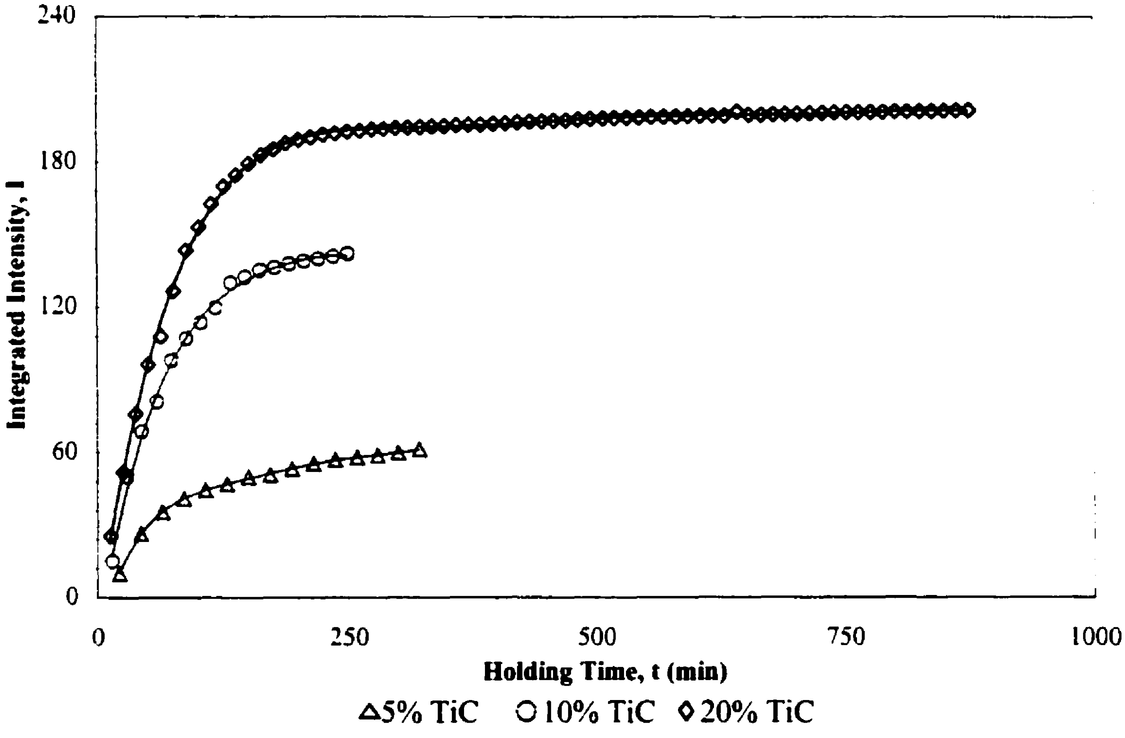

Figure 6.55 Change in the integrated intensity of the Ti_2C phase with increasing holding time for the Ti-6%Al-4%V composites sintered at 1250°C.

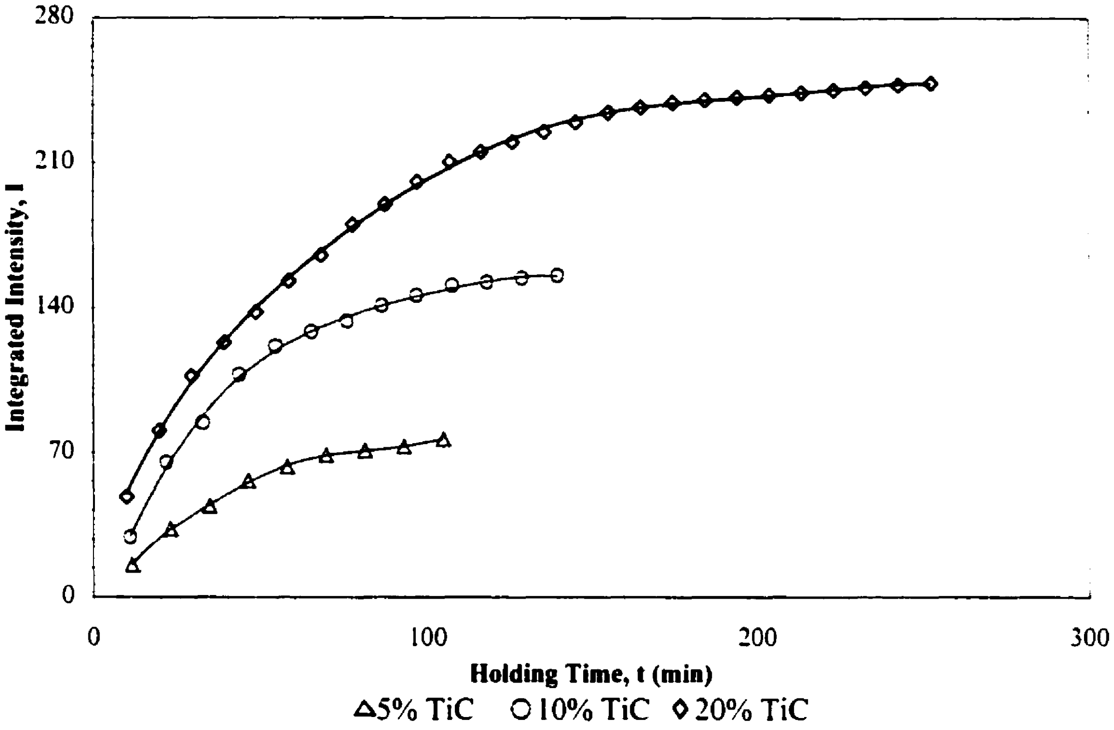

Figure 6.56 Change in the integrated intensity of the Ti_2C phase with increasing holding time for the Ti-6%Al-4%V composites sintered at 1300°C.

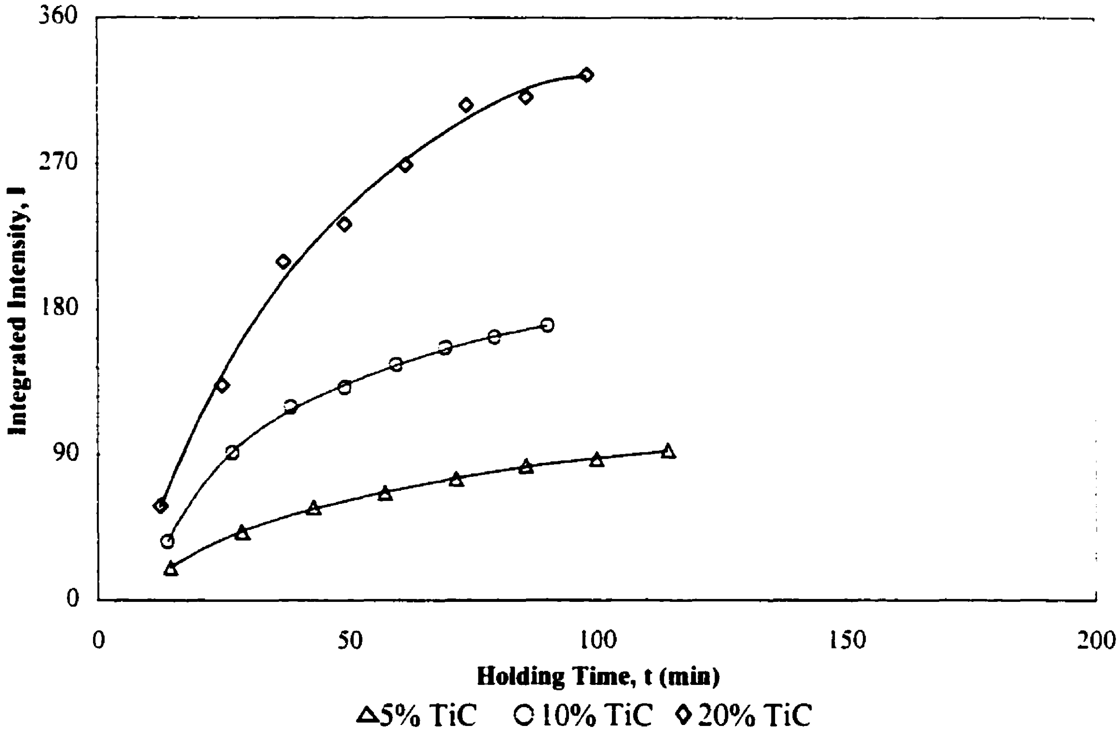

Figure 6.57 Change in the integrated intensity of the Ti_2C phase with increasing holding time for the Ti-6%Al-4%V composites sintered at 1350°C.

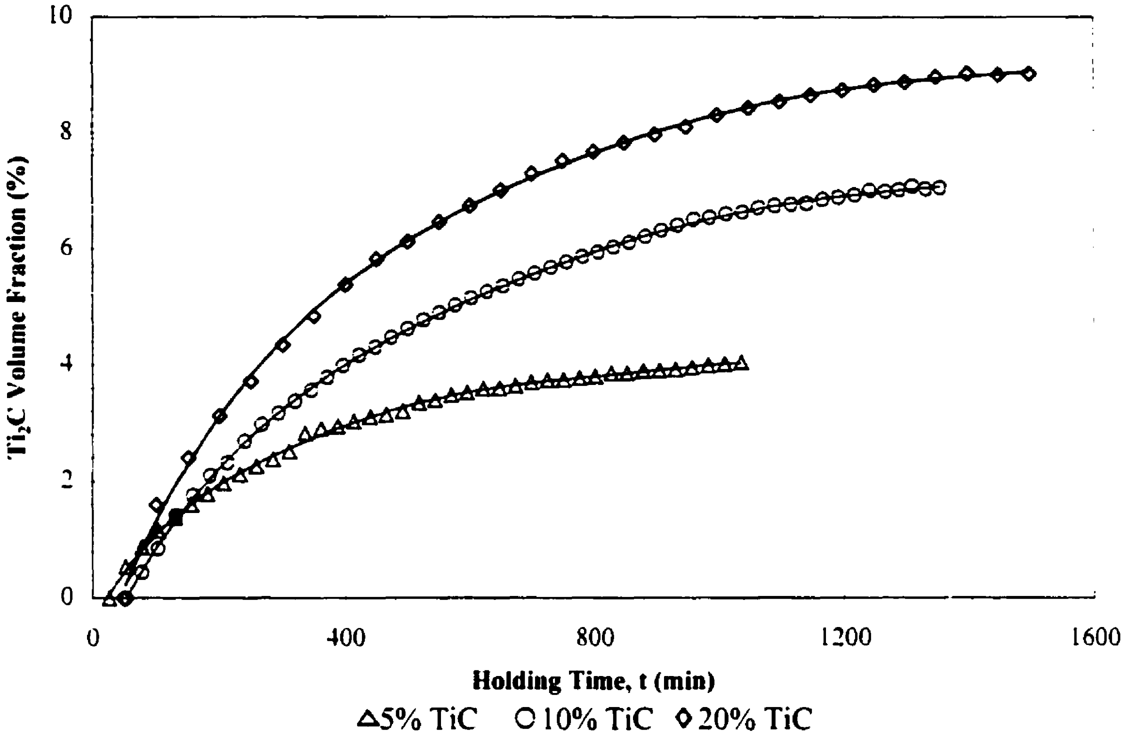

Figure 6.58 Change in the volume fraction of the Ti$_2$C phase with increasing holding time for the Ti-6%Al-4%V composites sintered at 1100°C.

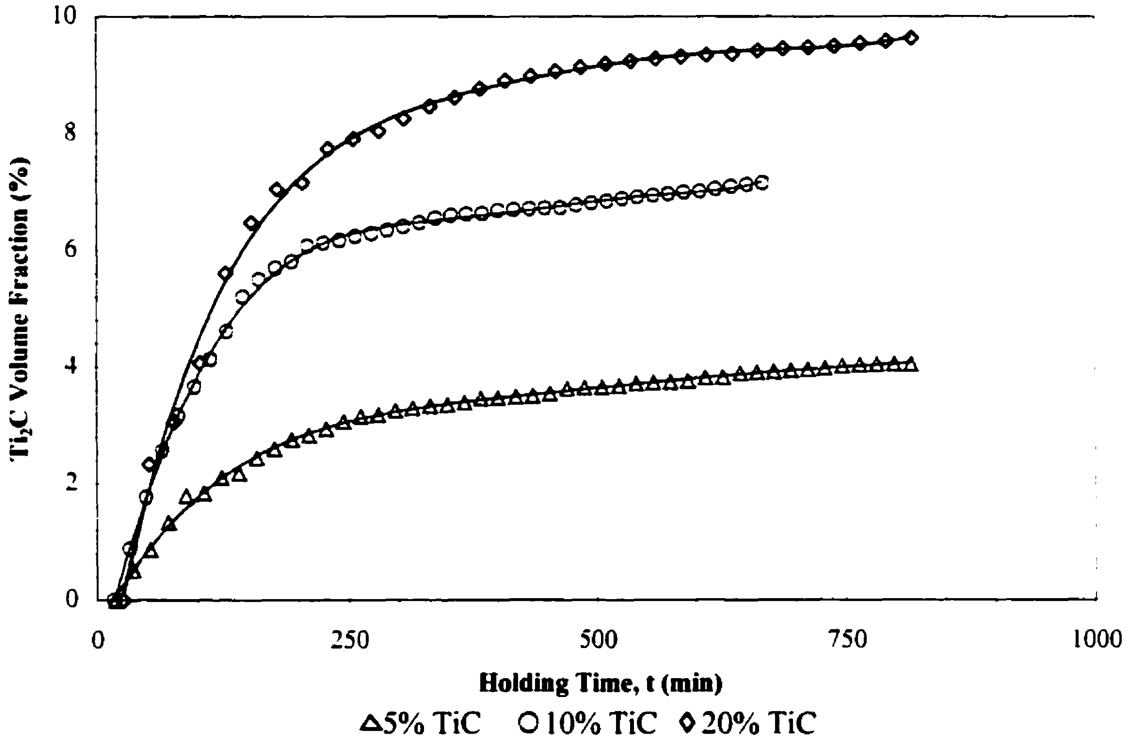

Figure 6.59 Change in the volume fraction of the Ti$_2$C phase with increasing holding time for the Ti-6%Al-4%V composites sintered at 1150°C.

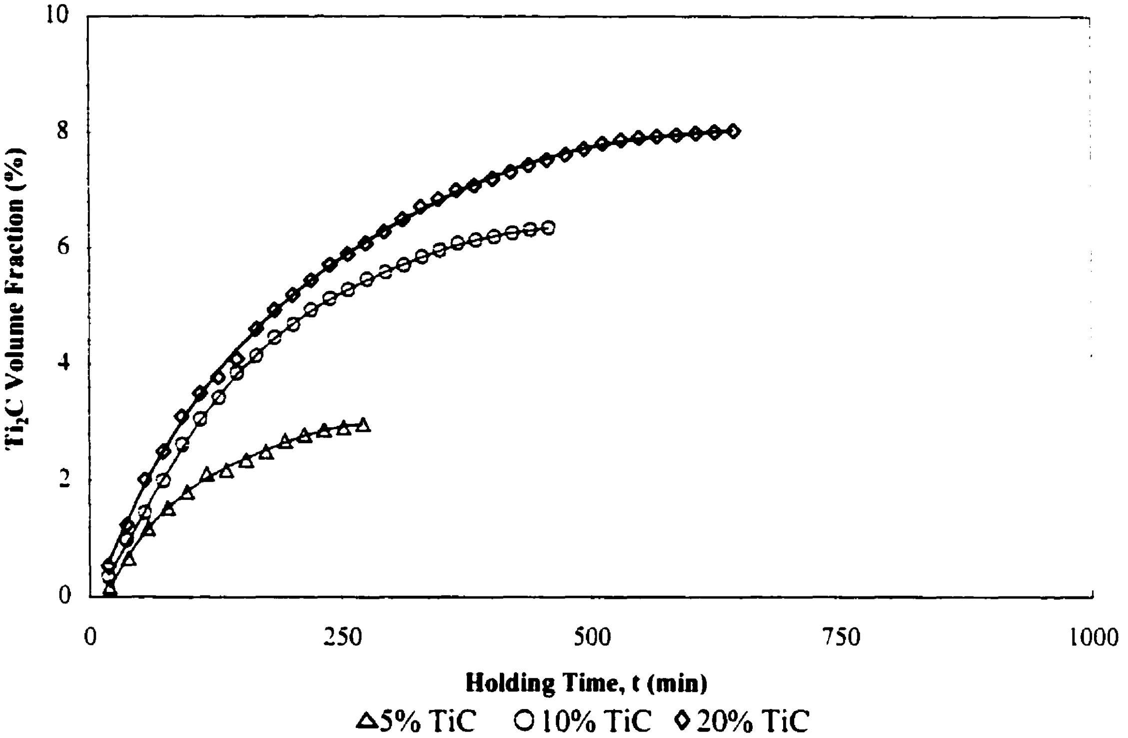

Figure 6.60 Change in the volume fraction of the Ti$_2$C phase with increasing holding time for the Ti-6%Al-4%V composites sintered at 1200°C.

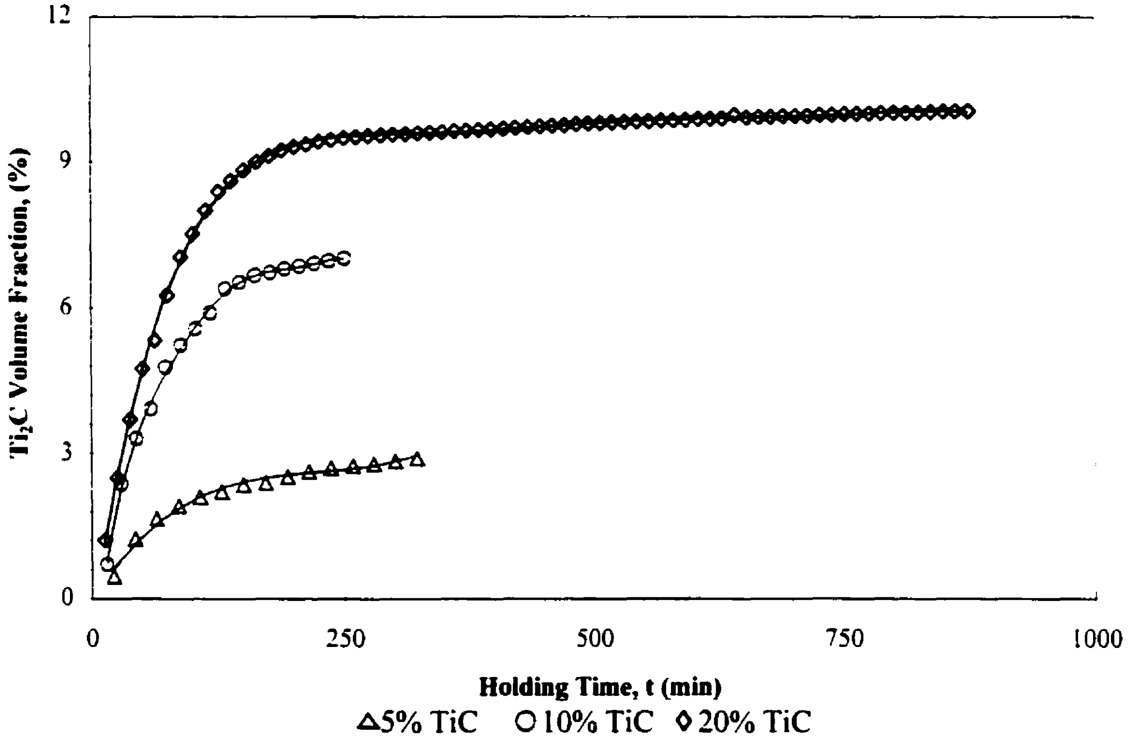

Figure 6.61 Change in the volume fraction of the Ti$_2$C phase with increasing holding time for the Ti-6%Al-4%V composites sintered at 1250°C.

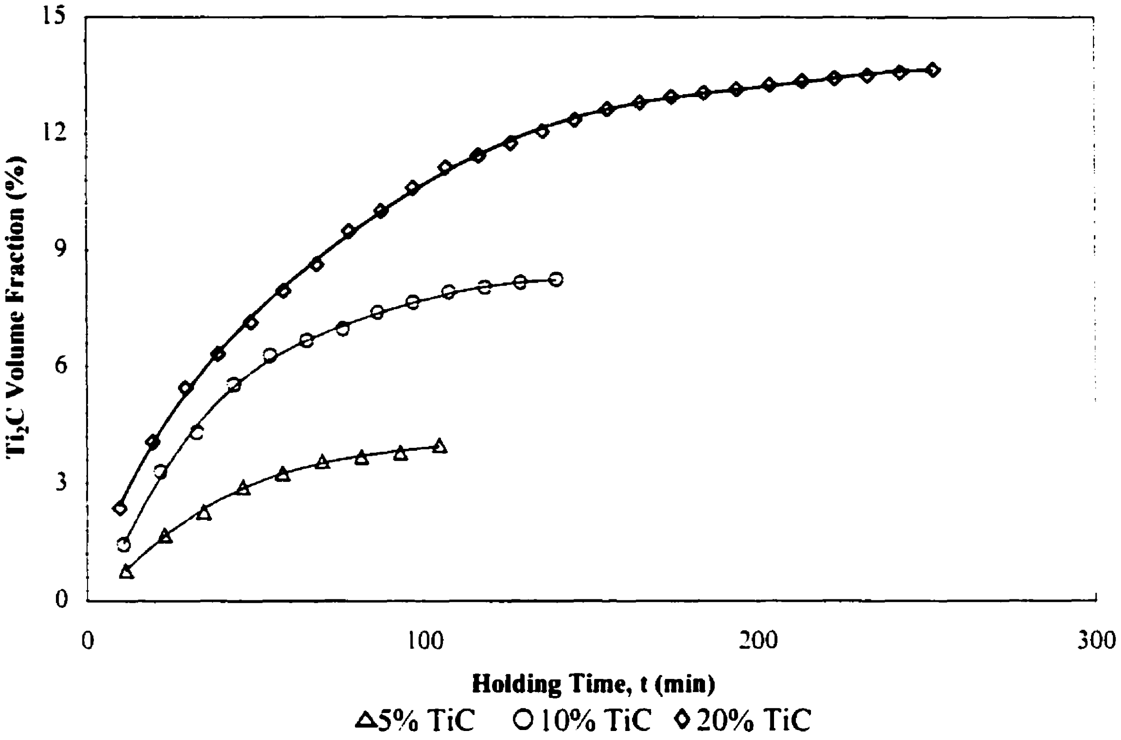

Figure 6.62 Change in the volume fraction of the Ti$_2$C phase with increasing holding time for the Ti-6%Al-4%V composites sintered at 1300°C.

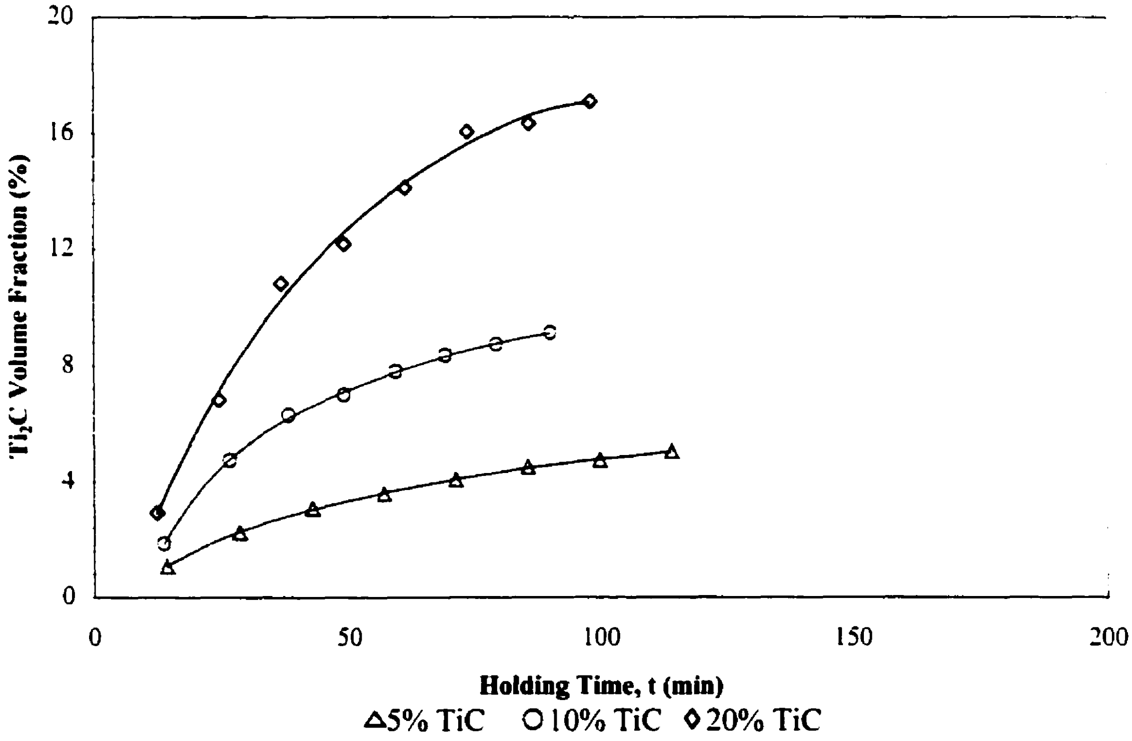

Figure 6.63 Change in the volume fraction of the Ti$_2$C phase with increasing holding time for the Ti-6%Al-4%V composites sintered at 1350°C.

Essentially, the interfacial reaction kinetics may be characterized by fitting the Ti_2C transformation results given in Figures 6.58 to 6.63 using the Avrami expression for the transformation rate of nucleation and growth mechanisms:[251]

$$V_{f_{Ti_2C}} = 1 - \exp\left(-kt^n\right) \tag{6.4}$$

where V_f is the volume fraction of Ti_2C transformed, k is a rate constant which involves the nucleation and growth rates of the interface, t is the time and n is an exponent dependent on time dependencies of the nucleation and growth rates of the interface as well as the dimensionality of the growth front. Fitting the curves in Figures 6.58 to 6.63 using equation 6.4, the time exponent was determined for the various materials sintered at temperatures in the range of 1100°C to 1350°C as given in Table 6.7.

Table 6.7 – Time Exponent Values Determined for Growth of the Ti_2C Interface

TiC Volume Fraction (%)	Time Exponent (n)					
	1100°C	1150°C	1200°C	1250°C	1300°C	1350°C
5	3.15	3.19	2.97	3.18	3.07	2.88
10	3.13	3.21	3.11	3.22	3.16	2.94
20	3.43	3.62	3.06	3.48	3.28	3.71

In general, the time exponent was determined to fall between 2.9 to 3.7. This is consistent with Avrami's proposal that, for a constant rate of nucleation and for three-dimensional growth, the time exponent is predicted to be 4, while with site saturated nucleation the value for n falls to 3. In two dimensional growth, the value for the time exponent ranges between 2 and 3.

Moreover, for the composite system, growth of the Ti_2C interface occurs by diffusional transport, which is a thermally activated process. As such it can be represented by an Arrhenius rate equation of the type:

$$t_{tr} = A_{tr} \exp\left(\frac{Q}{RT}\right) \tag{6.5}$$

where t is the time, Q is the activation energy, T is the temperature and R is gas constant. The subscript *tr* has been added to signify the volume fraction of Ti_2C transformed and was kept constant for each composite system. Specifically, for the 5 vol.% TiC reinforced composite the time for transforming 3 vol.% Ti_2C was chosen for each temperature (*i.e.* t_3), whilst for the 10 vol.% and 20 vol.% TiC composites the time for transforming 6 and 8 vol.% Ti_2C, respectively, was selected for each temperature (*i.e.* t_6 and t_8). Thus in equation 6.5 the constant A is dependent on the material composition and microstructure, as well as the transformation volume fraction (*tr*) selected.

Figure 6.64 is a plot of logarithmic time for transformation as an inverse function of temperature for the composite materials containing 5, 10 and 20 vol.% TiC. The activation energy is determined from the slope of this Arrhenius plot as follows:

$$Q = S_{ave} R \tag{6.6}$$

where R is the gas constant and has a value of 8.314 $J \cdot mol^{-1}K^{-1}$. The values for the activation energy were determined to be 302 $kJ \cdot mol^{-1}$ for the 5 vol.% TiC_p reinforced composite and 310 $kJ \cdot mol^{-1}$ for both the 10 and 20 vol.% TiC_p reinforced composite.

Although diffusion data for carbon in β-Ti-6%Al-4%V are lacking, much can be speculated by considering the diffusion of carbon in β-titanium and TiC. To form the interfacial phase either carbon can diffuse from the TiC particles to the β-Ti-6%Al-4%V matrix or titanium can diffuse from the Ti-6%Al-4%V alloy into the reinforcement phase. From the literature data,[250] the activation energy for diffusion of carbon in β-titanium has been determined to be approximately 100 $kJ \cdot mol^{-1}$. The activation energy for self diffusion of titanium in the β phase was reported to be 250 $kJ \cdot mol^{-1}$.[251,260] As carbon appears to be the faster diffusing element of the two, initial formation of the interface is likely to occur by carbon diffusion to the matrix. This is evidenced by the increase in lattice parameter of beta phase with holding time at the sintering temperature, as discussed previously.

With the formation of the Ti_2C interfacial phase, two possibilities can occur: (1) carbon diffuses from the TiC reinforcement particles, through the reaction zone and moves towards the matrix phase or (2) titanium diffuses from the Ti-6%Al-4%V matrix, through the reaction zone and moves towards the reinforcement phase. The work of Sarian[261-263] on the tracer diffusion of carbon and titanium in titanium carbide substrates of various compositions has indicated that carbon has a greater mobility than the titanium atoms. As such the activation energy for diffusion of carbon in TiC was reported to be approximately 330 kJ·mol^{-1} for all TiC_x ($0.5 \le x \le 1$) compositions[262-265] whereas that for titanium was roughly 739 kJ·mol^{-1}.[261] Hence the activation energy for growth of the interface is likely to be controlled by transport of carbon from the TiC reinforcing phase through the Ti_2C interface to the titanium alloy matrix. The activation energy values obtained in the present work are slightly below that given in the literature for carbon diffusion in TiC substrates. Hence, it appears that growth of the Ti_2C interface is most likely occurring by transport of carbon from the TiC reinforcement particle through the growing interface phase and to the Ti-6%Al-4%V alloy.

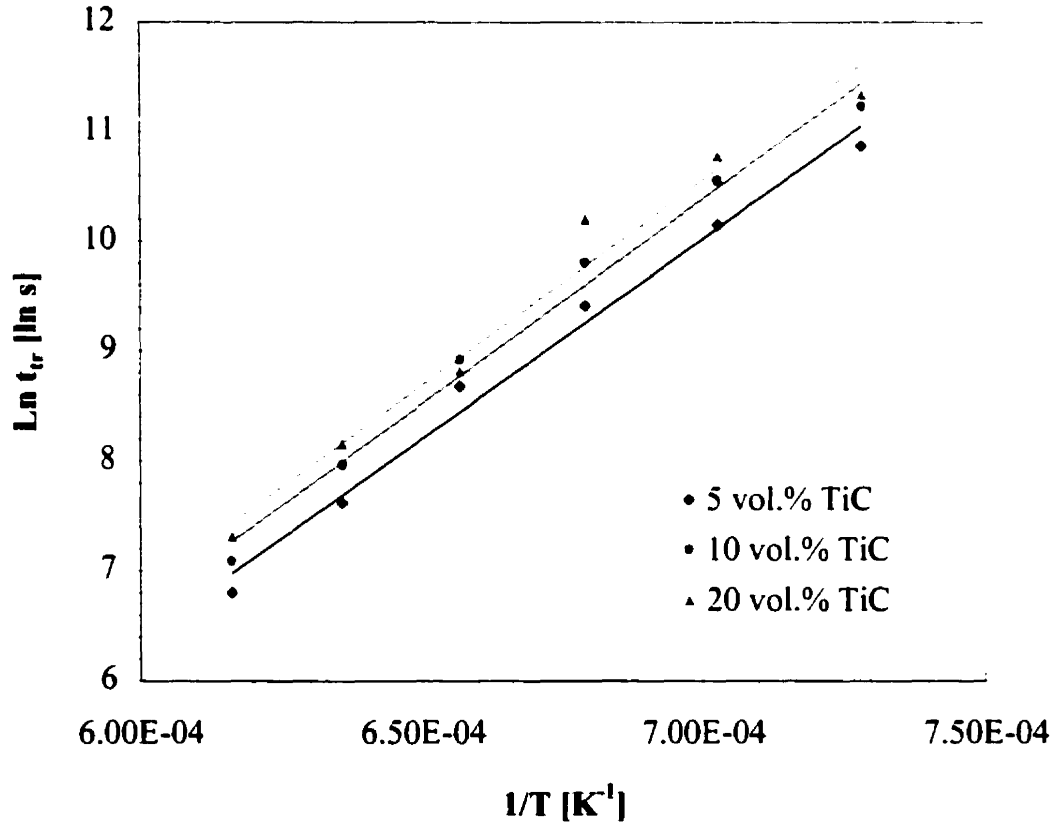

Figure 6.64 Variation of the time for transformation with temperature for the TiC particle reinforced Ti-6%Al-4%V composites.

6.5 Mechanical Property Measurement

6.5.1 Hardness Testing

The microhardness values of the TiC particles and the Ti-6%Al-4%V matrix in the composites sintered under the various processing conditions were measured. Figures 6.65a and 6.65b respectively give the Vickers microhardness for the reinforcement and matrix phases in the composites consolidated for 4 hours at temperatures in the range of 1100 to 1500°C. For the composites consolidated at 1100°C, the microhardness values of the reinforcement phase were found to be comparable to the microhardness of the as-received TiC particles, the latter of which is indicated by the upper and lower grey lines in Figure 6.65a. In general, the microhardness of the reinforcement phase was found to decrease with increasing sintering temperature and increase with increasing TiC volume fraction. In this work, increasing the isothermal sintering temperature has been shown to result in rapid formation and growth of the interfacial Ti_2C phase due to enhanced diffusion of carbon from the TiC reinforcement particles to the Ti-6%Al-4%V matrix. This loss of carbon from the TiC particles is reflected in the microhardness values. The small effect of increasing the reinforcement volume fraction on the microhardness values may be due to slightly lower carbon losses from each TiC particle to attain maximum carbon solid solubility of the titanium alloy matrix (*i.e.* Figs. 6.32 to 6.37).

With increasing temperature and TiC volume fraction, the microhardness of the matrix increased slightly, as illustrated in Figure 6.65b. With reference to the neutron diffraction data, at 1100°C the lattice parameter of the β-Ti-6%Al-4%V matrix after 4 hours of holding is approximately 3.3061 Å (*i.e.* using the equation in Fig. 6.32), approximately 0.002 Å higher than that obtained for the unreinforced alloy at the same temperature (as tabulated in Table 6.5). Further increases in the holding time at this temperature increase the β-Ti-6%Al-4%V lattice parameter, thereby suggesting that the matrix has yet to achieve carbon saturation. At 1300°C, the neutron diffraction data indicate that the lattice parameter of the β-Ti-6%Al-4%V matrix increases only slightly with holding time and that the curves reach an asymptotic lattice parameter value of 3.3174 Å after holding for approximately 3 hours (*i.e.* Fig. 6.36). This appears to suggest that for sintering temperatures above 1300°C the β-matrix in these composites rapidly reaches the maximum carbon solid solution solubility limit of approximately 0.2 wt.% carbon (*e.g.* Ti-TiC phase diagram in Fig. 2.2). Accordingly, the microhardness values of the Ti-6%Al-4%V matrix in the composites sintered at 1300°C and 1500°C are similar and higher than those obtained for the composites sintered at 1100°C.

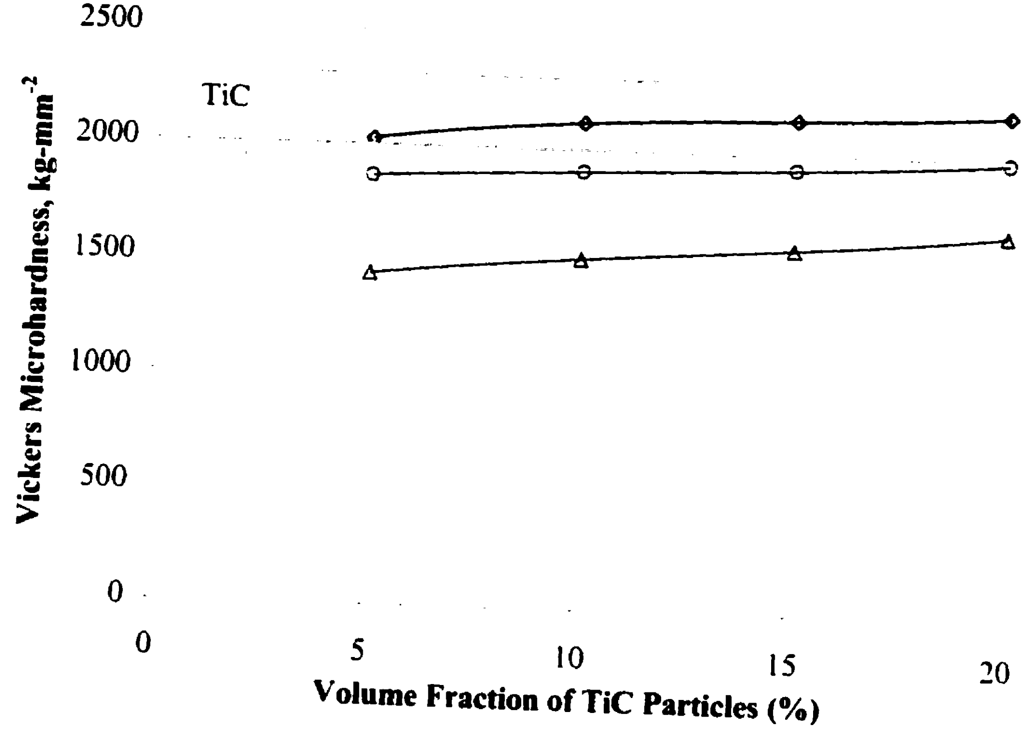

(a) TiC particles

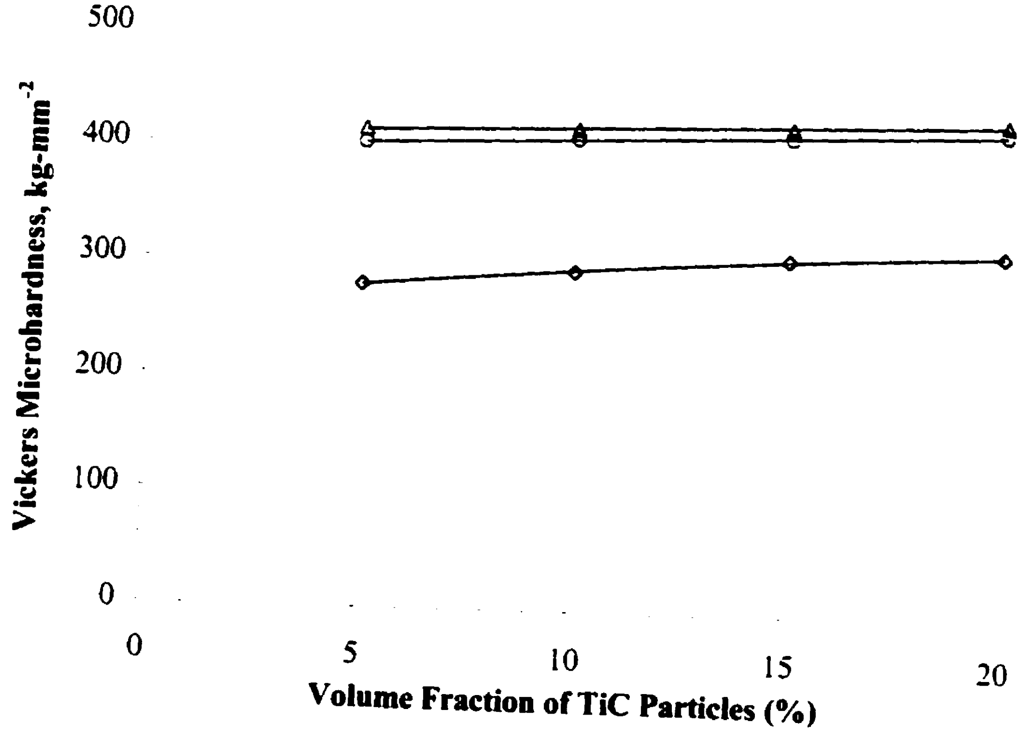

(b) Ti-6%Al-4%V matrix

◇1100°C ○1300°C △1500°C

Figure 6.65 Microhardness values of the TiC particle reinforced titanium alloy composites sintered for 4 hours.

The microhardness results for the reinforcement and matrix phases appear to indicate that, although high temperature sintering improves the sinterability of the titanium alloy composites, carbon diffusion from the TiC particles would reduce the effectiveness of TiC as a strengthening phase. Also, the dissolution of carbon in the Ti-6%Al-4%V, as confirmed through the microhardness and lattice parameter measurements, could lead to embrittlement of the matrix and correspondingly the composite.

To rationalize this decrease in the microhardness of the reinforcement phase with decreasing carbon concentration in the TiC particles, the strength of the metal to carbon covalent bond in the carbide must be considered. In general, when the carbon concentration in the TiC decreases, there is an increase in the number of carbon vacancies and the electronic structure changes.[266] The presence of empty carbon lattice sites leads to the formation of different bonds that are not present in stoichiometric TiC. The strength of the bond between the titanium and carbon atoms is reduced as bonding begins to occur between second nearest titanium neighbors across the vacancy sites.[266-267] Hence bond-strength related properties such as hardness, wear resistance, and strength are likely to be affected by the carbon loss from the TiC particles occurring during elevated temperature sintering.

The bulk hardness of these composites was evaluated using the Rockwell K hardness test. Figure 6.66 illustrates the variation in the hardness with increasing sintering temperature and TiC volume fraction. The hardness of the unreinforced matrix and TiC reinforced composites increased with temperature due to decreasing porosity. For the composites sintered at 1100°C, an increase in hardness was observed with increasing TiC volume fraction. At the higher sintering temperatures (1300°C and 1500°C), the greatest increase in hardness occurred for the first 5 vol.% TiC addition. Subsequent increases in the TiC volume fraction were observed to result in a small increase or even a decrease in the hardness. In general, the incorporation of TiC particles in the Ti-6%Al-4%V matrix was observed to improve the relative density in the composites sintered at 1100°C for 4 hours (Fig. 6.5), thereby contributing to the successive increase in hardness obtained with increasing TiC volume fraction. However, increases in the relative density of the composites after four hours holding at 1300°C (or 1500°C) were negligible with increasing TiC volume fraction. In fact there is evidence that at four hours holding de-sintering occurs at the elevated temperatures and there is substantial microstructural coarsening. Nonetheless, the presence of the TiC reinforcement particles was observed to reduce microstructural coarsening of the matrix (Fig. 6.15). However, at the higher temperatures, rapid reaction of the TiC reinforcement with the Ti-6%Al-4%V matrix occurs and forms Ti_2C at the interface, as discussed previously. Moreover, for sintering at 1500°C, the entire reinforcement particle has transformed to Ti_2C and considerable particle growth is observed

(Fig. 6.15). As such, the increment in hardness from 1300°C to 1500°C is not as great as that from 1100°C to 1300°C for all TiC volume fractions. Regardless, the above mentioned arguments (density, carbon loss and microstructure) suggest that strength improvement should occur with increasing TiC volume fraction for the composites sintered at 1300°C and 1500°C. The leveling in the hardness values observed may then be a result of poorer bonding in the composites with increasing TiC volume fraction. Inherently, with increasing TiC volume fraction, agglomeration of the particles occurred (Fig. 6.15). It is possible that this clustering of TiC particles tends towards poorer bonding (as ceramic to ceramic bonding would necessitate higher temperatures for densification) and limits further increases in hardness. These results are consistent with previous work on the sintering of TiC particulate reinforced titanium composites in which the highest increase in hardness was determined for additions of 2.5 % TiC and no further increase in the hardness was observed with increasing TiC content.[89]

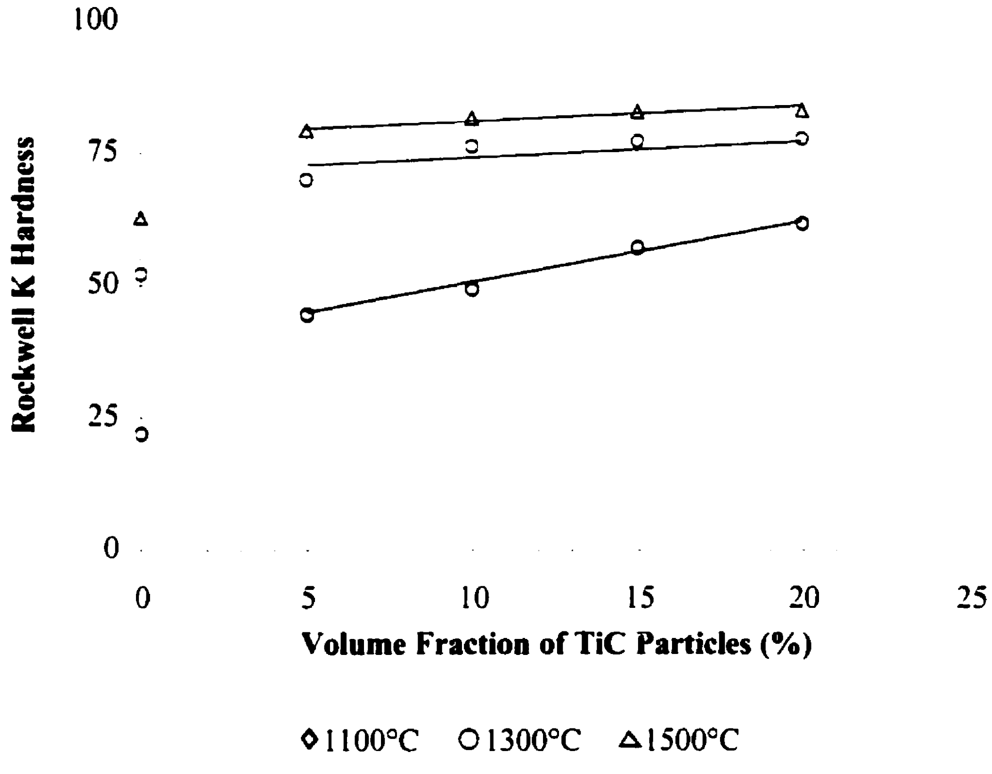

Figure 6.66 Rockwell hardness values of the Ti-6%Al-4%V-TiC composites sintered for 4 hours.

6.5.2 Shear Punch Testing

Having calibrated the shear punch test for composite materials, the mechanical properties of the titanium alloy composites sintered at the various processing conditions were evaluated. Figure 6.67 shows the variation in the yield and tensile strength of the various titanium-based materials with increasing sintering temperature. For all temperatures, the yield (0.1% proof stress) and tensile strengths for the composites were superior to those of the unreinforced alloy. For the composites sintered at 1100°C, the strength properties are poor due to inadequate bonding between the powder particles during low temperature processing. Increasing the sintering temperature was found to improve both the yield and tensile strength of the composites. Nonetheless the increase in strength properties from 1300°C to 1500°C is not as great as that from 1100°C to 1300°C for all TiC volume fractions. This may be an effect of microstructural coarsening and transformation of the reinforcement particles from TiC to Ti_2C in the composites sintered at 1500°C. Additionally for all sintering temperatures, large increases in the yield and tensile strengths occurred for the first 5 vol.% TiC addition and subsequent increases in the reinforcement volume fraction resulted only in marginal further increases, similar to the trend discussed previously in the hardness results.

Figure 6.68 shows the variation in the percent elongation with processing temperature for the various composites. The titanium alloy processed at 1100°C exhibited the lowest ductility and there was a progressive rise in the total elongation with increasing sintering temperature. For the composites, the increase in ductility with increasing sintering temperature was not as marked especially at the higher TiC volume fractions. Moreover, for all sintering temperatures, the ductility was found to fall rapidly with increasing TiC volume fraction. This can be related to the influence of density, reinforcement transformation and coarsening, microstructural coarsening of the matrix and matrix-reinforcement bonding (as well as the reinforcement-reinforcement bonding in the regions of clustering). Essentially at 1100°C, successive increases in the TiC volume fraction improve the density and due to the lower sintering temperature microstructural coarsening and reinforcement transformation are minimal. Hence the main reason for the low ductility values is likely due to the poor matrix-reinforcement bonding. At 1300°C, better matrix-reinforcement bonding is combined with limited particle coarsening and transformation. As such the elongation values are higher for the composites containing up to 10 vol.% TiC particles. For the 20 vol.% TiC reinforced composite, the ductility at 1300°C is similar to that 1100°C and may be an effect of TiC agglomeration. At 1500°C, albeit the higher density, little improvement in the ductility is observed for the composites because of microstructural coarsening as well as particle transformation to Ti_2C.

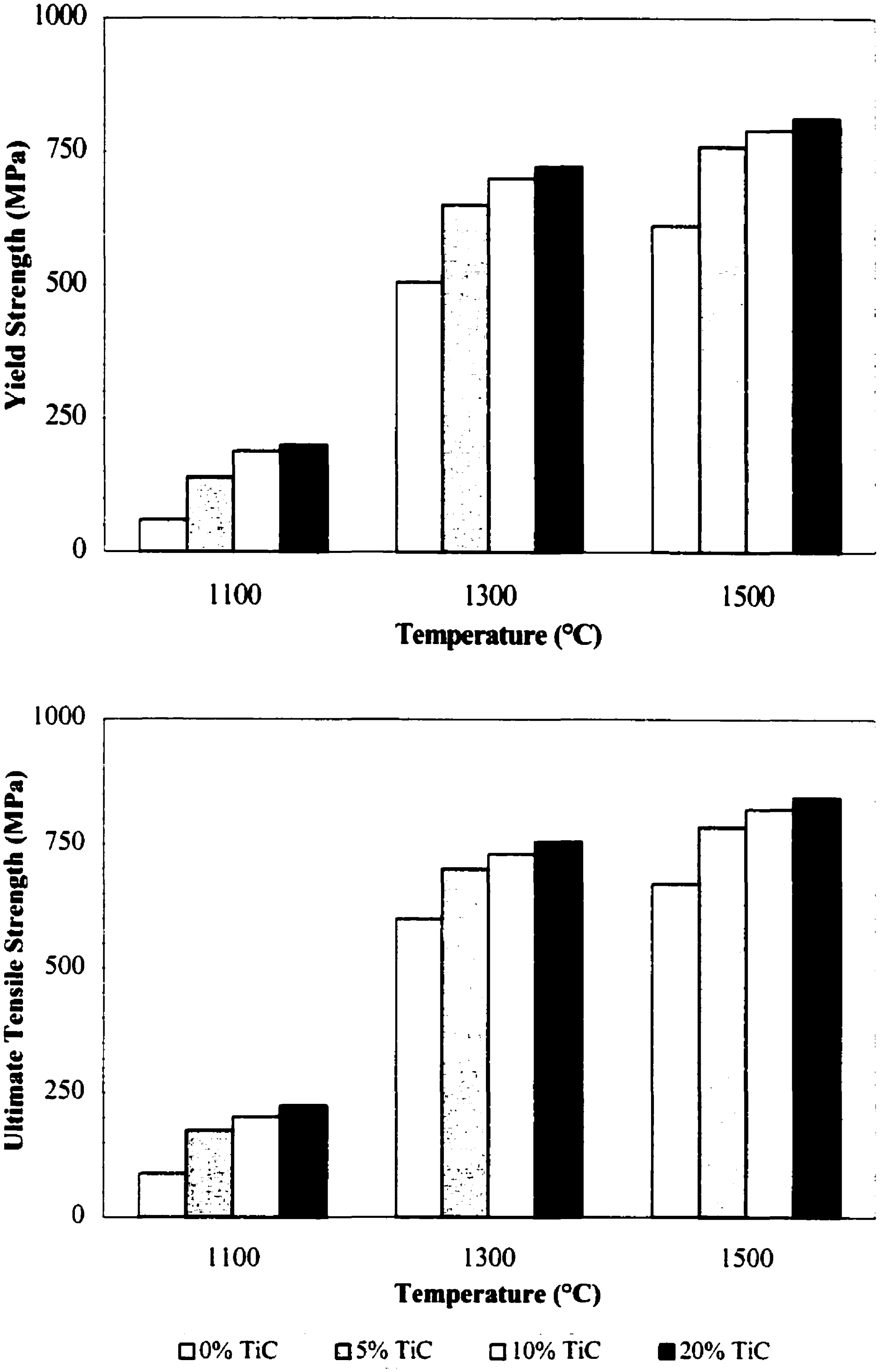

Figure 6.67 Strength properties as a function of sintering temperature for the TiC particulate reinforced Ti-6%Al-4%V composites sintered for 4 hours.

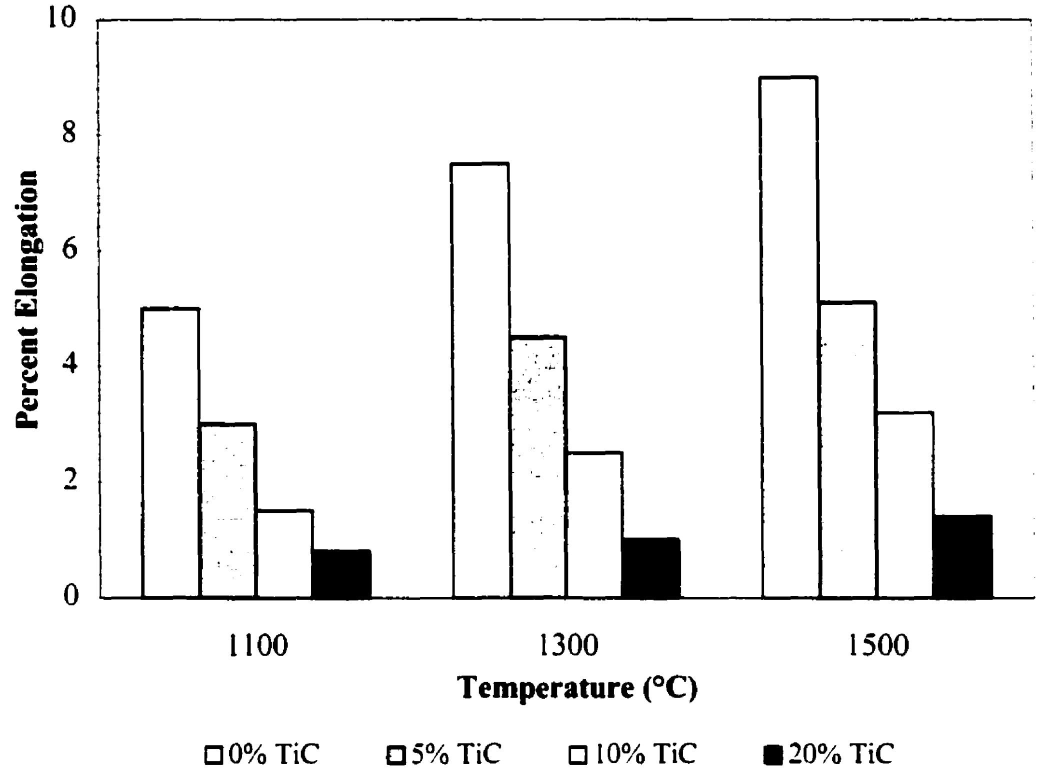

Figure 6.68 Total percent elongation as a function of sintering temperature for the TiC particulate reinforced Ti-6%Al-4%V composites sintered for 4 hours.

As compared to wrought Ti-6%Al-4%V alloy, the strength properties obtained for these P/M composites processed by sintering alone appear to be inferior on account of either residual porosity from processing at low temperatures or microstructural degradation at higher consolidation temperatures. Hence removal of residual pores by processing to complete densification at low temperatures has considerable potential in improving the strength properties of the titanium alloy and the TiC reinforced composites.

6.5.3 Fractography

Scanning electron micrographs taken from the tensile fracture surface of the titanium-based composites are shown in Figure 6.69. Irrespective of the TiC volume fraction, the fracture surface of the composite consisted of regions of both cleavage and dimpled fracture. That is, brittle fracture appears to occur within the TiC phase as evidenced by cracking of the reinforcement particles whereas the matrix fails in a ductile manner. Additionally, it appears that the cracks in the TiC phase tend to traverse through the porosity within the particles (Fig. 6.69b). Lastly, it seems most noteworthy that fracture has occurred within the TiC particulates in conjunction with dimpled ductile fracture of the titanium alloy matrix. For failure to occur by both cleavage and dimples, sufficient bonding at the interface must exist to accomplish load transfer from the matrix to the TiC particles.[123,127] Therefore, cracking of TiC is indicative of bond transfer.

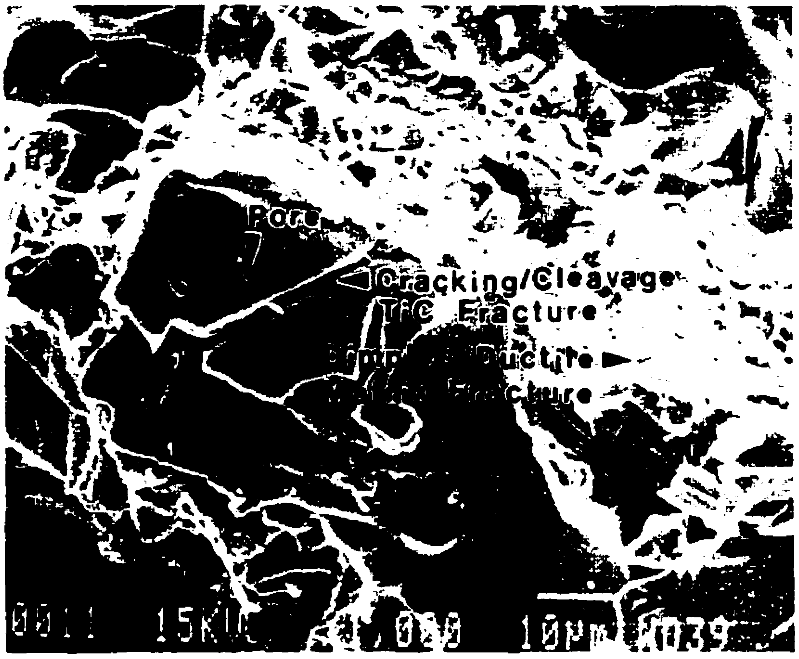

(a) 10 vol.% TiC (1400°C, 2 hours)

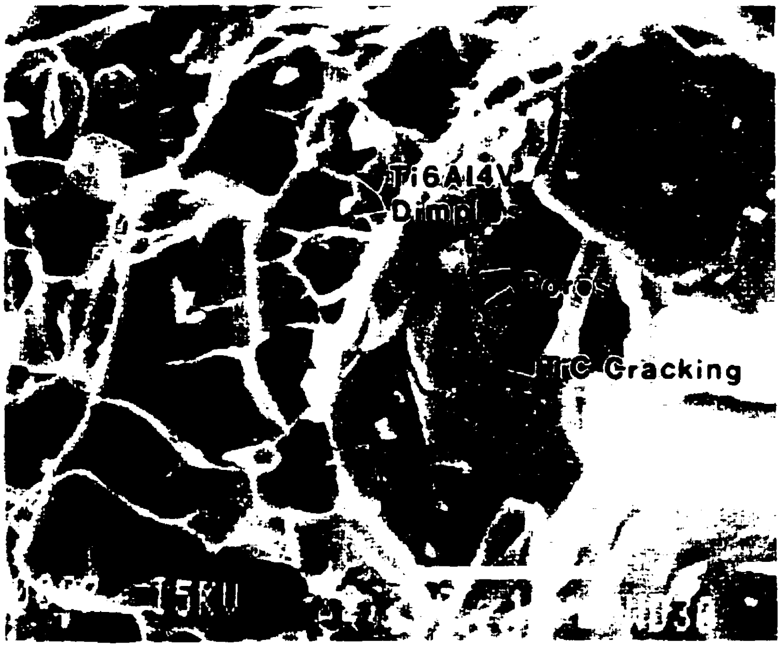

(b) 20 vol.% TiC (1400°C, 2 hours)

Figure 6.69 Scanning electron micrographs taken using secondary electron imaging of the fracture surface of TiC_p reinforced Ti-6%Al-4%V composites tested to tensile failure at room temperature.

CHAPTER 7

PROCESSING BY HOT DEFORMATION

In the previous chapter it was shown that, during elevated temperature processing, a reaction occurs between the TiC particles and the Ti-6%Al-4%V matrix, forming Ti_2C at the interface. Fabrication of the titanium-based composites by sintering alone indicated that high temperatures (> 1500°C) and long times (> 4 hours) were necessary to achieve near complete densification. However, at temperatures above 1300°C, the rapid interfacial reaction results in extensive carbon loss from the reinforcement particles and the formation of a thick interfacial layer of Ti_2C. Specifically, the interfacial reactivity resulted in transformation of the TiC reinforcement to Ti_2C either locally, at the interface, or in its entirety, depending on the processing conditions. In addition, microstructural investigation of these composites has indicated that substantial microstructural coarsening of the lamellar α and β phase morphology results with increasing sintering temperature. Moreover, mechanical property assessment of the as-sintered composites has indicated that both the strength and ductility are inferior in comparison to those achievable for this material that was processed by hot isostatic pressing (Table 2.6 in the literature review).

From the neutron diffraction work on the sintered composites, it appears that low-temperature processing would be beneficial in controlling the interfacial reaction. However, it is envisioned that full densification at these lower temperatures will be achievable only though the aid of some hot working method. This chapter focuses on the deformation response (*i.e.* uniaxial frictionless compression testing) during powder processing of the titanium matrix composites reinforced with up to 20 vol.% TiC particles.

7.1 Densification Behavior

Compacts of the composites, containing up to 20 vol.% of TiC, were fabricated using the powder metallurgy technique of powder blending and cold pressing, as described in the experimental procedure. The green compacts of the various Ti-6%Al-4%V/TiC$_p$ mixtures were roughly 11 mm in diameter and 6 mm in height, giving a height-to-diameter ratio of 0.8. The green density of these compacts was found in the previous chapter to range from approximately 62% to 67%, depending on the TiC volume fraction (Fig. 6.3).

The compacted specimens were then deformed at temperatures ranging from 850°C to 1200°C using a constant strain rate between 5×10^{-4} to 5×10^{-2} s^{-1} up to a total strain of 0.3, 0.5 and 0.8. As deformation at temperatures lower than 850°C or at strain rates higher than 5×10^{-2} s^{-1} led to substantial surface cracking in the specimens, the hot working conditions could be examined to these limits only. After deformation, the densities of the deformed materials were determined by the Archimedes' method and image analysis. Unlike the sintered composites, the densities determined by both techniques for the deformed composites gave similar values. This is likely due to the lower deformation temperatures and processing times utilized during hot working that considerably reduced the degree of oxidation, thereby decreasing the size of the porous surface oxide layer (Fig. 7.1 as compared to Fig. 6.6).

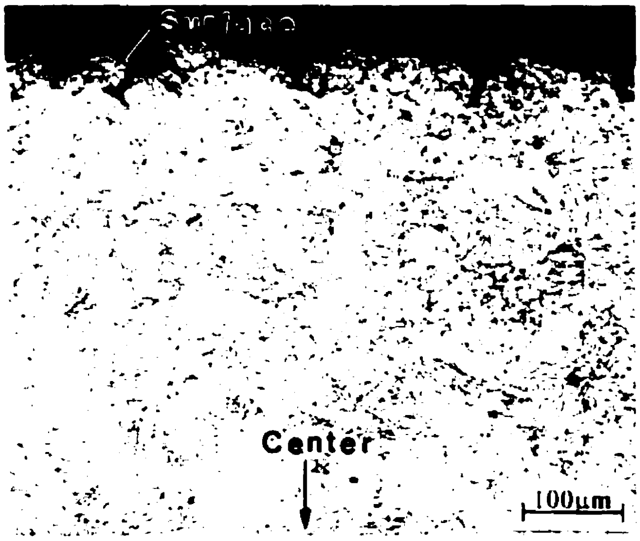

Figure 7.1 Optical micrograph of a typical surface region produced from hot deformation processing of the titanium-based composites.

Figure 7.2 illustrates the effect of temperature and total strain on densification of the composites containing up to 20 vol.% TiC_p. The curves indicate that the temperatures for near complete densification (> 90%) are substantially lower than for sintering alone (*i.e.* 1000°C versus 1500°C). In general, it was observed that the influence of strain rate, within the range of 5×10^{-4} to 5×10^{-2} s^{-1}, on densification of the specimens was negligible.

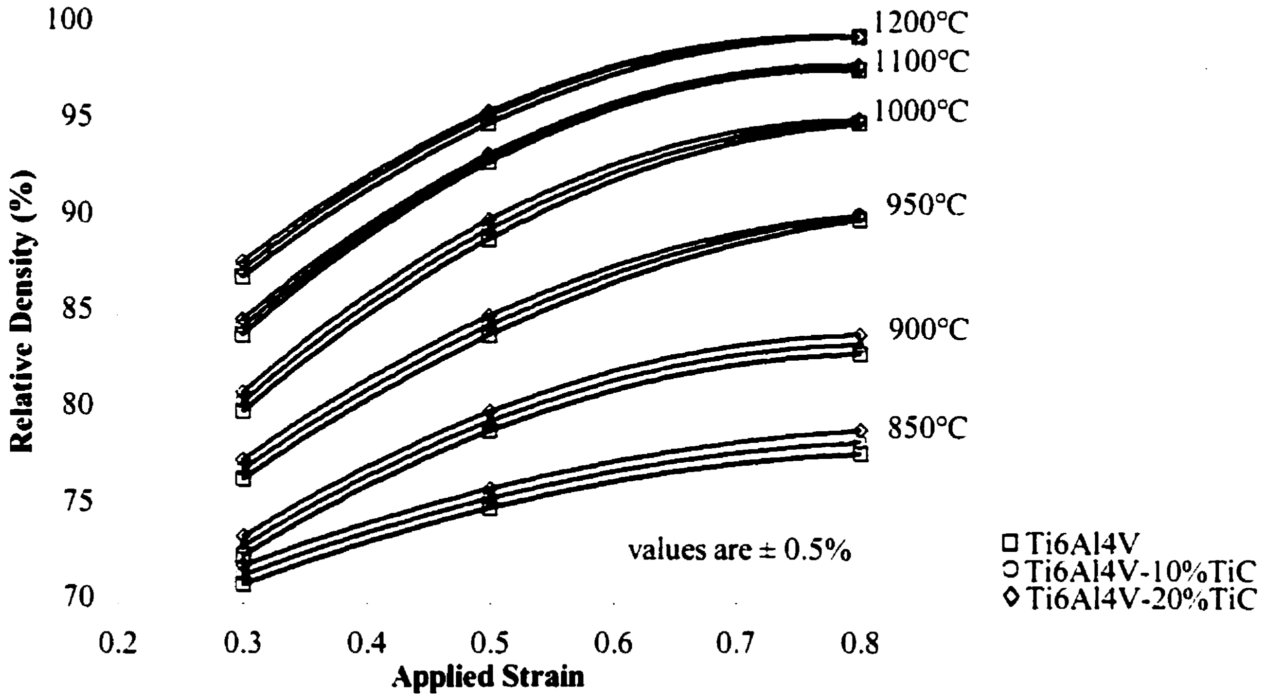

Figure 7.2 Density as a function of the deformation temperature and total strain.

7.2 Deformation Behavior

To determine the flow behavior of the titanium-based materials, the densification response described by the curves in Figure 7.2 can be modeled as a function of the applied strain. The best-fit polynomial regression is of the form

$$\rho = A\varepsilon_a^2 + B\varepsilon_a + C \qquad (7.1)$$

where ρ is the relative density, ε_a is the applied strain and A, B, and C are constants that depend on the deformation temperature and TiC volume fraction. The values for these are given in Table 7.1 for the various curves shown in Figure 7.2 as well as other intermediate temperatures investigated. Having determined the dependence of density on applied strain through equation 7.1, the deformation strain in the porous materials (ε_d) can be calculated by accounting for the densification strain by combining equations 2.9 and 2.12 from the literature review to give the following:

$$\varepsilon_d = \frac{2\nu\varepsilon_a}{1-V_f} = \frac{2(0.5\rho^n)\varepsilon_a}{1-V_f} = \frac{\rho^n\varepsilon_a}{1-V_f} = \frac{(A\varepsilon_a^2 + B\varepsilon_a + C)^2\varepsilon_a}{1-V_f} \tag{7.2}$$

where V_f is the reinforcement volume fraction. For relative densities less than 0.9, the stress-intensification correlation developed by Shima and Oyane, equation 2.16, provided the most suitable correction to the flow component of the deformation behavior.[219] The stress in the porous material (σ_p) is then related to the measured stress (σ_m) by the following:

$$\sigma_p = \sigma_m \frac{A_m}{A_p} = \sigma_m\phi = \sigma_m \frac{1}{\rho^n} = \frac{\sigma_m}{(A\varepsilon_a^2 + B\varepsilon_a + C)^{2.5}} \tag{7.3}$$

At relative densities greater than 0.9, the random pore distribution relation formulated by Coble[214] (equation 2.13) was used to correct the flow component of the deformation behavior as follows:

$$\sigma_p = \sigma_m \frac{A_m}{A_p} = \sigma_m\phi = \sigma_m \frac{1}{\rho} = \frac{\sigma_m}{A\varepsilon_a^2 + B\varepsilon_a + C} \tag{7.4}$$

Using equations 7.2 to 7.4, the compression stress-strain behavior of the unreinforced alloy and the composites was determined, as illustrated in Figures 7.3 to 7.10. For the conditions investigated, a maximum applied strain of 0.8 was imparted during compression testing to the titanium-based materials. From equation 7.2, the deformation strain (ε_d) stored in the consolidating compact was calculated from the applied strain data of the compression test. The pre-multiplying factor for ε_a in equation 7.2 accounts for the changing density with increasing applied strain. Hence, the density factor removes the component of strain that is imparted to the porous compact for consolidation. Consequently, the true strain stored in the material is lower than the applied strain once the consolidation strain is removed. The term ($1-V_f$) in equation 7.2 corrects for the presence of undeforming TiC particles. This factor increases the deformation strain stored in the composites on the basis that rigid particles constrain the plastic flow of the matrix. Thus, the true strain in the matrix (the x-axis in the curves of Figs. 7.3 to 7.10) is found to be lowest for Ti-6%Al-4%V and increases with increasing TiC volume fraction. The true strain values for the matrix are observed to decrease slightly with decreasing deformation temperature on account of the slower removal of porosity (Fig. 7.2) at these temperatures.

Table 7.1 – Values for the Constants A, B and C in Equation 7.1

Temperature (°C)	Material	A	B	C
850	Ti6Al4V	-20.636	36.263	62.003
	Ti6Al4V-10%TiC	-14.526	29.454	64.188
	Ti6Al4V-20%TiC	-7.942	22.098	66.511
900	Ti6Al4V	-21.131	43.33	62.009
	Ti6Al4V-10%TiC	-15.251	36.554	64.221
	Ti6Al4V-20%TiC	-8.719	29.023	66.623
950	Ti6Al4V	-28.080	57.521	62.015
	Ti6Al4V-10%TiC	-22.929	50.878	64.297
	Ti6Al4V-20%TiC	-17.522	43.467	66.842
1000	Ti6Al4V	-39.591	72.998	62.031
	Ti6Al4V-10%TiC	-34.647	66.357	64.347
	Ti6Al4V-20%TiC	-28.738	58.604	66.944
1050	Ti6Al4V	-45.459	79.235	62.034
	Ti6Al4V-10%TiC	-40.388	72.447	64.387
	Ti6Al4V-20%TiC	-34.534	64.757	66.968
1100	Ti6Al4V	-57.162	90.434	62.044
	Ti6Al4V-10%TiC	-50.674	82.424	64.445
	Ti6Al4V-20%TiC	-43.639	73.784	67.005
1150	Ti6Al4V	-63.418	96.205	62.049
	Ti6Al4V-10%TiC	-58.003	89.021	64.502
	Ti6Al4V-20%TiC	-52.379	81.596	67.016
1200	Ti6Al4V	-68.686	101.540	62.059
	Ti6Al4V-10%TiC	-62.637	93.628	64.597
	Ti6Al4V-20%TiC	-56.083	85.308	67.111

Variation in the flow stress with increasing strain for the titanium-based materials (Figs. 7.3 to 7.10) is observed to consist of three regions. The initial stage appears to be typified by a continuously decreasing rate of increase in stress with strain (*i.e.* the slope of the curve diminishes with strain). This suggests that the material is experiencing strain hardening through the removal of porosity – deformation becomes more difficult as the material densifies. As shown in Figure 7.2, consolidation occurs with increasing strain. At low deformation temperatures, the porosity remains high even after a strain 0.8. For an equivalent strain value, increases in temperature lead to a decrease in porosity and near complete density is obtained by deforming at 1200°C to a strain of 0.8. The incremental removal of porosity leads to an increase in stress (strain hardening) in the solid material. A steady state region follows during which the stress remains constant with strain. The constancy in stress in this region can be explained on the basis of a balance between competitive processes of strain hardening and *stress recovery*. Porosity reduction leads to an increase in stress and the solid material strain hardens. However, the removal of porosity (*i.e.* replacement of higher energy solid-vapor interfaces with lower energy solid-solid boundaries) is accompanied by a reduction in the internal stress of the consolidating system (as discussed in the literature review). A balance between the strain hardening and stress recovery then accounts for the appearance of a steady state region. Finally there is a continual increase in flow stress with increasing strain. This is due partly to the fact that the nearly fully dense material continues to strain harden further with plastic flow; however the stress recovery, from spherical pores isolated within the grain structure of the matrix, is slower (as discussed in the literature review). Also during deformation in compression, as the material spreads over the compression anvils to increase its diameter, frictional forces oppose the outward flow of metal (*i.e.* even using boron nitride powder and mica sheets for lubrication does not attain a completely frictionless condition between the specimen and anvils). This frictional resistance occurs in the region of the specimen in contact with the compression anvils, while the material at the specimen mid-height can flow outward undisturbed. This leads to a barreling of the original cylindrical specimen profile, and internally a region of undeformed material forms near the anvil surfaces. As these zones approach and overlap, an increase in the stress occurs for a given increment of deformation strain and the flow curve begins to bend upward.

The flow stresses of the titanium-based materials were found to decrease with increasing deformation temperature. This is primarily due to the role of thermally activated dislocation movement as well as increased recovery with increasing temperature. Referring to the general form of the constitutive equation and the expression for high temperature flow strength calculation[268], when the temperature changes the stress can be defined by:

$$\varepsilon = A \sinh(\alpha\sigma)^{n'} \exp\left(\frac{-Q_{def}}{RT}\right) \tag{7.5}$$

Rearranging for the flow stress gives:

$$\sigma = \frac{\sinh^{-1}(X)}{\alpha}, \quad \text{where } X = \left[\frac{\dot{\varepsilon} \exp\left(\frac{Q_{def}}{RT}\right)}{A}\right]^{1/n'} \tag{7.6}$$

where σ is the flow stress, $\dot{\varepsilon}$ is the strain rate, R is the gas constant, and A, n′ and α are nearly constant for a given material, but are likely to change slightly with temperature.

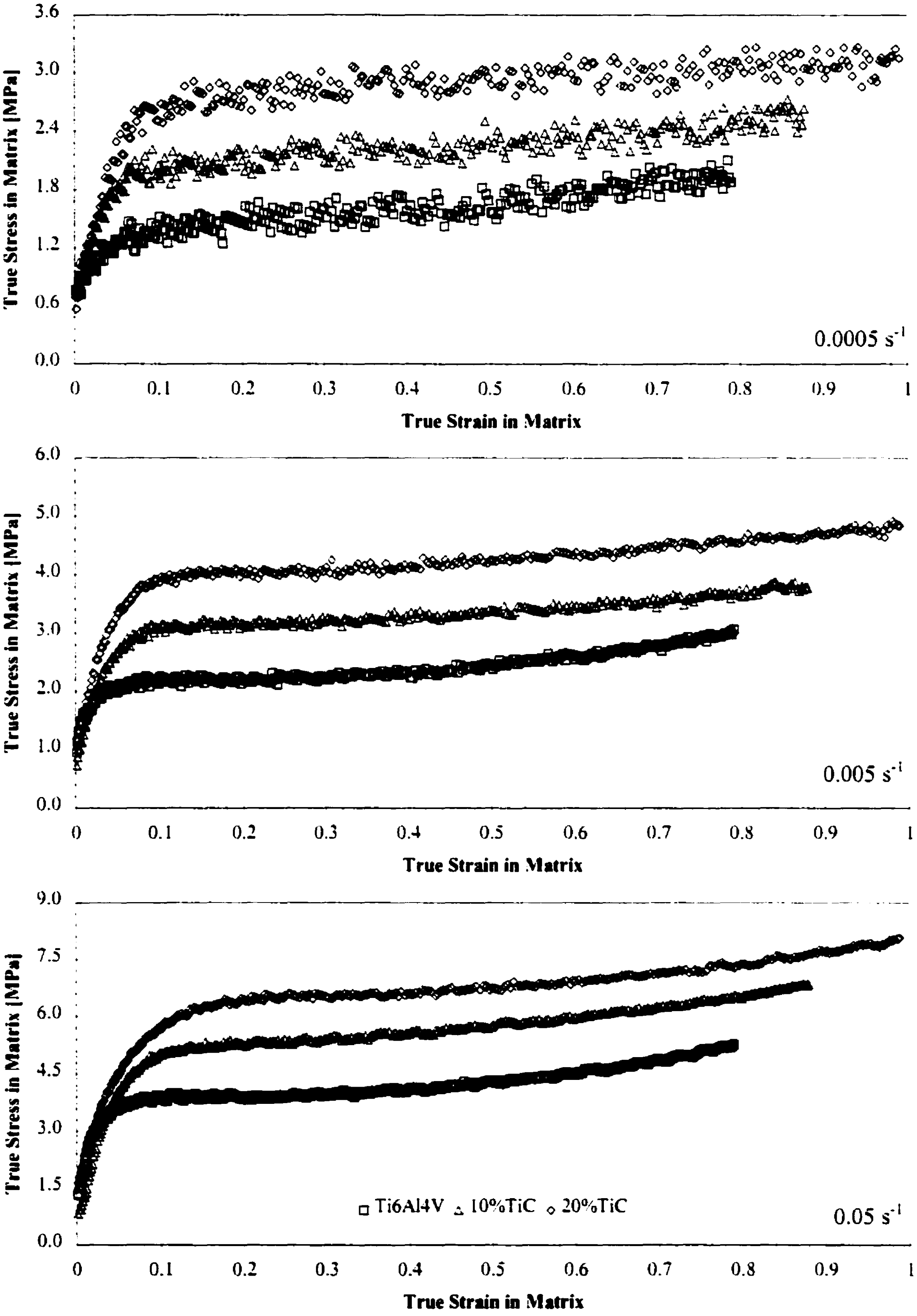

Figure 7.3 Flow behavior of the various materials at 1200°C.

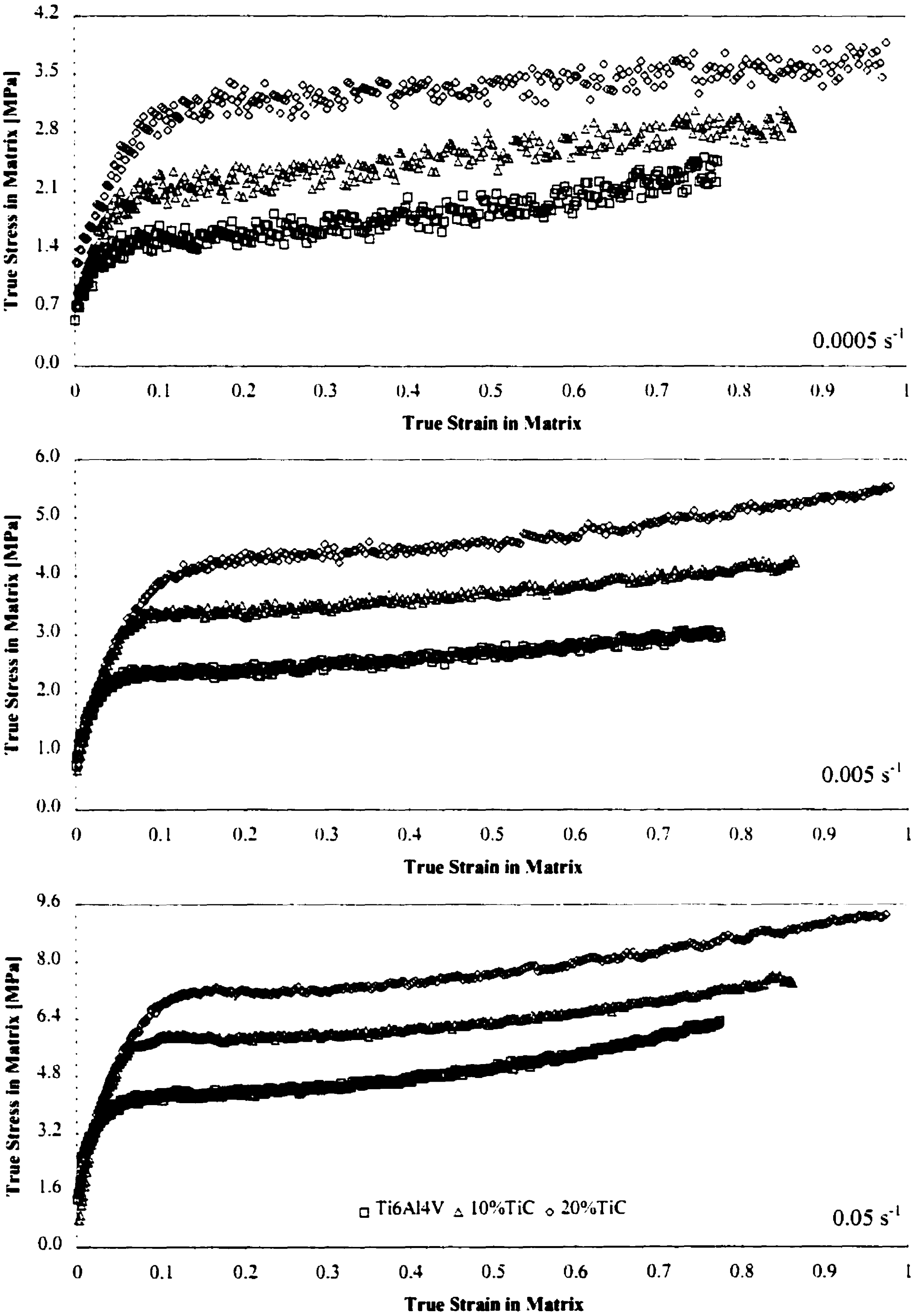

Figure 7.4 Flow behavior of the various materials at 1150°C.

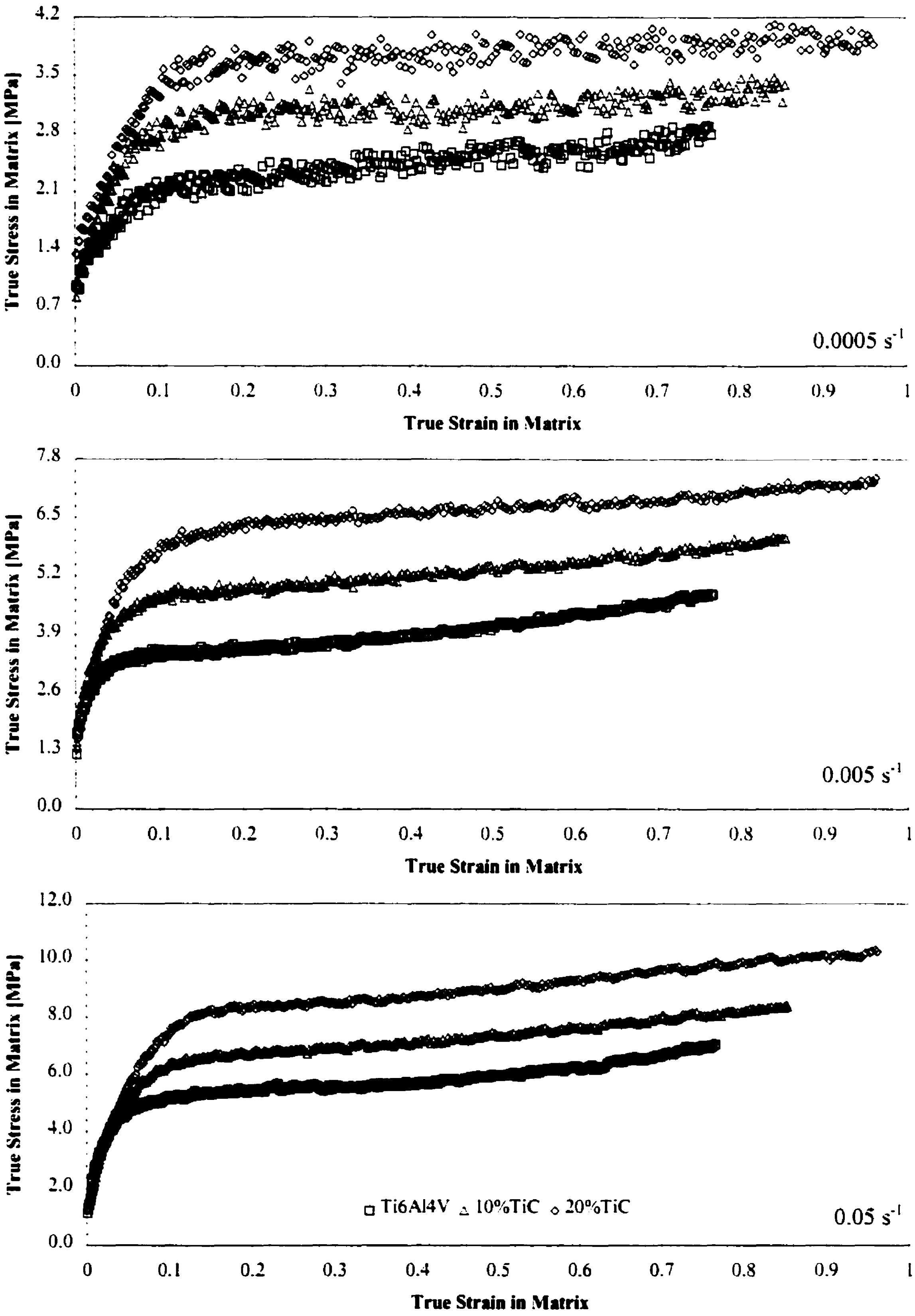

Figure 7.5 Flow behavior of the various materials at 1100°C.

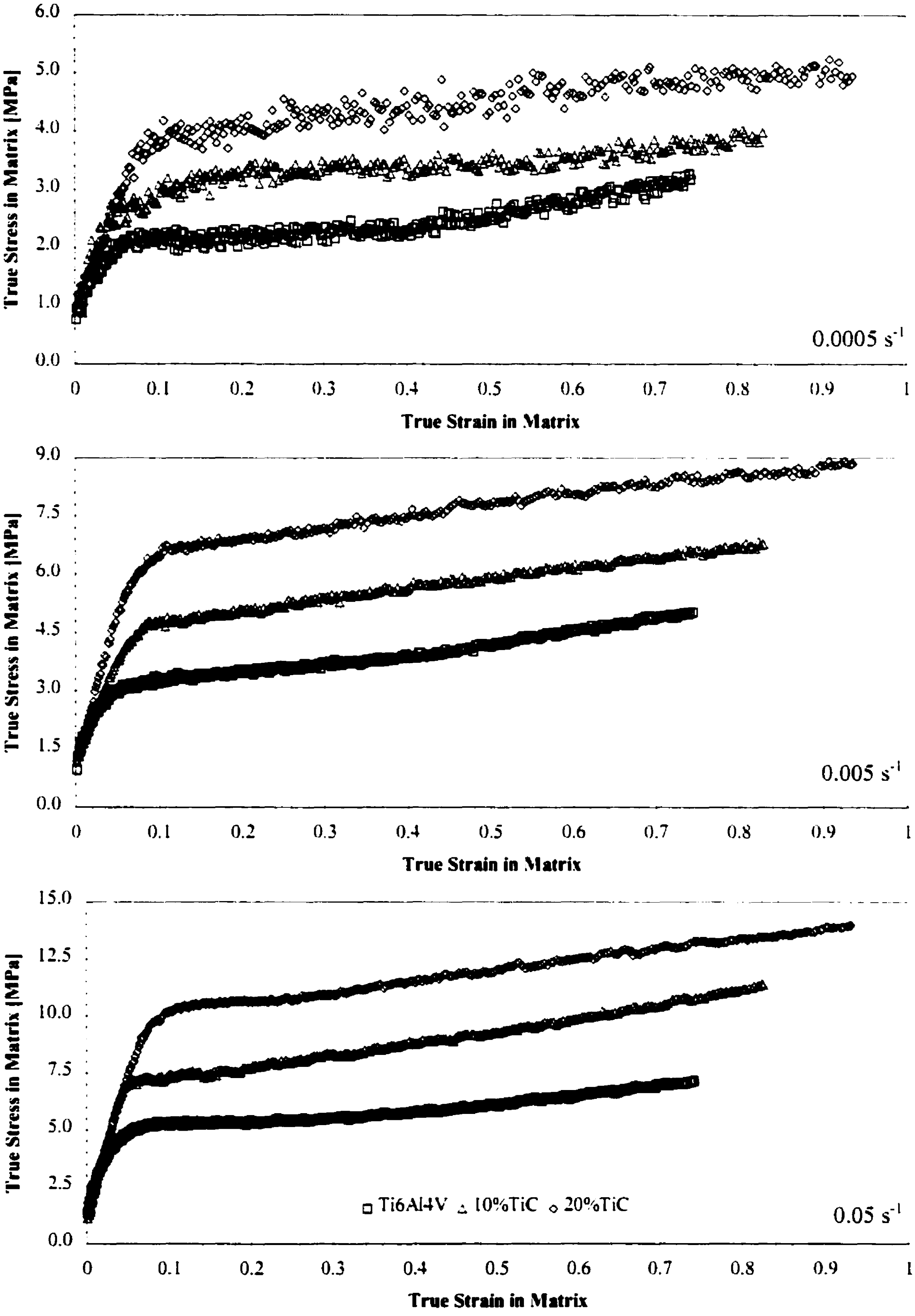

Figure 7.6 Flow behavior of the various materials at 1050°C.

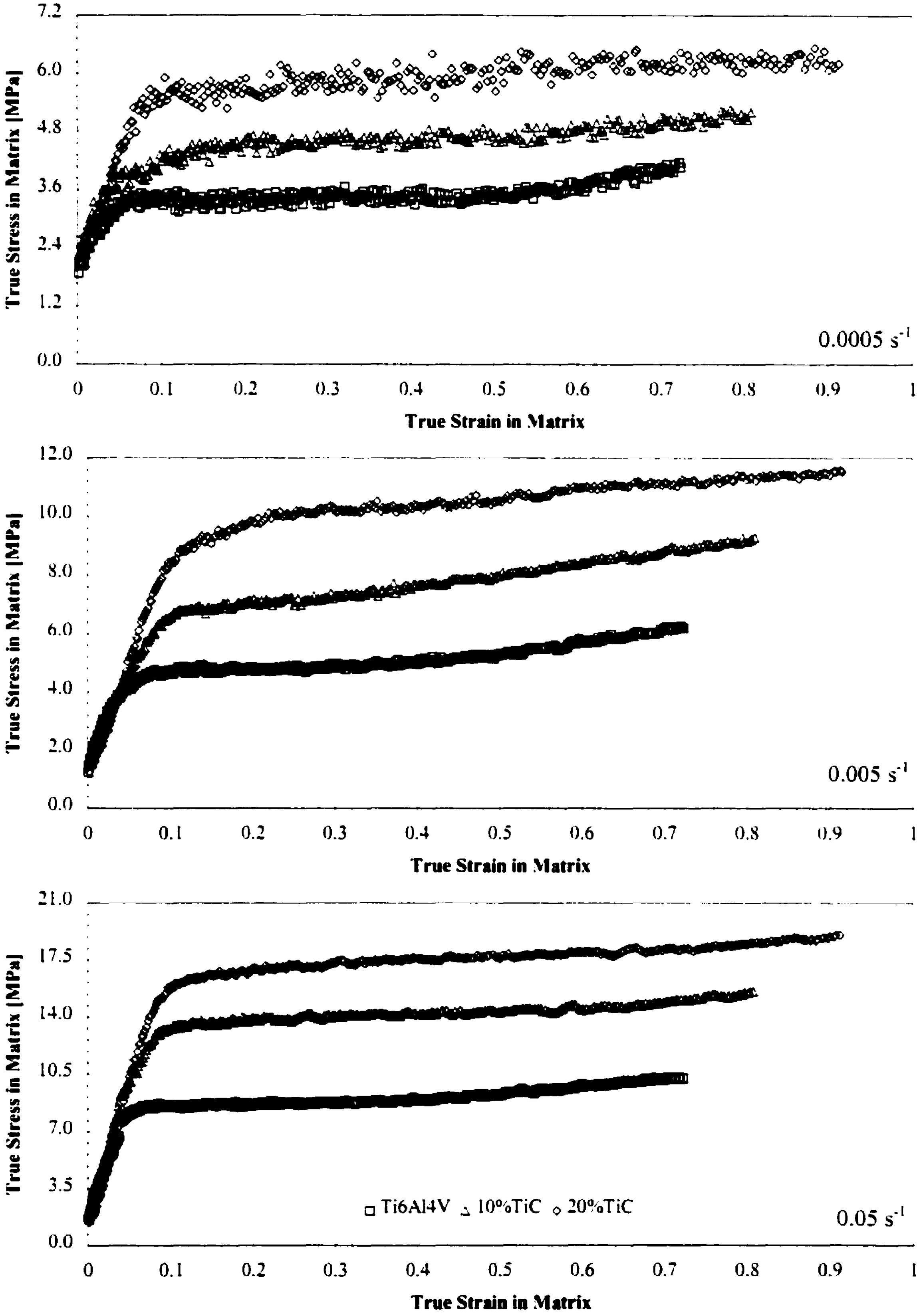

Figure 7.7 Flow behavior of the various materials at 1000°C.

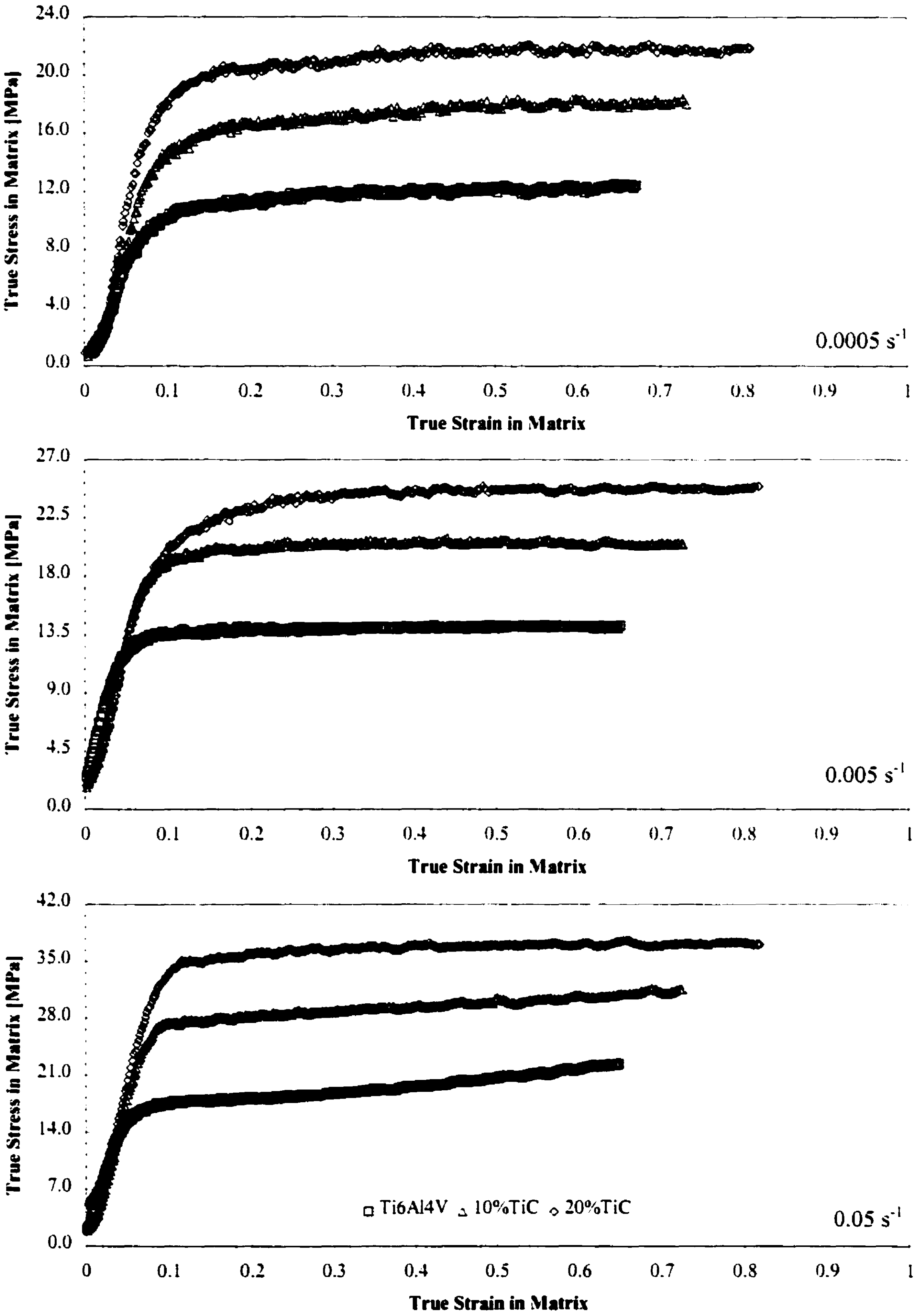

Figure 7.8 Flow behavior of the various materials at 950°C.

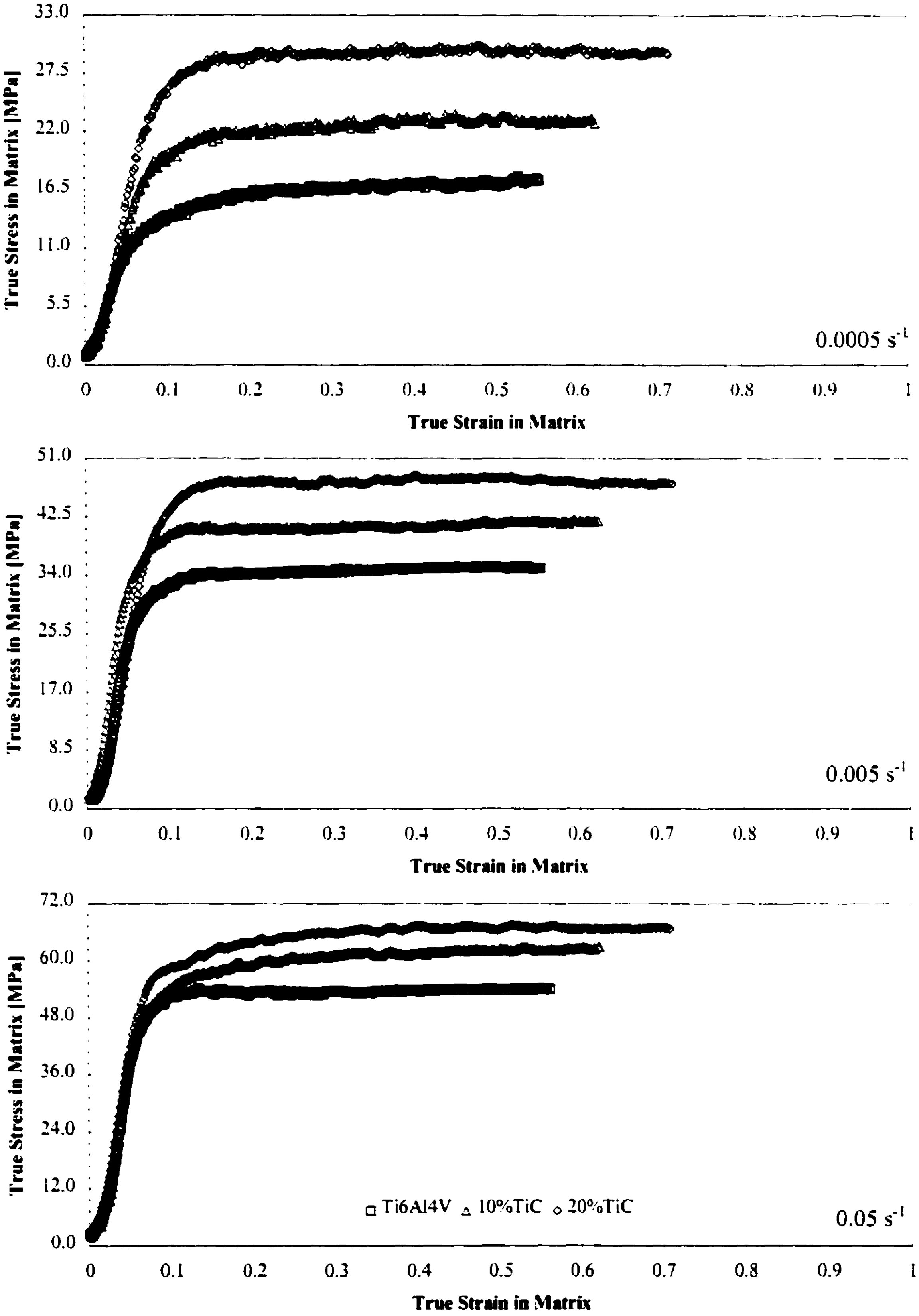

Figure 7.9 Flow behavior of the various materials at 900°C.

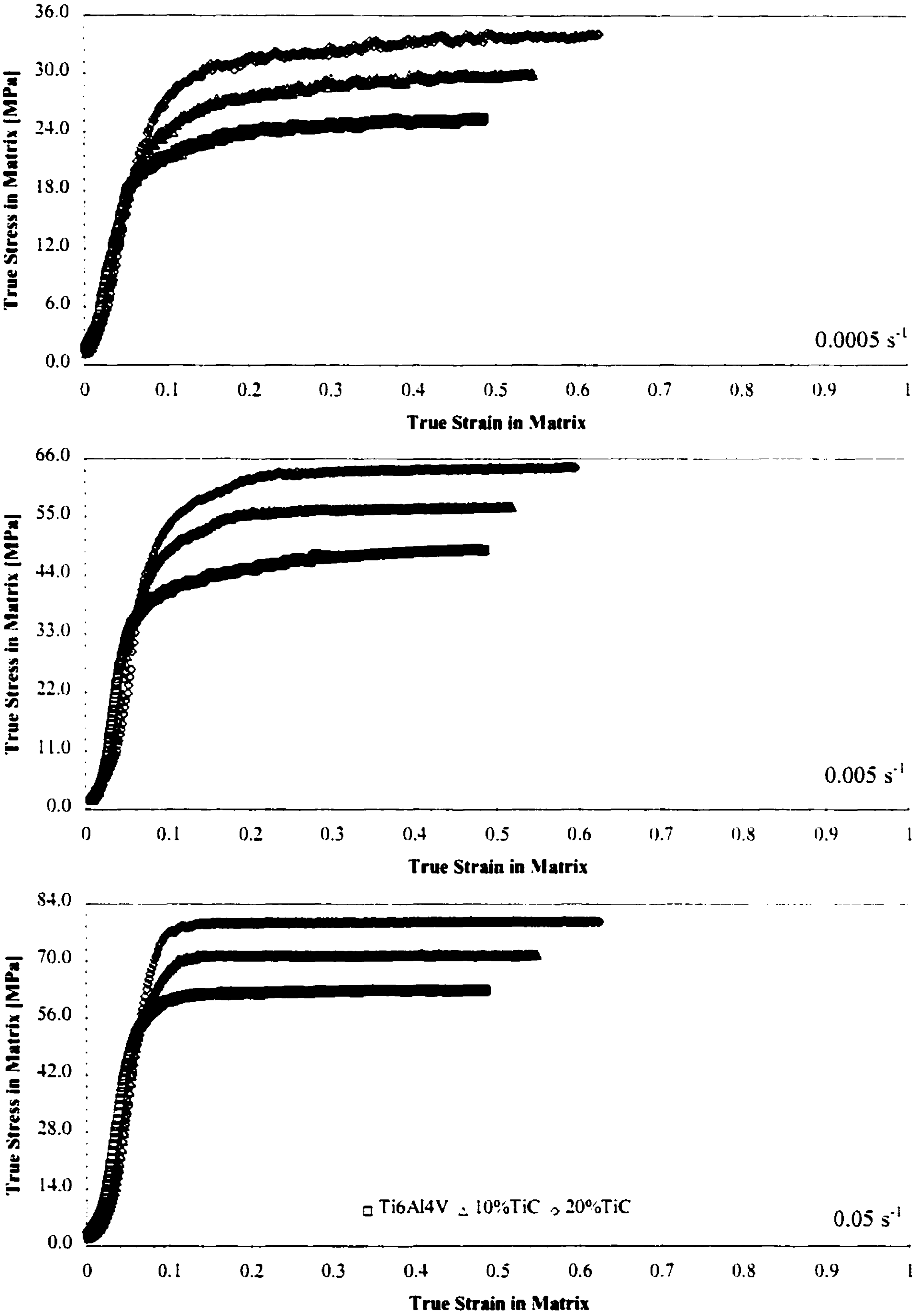

Figure 7.10 Flow behavior of the various materials at 850°C.

The above relationship indicates that the flow stress will increase smoothly in response to decreasing temperature, provided that the microstructure does not change (Fig. 7.11). Thus a deviation from this behavior can be related to a microstructural change.

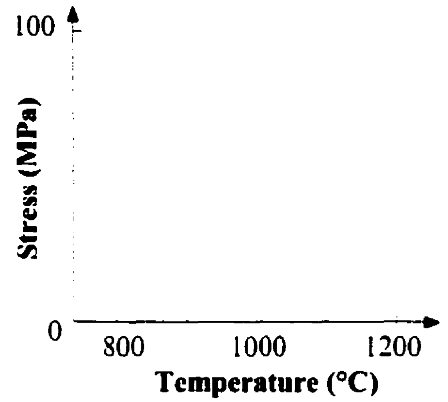

Figure 7.11 Expected stress-temperature relationship.

For the Ti-6%Al-4%V based materials, a discontinuity in the flow stress behavior is expected at the beta transformation temperature (1017°C from Fig. 6.27), below which alpha forms exponentially with temperature in the following manner:[269]

$$V_{f_\alpha} = 0.925\{1 - e^{-0.0085(T_\beta - T)}\} \tag{7.7}$$

where V_{f_α} is the volume fraction of α at a certain absolute temperature, T [K] and T_β is the beta transus temperature of the Ti-6%Al-4%V alloy (1290 K).

In the literature, deformation in the β phase region has been found to have a low temperature dependence whilst for the α phase there is a strong dependence of temperature on the flow stress, as shown in Figure 7.12.[52,270] For the titanium-based materials examined in this work, the effect of temperature on the flow stress for various strain rates was examined in greater detail by plotting the stress at 0.2 strain, from Figures 7.3 to 7.10, as a function of deformation temperature (Fig. 7.13). The stress-temperature data at each strain rate were fitted with two exponential regressions, one below the β transus and one above the transformation temperature, to account for the microstructural change at 1017°C. Plastic deformation of the materials was observed to be relatively insensitive to the hot working temperature above the β transus and increasingly difficult below the β transus, contributing to the much higher flow stress at the lower deformation temperatures, as shown in Figure 7.13. Also, just below the β transus temperature the increase in flow stress is not as marked as at temperatures well into the two-phase region. This is because the α phase has a much greater temperature dependence of the flow stress than the β phase. Moreover, with the α phase transforming from the β phase in an exponential manner (*i.e.*

equation 7.7), it rapidly becomes a continuous phase in the Ti-6%Al-4%V matrix and begins to dominate the characteristics of flow. Thus, even deformation in the α+β phase region shows a strong flow stress-temperature relationship, particularly when α is the major phase constituent (Fig. 7.12-7.13). For temperatures at which β becomes the continuous phase, the flow stress reflects the character of this phase rather than the isolated α phase, which then has been suggested to behave similar to rigid particles in a soft β matrix.[270] Additionally, Malcor and Montheillet have found that an initial lamellar microstructure has a greater flow stress dependence on temperature for both α and β phases as compared to an initial equiaxed structure as depicted in Figure 7.12b.[270]

A noticeable feature in the curves of Figure 7.13 is that the flow stress at 850°C is consistently below the respective regression curves most likely due to incomplete densification at these processing conditions. Comparing the flow stress-temperature behavior during powder metallurgy working of the Ti-6%Al-4%V alloy (which was lamellar in microstructure prior to deformation) with that of the wrought titanium alloy from the literature (Fig. 12b) indicates that the flow stresses in this work are consistently lower for all the processing conditions investigated. This occurrence possibly stems from a lower resistance to deformation for porous Ti-6%Al-4%V alloy as compared to that of the solid alloy. Microscopically, in a porous material, at the void regions in the matrix, the local stress (under an applied load) would be greater. Due to this stress concentration at the pores, the material will begin to yield locally even though the applied load may be insufficient to cause plastic deformation in the solid matrix.

Besides the temperature dependence of the flow stress, a progressive rise in the flow stress was also observed with increasing TiC volume fraction, as illustrated in Figures 7.3 to 7.10. The reasons for the latter may be explained in two ways: (1) After densification, due to the differential thermal expansion coefficient between the reinforcing particles and the matrix (roughly 2×10^{-6} °C^{-1}), a high dislocation density is generated around the TiC particles, which increases the flow stress during subsequent working; (2) The rise in flow stress must be related also to the constraint to plastic deformation of the matrix alloy caused by the presence of a large volume fraction of rigid (*i.e.* undeforming) TiC particles.

Analysis of the effect of strain rate from Figures 7.3 to 7.10 indicates that there is a progressive rise in the flow stress of the matrix alloy and the composites when the strain rate is increased for all deformation temperatures tested. Using the information from the stress-strain curves, the strain rate dependence of the flow stress at a strain of 0.2 was modeled using the creep power law form of the constitutive equation for hot-deformation conditions as proposed by Sellars and Tegart (equation 7.5):[268]

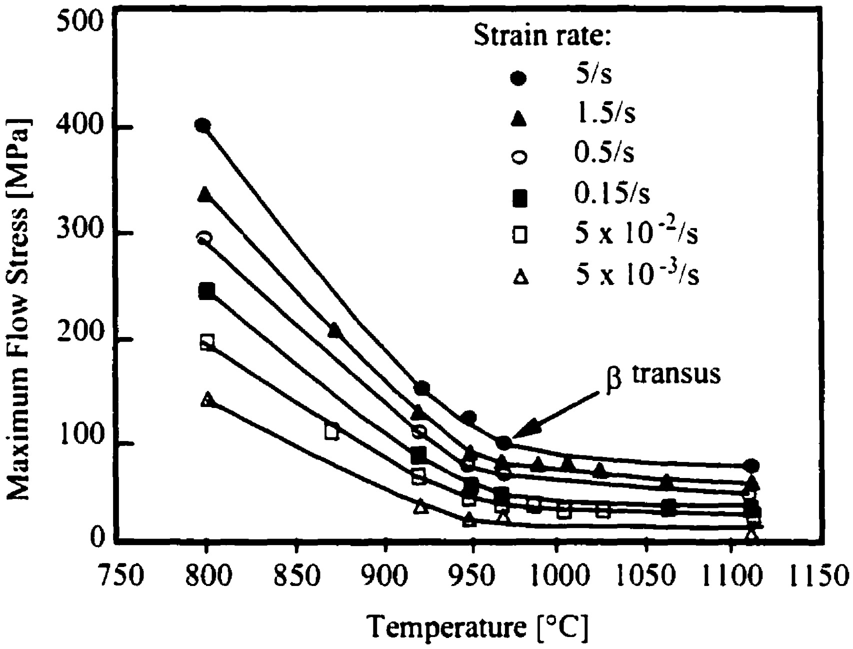

(a) Initial Equiaxed Structure

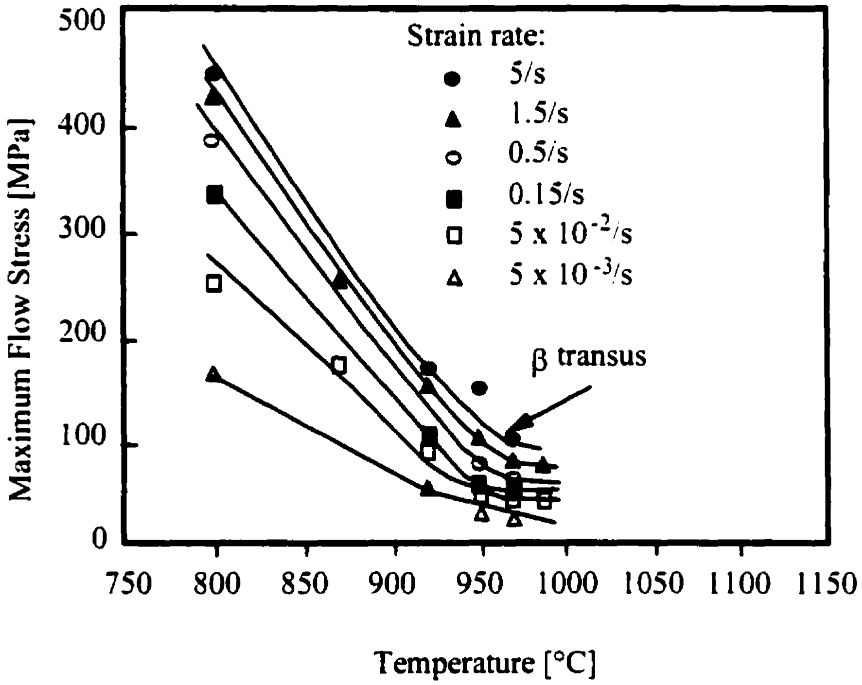

(b) Initial Lamellar Structure

Figure 7.12 Temperature dependence of flow stress at various strain rates for Ti-6%Al-4%V. Replotted from the work of Malcor and Montheillet.[270]

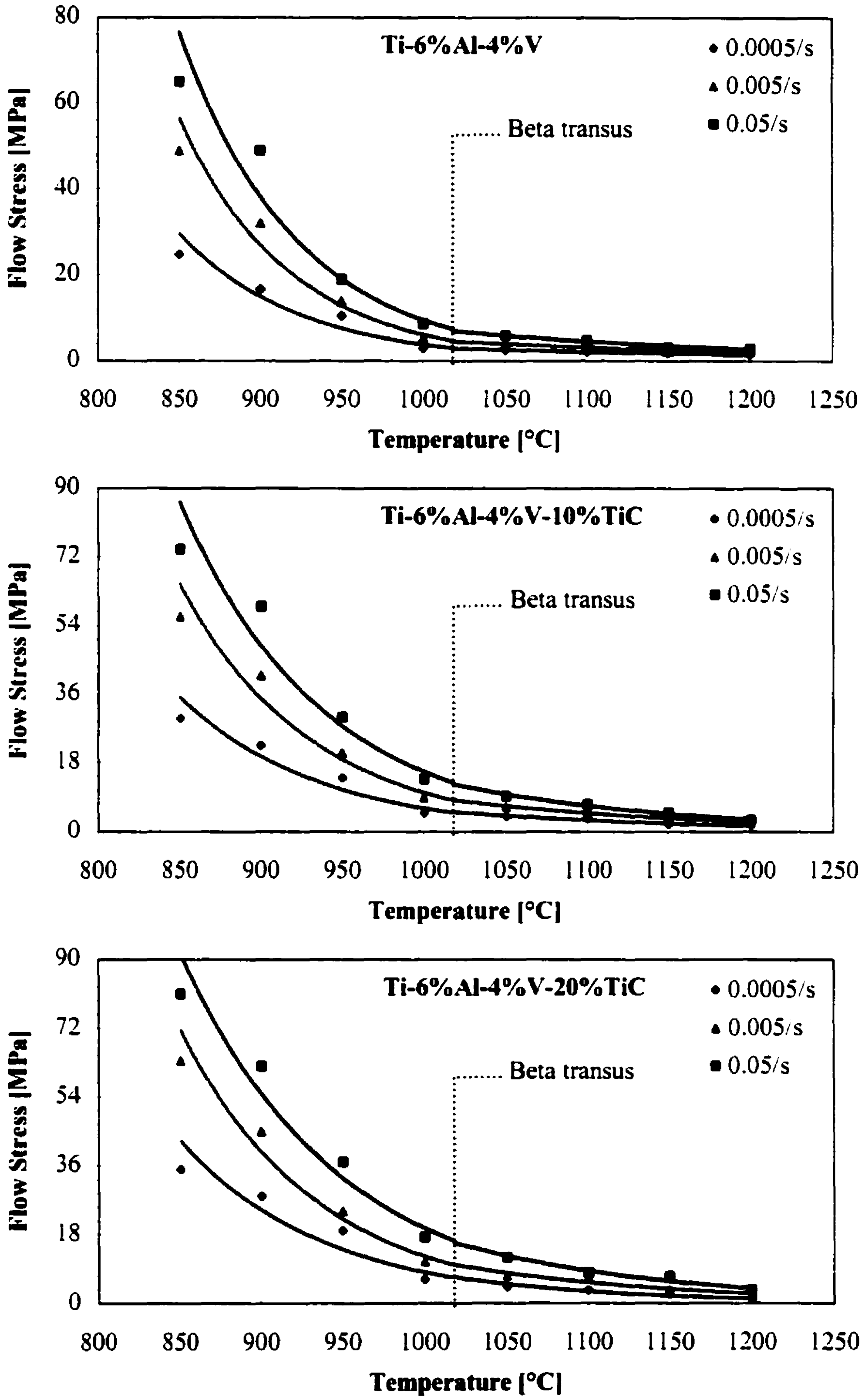

Figure 7.13 Temperature dependency of the flow stress above and below the beta transus for the titanium-based materials compressed at various strain rates.

$$\dot{\varepsilon} = A\,\sigma^{n'} \exp\left(\frac{-Q_{def}}{RT}\right) \tag{7.8}$$

The stress exponent, n', is the slope of constant temperature points on a plot of log $\dot{\varepsilon}$ versus log σ. The creep power law formulation of the constitutive equation can also be used to determine the strain rate sensitivity, m, of the material. The inverse of the stress exponent gives m (*i.e.* m is the slope of constant temperature points on a plot of log σ versus log $\dot{\varepsilon}$). On the plots of log σ versus log $\dot{\varepsilon}$ (Fig. 7.14), the slope, m, was calculated by a least squares regression of each isothermal line. The average values of n' and m for the matrix alloy and composites are summarized in Table 7.2 for temperature ranges above and below the beta transus.

Previous work[52,270-271] on these materials indicates that the log $\dot{\varepsilon}$ versus log σ plot is not linear over a wider range of strain rates or at strain rates higher than 0.5 s^{-1}. In this case, equation 7.5 has been used to obtain the stress exponent, while the strain rate sensitivity was determined using the creep power law form (equation 7.8).[52,271] However, for the present work, the creep power law relationship appears to hold over the strain rate range tested (Fig. 7.14).

The values found in the literature for the strain rate sensitivity and the stress exponent are indicated in Table 7.3. Overall, there appears to be good agreement between the present work and previous results. For the titanium-based materials, the stress exponent increased with increasing TiC volume fraction, thereby suggesting a lower strain rate sensitivity of the composites (*i.e.* the sensitivity to changes in temperature and strain rate decreases). This is consistent with the work of Johnson et al. in their findings of a lower strain rate sensitivity for composites as compared to the unreinforced matrix.[166] However, the strain rate sensitivity values in their work are considerably higher than those of other investigators as indicated in Table 7.3.[52,270-271] In the work of Malcor and Montheillet,[270-271] the initial microstructure was also found to have an influence on the stress exponent and strain rate sensitivity of the titanium alloy. The greatest influence of the initial lamellar structure appears to be a larger scatter in the strain rate sensitivity values as compared to the equiaxed structure.

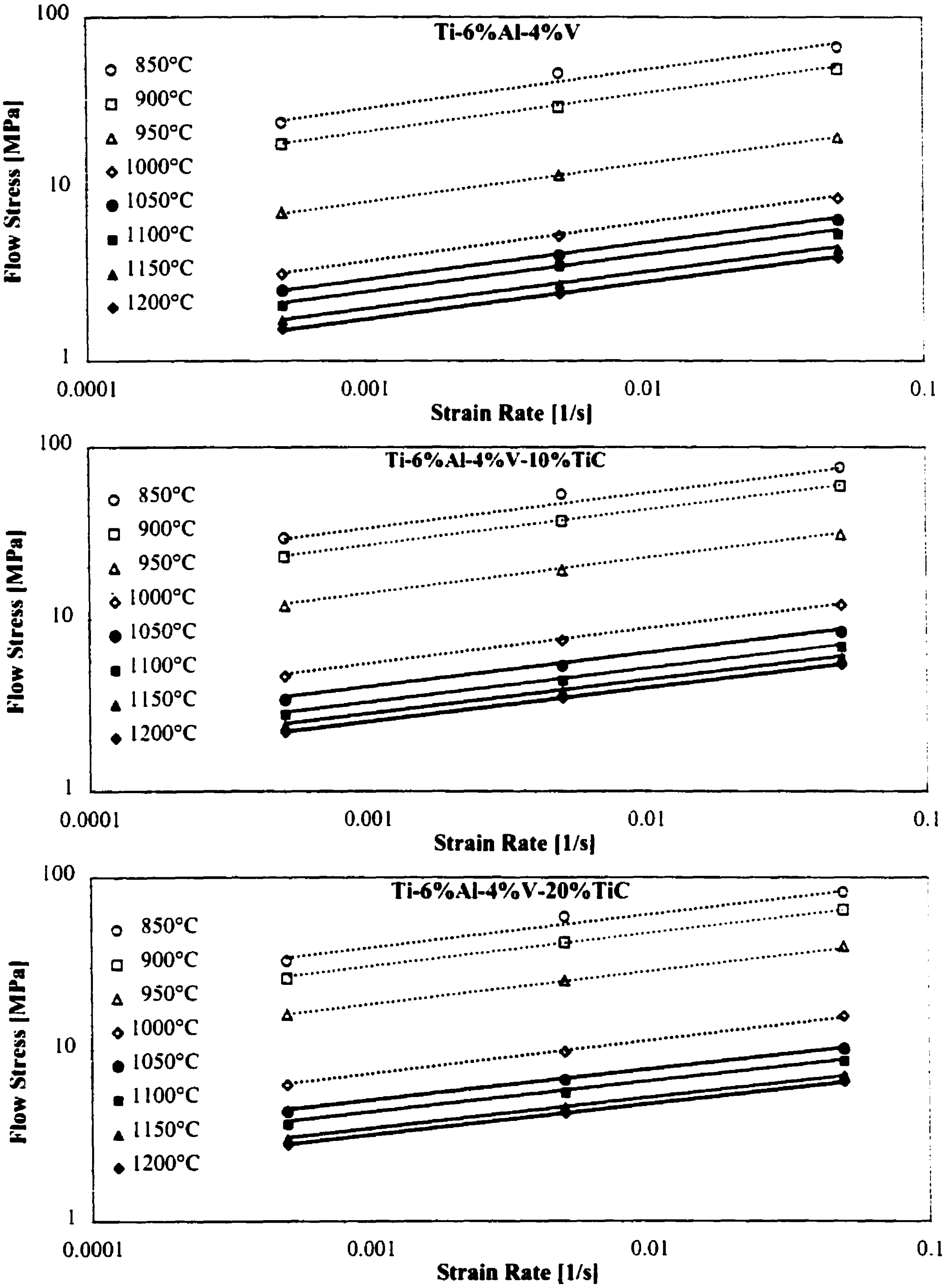

Figure 7.14 Isothermal plots of log σ versus log $\dot{\varepsilon}$ for various deformation temperatures above and below the beta transus. For each material, the approximately parallel solid or dashed lines are the regression lines.

Table 7.2 – Values for the Stress Exponent and Strain Rate Sensitivity

Material	Temperature Range (°C)	Stress exponent (n')	Strain Rate Sensitivity (m)
Ti-6%Al-4%V (lamellar)	850-1017	4.55	0.22
	1017-1200	4.85	0.21
Ti-6%Al-4%V/10%TiC	850-1017	4.84	0.21
	1017-1200	5.12	0.19
Ti-6%Al-4%V/20%TiC	850-1017	5.03	0.20
	1017-1200	5.43	0.18

Table 7.3 – Literature Values for the Stress Exponent and Strain Rate Sensitivity

Material	Temperature Range (°C)	Stress exponent (n')	Strain Rate Sensitivity (m)
Ti-6%Al-4%V (lamellar)[271]	850-950	3.70-4.37	0.09-0.23
Ti-6%Al-4%V (equiaxed)[271]	850-950	4.58-5.20	0.12-0.20
	970-1120	3.83-4.58	0.14-0.21
Ti-6%Al-4%V[166]	950	-	0.4-0.6
Ti-6%Al-4%V/20%TiC[166]	950	-	0.2-0.5

Using the creep power law relationship (equation 7.8), the temperature dependence of flow stress at a strain of 0.2 was also modeled by plotting log σ versus 1/T to obtain the activation energy. Figure 7.15 shows the relationship between log σ versus 1/T for temperatures above and below the beta transus. Least squares regression lines were fitted to the constant $\dot{\varepsilon}$ data to determine the average slope, S_{av}, of each material both above and below the beta transus temperature. From the linear relationships, activation energies for each material in the two phase α+β region (850°C to 1017°C) and in the single phase β field (1017°C to 1200°C) were obtained, as indicated in Table 7.4, using the following relationship:

$$Q_{def} = 2.3\, n'\, R\, S_{av} \tag{7.9}$$

where R is 8.314 $J \cdot mol^{-1} \cdot K^{-1}$ and n' depends on the temperature range and material as indicated in Table 7.2.

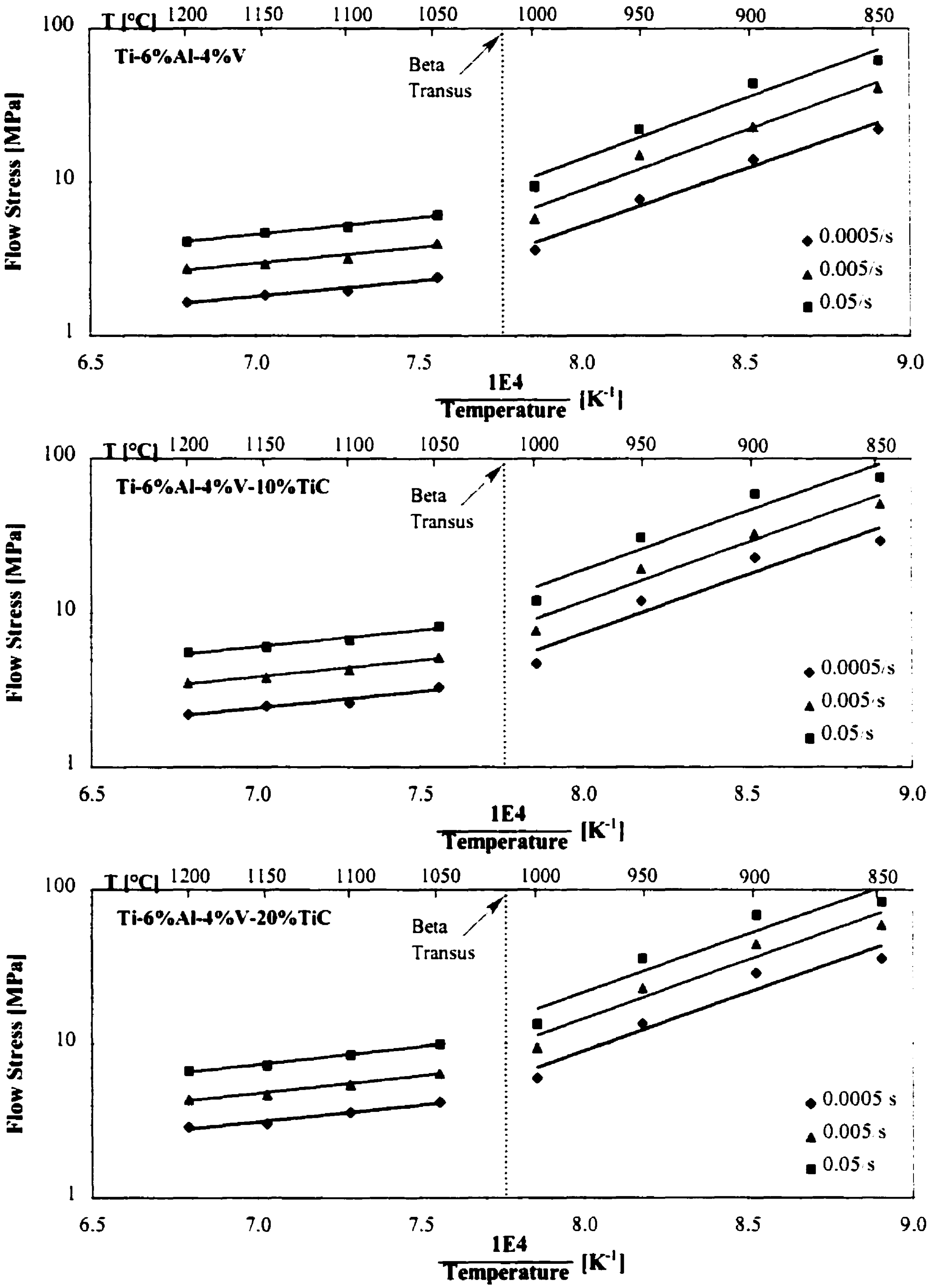

Figure 7.15 Constant strain rate plots of flow stress versus temperature for the titanium-based composites deformed above and below the beta transus temperature.

Table 7.4 – Values for the Activation Energy

Material	Temperature Range °C	Activation Energy Present work kJ·mol^{-1}	Activation Energy Literature kJ·mol^{-1}
Ti-6%Al-4%V (lamellar)	850-1017	668	600-720[271-273]
	1017-1200	190	150-250[271-273]
Ti-6%Al-4%V/10%TiC	850-1017	704	-
	1017-1200	209	-
Ti-6%Al-4%V/20%TiC	850-1017	732	-
	1017-1200	231	-

Although for pure metals the apparent activation energy of flow has frequently been observed to be close to that for self diffusion, deformation in two phase materials has indicated the contrary, with activation energies usually much higher or much lower than that for self diffusion.[272-273] Dyment calculated the activation energy for self diffusion in pure titanium in the alpha phase to be 169 kJ·mol^{-1}.[274] With respect to self-diffusion in the beta phase of pure titanium, Murdock et al.[251,260] calculated a value of 250 kJ·mol^{-1} while Reca et al[274] obtained 152 kJ·mol^{-1}. In the present work, the activation energy in the beta phase region of the titanium alloy was determined to be 190 kJ·mol^{-1} for temperatures between 1050°C and 1200°C. For this alloy, the activation energy for deformation in the β phase was reported by Briottet et al. to be 180 kJ·mol^{-1} for an initial lamellar microstructure, while Malcor and Montheillet reported a value of 150 kJ·mol^{-1} for an initial equiaxed structure.[271-272] The activation energy obtained in this work for deformation at temperatures above the beta transus (190 kJ·mol^{-1}) thus falls within the range (152-250 kJ·mol^{-1}) expected for Ti-6%Al-4%V having an initial lamellar structure (Table 7.4).

Previous work on this alloy has also shown that the activation energy for deformation in the α+β phase region can be substantially higher than that of the individual phases, due to the influence of the transformation of α with temperature (which led to scatter in the data below the beta transus temperature in Fig. 7.15).[272] Briottet et al. developed a model to calculate the activation energy of the α phase since Ti-6%Al-4%V does not exhibit a single phase α region at low temperatures.[272] An activation energy of 220 kJ·mol^{-1} for the α phase was calculated in their work.[272] Bryant in his review of Ti-6%Al-4%V assembled the available data on the alloy and performed an analysis in terms of the Zener-Hollomon parameter.[273] He found an activation energy of 355 kJ·mol^{-1} for deformation in the two phase region at low temperatures (700°C).[273] This value is considerably greater than the activation energies of the alpha or beta phase counterparts. Moreover, at temperatures in the range of 750°C to just below the beta transus, Bryant reported a value of 720 kJ·mol^{-1} while that in work of Malcor and Montheillet was between 600-630 kJ·mol^{-1}.[271,273] Additionally, Braga et al.[275] determined an activation energy of 588 kJ·mol^{-1} for isothermal compression of Ti-6%Al-4%V at temperatures ranging from 800°C to 950°C. These experimental observations support the activation energy value (668 kJ·mol^{-1}) obtained in this work for the temperature range of 850°C to 1000°C.

In the single phase beta region of Ti-6%Al-4%V, the closeness in the values of the activation energy for deformation with that for self diffusion of titanium suggests some similarity in the deformation characteristics of the former with the BCC phase in pure titanium. Although the stacking fault energy values have not been determined for the BCC beta phase of titanium, generally such a crystal structure leads to high stacking fault energy values because of the ease with which cross-slip and climb can occur in such materials.[276] As such, dynamic recovery should occur in the beta phase, but has been difficult to prove because during rapid cooling the beta phase transforms to martensitic alpha and eliminates the deformation substructure. However, Sheppard and Norley found through their hot torsion work that the torque-twist behavior of Ti-6%Al-4%V in the single-phase beta region was indicative of a dynamic recovery deformation process.[276]

In the basal planes of the HCP alpha phase of pure titanium, the reported stacking fault energy value of 300 MJ·m^{-2} suggests that titanium can be characterized as a high stacking fault energy metal in which dynamic recovery can occur in the alpha phase.[276] Although the influence of aluminium and vanadium on the stacking fault energy values has not been studied to the author's knowledge, the formation of a two phase region suggests that a different deformation mechanism may be possible. In the two phase ($\alpha+\beta$) region, activation energies considerably greater than those for self-diffusion indicate that deformation is more difficult below the beta transus. Moreover, the high activation energy in the $\alpha+\beta$ region has led several authors[274-275] to suggest that dynamic recrystallization is occurring during hot deformation. The hot torsion work of Sheppard and Norley coupled with their microstructural results has indicated that both dynamic recovery and dynamic recrystallization occur in Ti-6%Al-4%V during deformation in the two-phase region.[276]

Finally, there was an increase in the activation energy of deformation with increasing TiC volume fraction for regions both above and below the beta transus temperature of the Ti-6%Al-4%V alloy. This may be attributed to an increase in dislocation density occurring in the composite materials.

7.3 Microstructural Evolution

Besides enhanced densification, deformation processing can control the microstructure and therefore properties by means of the deformation temperature, strain and strain rate. The influence of the deformation temperature on the matrix alloy microstructure is shown in Figure 7.16. Deformation at temperatures above 1017°C occurs in the single-phase β region and below 1017°C in the two-phase (α+β) region. Above the beta transus, transformation of the deformed beta grains upon slow cooling produces α having a lamellar morphology, as observed in Figure 7.16 for temperatures of 1050°C and greater. The effect of deformation temperature for hot working above the beta transus appears to be negligible.

The alternative microstructure for this alloy is the equiaxed structure, which can only be formed by work hardening the lamellar structure (plastically deforming below the beta transus) followed by recrystallization. As shown in Figure 7.16, deformation in the two phase (α+β) region can produce not only a refinement in the structure, but also a change in the microstructural features depending on the hot working temperature. These microstructural changes observed during processing below the beta transus can be related to the morphology and the amount of the primary alpha phase. The primary alpha morphology depends on the extent of working performed below the beta transus temperature and can vary from elongated plates in lightly worked material to equiaxed grains in heavily worked material. According to equation 7.7, the amount of primary alpha increases exponentially with decreasing deformation temperature. During isothermal deformation at 1000°C, 950°C and 850°C, the volume fraction of primary alpha in the microstructure of the Ti-6%Al-4%V alloy consists of approximately 12%, 40% and 70% alpha, respectively.

Deforming just below the beta transus temperature (1000°C) produced a bimodal microstructure consisting of lamellar alpha and what appears to be equiaxed alpha. Hot working at temperatures below 950°C produced a microstructure consisting of distorted (wavy) and elongated lamellar alpha platelets. Moreover, these deformed alpha platelets were found to break up increasingly with decreasing deformation temperature, as shown in Figure 7.17. The bending, distortion, shearing and break up of the lamellar structure is indicative of work hardening, and heat treatment of these worked microstructures could lead to recrystallization. The higher degree of distortion at the lower temperatures (*i.e.* 850°C as compared to 950°C) may be due to strain accumulation in view of the decrease in recovery with temperature.

The formation of equiaxed alpha at 1000°C may be due to a higher strain concentration in the alpha phase in the vicinity of the beta transus temperature as compared to the lower deformation temperatures. A deformation strain (ε_d) of 0.5 on the volume fraction of primary alpha at 1000°C appears to achieve sufficient working of this phase to cause it to recrystallization at the deformation temperature. During slow cooling after deformation, the prior beta volume fraction transforms to lamellar alpha, giving the bimodal microstructure. At lower temperatures (below 950°C), an equivalent deformation strain (*i.e.* 0.5) applied to the microstructure is insufficient to cause recrystallization of the primary alpha phase perhaps due to this strain being distributed over a greater volume fraction of alpha. Hence the primary lamellar alpha structure is deformed in the working direction and the prior beta fraction transforms to undeformed lamellar alpha during slow cooling. Thus, the microstructural differences observed with decreasing deformation temperature below the beta transus are a direct consequence of the recrystallization kinetics, which depend on both the amount of deformation and the recrystallization time and temperature. The microstructure at 1000°C, having the higher recrystallization kinetics (*i.e.* higher temperature and greater amount of deformation in the primary alpha), exhibits regions of equiaxed alpha, while at 950°C and 850°C, the slower recrystallization kinetics (*i.e.* the lower deformation temperatures and higher volume fraction of primary alpha) results in mostly a lamellar structure. (A few regions of equiaxed primary alpha can be seen in the microstructure of the specimen deformed at 950°C, as shown in Fig. 7.16.)

The effect of strain rate on microstructural modification of the Ti-6%Al-4%V alloy is shown in Figures 7.18 and 7.19 for temperatures above and below the beta transus, respectively. In the single-phase beta region, the effect of increasing the strain rate on the microstructure appears to be negligible. This is supported by the low strain rate sensitivity of the beta phase as mentioned in the previous section of this chapter. For the range of strain rates investigated in this work, the strain rate effect in the two phase (α+β) region appears to be an increase in the distortion of the lamellar structure and a reduction (or elimination) in the amount of equiaxed primary alpha. Basically with decreasing deformation strain rate, the kinetics for recrystallization improve due to the greater time at temperature. This may promote recrystallization in the regions of highly deformed primary alpha during deformation at 950°C for lower strain rates (0.0005 s^{-1}). At the higher strain rates, substantial deformation of the primary alpha occurs (distorted lamellae). However due to the insufficient time at temperature the structure does not appear to recrystallize during hot working.

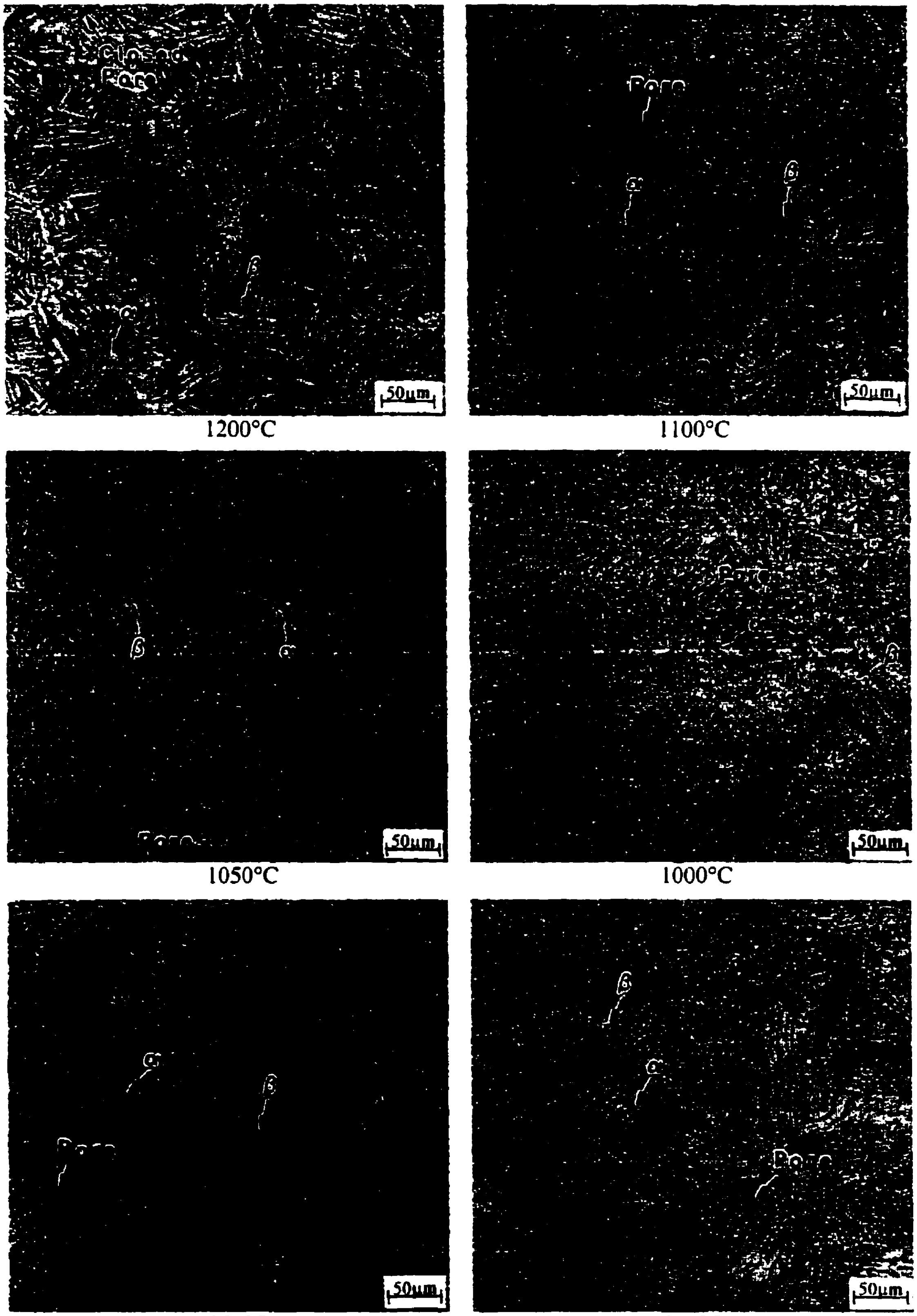

1200°C 1100°C

1050°C 1000°C

950°C 850°C

Figure 7.16 Optical micrographs of etched Ti-6%Al-4%V deformed at a strain rate of 0.0005 s^{-1} to a deformation strain (ε_d) of 0.5.

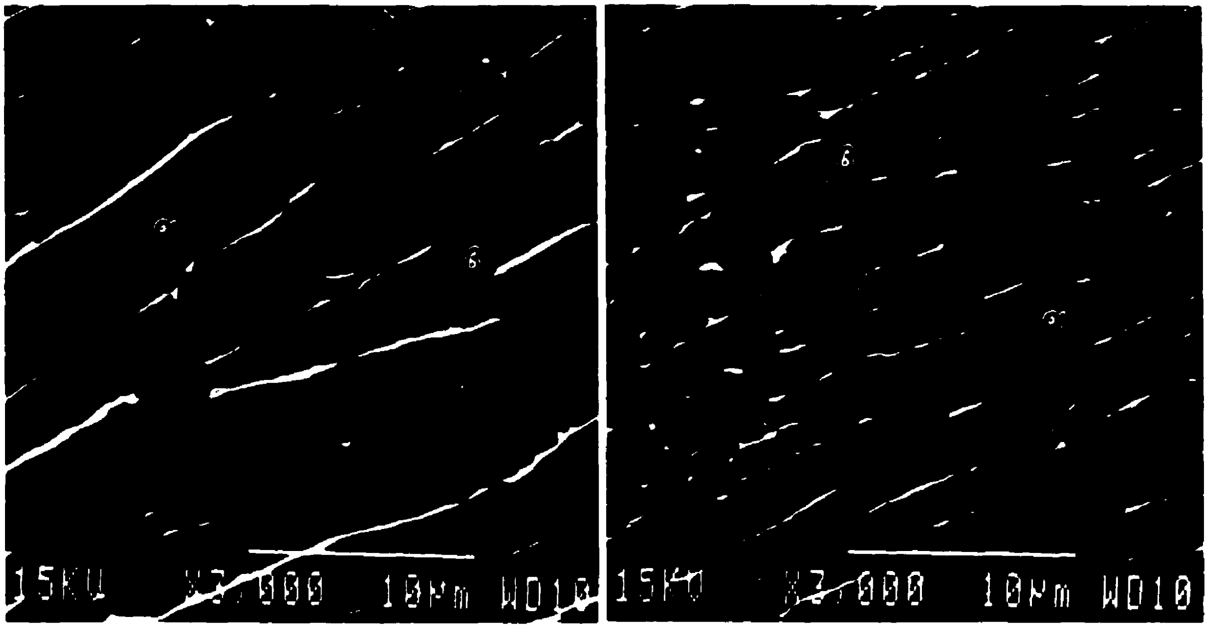

950°C 850°C

Figure 7.17 SEM photographs showing the effect of deformation temperature on the beta phase structure for Ti-6%Al-4%V deformed at 0.0005 s^{-1} to a deformation strain (ε_d) of 0.5.

In the composite materials, the presence of TiC particles can lead to inhomogeneities in the straining of the matrix. During working, the dislocations generated at the interface between the non-deformable particles and the deforming matrix can give rise to the formation of zones of relatively high dislocation density. The size and shape of the deformation zones are related to reinforcement size and shape, with angular morphologies (such as the TiC particles) leading to enhanced dislocation densities in the region closest to their stress-concentrating corners.[233] Also, since the matrix strain around the rigid particles is accommodated by diffusive plastic relaxation, the size of the deformation zone will decrease with increasing deformation temperature and decreasing strain rate. In other words, regions in the proximity of the particles lead to relatively high dislocation densities, which may recrystallize at the deformation temperature.

Also, during deformation of the composites, reaction of the TiC particles with the Ti-6%Al-4%V matrix initially leads to carbon dissolution into the titanium alloy lattice. Since carbon is an alpha stabilizer, the beta transus temperature may increase slightly. In the titanium-carbon phase diagram, the addition of approximately 0.2 wt.% carbon in titanium appears to increase the beta transus temperature by approximately 40°C, as shown in Figure 2.2. Assuming a similar effect of carbon in Ti-6%Al-4%V, the beta transus temperature can be as high as 1060°C for the TiC reinforced titanium alloy composites.

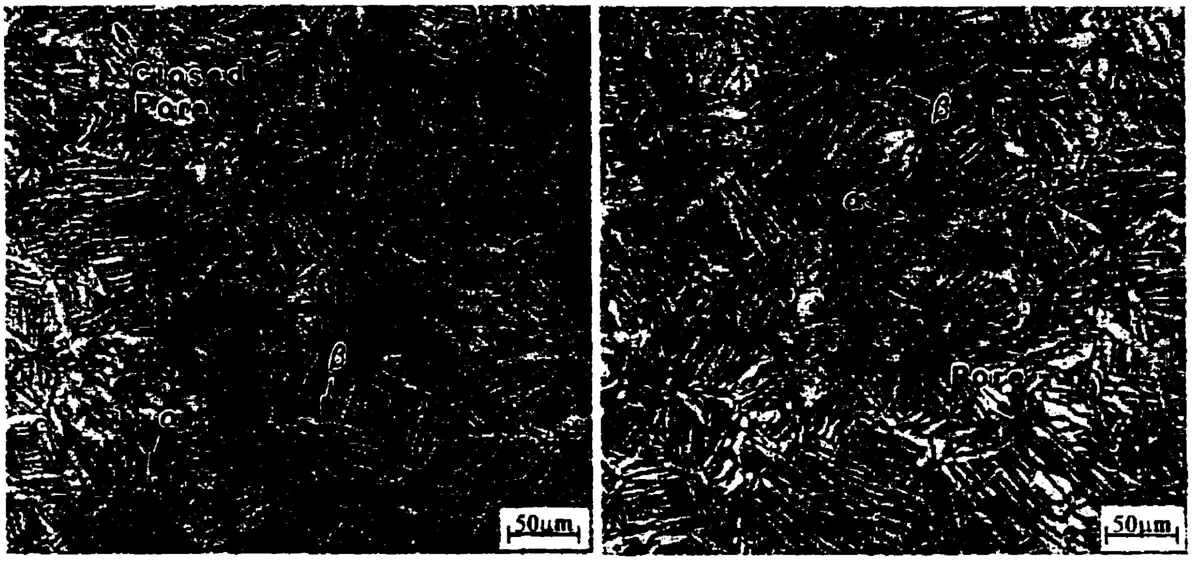

0.0005s^{-1} 0.05s^{-1}

Figure 7.18 Optical micrographs of etched Ti-6%Al-4%V deformed at 1200°C (above the beta transus temperature) to a deformation strain (ε_d) of 0.5 and showing the effect of increasing strain rate.

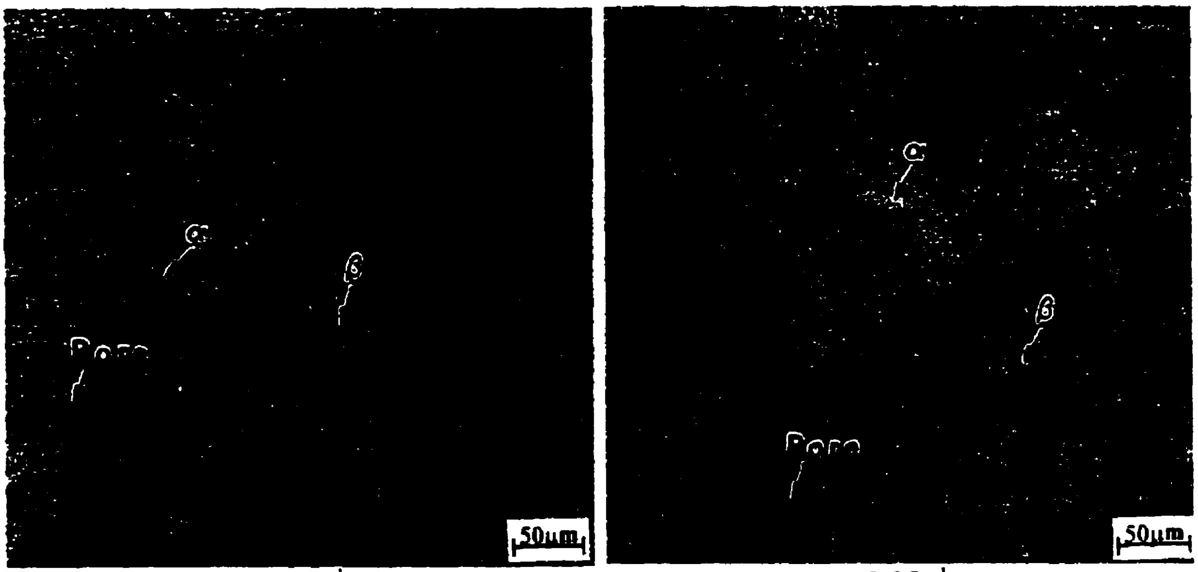

0.0005s^{-1} 0.05s^{-1}

Figure 7.19 Optical micrographs of etched Ti-6%Al-4%V deformed at 950°C (below the beta transus temperature) to a deformation strain (ε_d) of 0.5 and showing the effect of increasing strain rate.

Observation of the effect of deformation temperature on the microstructure of the 10 vol.% and 20 vol.% TiC particle reinforced Ti-6%Al-4%V composites is shown in Figure 7.20 and 7.21, respectively. The incorporation of TiC particles appears to provide an addition means of modifying the matrix microstructure. At temperatures clearly in the single-phase beta region (*i.e.* 1200 °C to 1100°C), the matrix microstructure consists of lamellar alpha, similar to the unreinforced matrix. However, most of the alpha lamellae are not in the form of colonies in which several alpha platelets have nearly identical orientations. Lamellar colony formation is a result of alpha transforming from beta by nucleation and growth along one set of preferred crystallographic planes of the prior beta grains. It appears that the TiC particles provide an additional interface for alpha nucleation sites most likely due to the influence of carbon as an alpha stabilizer. Consequently, the matrix microstructure for the 10 vol.% TiC composites, as shown in Figure 7.20, is basket-weave like in appearance, suggesting that the alpha phase transformed along several sets of preferred crystallographic planes. For the 20 vol.% TiC composites, a further increase in the number of nucleation sites results in alpha platelets forming with very little preferred orientation, as shown in Figure 7.21. Besides this, the overall effect in the presence of TiC particles is a refinement of the platelet microstructure as compared to the unreinforced alloy processed under similar deformation conditions. This occurs because the TiC particles restrict the growth of the alpha platelets as discussed previously in the microstructural results for sintering.

For temperatures close to the beta transus of the unreinforced titanium alloy (*i.e.* 1017°C), the microstructure consists of equiaxed and platelet alpha morphologies. In the case of the 10 vol.% TiC reinforced composites, the matrix microstructure for material deformed at 1050°C should be similar to that at 1100°C or 1200°C. However, there appears to be an overall refinement in microstructure at 1050°C, as well as the presence of equiaxed alpha as shown in Figure 7.20. The formation of equiaxed alpha at 1050°C can be due to an increase in the beta transus temperature (resulting from carbon dissolution in the matrix) as well as enhanced dislocation density in the presence of reinforcement particles. As determined in the neutron diffraction section of the previous chapter, interaction between the TiC particles and the titanium alloy initially leads to carbon dissolution into the Ti-6%Al-4%V lattice until saturation occurs (at which point the Ti_2C interfacial phase begins to form). This carbon dissolution can occur during heating to the deformation temperature. Hence heating of the TiC_p reinforced Ti-6%Al-4%V compact may dissolve carbon in the titanium alloy lattice, which can cause an increase in the beta transus temperature (above 1017°C). Thus, the complete transformation of primary alpha to beta at 1050°C may not occur if the amount of carbon dissolved increases the beta transus temperature to above the deformation temperature. Alternatively, if the beta transus temperature prior to the start of deformation is below the hot working temperature, forced interaction of the reinforcement and matrix phases during compression may cause the transus temperature to increase as additional carbon dissolves in the titanium alloy lattice, until saturation occurs. Moreover, saturation of the beta phase occurs at 0.2 wt.% carbon whereas alpha titanium can dissolve up to 0.4 wt.% carbon. Hence, transformation of alpha to beta during heating may reject some carbon into the remaining alpha phase, stabilizing it further. The persistence of primary alpha during deformation at 1050°C may cause recrystallization to occur, especially in the presence of TiC particles, which can cause strain inhomogeneities in the matrix and the formation of deformation zones of high dislocation density. Hence the matrix microstructure of the 10 vol.% TiC composite appears to have more equiaxed alpha than the unreinforced alloy processed at 1000°C (compare Fig. 7.20 with 7.16). Also, the platelet alpha morphology of the matrix in the 10 vol.% TiC composite (Fig. 7.20) is not oriented in the form of lamellar colonies, as the matrix of the unreinforced titanium alloy (Fig. 7.16).

The matrix microstructure for composites hot worked at 1000°C reveals the presence of finer equiaxed and platelet alpha morphologies, as shown in Figure 7.20. This deformation temperature is below the beta transus even in the absence of carbon dissolution into the titanium alloy lattice. Hence some primary alpha is present during deformation at 1000°C and with carbon dissolution the amount of primary alpha will increase. However, during heating to this slightly lower deformation temperature, the amount of carbon dissolution into the titanium alloy lattice will be lower and thus increases in the beta transus temperature may not be as marked. Nonetheless, interaction of the TiC particles and the matrix during deformation may lead to some increases in the carbon content of the titanium alloy lattice and the beta transus temperature. As a consequence, it is possible that some of the beta titanium transforms to alpha titanium during deformation and results in the refined equiaxed and platelet structure observed. Previous work on forging of Ti-6%Al-4%V indicates that transformation of beta to alpha during deformation produces equiaxed alpha.[277] The platelet alpha is then just a transformation product of the remaining beta during slow cooling. The significance of TiC particles in the formation of the platelet alpha morphology is basically increased nucleation sites that inhibit preferred crystallographic orientation, thereby preventing colony formation. Additionally, the TiC particles restrict the growth of the alpha plates contributing further to the refinement effect.

For composites containing 20 vol.% TiC reinforcement particles, the matrix microstructure at 1050°C is similar to that of the 10 vol.% TiC material (compare Figs. 7.21 and 7.20). However, hot working the 20 vol.% TiC composites at 1000°C reveals mostly distorted alpha platelets with little equiaxed alpha, as shown in Figure 7.21.

As mentioned previously, since 1000°C is below the beta transus temperature of the unreinforced alloy, the matrix microstructure consists of mostly beta with some primary alpha. In the presence of TiC particles, the beta transus temperature may increase on account of carbon dissolution occurring either during heating to the deformation temperature or during hot working. However, in the presence of a greater carbon source (*i.e.* 20 vol.% versus 10 vol.% TiC particles), carbon dissolution during heating is likely to be greater. As such, the beta transus temperature prior to deforming the 20 vol.% TiC composite can be higher as well as the amount of primary alpha. As compared to the 10 vol.% TiC composite, the greater volume fraction of primary alpha in the microstructure of the 20 vol.% TiC composite may have resulted in lower recrystallization kinetics, giving the platelet structure in the latter material.

At temperatures below 950°C, the matrix microstructure of both the 10 vol.% and 20 vol.% TiC reinforced composites show a highly distorted lamellar alpha structure, similar to that observed for the unreinforced titanium alloy. Optically, the presence of TiC particles appears to have little influence on the microstructure of Ti-6%Al-4%V matrix. However, the microhardness values for the titanium alloy, as given in Table 7.5, suggest that the dislocation density increases in the matrix with increasing TiC volume fraction.

The effect of strain rate on microstructural modification of the matrix in the TiC reinforced composites is shown in Figures 7.22 and 7.23 for temperatures above and below the beta transus temperature, respectively. As for the unreinforced titanium alloy, the matrix microstructure of the composite appears to be unaffected by an increase in the strain rate above the beta transus. However, even in the two phase ($\alpha+\beta$) region there appears to be no change in matrix microstructure of the reinforced composite material. This can be attributed to the lower strain rate sensitivity of the composite material as determined previously in this chapter and as indicated by the microhardness values given in Table 7.5.

Table 7.5 – Microhardness Values of the Titanium Alloy Matrix

Material	Strain Rate of 0.0005 s^{-1}		Strain Rate of 0.05 s^{-1}	
	950°C [kg·mm^{-2}]	850°C [kg·mm^{-2}]	950°C [kg·mm^{-2}]	850°C [kg·mm^{-2}]
Ti-6%Al-4%V	345	396	388	433
Ti-6%Al-4%V/10%TiC	392	429	404	438
Ti-6%Al-4%V/20%TiC	428	447	431	449

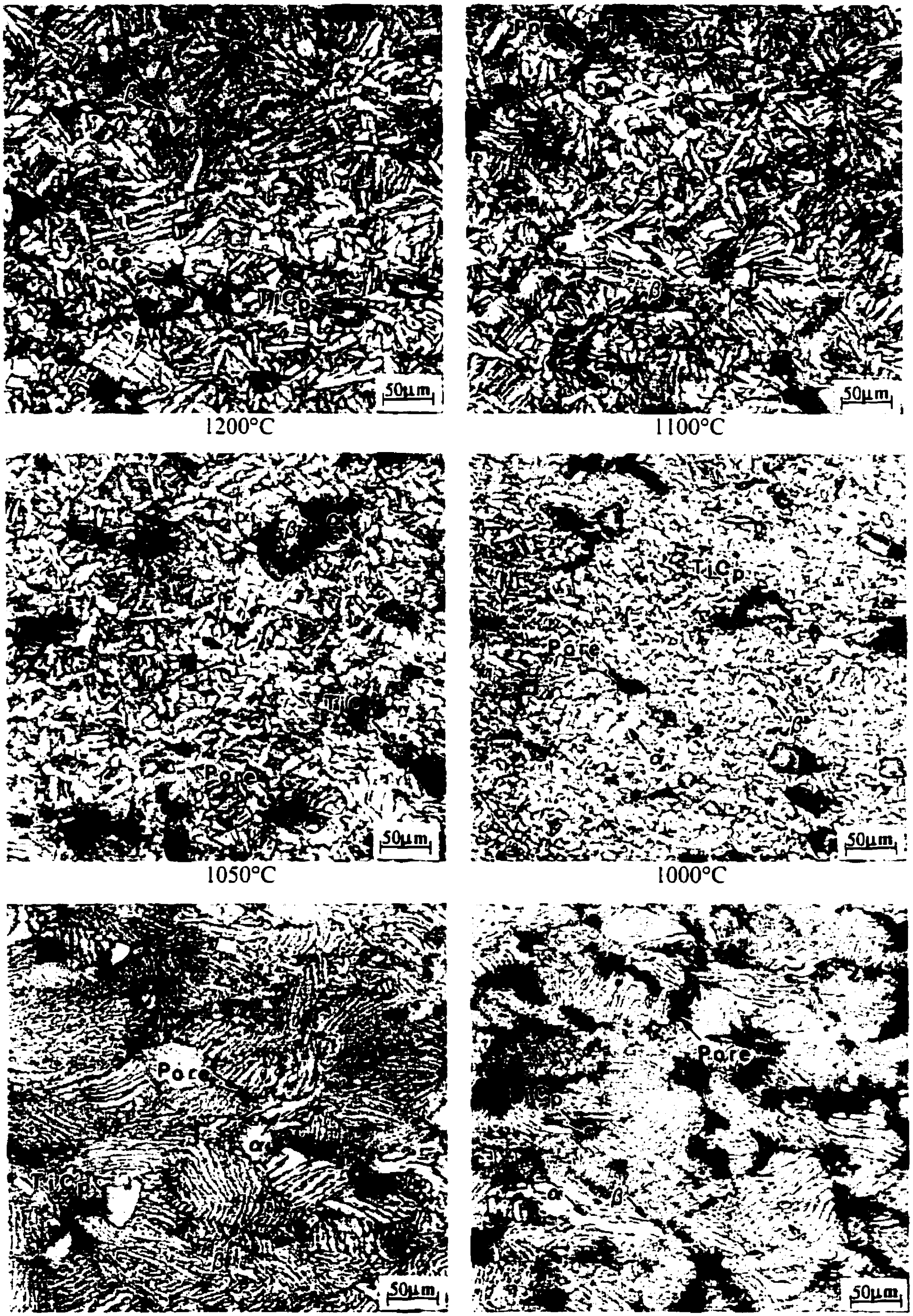

1200°C 1100°C

1050°C 1000°C

950°C 850°C

Figure 7.20 Optical micrographs of etched 10 vol.% TiC_p reinforced Ti-6%Al-4%V deformed at a strain rate of 0.0005 s^{-1} to a deformation strain (ε_d) of 0.5.

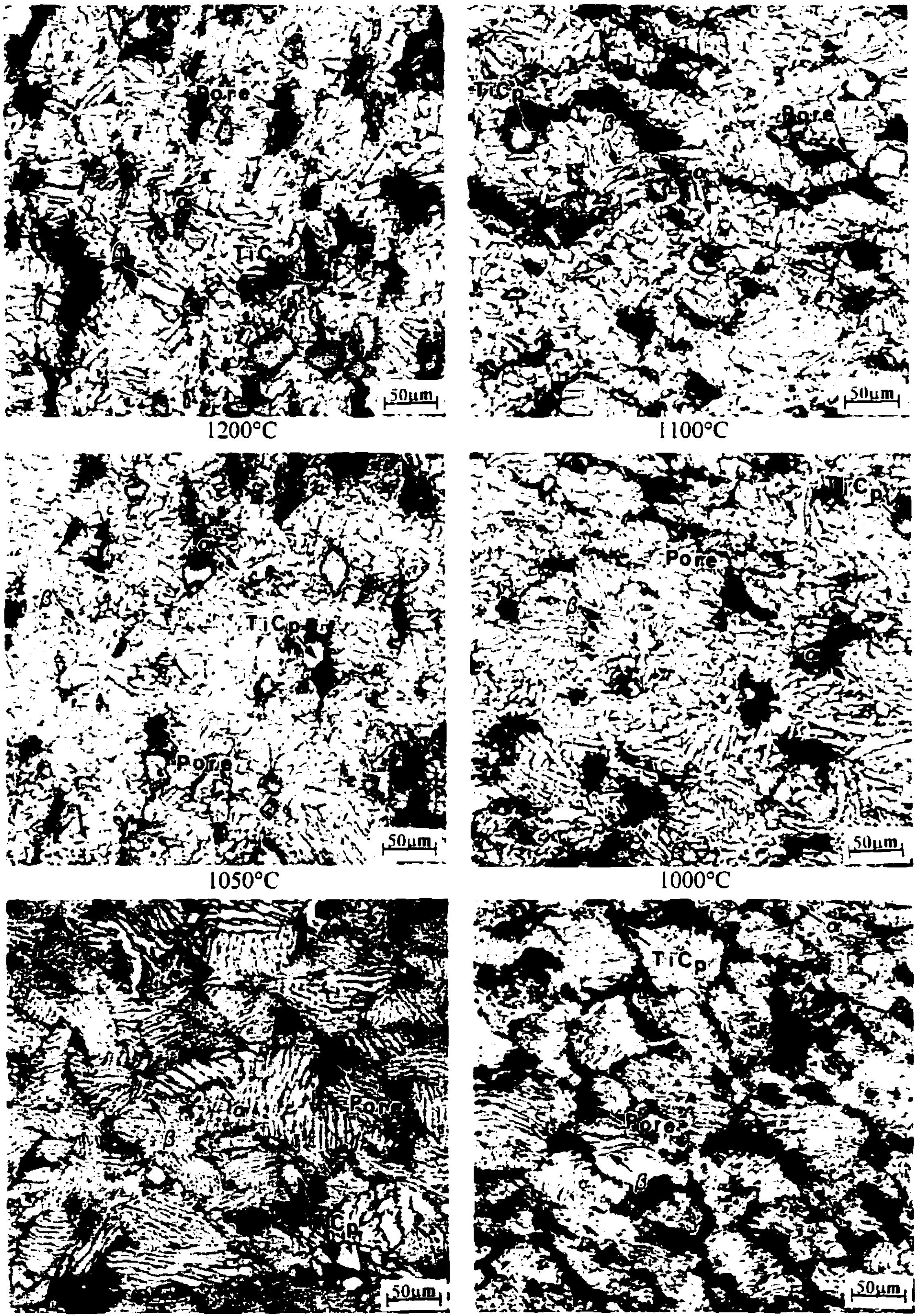

1200°C 1100°C

1050°C 1000°C

950°C 850°C

Figure 7.21 Optical micrographs of etched 20 vol.% TiC_p reinforced Ti-6%Al-4%V deformed at a strain rate of 0.0005 s^{-1} to a deformation strain (ε_d) of 0.5.

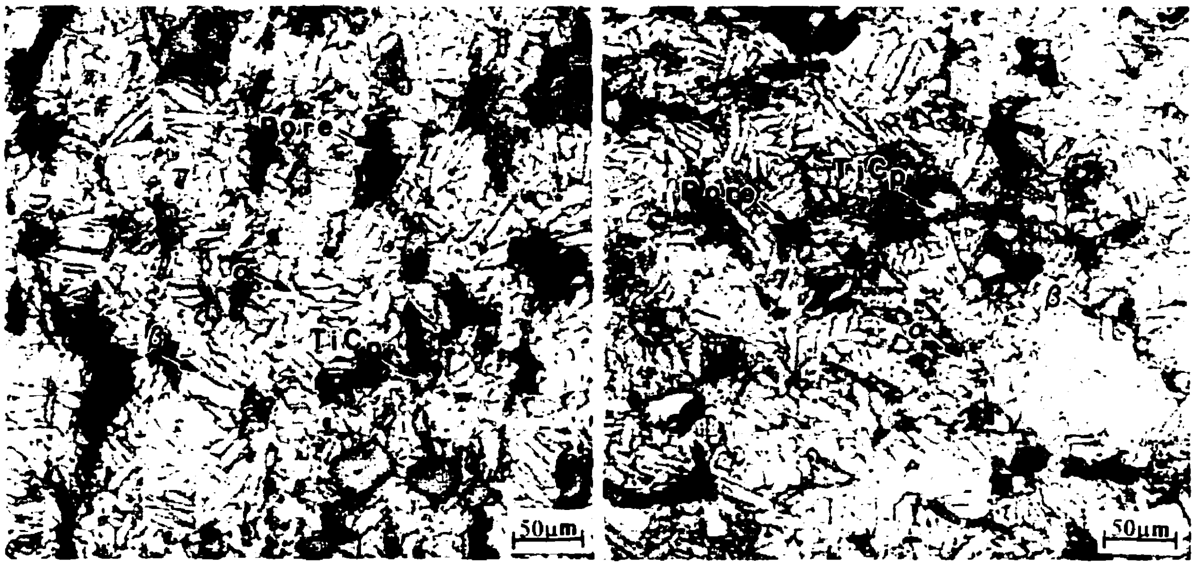

0.0005s^{-1} 0.05s^{-1}

Figure 7.22 Optical micrographs of etched 20 vol.% TiC$_p$ reinforced Ti-6%Al-4%V deformed at 1200°C (above the beta transus temperature) to a deformation strain (ε_d) of 0.5 and showing the effect of increasing strain rate.

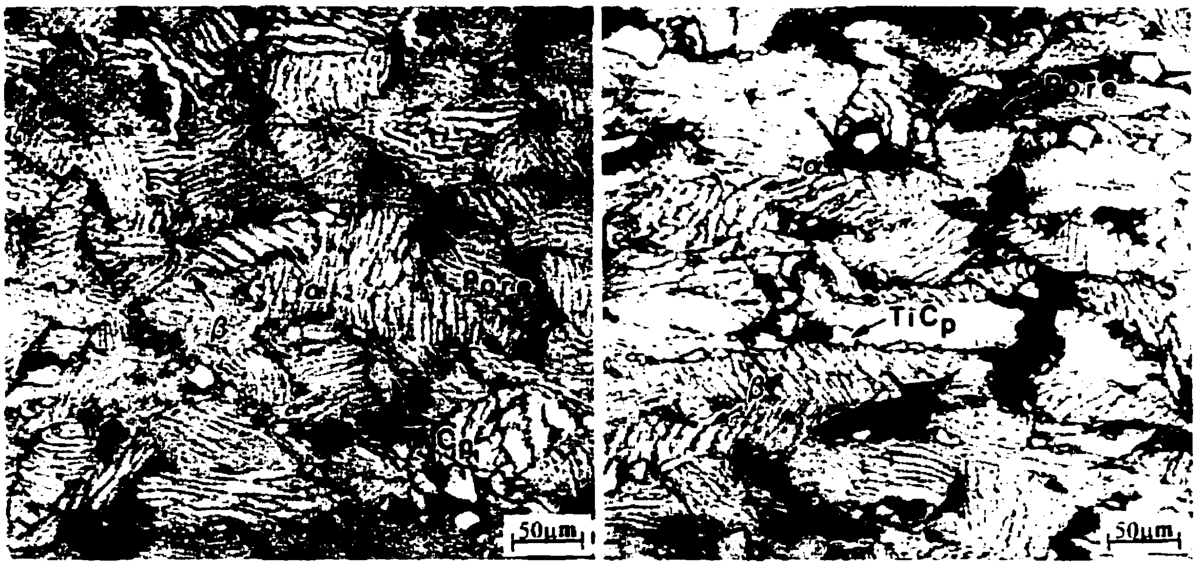

0.0005s^{-1} 0.05s^{-1}

Figure 7.23 Optical micrographs of etched 20 vol.% TiC$_p$ reinforced Ti-6%Al-4%V deformed at 950°C (below the beta transus temperature) to a deformation strain (ε_d) of 0.5 and showing the effect of increasing strain rate.

7.4 Interfacial Analysis

Similar to the interfacial examination results obtained in the previous chapter, only low voltage electron microscopy on the *Hitachi S-4500* cold field emission gun SEM was effective in revealing the interfacial phase region in TiC particulate reinforced titanium composites processed by hot working.

7.4.1 Low Voltage Field Emission Gun SEM

Figure 7.24 shows the interfacial region in the composites processed by hot compression working at a strain rate of 0.0005 s^{-1} to a total applied strain of 0.8 at a temperature of 1000°C and 1200°C. The thickness of the interfacial layer appears to increase slightly with increasing deformation temperature, being approximately 0.24 µm at 1000°C and 0.31 µm at 1200°C, as depicted in Figure 7.24. Compared to the interfacial region formed in the sintered composites (Fig. 6.19), the boundary layer formed by deformation processing is thinner (approximately 0.5 µm by sintering at 1100°C for 4 hours) yet clearly distinct.

During sintering, void closure as well as the formation of the interfacial region occurs by diffusion. Hence regions in which the reinforcement and matrix are initially in contact (from compaction) begin to react while regions separated by voids will densify prior to reacting. This results in the formation of a diffuse and uneven interfacial region in the composites formed by sintering, as shown in Figure 6.19. In the case of deformation processing, the temperatures and holding times are considerably lower than for sintering, thereby decreasing the diffusion kinetics. However, the applied stress at the deformation temperature causes rapid closure of the voids by plastic flow of the matrix phase around the TiC reinforcement particles. The forced contact of the matrix phase around the reinforcement particles forms a uniform reaction layer on the periphery of the TiC phase, as shown in Figure 7.24.

Chemical composition analysis for carbon across the interfacial reaction region was performed on the composites processed by hot working using energy dispersive x-ray spectroscopy. However, due to the smaller size of the interfacial boundary layer in the deformed composites, as compared to that formed during sintering, the results from this investigation gave inconclusive profiles for carbon concentration from the TiC reinforcement particles to the titanium alloy matrix phase.

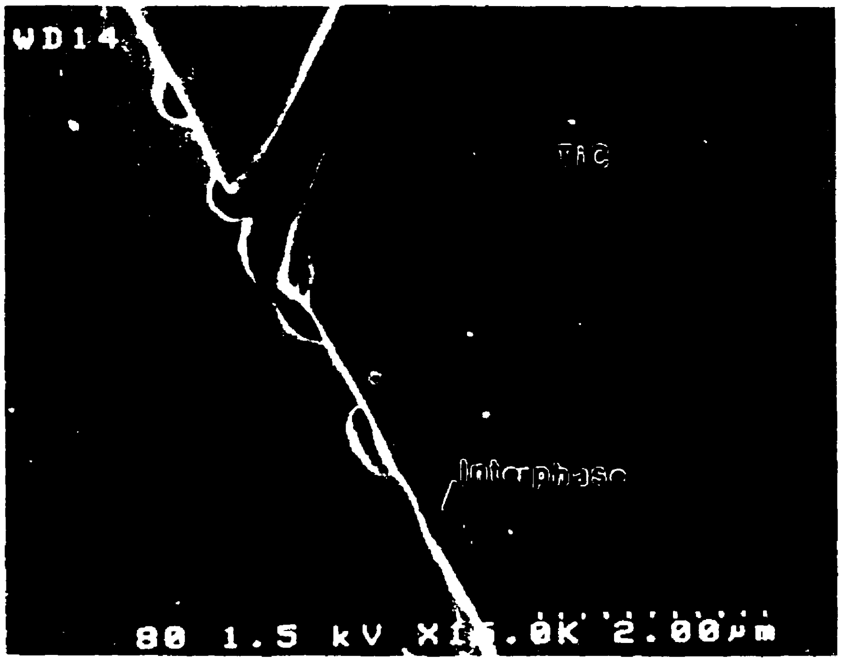

(a) 1000°C, 0.8 applied strain and 0.0005 s^{-1}

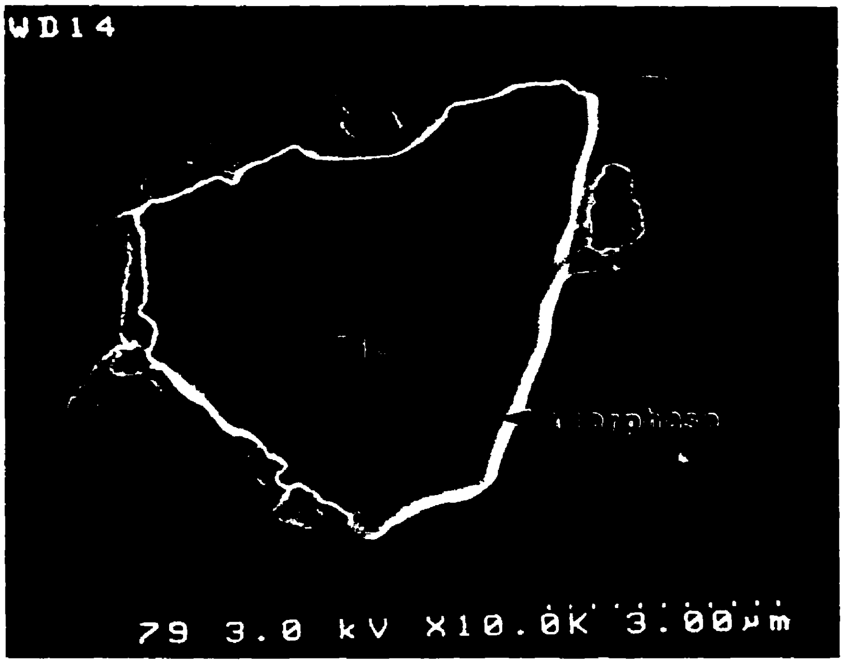

(b) 1200°C, 0.8 applied strain and 0.0005 s^{-1}

Figure 7.24 Interfacial reaction analysis using low voltage imaging on a FEGSEM equipped with a through-the-lens detector for 20 vol.% TiC_p reinforced Ti-6%Al-4%V composite processed by hot working.

7.4.2 Neutron Diffraction Examination

For the composites processed by hot working, the nature of the interfacial reaction between the titanium alloy matrix and the TiC reinforcement particles was investigated using neutron diffractometry. This was performed by obtaining the neutron diffraction pattern for the deformed composite material at a temperature in the single-phase beta region. Figure 7.25 illustrates the neutron diffraction pattern obtained at 1100°C for the as-deformed composites processed at a strain rate 0.0005 s^{-1} to an applied strain of 0.8 at 1000°C and 1200°C.

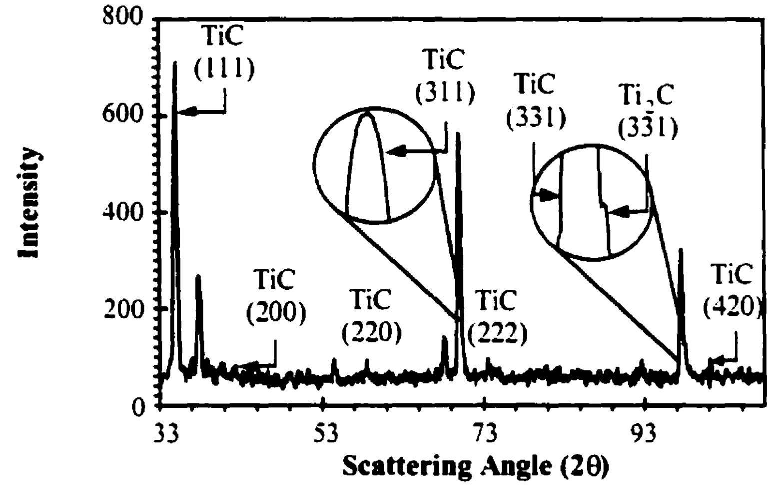

(a) As-deformed 1000°C (Spectrum at 1100°C, 0 hours)

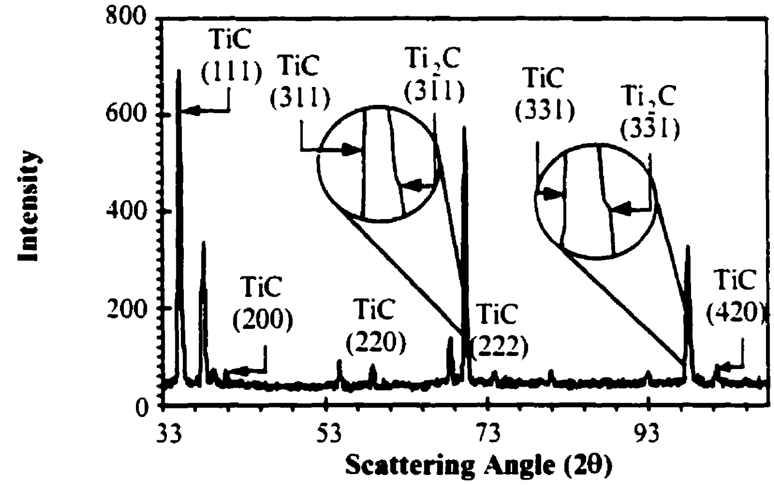

(b) As-deformed 1200°C (Spectrum at 1100°C, 0 hours)

Figure 7.25 Variation in the diffraction peaks of TiC and β-titanium phases for the 20 vol.% TiC particulate reinforced Ti-6%Al-4%V composite processed by hot working to an applied strain of 0.8 at a strain rate of 0.0005 s^{-1}. (Unlabeled peaks are the β phase of the Ti-6%Al-4%V alloy.)

For the diffraction patterns obtained, the various phases in the as-deformed composites were identified. Besides β-titanium and TiC, a small volume fraction of Ti_2C was present in the titanium alloy composites. Comparing the patterns illustrated in Figure 7.25, it appears that the amount of Ti_2C in the composite material increases slightly with deformation temperature. The volume fraction of Ti_2C was determined to be approximately 0.9%, 1.7% and 3.2% for the composites processed at 850°C, 1000°C and 1200°C, respectively. This is consistent with the FEGSEM work in which a smaller reaction layer thickness was observed for composite material deformed at 1000°C as compared to that processed at 1200°C, as illustrated in Figure 7.24.

Figure 7.26 illustrates the difference in the amount of Ti_2C present for composite material processed to a similar density but by different processing techniques (*i.e.* sintering versus deformation processing). Considering that the density of the as-deformed composite processed at 1000°C to an applied strain of 0.8 is only slightly greater than that of material sintered at 1300°C for 4 hours, the diffraction patterns reveals a considerable difference in the intensity (or volume fraction) of the Ti_2C phase. The volume fraction of Ti_2C for the composite material sintered at 1300°C for 4 hours is approximately 13.5% (Fig. 6.62), which is substantially greater than material deformed at 1200°C to an applied strain of 0.8.

The effect of heat treatment at 1100°C on the growth of the Ti_2C phase in the as-deformed composites processed at 1000°C and 1200°C is illustrated in Figures 7.27 and 7.28, respectively. Within eight hours of holding at 1100°C, the composites deformed at 1000°C and 1200°C contained nearly 12 vol.% Ti_2C and 16 vol.% Ti_2C, respectively. The faster rate of interfacial formation during heat treatment of the as-deformed composites at 1100°C is most probably due to the higher starting density (*i.e.* the initial relative density is 67% for sintering at 1100°C as opposed to 94% and 99% for the composites deformed at 1100°C and 1200°C, respectively). The significance of this heat treatment analysis will depend on the influence of the interfacial phase on the properties of the composites processed by hot working. Essentially, the thickness of the interfacial reaction region can be varied by heat treating the as-deformed composite material. The interfacial thickness, as well as processing conditions, giving the optimal mechanical properties can then be determined for the titanium-based composites.

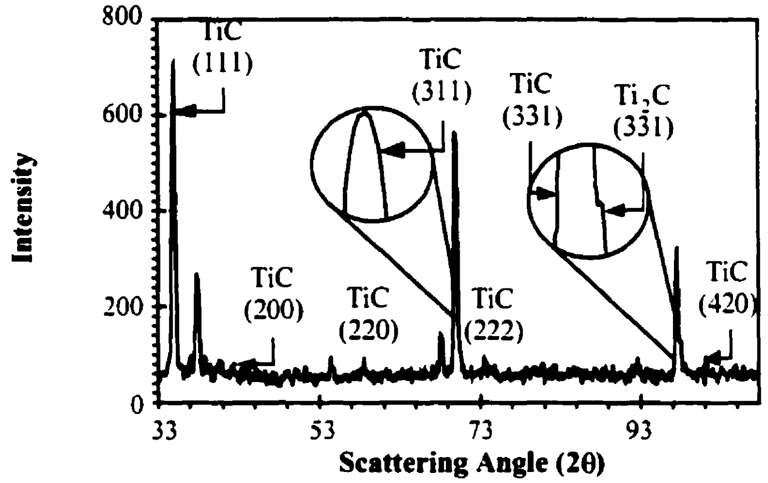

(a) As-deformed 1000°C, 0.8 applied strain, 0.0005 s^{-1}
(Spectrum at 1100°C, 0 hours)
94% relative density, 1.7 Vol.% Ti_2C

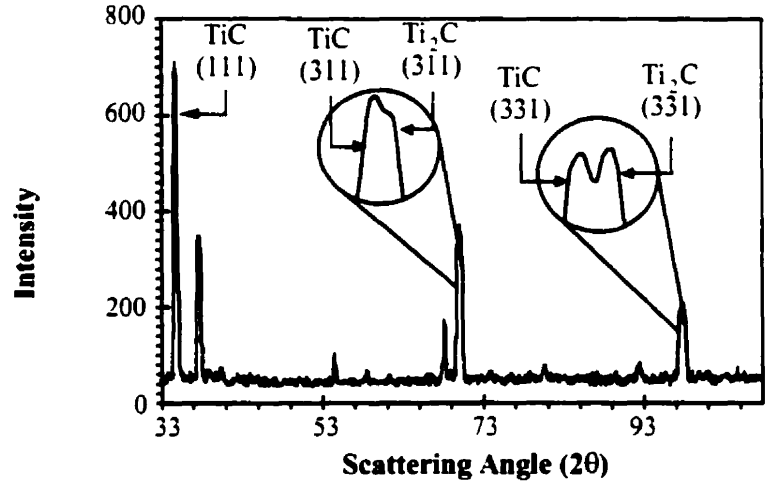

(b) Sintered 1300°C, 4 hours
(Spectrum at 1100°C, 0 hours)
90% relative density, 13.5 Vol.% Ti_2C

Figure 7.26 Comparison of the diffraction pattern for the 20 vol.% TiC particulate reinforced Ti-6%Al-4%V composite processed by sintering at 1300°C for 4 hours with hot working at 1000°C to an applied strain of 0.8 at a strain rate of 0.0005 s^{-1}. (Unlabeled peaks are the β phase of the Ti-6%Al-4%V alloy.)

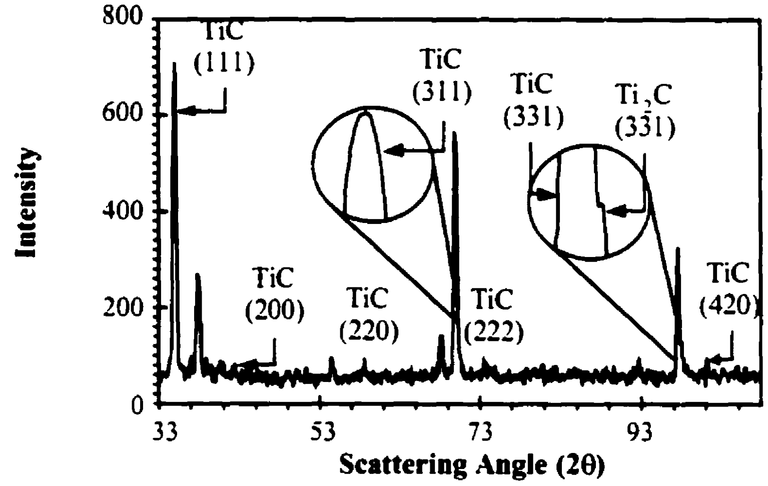

(a) As-deformed 1000°C, 0.8 applied strain, 0.0005 s^{-1}
(Spectrum at 1100°C, 0 hours)

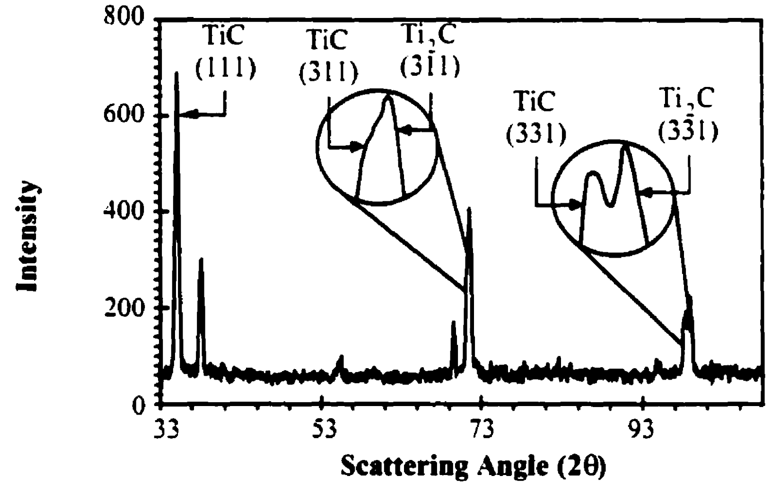

(b) Heat treatment of deformation composite material
(Spectrum at 1100°C, 8 hours)

Figure 7.27 Variation in the diffraction peaks of TiC and β-titanium phases with heat treatment of the 20 vol.% TiC particulate reinforced Ti-6%Al-4%V composite processed by hot working at 1000°C to an applied strain of 0.8 at a strain rate of 0.0005 s^{-1}. (Unlabeled peaks are the β phase of the Ti-6%Al-4%V alloy.)

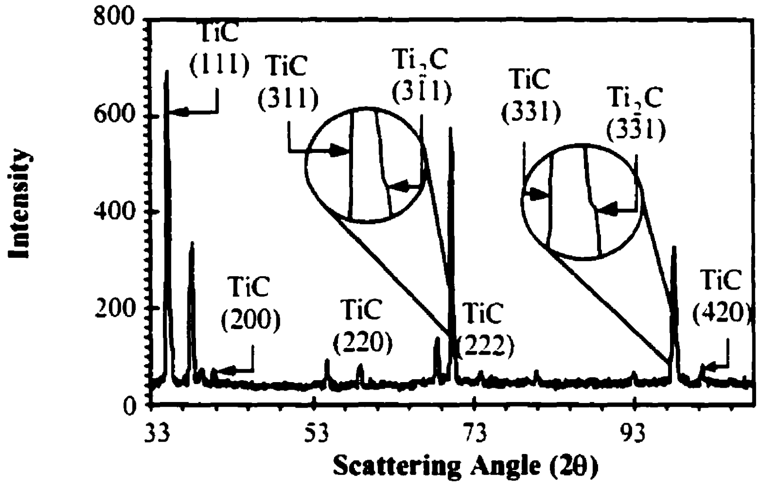

(a) As-deformed 1200°C, 0.8 applied strain, 0.0005 s^{-1} (Spectrum at 1100°C, 0 hours)

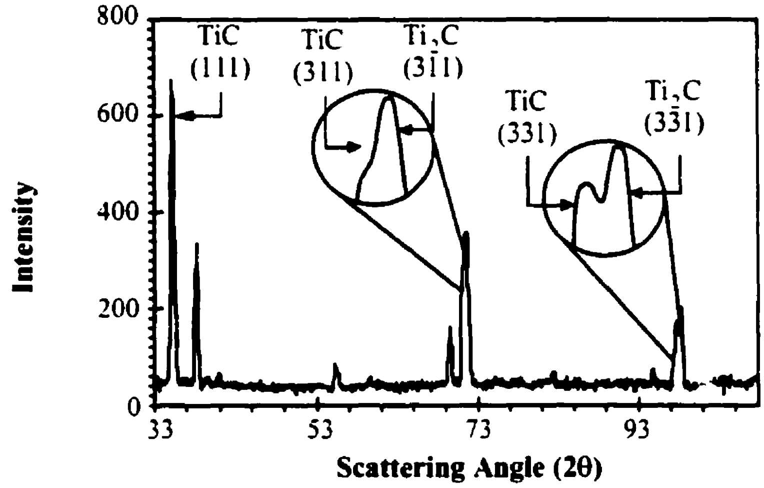

(b) Heat treatment of deformation composite material (Spectrum at 1100°C, 8 hours)

Figure 7.28 Variation in the diffraction peaks of TiC and β-titanium phases with heat treatment of the 20 vol.% TiC particulate reinforced Ti-6%Al-4%V composite processed by hot working at 1200°C to an applied strain of 0.8 at a strain rate of 0.0005 s^{-1}. (Unlabeled peaks are the β phase of the Ti-6%Al-4%V alloy.)

7.5 Mechanical Property Measurement

The tensile properties of the composites processed by hot working were evaluated using shear punch testing. Figure 7.29 shows the variation in the yield (0.1% proof stress) and tensile strengths of the various composites with increasing deformation temperature. For all temperatures, the yield and tensile strengths of the TiC reinforced composites were superior to those of the unreinforced Ti-6%Al-4%V alloy. Below the β transus temperature, the yield and tensile strengths of all materials were found to increase with increasing deformation temperature, mostly due to an increase in density. Also, the variation in the ductility with increasing deformation temperature is plotted in Figure 7.30 for the titanium-based materials. In general, the ductility was found to be lower for the composites as compared to the unreinforced titanium alloy.

For Ti-6%Al-4%V, Table 7.6 summarizes the relationship between the mechanical properties obtained and the microstructures observed. In the single-phase β region (temperatures greater than 1017°C), increases in the deformation temperature lead to a slight increase in the strength and ductility, as indicated in Table 7.6 and Figure 7.29. Essentially, the microstructure after deforming in the single-phase β region consisted of lamellar α plates separated by the β phase (Fig. 7.16). The only microstructural change occurring with increasing deformation temperature is an increase in the density, from approximately 96% relative density at 1050°C to 99.5% at 1200°C (Fig. 7.2).

Table 7.6 – Room Temperature Properties of Ti-6%Al-4%V alloy
Worked to a Deformation Strain (ε_d) of 0.5 at a Strain Rate of 0.0005 s^{-1}

Deformation Temperature (°C)	0.1% Yield Strength (MPa)	Ultimate Tensile Strength (MPa)	Percent Elongation (%)	Microstructure
850	509	533	6.9	Lamellar ^{C} 22.2% porosity
950	804	852	8.1	Lamellar ^{C} 10% porosity
1000	885	975	10.6	Bimodal 5% porosity
1050	843	931	9.1	Lamellar ^{C} 3.6% porosity
1100	852	949	9.3	Lamellar ^{C} 2.2% porosity
1200	874	972	9.6	Lamellar ^{C} 0.5% porosity

^{C} represents colony appearance of lamellae

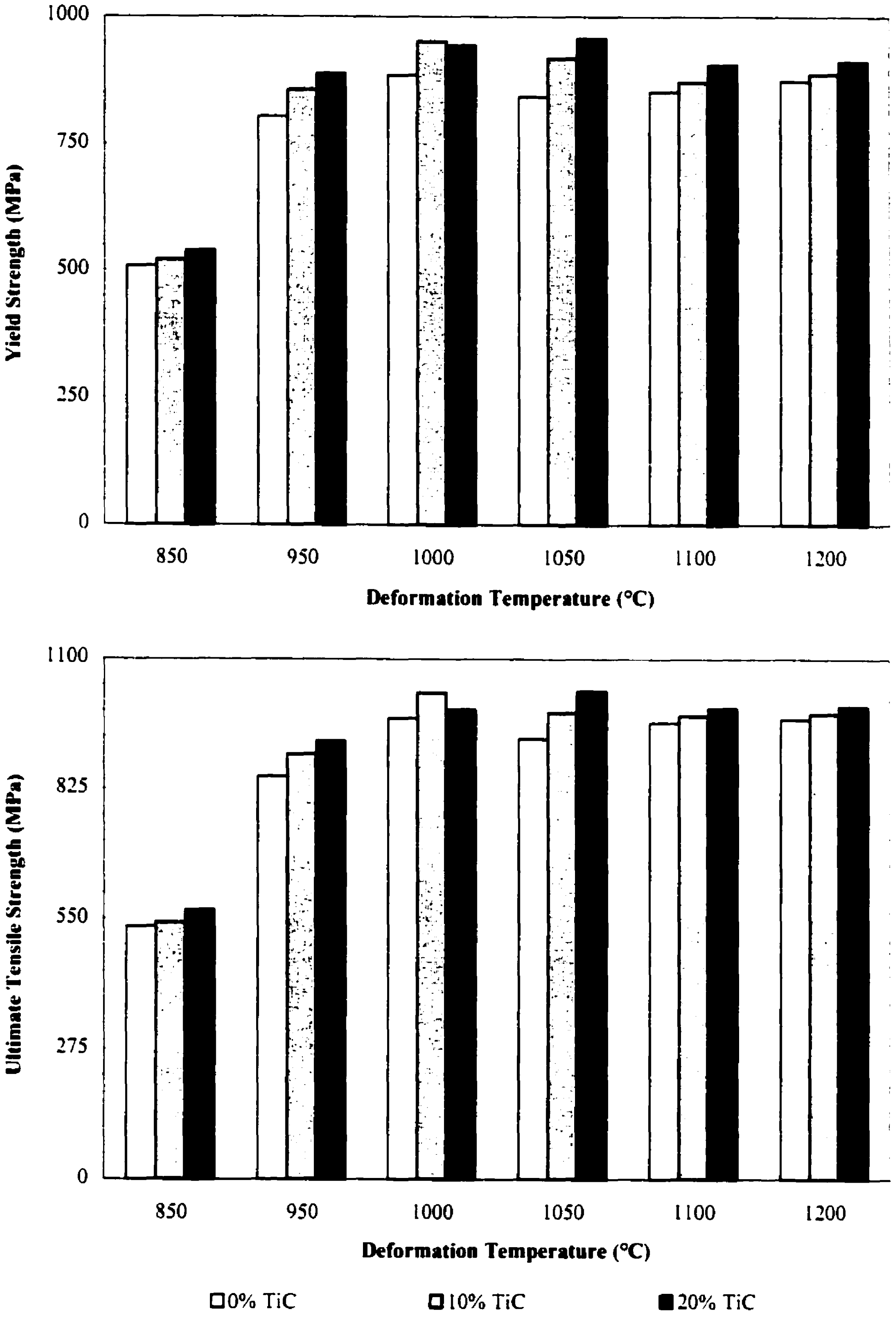

Figure 7.29 Strength properties as a function of deformation temperature for the TiC particulate reinforced Ti-6%Al-4%V composites hot worked to a deformation strain (ε_d) of 0.5 at a strain rate of 0.0005 s^{-1}.

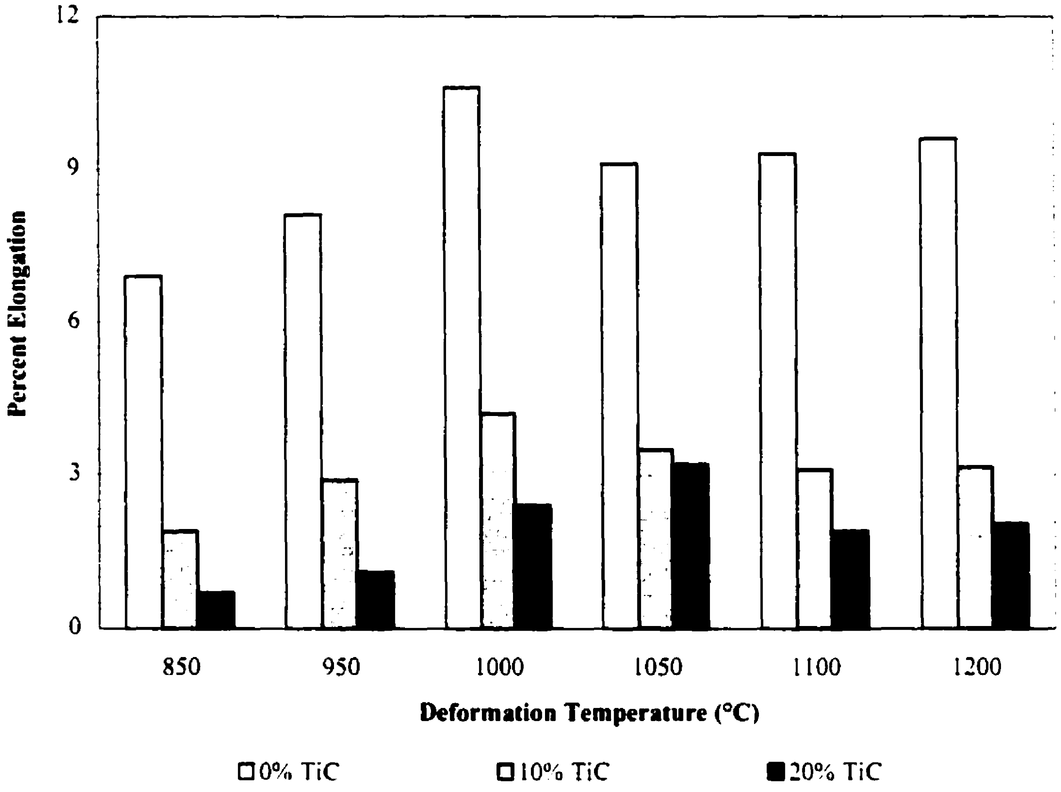

Figure 7.30 Total percent elongation as a function of deformation temperature for the TiC particulate reinforced Ti-6%Al-4%V composites hot worked to a deformation strain (ε_d) of 0.5 at a strain rate of 0.0005 s^{-1}.

In the two phase (α+β) region, the microstructure after hot working the Ti-6%Al-4%V alloy at 850°C and 950°C consisted of a deformed lamellar structure, while at 1000°C a bimodal structure of equiaxed and lamellar α was observed, as shown in Figure 7.16. The poor strength and ductility values for the Ti-6%Al-4%V alloy deformed at 850°C and 950°C (Table 7.6) are probably due to the inadequate bonding (low relative density) between the powder particles during low temperature processing. Deformation at 1000°C was found to give the highest strength and ductility in the Ti-6%Al-4%V alloy. As compared with working at 1050°C, the difference in the relative density for the alloy processed at 1000°C is approximately 1%. However, as indicated by Table 7.6, the properties are noticeably better for the alloy deformed at 1000°C and suggest an influence of microstructure.

For the Ti-6%Al-4%V wrought alloy, the general effects of microstructure on the room temperature mechanical properties are given in Table 2.5. Essentially, the strength and ductility are higher for an equiaxed microstructure as compared to a lamellar structure.

However, lamellar microstructures have higher fracture toughness resistance, creep resistance and lower crack propagation resistance, as indicated in Table 2.4. For bimodal microstructures, the mechanical property values are generally between those of equiaxed and lamellar structures and are dependent on their volume fraction in the microstructure. In the present work, the bimodal microstructure observed for the Ti-6%Al-4%V deformed at 1000°C (Fig. 7.16) had strength and ductility values greater than the lamellar structure of the alloy deformed at 1050°C (Table 7.6).

As compared to the literature values of strength and ductility for the lamellar structure (Table 2.7), the properties obtained in this work for the Ti-6%Al-4%V alloy having a lamellar structure are similar. However, there is a slight reduction in properties obtained for the powder metallurgy Ti-6%Al-4%V alloy due to the presence of residual porosity (0.5% to 4% depending on the deformation temperature).

The mechanical properties and matrix microstructures of the TiC reinforced Ti-6%Al-4%V composite materials are summarized in Table 7.7. At low temperatures in the two phase ($\alpha+\beta$) region (*i.e.* 850°C and 950°C), the matrix microstructure of the composites was observed to be a highly distorted lamellar alpha structure with considerable porosity. Similar to the mechanical properties of the unreinforced titanium alloy, the strength and ductility of the composites deformed at 850°C to 950°C were poor on account of the low density.

For deformation temperatures high in the single phase beta region (*e.g.* 1200°C and 1100°C), the matrix microstructure of the 10 vol.% TiC composite consisted of alpha lamellae having a basketweave appearance (Fig. 7.20). As compared to the unreinforced alloy, the aspect ratio of the alpha lamellae appears to have decreased for the matrix phase in the composite. The incorporation of an additional 10 vol.% TiC particles, for these deformation temperatures, appears to randomize the orientation of the alpha lamellae and decrease the aspect ratio further, as observed for the matrix microstructure of the 20 vol.% TiC composites (Fig. 7.21). With regard to the mechanical properties, the change in the lamellar microstructure of the alpha phase from platelets oriented in colonies to the interleaved or randomly oriented structures may improve the strength and ductility, on account of the lower aspect ratio of lamellae with increasing TiC volume fraction. The addition of TiC would increase the strength further at the expense of ductility. Also, the decrease in porosity with increasing deformation temperature would improve the strength and ductility. It is noteworthy that for a given deformation temperature, the percent porosity was similar for all the titanium-based materials. Thus the increase in strength properties at 1200°C or 1100°C with increasing TiC volume fraction can be attributed to the presence of the reinforcement phase and the change in microstructure.

Table 7.7 – Room Temperature Properties of the TiC reinforced Ti-6%Al-4%V Composites Worked to a Deformation Strain (ε_d) of 0.5 at a Strain Rate of 0.0005 s^{-1}

Deformation Temperature (°C)	Volume Fraction TiC	0.1% Yield Strength (MPa)	Ultimate Tensile Strength (MPa)	Percent Elongation (%)	Microstructure
850	10%	521	542	1.9	Lamellar[C] 21.6% porosity
	20%	539	568	0.7	Lamellar[C] 21% porosity
950	10%	857	899	2.9	Lamellar[C] 9.8% porosity
	20%	888	926	1.1	Lamellar[C] 9.8% porosity
1000	10%	951	1028	4.2	Bimodal[BW-F] 4.9% porosity
	20%	944	993	2.4	Bimodal[C] 4.8% porosity
1050	10%	919	987	3.5	Bimodal[BW] 3.5% porosity
	20%	957	1032	3.2	Bimodal[R] 3.4% porosity
1100	10%	871	979	3.1	Lamellar[BW] 2.1% porosity
	20%	905	995	1.9	Lamellar[BW-R] 2% porosity
1200	10%	887	984	3.2	Lamellar[BW] 0.5% porosity
	20%	912	999	2.1	Lamellar[BW-R] 0.5% porosity

[C] represents colony appearance of lamellae
[BW] represents basket-weave appearance of lamellae
[R] represents random appearance of lamellae
[F] represents fine structure

The composites processed at temperatures close to the beta transus temperature (*i.e.* 1000°C or 1050°C) were observed to give good strength and ductility combinations, as indicated in Table 7.7. For the composites containing 10 vol.% TiC, processing below the transus temperature (1000°C) produced a fine structure of lamellar and equiaxed alpha. The alpha lamellae, however, were basket-weave like in appearance and not oriented in the form of colonies, as in the case of the unreinforced alloy processed at the same temperature. This microstructure was observed to have the highest ductility in the composite material. The lower strength and ductility values for the 10 vol.% TiC composite processed at 1050°C are then attributed to the coarser microstructure and/or change in the relative volume fractions of equiaxed and lamellar alpha.

For the 20 vol.% TiC composite, the bimodal microstructure after deforming at 1050°C appeared to be slightly different from that observed for the material containing 10 vol.% TiC and processed at 1050°C, in that the lamellar alpha of the bimodal structure was randomly oriented. This material condition was observed to give the highest strength properties and good ductility (considering the volume fraction of reinforcement). The high strength is most probably due to the presence of equiaxed alpha and/or randomly orientated alpha lamellae as well as 20 vol.% TiC. Alternatively, increasing the TiC volume fraction to 20% and the coarser microstructure decreased the ductility in spite of the higher relative density at 1050°C, as compared to the 10 vol.% TiC composite processed at 1000°C.

As compared to the mechanical properties obtained in the literature for TiC particle reinforced Ti-6%Al-4%V composites (Table 2.6), the strength and ductility values are slightly lower inevitably due to residual porosity. However, processing the composites at 1000°C and 1050°C merits further investigation as secondary processing to increase the density may give an exceptional combination of strength and ductility properties for the fine bimodal microstructures. This secondary processing can be a heat treatment stage or further deformation.

Figure 7.31 gives the mechanical properties as a function of heat treatment time at 1100°C for the 20 vol.% TiC composite that was worked at 1000°C and 1200°C to a deformation strain (ε_d) of 0.5 at a strain rate of 0.0005 s^{-1} (see as-deformed micrograph in Fig. 7.23). In general, the properties of the composite were found to degrade with heat treatment time. As indicated by the Ti_2C volume fraction data plotted in Figure 7.31, progressive transformation of the TiC reinforcement phase occurs with hold time at 1100°C. Besides grain growth, increase in the Ti_2C interfacial layer thickness is probably the main reason for the degradation in the mechanical properties. As observed in the sintering section (chapter 6), a reduction in the carbon concentration in the TiC reinforcement particles was determined to lower the microhardness through what was reasoned to be a change in the Ti-C bond character. Thus, to remove the residual porosity it is suggested that full consolidation be achieved by hot deformation only to minimize the interfacial boundary layer in the TiC reinforced titanium alloy composites and achieve the optimum mechanical properties.

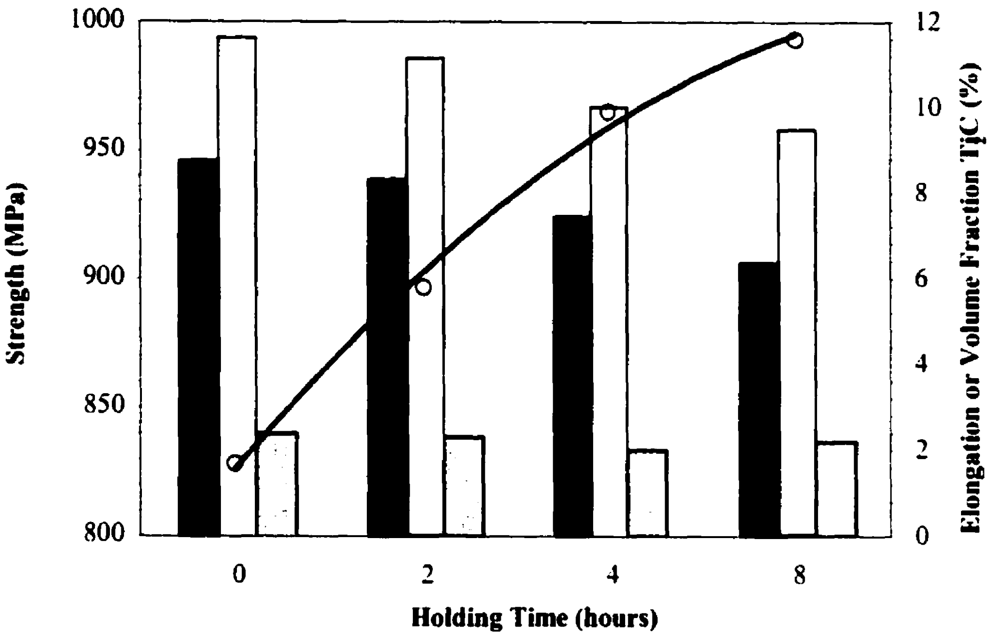

(a) 1000°C

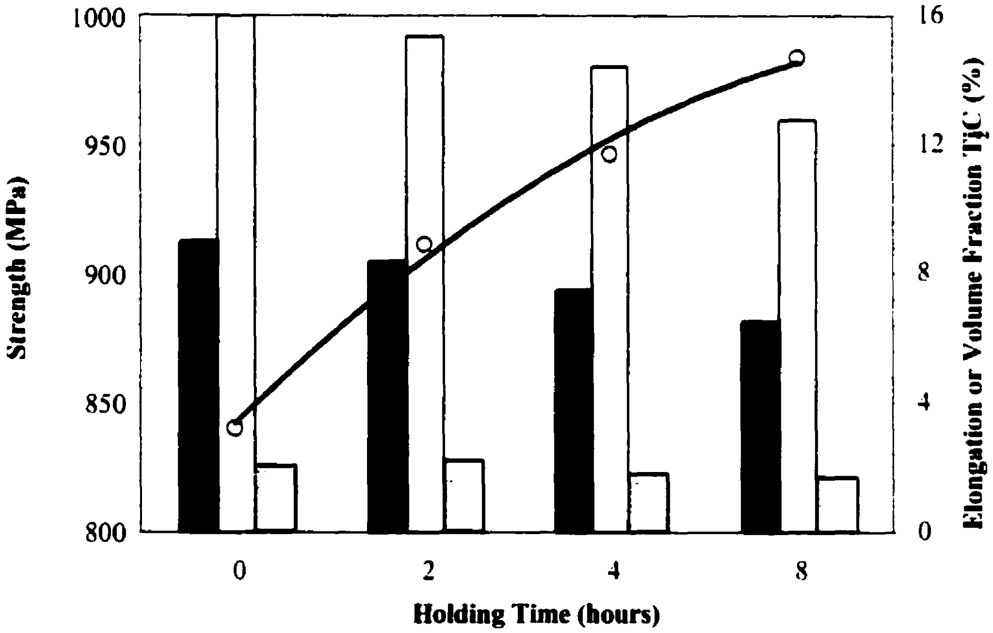

(b) 1200°C

Figure 7.31 Mechanical properties after heat treatment at 1100°C of the 20 vol.% TiC_p reinforced Ti-6%Al-4%V composites hot worked to a deformation strain (ε_d) of 0.5 at a strain rate of 0.0005 s^{-1} at a temperature of (a) 1000°C and (b) 1200°C. The volume fraction of the interfacial phase, Ti_2C, is also plotted.

CHAPTER 8

DISCUSSION

The results on high temperature processing of TiC particulate reinforced Ti-6%Al-4%V composites provide an increased understanding of the influence of the various consolidation parameters on the evolution of density and pore structure, the modification of the matrix microstructure and the nature of interaction between the matrix and reinforcement phases, as well as the effect of these on the mechanical properties. Here, the information from the two processing techniques used will be considered in greater detail to effectively compare the pressureless sintering and deformation-assisted sintering results and discuss the knowledge gained from this work.

8.1 Densification Behavior

The densification results from pressureless sintering and deformation-assisted sintering indicate similar trends for the effect of temperature, hold time and TiC volume fraction on density (compare Fig. 6.5 with Fig. 7.2). Temperature has a greater influence on density than hold time (where the applied strain divided by the strain rate gives the hold time for the deformed material), and an increase in the TiC volume fraction increased the density slightly (1 to 3% increase for every 5% increase in TiC volume fraction). The main difference in the consolidation behavior of pressureless sintering as compared to deformation-assisted sintering is that to attain a specific final density, the conditions for both the isothermal temperature and hold time are considerably reduced for the latter processing technique. For example, to achieve 95% relative density by pressureless sintering, isothermal holding at 1500°C for 2 hours is necessary, while deformation at 1100°C to a strain of 0.8 at a strain rate of 0.0005 s^{-1} (approximately 27 minutes) is sufficient (compare Figs. 6.5 and 7.2). Additionally, to achieve complete densification by pressureless sintering only may be difficult, as the driving force for the removal of the residual porosity is small during the final stages of sintering (as explained in the literature review). Consider, for example, the Ti-6%Al-4%V alloy sintered at 1500°C for four hours. From Figure 6.14 it is observed that the morphology of the pores is spherical and the isolation of some pores within the grain boundaries has occurred. At 1500°C, further densification of this material (with spherical and isolated pores) would be slow.

It is arguable, however, as to which technique will be most cost efficient, as the lower equipment related costs for pressureless vacuum sintering may be offset by the higher processing costs due to the increased temperature and hold time requirements, which may reduce the overall cost differential. Yet, the choice of processing technique cannot be made on the basis of cost alone for the titanium-based composites, as indicated by the microstructural and mechanical property characteristics of the composite material produced. For identical relative density values, it has been observed that the nature of the Ti_2C interface is improved substantially, as indicated by the mechanical properties for the composites processed by deformation-assisted sintering as compared to those from pressureless sintering. Moreover, modeling the hot deformation behavior of the titanium alloy and composite materials using the creep power law form of the constitutive equation gave values for the stress exponent and activation energy which agreed reasonably well with those of previous investigators, and these values suggest that both dynamic recovery and dynamic recrystallization can occur in Ti-6%Al-4%V during processing in the two phase ($\alpha+\beta$) region. Hence the matrix microstructure and overall mechanical properties can be tailored to achieve the conditions necessary for specific applications.

Nonetheless, through the pressureless sintering results the primary material transport mechanism for the TiC-titanium alloy system was determined to be volume diffusion, most likely by a combination of atomic movement through the lattice and along grain boundaries. Also, the use of this processing technique in conjunction with neutron diffractometry provided a fundamental understanding of the reactivity of Ti-6%Al-4%V with TiC, as will be discussed later in the interfacial reaction section. In addition, these latter results may be of interest for determining component lifetime at various service temperatures for elevated temperature application of the titanium-based composites.

8.2 Microstructural Characteristics

Pressureless sintering of the composites was investigated only at temperatures in the single phase beta region because appreciable densification begins to occur above $0.6T_m$. For Ti-6%Al-4%V, the melting temperature is approximately 1650°C. Thus, temperatures above 1000°C, which incidentally coincides with the beta transus of this alloy, are necessary to activate and maintain material transport for pressureless sintering to progress within a reasonable time period. As such, microstructural development during pressureless sintering only constituted modification to the lamellar structure of plate-like alpha separated by interplate beta. With increasing processing temperature, the lamellar microstructure of the matrix was found to coarsen as indicated in Figure 6.14 by the successive increase in the alpha plate width. For a given isothermal sintering temperature, an increase in the hold time similarly coarsened the lamellar microstructure. However, the effect was not as marked as that observed with increasing temperature. The addition of TiC particles to Ti-6%Al-4%V was observed to inhibit coarsening of the lamellar structure, as indicated by the finer plates of alpha in the composite as compared to the unreinforced alloy. Overall, the presence of the reinforcement phase appeared to have a homogenizing effect on the lamellar microstructure of the matrix, with the incorporation of 20 vol.% TiC giving a similar alpha plate size regardless of the processing conditions investigated.

The use of deformation-assisted processing achieved appreciable densification at lower processing temperatures, however the physical limitation to decreasing the temperature below 850°C or increasing the strain rate above $5 \times 10^{-2}\ s^{-1}$ was due to cracking or crumbling of the green compacts during compression testing. Microstructural modification by deformation was greater than that by pressureless sintering, because hot working at temperatures in the single phase beta region achieved a lamellar structure, while in the two phase ($\alpha+\beta$) region combinations of lamellar and equiaxed structures formed.

Deformation processing of Ti-6%Al-4%V at temperatures above the beta transus (1017°C) achieved a lamellar microstructure similar to that obtained by pressureless sintering with the difference of higher densities (fewer and smaller pores) and finer alpha plate width for the hot worked material. In the $\alpha+\beta$ phase region, deforming just below the transus (1000°C) produced a bimodal microstructure, while lower deformation temperatures produced a microstructure consisting of distorted (wavy) and elongated lamellar alpha platelets. The presence of equiaxed and lamellar alpha at a deformation temperature just slightly below the beta transus was reasoned to form due to the greater recrystallization kinetics (higher temperature and greater working of a small volume fraction of alpha), as compared to that possible by deforming at lower temperatures.

Although the effect of strain rate on the as-processed microstructure was negligible over the strain rates examined, the presence of the reinforcement phase contributed further to the potential of microstructural modification by deformation-assisted sintering. At deformation temperatures well above the beta transus of Ti-6%Al-4%V (*i.e.* 1100°C and 1200°C), the matrix microstructure, in the presence of 10 vol.% or 20 vol.% TiC particles, is lamellar (Figs. 7.20 and 7.21). However, as compared to the colony orientation of the alpha lamellae in the unreinforced alloy, the microstructure for the 10 vol.% TiC composite shows a basket-weave appearance for the alpha plates while an overall random orientation of the alpha structure is observed for the 20 vol.% TiC composite. As discussed previously in the deformation section (chapter 7), the change in alpha plate orientation that occurs with increasing TiC volume fraction can be attributed to an increase in the nucleation sites for alpha in the presence of the particles. Additionally, with increasing TiC volume fraction, the aspect ratio of the alpha plates decreased and a change in the static and dynamic mechanical properties is possible as the smaller aspect ratio alpha phase of the matrix in the composite has the semblance of an equiaxed structure.

The presence of the TiC particles were also found to influence the beta transus temperature of Ti-6%Al-4%V through carbon dissolution during heating to the deformation temperature, as well as during deforming at the isothermal temperature. The effect of an increase in the beta transus temperature was evidently most pronounced for the composites deformed at 1050°C and 1000°C, that is slightly above and below the transus temperature of the alloy (1017°C). For composites containing 10 vol.% TiC, the microstructure formed by deformation at 1050°C and 1000°C was bimodal as shown in Figure 7.20. As compared to the unreinforced alloy, the 10 vol.% TiC composites deformed at 1050°C were observed to contain a higher fraction of equiaxed alpha and randomly oriented lamellar alpha plates. At 1000°C, this TiC volume fraction achieved the most refined equiaxed and lamellar alpha structures (approximately 5 μm equiaxed grain size as compared to a 10 μm equiaxed grain size for 10 vol.% TiC composite deformed at 1050°C and 12 μm equiaxed grain size for the unreinforced alloy deformed at 1000°C).

For a deformation temperature of 1050°C, composites containing 20 vol.% TiC particles were comparable in microstructure with the 10 vol.% TiC composites, with an additional disorientation of the alpha plates in the lamellar structure (Fig. 7.21). On the other hand, no additional refinement of the bimodal microstructure was observed by increasing the TiC volume fraction from 10% to 20% for the material deformed at 1000°C (compare Fig. 7.20 to 7.21). Moreover, the microstructure of the 20 vol.% TiC composite processed at 1000°C revealed mostly deformed alpha plates with perceptibly small amounts of equiaxed alpha (Fig. 7.21). This microstructural change in the matrix can be attributed to the influence of a higher TiC volume fraction on increasing the beta transus temperature and, as a result, the volume fraction of the primary alpha being deformed (see section 7.3).

At temperatures well below the beta transus, 850-950°C, the matrix microstructures of the composites were similar to the unreinforced titanium alloy and a highly distorted lamellar structure was observed, as revealed in Figures 7.20 and 7.21. From microhardness testing, the primary effect of increasing the TiC volume fraction at these deformation temperatures was an increase in the hardness of the matrix phase, probably due to an increase in the dislocation density with increasing reinforcement fraction.

In light of these microstructural results, the greatest possibility for structural modification of the alpha morphology appears to be attainable at deformation processing temperatures close to the beta transus and in the presence of the reinforcement particles. Although the incorporation of TiC achieves refinement of the alpha structure, a change in the beta transus temperature, which occurs due to carbon dissolution from the interaction between the reinforcement and matrix during processing, adds uncertainty to the exact magnitude of refinement possible. Regardless, extensive working of a small volume fraction of primary alpha was generally observed to form a fraction of equiaxed alpha. By maintaining the deformation temperature just slightly below the beta transus temperature of the matrix phase, about 1017°C for the unreinforced titanium alloy, the small volume fraction of primary alpha (approximately 10% to 12%) can be worked to form equiaxed alpha grains dynamically. In the case of the composites, a combination of optimizing the deformation temperature and TiC volume fraction can reduce the average alpha grain size by half, as observed for the 10 vol.% TiC composite processed at 1000°C. As such, for the 20 vol.% TiC composites, a slightly higher deformation temperature, possibly 1025°C, may generate a similar refinement in the microstructural constituents of the matrix phase.

As compared to previous work on these composites, the deformation processing temperatures are slightly higher (1000°C versus 900°C).[278] However, the microstructural characteristics of the composites in this work show considerable refinement of the alpha structures, as well as a homogeneous distribution of the reinforcement phase.[123,142,149] The alpha plate size in previous work has been noted to range from 10 to 20 μm and clustering of the reinforcement phase is a common occurrence. In this work, the further refinement that is observed in the presence of the particles and at processing temperatures close to the beta transus suggests a possible means of enhancing recrystallization of the alpha structure. Hence a possibility for future hot deformation work on this composite system is to examine the near transus temperature regime to define the material and processing parameters that produce the greatest refinement of the matrix microstructure.

8.3 Interfacial Reaction Characteristics

For composites, influence of processing conditions on the formation and characteristics of the interfacial reaction products can be a concern that overrides the matrix microstructural evolution discussed previously. For the TiC-titanium alloy system, previous work on resolving the nature of the interfacial boundary area using standard optical and scanning electron imaging techniques have been unsuccessful.[26,110-111] For the first time, using low voltage imaging on a cold field emission gun SEM, the interfacial region between TiC and Ti-6%Al-4%V was established in the present work (Fig. 6.18). There appears to be a high coherency between the reinforcement and matrix, as perceived in the various photomicrographs of the boundary region shown in Figures 6.19 and 7.23.

From the low voltage field emission gun SEM work, the thickness of the interfacial boundary region appears to increase rapidly with increasing temperature for the composites processed by pressureless sintering (Fig. 6.19). An increase in the sintering temperature from 1100°C to 1300°C increased the interfacial boundary layer from roughly 1 μm to 3 μm (compare Figs. 6.19 a and 6.19 b). For the composites processed at 1500°C no boundary layer was observed on the periphery of the reinforcement (Fig. 6.19 c) and a chemical analysis for carbon indicated that the composition of the entire particulate was homogeneous (Fig. 6.20 c). In comparison, a similar carbon analysis for the composites processed at 1100°C and 1300°C indicated a lower carbon level for the interfacial boundary layer. Additionally, the carbon content at the particle center was nearly twice that of the interfacial boundary region in the composites sintered at 1100°C and 1300°C, while the carbon level of the entire reinforcement in the composite sintered at 1500°C corresponded to that of the boundary layer in the material processed at lower temperatures (Fig. 6.20).

These findings contradict the SEM and quantitative micro-analysis work of Gu et al.[111] on these composites in which a continuous carbon deficient region was determined to form from a dissolution-type reaction between the matrix and reinforcement. In reference to the titanium-carbon phase diagram (Fig. 2.2), a dissolution-type reaction is suggested for the composite system. As such, the particles would dissolve in the matrix until either all the carbon is in solution or equilibrium occurs between a saturated solution of carbon in titanium and some remaining TiC that would then be non-stoichiometric (*i.e.* TiC_x).[113-115] Nonetheless, a reduction of nearly 50% in the carbon content determined in this work for the boundary layer is consistent with the micro-analysis work of Konitzer and Loretto by electron-energy loss spectroscopy (EELS) that revealed a carbon content of approximately 12 wt.% on the reinforcement periphery and 20 wt.% at the particle center. However, it is uncertain from their findings whether the entire carbon-deficient boundary layer corresponded to a single composition as that observed in this work.

Also, the electron probe micro-analysis work (Fig. 6.22) indicated a compositional gradient for carbon across the boundary region between the particle and matrix, thus supporting previous findings. However, the size of the x-ray volume from the electron beam size of the micro-probe was the same order of magnitude (Fig. 6.23) as the size of the boundary layer observed with the field emission gun SEM. Hence, the interfacial region would be difficult to analyze with this technique. The carbon composition in the particles decreased from approximately 20 wt.% in the composites sintered at 1100°C to as low as 12 wt.% for composites sintered at 1500°C. Combining the electron micro-probe work with the field emission gun results, it is reasonable to say that the carbon composition at the reinforcement center for the composites sintered at 1100°C and 1300°C is approximately 20 wt.%, while the carbon content of interfacial boundary region and for the entire particle in the composites sintered at 1500°C is 12 wt.%. These compositional values inferred for the reinforcement center and periphery correspond well with the findings of Konitzer and Loretto. Additionally, the carbon composition of the matrix remained nearly constant, falling in the range of 0.3 wt.% to 0.6 wt.% (solubility limit of titanium for carbon is 0.4 wt.%). This suggests the formation of a stable phase at the interfacial boundary between the particle and matrix, as evidenced by the field emission gun SEM work and the growth of the reinforcement for pressureless sintering temperatures of 1500°C. Yet the work from the low voltage field emission gun SEM and the electron micro-probe cannot irrevocably ascertain the chemical composition and the exact nature of the interfacial reaction region (*i.e.* a single phase or compositional gradient in carbon).

However, the low voltage field emission gun SEM analysis of the interfacial region provided an unprecedented means of viewing the boundary layer between the matrix and reinforcement. Even for the composites processed by hot deformation, in which the boundary layer is smaller in thickness, the characteristics of the interface are resolved distinctly. For the deformed composites, the interfacial reaction layer appeared to form uniformly on the periphery of the reinforcement, as compared to the diffuse and irregular layer around the particles in the composites processed by pressureless sintering (compare Fig. 7.23 with 6.19). Chemical compositional analysis across the interfacial reaction layer in the deformed composites could not be performed due to the smaller thickness of the boundary region. Regardless, the inherently different characteristics observed for the interfacial reaction region for the two processing techniques may conceivably influence the properties of the composite.

To study the formation and composition characteristics of the interfacial reaction with processing, systematic monitoring of the Ti-6%Al-4%V/TiC composite system was performed using a neutron powder diffractometer equipped with elevated temperature sintering capabilities. The concept was to observe changes in the lattice parameters of the starting phases to monitor the reaction between the TiC particles and β-Ti-6%Al-4%V matrix. The preliminary work involved determining the temperature dependence of the lattice parameter and the coefficient of linear thermal expansion for both Ti-6%Al-4%V and TiC. Although this information provided the basis for monitoring the interfacial reaction for this work, the lattice parameter and coefficient of linear thermal expansion data determined for the beta phase of Ti-6%Al-4%V extend considerably the existing data for such parameters in the literature.[254]

The most remarkable change in the diffraction spectrum with holding time at temperature was observed for the (331) and (311) peaks of the TiC phase. (The (111) peaks of TiC could not be de-convoluted, but the peak was observed to shift to higher scattering angles with holding time at temperature.) With the progression of sintering, these peaks were observed to diminish in intensity and two distinctive peaks, at slightly higher scattering angles, formed. Careful analysis of the diffraction spectrum indicated that the peak pattern corresponding to the beta-phase of Ti-6%Al-4%V also evolved. The lattice parameter of the alloy was determined to increase during holding at temperature, whilst the intensity was observed to decrease. The significance of a continual reduction in the integrated intensities of the starting materials and the emergence and growth of new peaks with the progression of sintering is that a reaction occurs between Ti-6%Al-4%V and TiC and forms a *distinct* phase at the interface. As part of the initial reaction between the matrix and reinforcement, it appears that carbon diffuses from the TiC phase and dissolves in Ti-6%Al-4%V, thereby increasing the lattice parameter, until saturation of the alloy occurs. It is noteworthy that the lattice parameter of the TiC phase did not change with holding time at constant temperature, as illustrated in Figure 8.1 for consolidation of a 20 vol.% TiC composite at 1100°C. Hence, the increase in the lattice parameter of the beta-Ti-6%Al-4%V phase cannot be attributed to particle-matrix stresses.

Further reaction of carbon with Ti-6%Al-4%V formed between the matrix and reinforcement an interfacial phase having a stoichiometry of Ti_2C (lattice parameter of 4.290-4.296 Å) and a face centered cubic crystal structure (similar to that of TiC). Growth of the interfacial phase was observed through a decrease in the integrated intensities of both β-Ti-6%Al-4%V and TiC phases and an increase in the integrated intensity of the Ti_2C phase. Moreover, the mechanism for growth of the Ti_2C interface was determined to occur by carbon transport from the particles through the Ti_2C interface to the matrix.

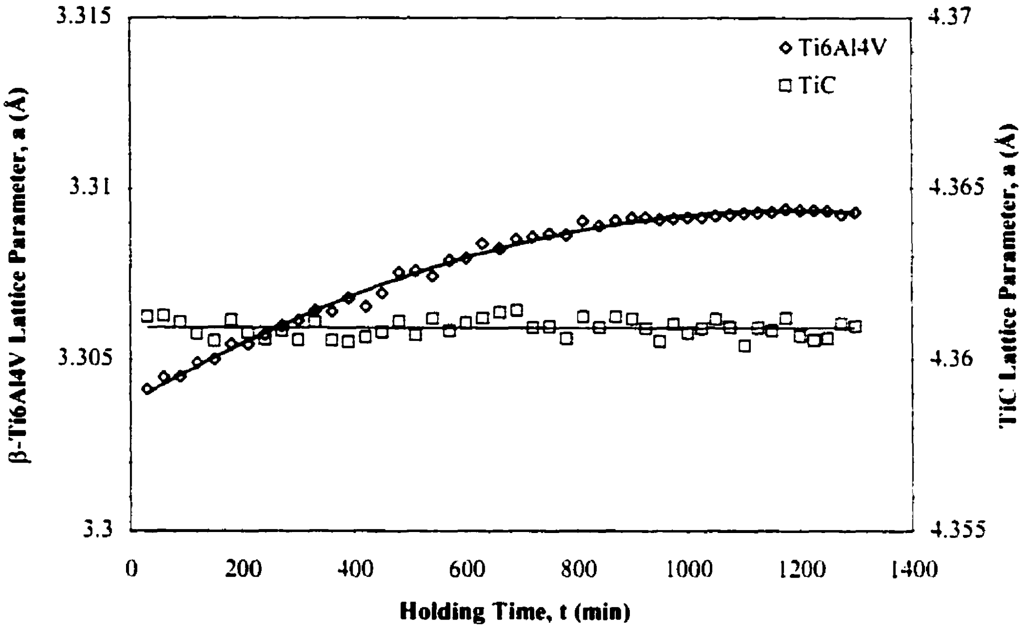

Figure 8.1 Variation in the lattice parameter of the beta-Ti-6%Al-4%V and TiC phases with holding time for a 20 vol. TiC composite sintered at 1100°C.

The present interfacial results can be used to revisit the titanium-carbon phase diagram and in particular the neutron diffraction work of Goretzki on the titanium-carbon system.[117] Goretzki hot-pressed compositional mixtures between 32 and 48.8 atomic percent carbon and annealed these at temperatures between 1100°C and 2000°C. For the titanium-carbon system he determined that a carbon concentration of 33 at.% resulted in an ordered phase arrangement of carbon atoms in the octahedral sites of the titanium lattice. Through different annealing and quenching treatments, the stability of this phase was determined to be 1900°C at 33 atomic percent carbon. Although Goretzki proposed the existence of stable Ti_2C (33 at.% C) as early as 1967, no particular distinction has been made between the equilibria involving TiC and those involving Ti_2C, because most investigators did not distinguish the two structures and little information is available on the stability range of the Ti_2C phase.

The discrepancy in the findings of Goretzki[117] and the work of other investigators[113-116,119] on which the present titanium-carbon phase diagram is based is a result of the nature of the experimental techniques used to determine the phases present. Whilst the work of Goretzki involved phase determination by neutron diffractometry, the studies conducted by Cadoff and Nielsen,[113] Ogden et al.,[114] Wagner et al.,[119] Bickerdike and Hughes,[115] and Rudy et al.,[116] utilized metallography, x-ray diffractometry (employing CuKα radiation) and chemical analysis. Specifically the techniques used for metallographic examination of the phases present in the titanium-carbon system consisted of optical and *conventional* electron microscopy. As revealed from the present work as well as that of previous investigators,[26,30,110,113-114,120,123,139,143] no phase contrast between TiC and Ti_2C is apparent using optical or *conventional* SEM (using either secondary or backscattered electron imaging) techniques. Unprecedented viewing of the boundary layer between the reinforcement and matrix was only possible using high resolution low voltage field emission gun SEM analysis as revealed in the present work. Moreover the observations from x-ray diffractometry seemed to support the existence of non-stoichiometric TiC_x, as a reduction in the carbon concentration in TiC was found to broaden the diffraction peaks and shift these to higher angles.[113] Hence in the visual absence of a phase transformation, there was no reason to question the conclusions based on the x-ray diffraction observations, where the peaks from TiC and Ti_2C were not easy to resolve due to similarities and overlapping of the diffraction patterns (as discussed in the sintering chapter).

Recently, the transmission electron microscopy work of Konitzer and Loretto[110] on the interfacial reaction region in TiC_p reinforced Ti-6%Al-4%V composites did reveal a circular dislocation network on the periphery of the reinforcement which had a lattice parameter and chemical composition corresponding to Ti_2C. Yet, uncertainty remained with regard to the composition of the entire interface because the number of measurements possible across the periphery region is limited using EELS. Moreover, the micro-analysis findings of Gu et al.[111] had indicated a compositional gradient for carbon between the matrix and particle center supporting the findings of previous investigators[26,30,110,113-114,120,123,139,143] and the existing titanium-carbon phase diagram. Similar observations were noted in the electron microprobe results of the present work, but it has been remarked that abrupt changes in composition may be difficult to observe, especially if the electron beam diameter and interfacial thickness are similar in size (Fig. 6.23).

From the low voltage field emission gun SEM work, visual evidence was found for the formation of an interfacial phase between the particles and matrix (Figs. 6.19 and 7.23). Moreover, chemical compositional analysis using energy dispersive spectroscopy at low accelerating voltage revealed abrupt changes in the carbon content in this region (Fig. 6.20). Finally using neutron diffractometry the interfacial phase was identified as having a distinct chemical composition with a lattice parameter value (4.290-4.296 Å) corresponding to stoichiometric Ti_2C with a face centered crystal structure. Undoubtedly, the similarity in the crystal structures of TiC and Ti_2C leads to the good phase coherency and compatibility which is often remarked in the literature when describing the nature of the interfacial reaction region in the TiC-titanium composite system. In fact, it appears that it is this that has prevented proper determination of the interfacial reaction in these composites.

To correlate the field emission gun SEM images of the interfacial layer formed in the composites (Fig. 6.19), Figure 8.2 was plotted to show the effect of processing temperature on the diffraction pattern in the region of the (331) diffraction peak of TiC. In a 20 vol.% TiC composite, holding at 1100°C for one hour clearly reveals the single (331) peak for TiC and perhaps a slight evidence of a small peak corresponding to the interfacial phase at an angle near the original (331) diffraction peak for TiC (Fig. 8.2c). For a similar holding time, the 20 vol.% TiC composite shows two peaks for a processing temperature of 1300°C. At this intermediate temperature, one peak corresponds to the (331) diffraction peak for TiC whilst the other is that of the interfacial phase (Fig. 8.2b). Also, there is a shift in peaks to lower scattering angles, as the lattice parameter of both carbide phases was observed to increase with temperature. A diffraction pattern of the same material processed for one hour at 1500°C was obtained by re-heating to 1100°C. The pattern showed a single diffraction peak whose lattice parameter did not correspond to that of TiC (Fig. 8.2a) but to that of the interfacial phase, as noted by the similarity in scattering angle positions. These neutron diffraction results correlate well with field emission gun SEM micrographs showing the interfacial region in these composites. At 1100°C a 0.6 μm interfacial layer was present for holding time of 4 hours. Hence the size of the neutron diffraction peak of the Ti_2C phase after an hour of holding at 1100°C is relatively small (Fig. 8.2c). An hour

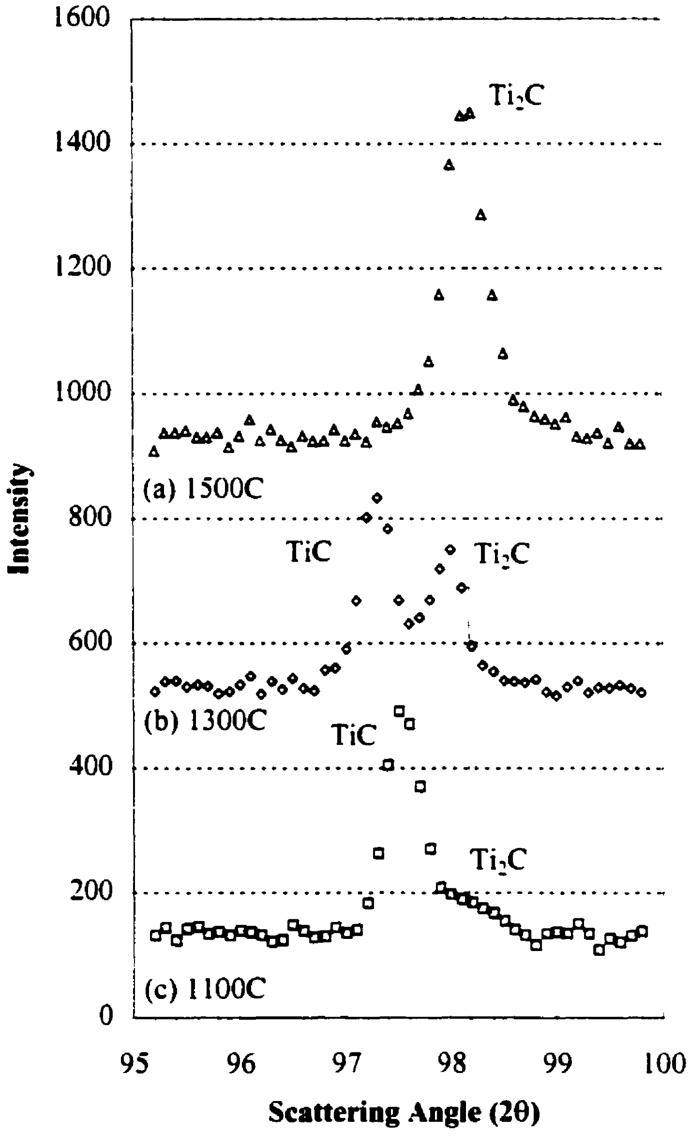

Figure 8.2 Neutron diffraction pattern showing the evolution of the (331) TiC peak with processing temperature for a hold time of 1 hour for 20 vol.% TiC composites.

at 1300°C results in considerable reaction of the matrix and reinforcement phases (Fig. 6.19) and both TiC and Ti_2C are present in the neutron diffraction pattern. At 1500°C, complete transformation of the TiC particles is evident in the field emission gun SEM results and the absence of TiC is remarked in the neutron diffraction pattern (Fig. 8.2).

In light of the present findings, it is appropriate that changes to the titanium-carbon phase diagram be considered by examining annealed microstructures of compositional mixtures between 10 and 20 wt.% carbon in titanium using improved resolution techniques such as the field emission gun SEM and/or neutron diffractometery. Specifically, the existence of stoichiometric Ti_2C phase at a composition of 33 at.% (or 12 wt.%) has been determined unequivocally using neutron diffractometery. The stability of stoichiometric Ti_2C was determined presently to be 1500°C; however Goretzki[117] has suggested temperatures as high as 1900°C. Hence a new titanium-carbon phase diagram can be proposed that incorporates the existence of Ti_2C and its stability range known to date, as suggested in Figure 8.3. The region between 10 wt.% and 20 wt.% carbon has been modified as indicated by the dashed lines in the proposed phase diagram, as compared to that from the literature (Fig. 2.2).[112] In the region between 12 wt.% and 20 wt.% carbon in titanium, Ti_2C and TiC most likely co-exist. The exact nature of the solidus and liquidus regions for the carbon composition range of 10wt.% to 20 wt.% carbon are uncertain, but these are speculated to lie above 1500°C. Of the two possibilities proposed in Figure 8.3, the isomorphic equilibria between TiC and Ti_2C may be more likely due to the similarity in their face centered cubic structures. (The formation of a eutectic between TiC and Ti_2C would imply less chemical compatibility and greater differences in their crystal structures.)

Interestingly, in the work of Cadoff and Nielsen[113] the region below the liquidus line was identified as containing liquid (L) plus a phase designated as δ. This δ phase was observed to extend to 11 wt.% carbon at 1750°C and gave a face centered cubic diffraction pattern. With decreasing temperature, structures of δ plus transformed β were found below 1648°C and δ plus α below 920°C. It is mentioned that "primary δ was found in alloys of carbon content as low as 0.2 wt.% carbon". These observations suggest the characteristics of a stable stoichiometric phase, Ti_2C, termed δ by Cadoff and Nielsen. However in their work, a 12 wt.% carbon composition was not investigated. Moreover, discrimination could not be made between Ti_2C and TiC using optical microscopy on the alloys beyond 13 wt.% carbon. As such, the δ phase was suggested to vary in composition and was designated as being sub-stoichiometric TiC_x over the carbon range illustrated in Figure 2.2. Through a reconstruction of their experimental work, the microstructural features between 12 and 20 wt.% carbon can be established (using the field emission gun SEM) to improve on the current labeling of the various regions on the carbon-titanium equilibrium phase diagram.

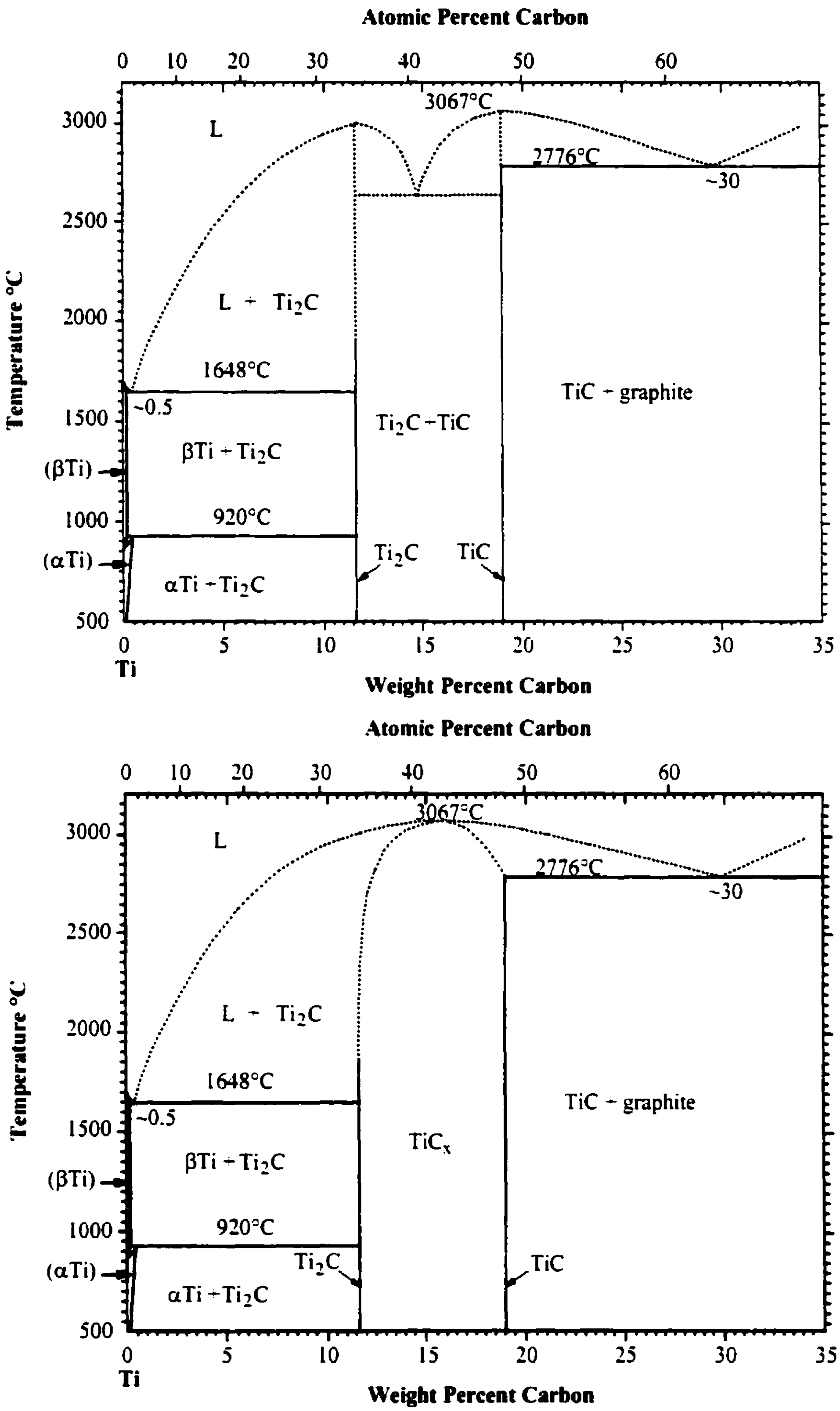

Figure 8.3 Possible titanium - carbon phase diagrams based on observations reported by Goretzki[117] and the findings from the present work.

8.4 Mechanical Properties

Hardness testing and shear punch testing techniques were used to evaluate the properties of the composites processed by pressureless and deformation-assisted sintering. Hardness testing is a method commonly used for inferring the mechanical properties from small specimen configurations. However, shear punch testing is not known as widely and information on its development, applicability and limitations, especially with regard to mechanical property evaluation of composites, has been discussed in chapters four and five. The use of this latter technique is particularly useful, since both strength and ductility information can be assessed from the material deformed to failure. The present extension of previous work on shear punch testing of metallic materials[239-242] to include discontinuously reinforced composites enables the tensile properties to be evaluated in a relatively simple and economical manner, which should facilitate research and development work on various composites because of relative ease of mechanical property determination.

For the composites processed by sintering alone, the overall tensile properties determined by hardness and shear punch testing were inferior to those obtained in the literature for the TiC_p-Ti-6%Al-4%V system.[27,147-150] At low processing temperatures, limitations in the strength and ductility are most probably a result of the high porosity and poor reinforcement-matrix bonding. With increasing sintering temperature the size and amount of pores decreased and consolidation to over 90% relative density was achieved at 1500°C. However, interaction of the matrix and reinforcement phases was observed to occur at an increasingly rapid rate with increasing temperature. This chemical reaction between the alloy and the particles consisted of carbon diffusion from the reinforcement to the matrix phase. Initially, the carbon was determined to dissolve in Ti-6%Al-4%V as evidenced by the increase in the lattice parameter with hold time at temperature (Figs. 6.32 to 6.37) and supported by the microhardness measurements in the matrix phase (Fig. 6.65). Ensuing carbon saturation of the alloy, further reaction occurs by carbon diffusion to the matrix-reinforcement interface to form stoichiometric Ti_2C on the periphery of the TiC particles. This reaction is evidenced by the growth of the particles in the optical microscopy work and by the resolution of the Ti_2C phase in field emission gun SEM and neutron diffractometry work. Reaction of this nature between the matrix phase and TiC particles was observed to have a deleterious effect on the properties of the composites as indicated by a reduction in the microhardness values of the reinforcement phase with increasing sintering temperature (Fig. 6.65). However, reaction between the matrix and reinforcement phases is arguably necessary for promoting good bonding characteristics. Nonetheless extensive reaction at elevated temperatures occurs and transforms much of the TiC particles to Ti_2C. This limits the overall strength and ductility properties of the composite despite the higher sintered density probably because of a reduction in the Ti-C bond strength for Ti_2C as compared to TiC. An indication of the lower bond strength for Ti_2C is indicated by the lower microhardness value of 1500 kg-mm^{-2} as compared to 2200 kg-mm^{-2} for TiC. (It should be noted that the microhardness measurement for Ti_2C was made on the reinforcement phase in composite sintered at 1500°C for 1 hour, since such sintering conditions were observed to completely transform the TiC particles to Ti_2C.)

Besides reinforcement transformation, microstructural coarsening of the lamellar arrangement of alpha and beta was observed to occur with increasing temperature (Fig. 6.14). The incorporation of TiC particles appears to diminish this coarsening effect of temperature (Fig. 6.15). However local agglomeration of the reinforcement phase can be seen with increasing TiC volume fraction (Fig. 6.15) and poorer bonding may occur in these regions as the ceramic particles in contact would require higher consolidation temperatures for bonding. This is a possible explanation for the asymptotic leveling in properties observed with increasing reinforcement volume fraction (Figs. 6.66 to 6.68).

Although the strength and ductility properties obtained for the as-sintered composites in this work were inferior to the potential of the TiC_p-Ti-6%Al-4%V system, analysis of the tensile fracture surface of the composites processed to near-complete density revealed both cleavage and dimple formation. This suggests that in these composites load transfer occurs between the matrix and reinforcement. Hence, by processing the composites to near-complete density, with minimal structural degradation, further increases in the mechanical properties are possible. Low temperatures are necessary to minimize the reaction between the reinforcement and matrix phases. Porosity removal can then be enhanced at low temperatures in the presence of an applied stress, as was achieved through deformation-assisted sintering.

Mechanical property evaluation of the deformed materials indicates that the strength and ductility values obtained are comparable to that reported in the literature for these materials (compare Tables 2.5 and 2.6 with 7.6 and 7.7). Also, as compared to the properties of the sintered composites, the strength and ductility were markedly improved by deformation processing. The enhancement in the mechanical properties can be attributed to lower residual porosity, matrix microstructure modification and interfacial reaction minimization.

The greatest amount of porosity, roughly 20%, was observed for the materials deformed at 850°C and their strength and ductility values were just slightly below those obtained for the composites processed by sintering at 1300°C for four hours, which had approximately 15% porosity. A 100°C increase in the deformation temperature halved the porosity and improved the properties to the extent that the materials deformed at 950°C had strength and ductility values which surpassed the materials processed to less than 5% porosity by sintering at 1500°C for four hours. Therefore, albeit the higher density of the sintered material, the properties are inferior most probably on account of the differences in the microstructure of matrix or interface characteristics. For example, the unreinforced alloy sintered at 1500°C for four hours reveals substantial coarsening of the lamellar matrix microstructure as compared to the Ti-6%Al-4%V deformed at 950°C (Fig. 6.14 versus Fig. 7.16). For the composite material, the reinforcement phase in the composites processed at 1500°C have completely transformed from TiC to Ti_2C within a half hour, as revealed by the neutron diffraction patterns (Fig. 6.30) and the field emission gun SEM results (Figs. 6.19 and 6.20). Alternatively, the size of the interfacial boundary layer in the composites deformed at 950°C is less than 0.25 μm in size.

The effect of porosity on strength can be isolated for the unreinforced alloy deformed above the beta transus since the differences in the lamellar structure appear to be negligible. Using equation 2.22, the strength-porosity data for Ti-6%Al-4%V deformed above the beta transus temperature were fitted and values for k, σ_{o_y} and $\sigma_{o_{uts}}$ were determined to be 1.44, 882 MPa and 979 MPa. The lower value for k than expected (usually in the range of 2 to 10) suggests that incremental changes in porosity have a smaller effect on increases in strength for deformation processing temperatures above the beta transus. In fact, a similar analysis for Ti-6%Al-4%V deformed at temperatures between 850°C and 950°C gave 3.78 for k, which is close to that commonly reported.[172-173] (It should be mentioned that k has a temperature dependency.) Also, the pore-free yield and tensile strengths (σ_{o_y} and $\sigma_{o_{uts}}$) for lamellar Ti-6%Al-4%V processed by deforming above the beta transus temperature fall in the range of such properties obtained for lamellar structures produced by annealing and are superior to microstructures of cast and hot isostatically pressed materials (Table 2.5).

For the composites deformed above the beta transus temperature, a similar analysis using equation 2.22 gave a slightly lower k value of 1 for both 10 and 20 vol.% TiC. The pore-free yield and tensile strengths were 891 MPa and 995 MPa for the 10 vol.% TiC composites and 920 MPa and 1010 MPa for the 20 vol.% TiC composites. As compared to the properties reported in the literature for such fully dense composites (Table 2.6) the values for the yield strength are somewhat lower whilst the tensile strengths are similar.[27,147-150] However, considering that certain differences in the matrix microstructure are possible and the simplicity of the present analysis, the strength values projected for the pore-free composites appear to be in good agreement with the literature.

Besides porosity, the matrix microstructure of Ti-6%Al-4%V also influences the mechanical properties and the structure-property relationships are summarized in Table 2.4 and 2.5. Deforming the materials near the transus temperature enabled the formation of some equiaxed alpha, and the overall matrix microstructure was bimodal. The presence of the equiaxed alpha fraction was observed to increase the strength and ductility simultaneously, as indicated by the structure-property interdependencies given in Table 7.6 for the unreinforced alloy and Table 7.7 for the TiC_p reinforced Ti-6%Al-4%V. For the composites deformed above the beta transus temperature, presence of the particles altered the microstructure further through a change in orientation of the alpha lamellae. The colony orientation of the alpha plates in the unreinforced titanium alloy was observed to have a basket-weave or random appearance in the 10 vol.% or 20 vol.% TiC composites, respectively. As the changes in matrix microstructure are convoluted with porosity and reinforcement volume fraction differences, it is difficult to isolate the influence of the alpha orientation and aspect ratio on the properties. However previous work on microstructural modification in the Ti-6%Al-4%V has indicated that lower alpha aspect ratio increases the yield strength and tensile elongation while the ultimate tensile strength is unaffected.[53,279]

Also the initial reaction between TiC and Ti-6%Al-4%V, which leads to carbon dissolution into the titanium alloy, is likely to affect the properties of the matrix and as a result the composite (*e.g.* increases the yield and tensile strengths and decreases the ductility). Moreover, the size of the interfacial reaction layer influences the properties as indicated by the heat treatment experiments on the deformed composites (Fig. 7.31). An increase in the volume fraction of Ti_2C occurred with holding time at temperature and this was observed to degrade both the strength and ductility of the composites. It is interesting to compare the 20 vol.% TiC composite processed by sintering for four hours at 1300°C with that deformed at 1200°C (strain of 0.5 and strain rate of 0.0005 s^{-1}) and heat treated for 8 hours at 1100°C, as given in Table 8.1. Heat treatment of the as-deformed composites results in a substantial decrease in the yield and tensile strengths and a slight decrease in percent elongation. As the matrix microstructure and relative density are similar, the degradation in the mechanical properties appear to be an effect of an increase in the Ti_2C volume fraction from 3.2% to 14.5%. Comparing the composite sintered at 1300°C for four hours with the deformed and heat treated composite, it appears that the mechanical properties are influenced by factors besides the Ti_2C volume fraction and relative density. For a similar Ti_2C volume fraction, the projected pore-free yield and tensile strengths of the as-sintered composite are considerably lower than the deformed composite heat treated for eight hours at 1100°C. This may be an effect of the alpha orientation in the lamellar microstructure and/or the nature of the interfacial boundary region (*i.e.* diffuse and irregular in thickness for the sintered composites and uniform for the deformed composites).

The heat treatment studies indicate that bonding between the matrix and reinforcement phases must be achieved by means of a minimum reaction at the interface for optimum properties. Hence full density processing necessitates the use of deformation-assisted sintering. (In the case of the unreinforced alloy, full density processing by sintering alone may also be detrimental to the properties through microstructural coarsening.) Depending on the mechanical property requirements for the final application, the composite can be processed above and/or below the beta transus temperature to produce lamellar structures, equiaxed structures or combinations of these. Moreover, deformation processing of the composite below the beta transus temperature by 20°C to 30°C appears to produce refinement in the bimodal alpha-beta structure and results in improved mechanical properties. In general, the titanium-based materials produced by deformation-assisted processing had bimodal or lamellar microstructures with less than 5% porosity. The strength and ductility properties obtained were similar to those reported in the literature for such materials. Although the dynamic properties were not evaluated, the present work suggests that full density processing by deformation-assisted sintering near the beta transus of these composite materials shows promise for good overall properties.

Table 8.1 – Comparison of 20 vol.% TiC_p reinforced Ti-6%Al-4%V Composite

Property	Sintered 1300°C, 4 hours	As Deformed 1200°C, 0.5, 5E-4s^{-1}	As-Deformed plus Heat Treated 1100°C, 8 hours
Matrix Microstructure Alpha Lamellae	Colony	Basket-weave/Random	Basket-weave/Random
Relative Density (%)	90.2	99.5	99.9
Volume Fraction Ti_2C (%)	13.5	3.2	14.5
Yield Strength (MPa)	725	912	880
Tensile Strength (MPa)	765	999	958
Percent Elongation (%)	1.1	2.1	1.6
Pore-free YS* (MPa)	800	916	881
Pore-free UTS* (MPa)	843	1004	959

* Projected values calculated assuming k as 1 in equation 2.22.

CHAPTER 9

CONCLUSIONS

TiC particulate reinforced Ti-6%Al-4%V composites have been processed using two powder metallurgy processing techniques, namely elevated temperature pressureless sintering and hot deformation-assisted sintering. The following are the main conclusions from this work.

- Influence of the processing parameters (*e.g.* hold time, temperature, strain and strain rate, as applicable) on the densification behavior of the titanium-based composites has indicated that temperature has a greater effect than holding time (and strain and strain rate for deformation processing) on achieving consolidation. The main difference in the processing routes for the densification of the composites is that for a given density, the conditions for both the isothermal temperature and hold time are considerably reduced by deformation-assisted sintering as compared to sintering alone. This occurs because in deformation assisted sintering the applied stress enhances consolidation by being superimposed on the existing material transport mechanism, that is volume diffusion (by lattice and grain boundaries) in the case of the TiC-titanium alloy system.

- The incorporation of the reinforcement particles into the Ti-6%Al-4%V matrix was observed to increase the as-processed density by approximately 1 to 3% for every 5% increase in TiC volume fraction. This effect is attributed to an increasing green density and decreasing pore size with increasing TiC volume fraction because the particle size difference between the reinforcement and matrix powders enabled the accommodation of TiC in the void spaces amidst adjacent Ti-6%Al-4%V particles.

- For pressureless sintering, the influence of the processing parameters on the matrix microstructure was coarsening of the lamellar structure of plate-like alpha separated by interplate beta with increasing temperature and holding time. Incorporation of TiC reinforcement particles in Ti-6%Al-4%V was observed to homogenize the matrix microstructure and inhibit coarsening of the lamellar structure as evidenced by the finer alpha plates.

- Deformation-assisted sintering was performed at temperatures above and below the beta transus. As such, microstructural modification by hot working was greater than that by sintering alone because deforming the unreinforced alloy at temperatures in the single phase beta region achieved a lamellar structure, while in the two phase ($\alpha+\beta$) region combinations of lamellar and equiaxed structures formed.

- The addition of TiC reinforcement particles to the titanium alloy matrix was observed to change the orientation of the lamellar alpha plates in the composites processed above the beta transus temperature. The alpha lamellae change from a colony orientation in the unreinforced alloy to a basket-weave microstructure for the 10 vol.% TiC composite or randomly orientated in the 20 vol.% TiC composite. This progressive change in alpha plate orientation with increasing TiC volume fraction is a result of an increase in the nucleation sites for alpha in the presence of the reinforcement particles. Additionally, with increasing TiC volume fraction, the aspect ratio of the alpha plates was observed to decrease.

- Hot working the composites near the beta transus temperature was observed to refine the matrix microstructure of equiaxed and lamellar alpha. For the 10 vol.% TiC composites, hot deformation at 1000°C achieved an alpha plate size of approximately 5 μm, as compared to a 10 to 20 μm size for other processing conditions.

- Besides the matrix microstructure, the nature of interfacial reaction between the titanium alloy and the TiC particles was observed for the composites processed with and without deformation using low voltage field emission gun scanning electron microcopy. In the composites processed by sintering, the thickness of the uneven and diffuse interfacial boundary region increased rapidly with increasing temperature to the extent that the carbon composition of the entire reinforcement particle in the material sintered at 1500°C was nearly half that of the original TiC. By hot deformation processing, a uniform interfacial boundary layer was formed between the reinforcement and matrix and was less than 0.3 μm in thickness for the composites sintered to near-complete density.

- *In situ* neutron diffraction sintering studies of the TiC particulate reinforced Ti-6%Al-4%V composites revealed that the lattice parameter of the matrix phase initially increases with holding time for the various sintering temperatures (1100°C to 1350°C), which suggests carbon diffusion from the reinforcement to the matrix. Beyond the carbon solubility limit of the Ti-6%Al-4%V alloy, the appearance of distinctive peaks in the neutron diffraction patterns suggest the formation of a stable stoichiometric phase. Treating this phase as a face-centered cubic structure, the room temperature lattice parameter was determined to be 4.290-4.296Å with a fractional occupancy of carbon of 0.45 ± 0.04 and suggests a chemistry of Ti_2C. Analysis of the diffraction intensities of the various phases indicated that the growth of the Ti_2C interfacial phase most likely occurs by carbon diffusion from the TiC reinforcement particles, through the reaction zone and to the titanium alloy matrix. Complete transformation of the TiC reinforcement phase to Ti_2C was observed in the composites sintered at 1500°C.

- The visual observation of the interfacial region by low voltage scanning electron microscopy combined with the neutron diffraction results of a phase forming in the carbon-titanium alloy system support the existence and stability of Ti_2C, a phase having a distinct chemical composition and a face centered crystal structure. Moreover, chemical compositional analysis using energy dispersive spectroscopy at low accelerating voltage on the field emission gun SEM revealed abrupt changes in the carbon content in the region between the TiC reinforcement particle and the Ti-6%Al-4%V matrix. These findings support amendment of the existing titanium-carbon phase diagram to include the presence of stoichiometric Ti_2C at 12 wt.% carbon (or 33 at.%) up to temperatures of at least 1500°C.

- To assess the influence of the various microstructural features of the as-processed composites, the mechanical properties of the composites were evaluated using hardness and shear punch testing. To employ the shear punch testing technique for discontinuously reinforced composites, the punch load-displacement data wer correlated to the deformation features and the empirical relationship between the mechanical properties from shear punch testing and tensile testing was refined to include composite materials.

- For the composites processed by sintering only, porosity limited the strength and ductility at low temperatures, whilst these were limited during near-complete density consolidation at high temperatures by the extensive formation of the interfacial Ti_2C phase.

- Using deformation-assisted sintering, the titanium-based composites could be processed at lower temperatures (1000°C to 1100°C) to high relative densities (> 95%) and with a minimal interfacial reaction region (< 0.3 μm) between the matrix and reinforcement. The resultant mechanical properties of the deformed materials were comparable to those reported in the literature. Titanium-based materials having a bimodal matrix microstructure showed better strength and ductility properties as compared to lamellar matrix structures. Moreover it was observed that deformation processing at temperatures slightly below (20°C-30°C) the beta transus refined the microstructure and produced mixtures of equiaxed and lamellar (bimodal) structures. These were determined to give good strength and ductility combinations.

- Heat treatment studies of the deformed titanium-based composites indicated that the degradation in the mechanical properties that occurs with holding time at temperature is due to an increase in the volume fraction of Ti_2C. Full density processing should thus aim to achieve bonding between the matrix and reinforcement phases with minimal exposure to elevated temperatures to control the reaction at the interface and optimize the properties of the material.

RECOMMENDATIONS FOR FUTURE WORK

Although work in the literature exists on the processing and properties of TiC particulate reinforced Ti-6Al-4%V composites, the present work indicates that previous findings on the characteristics of the interface in such materials are flawed. The following suggestions are made to continue the present work on powder metallurgy processing of the TiC – titanium alloy system.

- Although the composites have been produced by deformation-assisted sintering to relative densities greater than 95%, full density was not achieved for the temperatures investigated. Future work on these materials should involve the application of higher strains to reach complete consolidation in the materials.

- The influence of the certain microstructural aspects of the matrix on the mechanical properties is pending. Specifically, the change in aspect ratio and orientation of the alpha plates on the static properties of the composite material should be assessed. For varying the matrix microstructure in full density materials, double hit compression testing may be of particular interest. Essentially such testing could involve applying an initial deformation at a temperature above the beta transus to remove the porosity rapidly and standardize the initial microstructure and a second deformation below the transus to tailor the microstructure.

- The beta transus temperature of the Ti-6Al-4%V alloy used in this work was determined accurately by means of neutron diffractometry. However, the change in the beta transus temperature for the 10 vol.% and 20 vol.% TiC particulate reinforced composite materials needs to be investigated. Essentially, with carbon diffusion from the reinforcement particle to the matrix, the beta transus temperature of the titanium alloy will increase until the matrix reaches the solid solubility limit for carbon. Hence, during deformation-assisted sintering the beta transus temperature is increasing asymptotically and a processing temperature which initially is above the beta transus may fall below the beta transus upon interaction of the reinforcement and matrix phases. This leads to considerable uncertainty in the processing of the titanium-based composite materials and in determining the transpiration of the various microstructural features.

- In this work, the strength and ductility after synthesis of the titanium-based materials were assessed and compared to that of the literature. The static properties obtained appear to correlate satisfactorily with those of previous investigators and thus the dynamic properties of these materials should be considered for investigation, especially since certain applications necessitate good fracture toughness and fatigue behavior.

- The formation and characteristics of the interfacial region examined in this work indicate that the reaction between the matrix and reinforcement phase leads to the evolution of stoichiometric Ti_2C, which has a lattice parameter value at room temperature of 4.290-4.296 Å for the face centered cubic crystal structure. An investigation of the nature of the ordering of the vacancies in the Ti_2C phase as well as the stability range of this composition should be examined by preparing binary titanium-carbon alloys in the composition range from Ti_2C to TiC for high temperature studies *in situ* in a neutron powder diffractometer. Microstructural work to complement this investigation should be performed using the low voltage technique on a field emission gun SEM to differentiate between the TiC and Ti_2C phases. This fundamental examination should resolve the uncertainties in the equilibrium phase diagram for the titanium-carbon system.

STATEMENT OF ORIGINALITY AND CONTRIBUTIONS TO KNOWLEDGE

---

1. The first comprehensive examination of the transient reaction occurring during sintering of the TiC particulate reinforced Ti-6%Al-4%V composite system.

2. The use of low voltage microscopy on a field emission gun scanning electron microscope to resolve for the first time the interfacial reaction region on the periphery of the reinforcement particles.

3. The monitoring of the sintering process using a neutron diffractometer to examine the formation and growth of the interface reaction products.

4. The interfacial interaction between the matrix and reinforcement phases was distinguished and characterized. The reaction was shown to consist of carbon dissolution into the Ti-6%Al-4%V alloy followed by the formation of a stoichiometric compound having a face centered cubic crystal structure and a lattice parameter value corresponding to a composition of Ti_2C.

5. Subsequent growth of the interface was determined to occur by further diffusion of carbon from the TiC reinforcement particles, through the Ti_2C boundary layer to the titanium alloy matrix.

6. Unequivocal evidence for the existence and stability of stoichiometric Ti_2C up to temperatures of 1500°C which supports amending the existing titanium-carbon phase diagram to include Ti_2C at 12 weight percent (or 33 atomic percent) carbon.

7. Development of a technique to refine the microstructure of the Ti-6%Al-4%V matrix by hot deformation processing the TiC particulate reinforced composites at temperatures slightly below the beta transus.

8. Extension of the shear punch small specimen test to include the assessment of tensile mechanical properties of discontinuously reinforced composites.

9. *In situ* measurements of the lattice parameter for the beta phase of the Ti-6%Al-4%V alloy at temperatures in the range of 1000°C to 1350°C.

REFERENCES

1. F.L. Matthews and R.D. Rawlings, Composite Materials: Engineering and Science, Chapman and Hall, London, United Kingdom, 1994, p.3
2. G.F. Carter and D.E. Paul, Materials Science and Engineering, ASM International, Materials Park, Ohio, USA, 1991, p. 259.
3. B. Harris, "A Perspective View of Composite Materials Development", *Materials and Design*, October 1991, Vol. 12, No. 5, pp. 259-272.
4. A.M. Ramírez and E.V. Barrera, "Composite Materials", Synthesis and Properties of Advanced Materials, Eds. C. McHargue, J.B. Darby, M.J. Yacamán and J.R. Gasga, Kluwer Academic Publishers, Boston, Massachusetts, USA, 1997, pp. 149-194.
5. J.E. Schoutens, "Metal Matrix Composite Materials Today", *Journal of Metals*, June 1985, Vol. 37, No. 6, p. 43.
6. D.W. Richerson, Modern Ceramic Engineering, Second Edition, Marcel Dekker Inc., New York, New York, USA, 1992, pp. 731-801.
7. I.A. Ibrahim, F.A Mohamed and E.J. Lavernia, "Particulate Reinforced Metal Matrix Composites - A Review", *Journal of Materials Science*, March 1991, Vol. 26, No. 5, pp. 1137-1156.
8. J.A. Black, "Shaping Reinforcements for Composites", *Advanced Materials and Processes*, March 1988, Vol. 133, No. 3, pp. 51-54.
9. J.A. DiCarlo, "Fibers for Structurally Reliable Metal and Ceramic Composites", *Journal of Metals*, June 1985, Vol. 37, No. 6, pp. 44-49.
10. M.E. Buck, "Advanced Fibers for Advanced Composites", *Advanced Materials and Processes*, September 1987, Vol. 132, No. 3, pp. 61-65.
11. K.K. Chawla, P.K Liaw and S.G. Fishman, "High-Performance Composites: Commonality of Phenomena", *Journal of Metals*, February 1996, Vol. 48, No. 2, pp. 43-44.
12. E.J. Kubel Jr., "Reinforced Polymer Composites on the Move", *Advanced Materials and Processes*, May 1988, Vol. 133, No. 5, pp. 29-35.
13. F.H. Froes, "Is It Time to Throw in the Towel on Advanced Materials", *Journal of Metals*, March 1995, Vol. 47, No. 3, p. 12.
14. E.J. Kubel Jr., "A Composites 'Wish List'", *Advanced Materials and Processes*, October 1987, Vol. 132, No. 4, pp. 47-54.
15. T.W. Eagar, "Whither Advanced Materials?", *Advanced Materials and Processes*, June 1991, Vol. 139, No. 6, pp. 25-29.
16. L.M. Sheppard, "On The Road With Composites", *Advanced Materials and Processes*, December 1986, Vol. 130, No. 6, pp. 36-41.
17. E.P. Scala, "A Brief History of Composites in the U.S. - The Dream and the Success", *Journal of Metals*, February 1996, Vol. 48, No. 2, pp. 45-48.

18. P.R. Smith and F.H. Froes, "Developments in Titanium Metal Matrix Composites", *Journal of Metals*, March 1984, Vol. 36, No. 3, pp. 19-26.

19. R. Bushby and V. Scott, "Aluminium Composites Rediscovered", *Materials World*, February 1997, Vol. 5, No. 2, pp. 79-82.

20. D.J. Lloyd, "Particulate Reinforced Aluminium and Magnesium Matrix Composites", *International Materials Reviews*, 1994, Vol. 39, No. 1, pp. 1-23.

21. P. Rohatgi and R. Asthana, "The Solidification of Metal-Matrix Particulate Composites", *Journal of Metals*, May 1991, Vol. 43, No. 5, pp. 35-41.

22. A.L. Geiger and J.A. Walker, "The Processing and Properties of Discontinuously Reinforced Aluminum Composites", *Journal of Metals*, August 1991, Vol. 43, No. 8, pp. 8-15.

23. P. Niskanen and W.R. Mohn, "Versatile Metal Matrix Composites", *Advanced Materials and Processes*, March 1988, Vol. 133, No. 3, pp. 39-41.

24. I.W. Hall, J.-L. Lim and J. Rizza, "Interfacial Reactions in Titanium Matrix Composites", *Journal of Materials Science Letters*, March 1991, Vol. 10, No. 5, pp. 263-266.

25. M. Hunt, "Aerospace Composites", *Materials Engineering*, June 1991, Vol. 108, No. 6, pp. 27-30.

26. D.G. Konitzer and M.H. Loretto, "Microstructural Study of Ti-Based TiC Metal Matrix Composites", Sixth World Conference on Titanium, (Cannes, France), Eds. P. Lacombe, R. Tricot and G. Béranger, Les Éditions Physique, Les Ulis, France, 1988, pp. 1057-1062.

27. S. Abkowitz and P. Weihrauch, "Trimming the Cost of MMCs", *Advanced Materials and Processes*, July 1989, Vol. 136, No. 1, pp. 31-34.

28. J. Chen, Z. Geng and B.A. Chin, "The Tensile Properties and Microstructure of Ti-TiC Composites with Al Additions", High-Temperature Ordered Intermetallic Alloys III, Materials Research Society Symposium Proceedings, Volume 133, Eds. C.T. Liu, A.I. Taub, N.S. Stollof and C.C. Koch, Materials Research Society, Pittsburgh, Pennsylvania, USA, 1989, pp. 447-452.

29. D.G. Konitzer and M.H. Loretto, "Microstructural Assessment of Interaction Zone in Titanium Aluminide/TiC Metal Matrix Composite", *Materials Science and Technology*, July 1989, Vol. 5, No. 7, pp. 627-631.

30. D.G. Konitzer and M.H. Loretto, "Interfacial Reactions in Titanium-based Metal Matrix Composites", *Materials Science and Engineering A: Structural Materials: Properties, Microstructure and Properties*, January 1989, Vol. A107, No. 1-2, pp. 217-223.

31. R.Y. Lin, "Composite Interfacial Reactions", *Journal of Metals*, March 1993, Vol. 45, No. 3, p. 20.

32. J.A. DeKock and Y.A. Chang, "The Stability of Interfaces in High-Temperature Metal Matrix Composites", *Journal of Metals*, March 1993, Vol. 45, No. 3, pp. 21-23.

33. R. Mitra and Y.R. Mahajan, "Interfaces in Discontinuously Reinforced Metal Matrix Composites: An Overview", *Bulletin of Materials Science (India)*, August 1995, Vol. 18, No. 4, pp. 405-434.

34. S. Ochiai and Y. Murakami, "Theoretical Prediction of the Tensile Strength of Fibres with Brittle Layers on Their Surfaces", *Zeitschrift für Metallkunde*, December 1981, Vol. 72, No. 12, pp. 827-831.

35. S. Ochiai and Y. Murakami, "Tensile Strength of Composites with Brittle Reaction Zones at Interfaces", *Journal of Materials Science*, April 1979, Vol. 14, No. 4, pp. 831-840.

36. D.K. Hale, "The Physical Properties of Composite Materials", *Journal of Materials Science*, November 1976, Vol. 11, No. 11, pp. 2105-2141.

37. R. Phillips, "The Modeling of Interfaces: Atoms or Continua?", *Journal of Metals*, March 1995, Vol. 47, No. 3, pp. 37-42.

38. A.G. Metcalfe and M.J. Klein, "Compatible Alloys for Titanium Matrix Composites", Titanium Science and Technology, Vol.4, Eds. R.I. Jaffee and H.M. Burte, Plenum Press, New York, New York, USA, 1973, pp. 2285-2297.

39. M. Kobayashi and M. Miyagawa, "Research and Development of Superplastic Materials - Recent Progresses and Future Prospects", *Transactions of the Iron and Steel Institute of Japan (ISIJ) International*, September 1987, Vol. 27, No. 9, pp. 685-695.

40. H. Onodera, K. Ohno, T. Yamagata and M. Yamazaki, "Design of Titanium Alloys Suitable for Superplastic Forming", *Transactions of the Iron and Steel Institute of Japan (ISIJ) International*, September 1987, Vol. 27, No. 9, p. B-238 (Presented at 113th ISIJ Meeting, April 1987, Lecture No. S693).

41. K. Yang, Z.X. Guo and D.V. Edmonds, "Processing of Titanium Matrix Composites with Hydrogen as a Temporary Alloying Element", *Scripta Metallurgica et Materialia*, December 1992, Vol. 27, No. 12, pp. 1695-1700.

42. F.H. Froes, D. Eylon and C. Suryanarayana, "Thermochemical Processing of Titanium Alloys", *Journal of Metals*, March 1990, Vol. 42, No. 3, pp. 26-29.

43. O.N. Senkov, J.J. Jonas and F.H. Froes, "Recent Advances in the Thermohydrogen Processing of Titanium Alloys - Recent Progresses and Future Prospects", *Journal of Metals*, July 1996, Vol. 48, No. 7, pp. 42-47.

44. D. Eylon, "Beta Titanium Alloys - An Overview", Proceedings of the 1st International Symposium on Metallurgy and Technology of Practical Titanium Alloys, (Chiba, Japan)), Eds. S. Fujishiro, D. Eylon and T. Kishi, TMS, Warrendale, Pennsylvania, USA, 1994, pp. 29-36.

45. G.V. Aleksandrova, M.I. Yermolova and N.F. Zhebyneva, "Ductility of the Metastable Phases in Titanium Alloys", *Physics of Metals and Metallography (Poland)*, 1986, Vol. 62, No. 4, pp. 177-180.

46. ASM International Handbook Committee, ASM Handbook - Alloy Phase Diagrams, Vol. 3, ASM International, Materials Park, Ohio, USA, 1992, p. 4·12.

47. E.W. Collings, The Physical Metallurgy of Titanium Alloys, American Society for Metals, Metals Park, Ohio, USA, 1984, pp. 39-74.

48. J.J. Rausch, F.A. Crossley and H.D. Kessler, "Titanium-Rich Corner of the Ti-Al-V System", *Journal of Metals*, February 1956, Vol.8, pp. 211-214.

49. S.M.L Sastry, P.S. Pao and K.K Sankaran, "High Temperature Deformation of Ti-6Al-4V", Titanium 80' Science and Technology, Proceedings of the Fourth International Conference on

Titanium, (Kyoto, Japan), Eds. H. Kimura and O. Izumi, AIME, Warrendale, Pennsylvania, USA, 1980, pp. 873-886.

50. M. Peters, G. Lütjering and G. Ziegler, "Control of Microstructures of ($\alpha+\beta$)-Titanium Alloys", *Zeitschrift für Metallkunde*, May 1983, Vol. 74, No. 5, pp. 274-282.

51. B. de Gélas, L. Sèraphin, R. Tricot and R. Castro, "Etude des Traitements Thermomèchaniques de l'Alliage de Titane TA6V", *Revue de Métallurgie*, January 1974, pp. 51-81.

52. H.M. Flower, "Microstructural Development in Relation to Hot Working of Titanium Alloys", *Materials Science and Technology*, November 1990, Vol.6, No. 9, pp. 1082-1092.

53. I. Weiss, F.H. Froes, D. Eylon and G.E. Welsch, "Modification of Alpha Morphology in Ti-6Al-4V by Thermomechanical Processing", *Metallurgical Transactions A*, November 1986, Vol. 17A, No. 11, pp. 1935-1947.

54. F.H. Froes and D. Eylon, "Powder Metallurgy of Titanium Alloys", *International Materials Reviews*, 1990, Vol. 35, No. 3, pp. 162-182.

55. L. Guozhen, Z. Quanpu and D. Ju, "The Research and Development of TMCs", Titanium '95-Science and Technology, Vol.3, Proceedings of the Eighth World Conference on Titanium, (Birmingham, Great Britain), Eds. P.A. Blenkinsop, W.J. Evans and H.M. Flower, The Institute of Materials, London, United Kingdom, 1996, pp. 2704-2713.

56. B. Meddings, H.R. Huffman and V.N. Mackiw, "Technology and Application of Coated Powders", New Types of Metal Powders, Ed. H.H. Hausner, Gordon and Breach Science Publishers, New York, New York, USA, 1964, pp. 28-44.

57. D.G. Konitzer, J.T. Stanley, M.H. Loretto and H.L. Fraser, "The Nature of Dispersed Phases in Ti-0.7 at.% Er Prepared by Rapid Solidification Processing", *Acta Metallurgica*, July 1986, Vol. 34, No. 7, pp. 1269-1277.

58. A.G. Jackson, J. Moteff and F.H. Froes, "Advanced Titanium Alloy Development Via Powder Metallurgy", Powder Metallurgy of Titanium Alloys, Proceeding of a Symposium at 109th AIME Annual Meeting, (Las Vegas, Nevada, USA), Eds. F.H. Froes and J.E. Smugeresky, AIME, New York, New York, USA, 1980, pp. 229-241.

59. R.E. Tressler and T.L. Moore, "Mechanical Property and Interface Reaction Studies of Titanium-Alumina Composites", *Metals Engineering Quarterly*, February 1971, Vol. 11, No.1, pp. 16-22.

60. Y.-C. Lu, S.L. Sass, Q. Bai, D.L. Kohlstedt and W. Gerberich, "The Influence of Interfacial Reactions on the Fracture Toughness of Ti-Al_2O_3 Interfaces", *Acta Metallurgica et Materialia*, January 1995, Vol. 43, No. 1, pp. 31-41.

61. S.K. Choi, M. Chandrasekaran and M.J. Brabers, "Interaction Between Titanium and SiC", *Journal of Materials Science*, April 1990, Vol. 25, No. 4, pp. 1957-1964.

62. T. Christman, K. Heady and T. Vreeland Jr., "Consolidation of Ti-SiC Particle-Reinforced Metal Matrix Composites", *Scripta Metallurgica et Materialia*, March 1991, Vol. 25, No. 3, pp. 631-636.

63. S. Mridha, H.S. Ubhi, P. Holdway, T.N. Baker and A.W. Bowen, "Metal-Ceramic Composite Layer Formation on Titanium Surfaces Through Laser Treatment", Titanium '92-Science and Technology, Vol.3, Proceedings of the Seventh World Titanium Conference, (San Diego, CA,

USA), Eds. F.H. Froes and I.L. Caplan, TMS, Warrendale, Pennsylvania, USA, 1993, pp. 2641-2648.

64. A.J. Reeves, R. Taylor and T.W. Clyne, "The Effect of Interfacial Reaction on Thermal Properties of Titanium Reinforced with Particulate SiC", *Materials Science and Engineering A: Structural Materials: Properties, Microstructure and Properties*, July 1991, Vol. A141, No. 1, pp. 129-138.

65. I. Gotman and E.Y. Gutmanas, "Interaction of Si_3N_4 with Titanium Powder", *Journal of Materials Science Letters*, July 1990, Vol. 9, No. 7, pp. 813-815.

66. A.J. Todhunter and B. Ben-Nissan, "Finite Element Modelling of a Metal-Ceramic Interface", *Key Engineering Materials*, Proceedings of the International Ceramics Conference, AustCeram '90, Eds. P.J. Darragh and R.J. Stead, Vol. 53-55, Trans Tech Publications, Brookfield, Vermont, USA, 1991, pp. 107-110.

67. T. Koga, M. Mizuno and M. Nagumo, "Structural and Mechanical Properties of Fine Composites Prepared by Ti-Si_3N_4 Solid State Reactions", *Materials Science and Engineering A: Structural Materials: Properties, Microstructure and Properties*, May 1994, Vol. A179-A180, No. 1, pp. 153-157.

68. T. Namura, M. Nagumo, Y. Matsumoto, N. Sasaki and K. Ameyama, "Superplastic Behavior of Composites Prepared from Mechanically Alloyed Ti-Si_3N_4 Powders", *Materials Science Forum*, 1997, Vol. 233-234, pp. 251-260.

69. E.N.T. Jong, H.M. Flower and D.R.F. West, "Interfacial Reaction Kinetics in α- and β-Titanium Based Metal Matrix Composites", Titanium '92-Science and Technology, Vol.3, Proceedings of the Seventh World Titanium Conference, (San Diego, CA, USA), Eds. F.H. Froes and I.L. Caplan, TMS, Warrendale, Pennsylvania, USA, 1993, pp. 2561-2568.

70. J.H. Abboud and D. R. F. West, "Titanium/Ceramic Composites Produced by Laser Processing", Titanium '92-Science and Technology, Vol. 3, Proceedings of the Seventh World Titanium Conference, (San Diego, CA, USA), Eds. F. H. Froes and I. L. Caplan, TMS, Warrendale, Pennsylvania, USA, 1993, pp. 2503-2510.

71. S.P. Turner, R. Taylor, F.H. Gordon and T.W. Clyne, "Thermal Conductivities of Ti-SiC and Ti-TiB_2 Particulate Composites", *Journal of Materials Science*, July 1993, Vol. 28, No. 14, pp. 3969-3979.

72. A.J. Reeves, W.M. Stobbs and T.W. Clyne, "The Effect of Interfacial Reaction on the Mechanical Behaviour of Ti Reinforced with SiC and TiB_2 Particles", Metal Matrix Composites Processing, Microstructure, and Properties, Proceedings of 12th International Risø Symposium on Metallurgy and Materials Science, (Roskilde, Denmark), Eds. N. Hansen, D.J. Jensen, T. Leffers, H. Lilholt, T. Lorentzen, A. S. Pedersen, O. B. Pedersen, and B. Ralph, Risø National Laboratory, Roskilde, Denmark, 1991, pp. 631-636.

73. S.J. Zhu, Y.X. Lu, Z.G. Wang and J. Bi, "Creep Behaviour of TiB_2-Whisker and TiC-Particulate Reinforced Ti-6Al-4V Composite at Elevated Temperatures", Metal Matrix Composites, Vol.1, Proceeding of the 9th International Conference on Composite Materials (ICCM-9), (Madrid, Spain), Ed. A. Miravete, Published by University of Zaragoza, Zaragoza, Spain, 1993, pp. 549-556.

74. M. Hagiwara, S. Emura, Y. Kawabe, N. Arimoto and S. Mori, "Mechanical Properties of Ceramic Particulates-Reinforced Titanium-Based Composites Produced by Blended Elemental

Powder Metallurgy", Proceedings of Light Materials for Transportation Systems Conference, (Kyongju, Korea), Ed. N.J. Kim, Published by Pohang University of Science and Technology, Pohang, Korea, 1993, pp. 903-910.

75. Z. Fan, H.J. Niu, A.P. Miodownik, T. Saito and B. Cantor, "Microstructure and Mechanical Properties of *in situ* Ti/TiB MMCs Produced by a Blended Elemental Powder Metallurgy Method", *Key Engineering Materials*, Proceeding of the 1st International Conference on Ceramic and Metal Matrix Composites, CMMC96, Part I, (San Sebastián, Spain), Eds. M. Fuentes, J.M. Martínez-Esnaola and A.M. Daniel, Vol. 127-131, Trans Tech Publications, Enfield, New Hampshire, USA, 1997, pp. 423-430.

76. Z. Fan, H.J. Niu, B. Cantor, A.P. Miodownik and T. Saito, "Effect of Cl on Microstructure and mechanical Properties of *in situ* Ti/TiB MMCs Produced by a Blended Elemental Powder Metallurgy Method", *Journal of Microscopy*, February 1997, Vol. 185, Part 2, pp. 157-167.

77. T. Saito, T. Furuta and H. Takamiya, "Sintering Behaviour and Thermal Stability of a TiB Particle reinforced PM Beta-Titanium Matrix Composite", Titanium '95-Science and Technology, Vol.3, Proceedings of the Eighth World Conference on Titanium, (Birmingham, Great Britain), Eds. P.A. Blenkinsop, W.J. Evans and H.M. Flower, The Institute of Materials, London, United Kingdom, 1996, pp. 2763-2770.

78. M. Hagiwara, S. Emura, Y. Kawabe and S.-J. Kim, "In-Situ Reinforced Titanium-Based Metal Matrix Composites", Synthesis/Processing of Lightweight Metallic Materials, Proceedings of 124th TMS Annual Meeting, (Las Vegas, Nevada), Eds. F.H. Froes, C. Suryanarayana and C.M. Ward-Close, TMS, Warrendale, Pennsylvania, USA, 1995, pp. 97-106.

79. K. Funami, M. Kobayashi, S. Suzuki and C. Ouchi, "Superplasticity of Fine TiB Dispersed Ti-6Al-4V Alloy Composites Obtained by Reaction Sintering", *Materials Science Forum*, 1997, Vols. 243-245, pp. 515-520.

80. W.O. Soboyejo, R.J. Lederich and S.M.L. Sastry, "Mechanical Behavior of Damage Tolerant TiB Whisker-Reinforced *In Situ* Titanium Matrix Composites", *Acta Metallurgica et Materialia*, August 1994, Vol. 42, No. 8, pp. 2579-2591.

81. J.A. Philliber, F.-C. Dary, F.W. Zok and C.G. Levi, "Flow and Creep Behavior of Ti/TiB *In-Situ* Composites", Titanium '95-Science and Technology, Vol.3, Proceedings of the Eighth World Conference on Titanium, (Birmingham, Great Britain), Eds. P.A. Blenkinsop, W.J. Evans and H.M. Flower, The Institute of Materials, London, United Kingdom, 1996, pp. 2714-2721.

82. M. Kobayashi, S. Ochiai, K. Funami, C. Ouchi and S. Suzuki, "Superplasticity of Fine TiC and TiN Dispersed Ti-6Al-4V Alloy Composites", *Materials Science Forum*, 1994, Vol. 170-172, pp. 549-554.

83. M. Hagiwara, S. Emura, Y. Kawabe, N. Arimoto and S. Mori, "Properties of P/M Processed Titanium Alloy/Particulate Composites", Proceedings of the 1st International Symposium on Metallurgy and Technology of Practical Titanium Alloys, (Chiba, Japan), Eds. S. Fujishiro, D. Eylon and T. Kishi, TMS, Warrendale, Pennsylvania, USA, 1994, pp. 363-370.

84. M. Hagiwara, S. Emura, J. Takahashi, Y. Kawabe and N. Arimoto, "Microstructures and Properties of Titanium-Based Composites Produced by Powder Metallurgy", Titanium '92-Science and Technology, Vol. 3, Proceedings of the Seventh World Titanium Conference, (San

Diego, CA, USA), Eds. F. H. Froes and I. L. Caplan, TMS, Warrendale, Pennsylvania, USA, 1993, pp. 2487-2497.

85. J. Morgiel and E. Benko, "Microstructure of Boron Nitride Sintered with Titanium", *Materials Letters*, October 1995, Vol. 25, No. 1-2, pp. 49-52.

86. H. Shinoaki, T. Kitada, K. Tokumoto and S. Sakaguchi, "Development of Sintered Titanium Base Hard Alloy", *Nippon Tungsten Review*, 1992, Vol. 25, pp. 27-32.

87. J.M. Panchal and T. Vela, "Wear Resistant Titanium-Titanium Carbide Composites For Lightweight Applications", Advances in Powder Metallurgy, Proceedings of the Powder Metallurgy Conference and Exhibition, (Pittsburgh, PA, USA), Vol. 2, Eds. E.R. Andreotti and P.J. McGeeham, Metal Powder Industries Federation, Princeton, New Jersey, USA, 1990, pp. 497-515.

88. B.A. Chin, Y. Lin and R.H. Zee, "Novel 3-D TiC Reinforced TiAl and Alpha Ti Alloys", Proceedings of 6th Japan Institute of Metals International Symposium on Intermetallic Compounds - Structure and Mechanical Properties (JIMIS-6), Ed. O. Izumi, Japan Institute of Metals, Sendai, Japan, 1991, pp. 967-971.

89. S. Débouzy, Sintering of Ti-TiC Metal Matrix Composites, Masters Thesis, McGill University, Montreal, Quebec, Canada, 1994.

90. T.W. Clyne and H.M. Flower, "Titanium Based Composites", Titanium '92-Science and Technology, Vol. 3, Proceedings of the Seventh World Titanium Conference, (San Diego, CA, USA), Eds. F. H. Froes and I. L. Caplan, TMS, Warrendale, Pennsylvania, USA, 1993, pp. 2467-2478.

91. W.D. Kingery, H.K. Bowen and D.R. Uhlmann, Introduction to Ceramics, Second Edition, John Wiley and Sons Inc., New York, New York, USA, 1976, p. 777.

92. T. Saito, "A Cost-Effective P/M Titanium Matrix Composite for Automobile Use", *Advanced Performance Materials*, June 1995, Vol. 2, No. 2, pp. 121-144.

93. A.J. Reeves, H. Dunlop and T.W. Clyne, "The Effect of Interfacial Reaction Layer Thickness on Fracture of Titanium-SiC Particulate Composites", *Metallurgical Transactions A*, March 1992, Vol. 23A, No. 3, pp. 977-988.

94. S. Mridha, C. Hu, H.S. Ubhi, A.W. Bowen and T.N. Baker, "Characteristic Features of the MMC Layer Formed on Ti-6Al-4V (IMI318) Alloy Surfaces Through Laser Treatment by Using SiC Powder Injection and Preplacement Techniques", Titanium '95-Science and Technology, Vol.3, Proceedings of the Eighth World Conference on Titanium, (Birmingham, Great Britain), Eds. P.A. Blenkinsop, W.J. Evans and H.M. Flower, The Institute of Materials, London, United Kingdom, 1996, pp. 2835-2842.

95. W. Tong, G. Ravichandran, T. Christman and T. Vreeland Jr., "Processing SiC-Particulate Reinforced Titanium-Based Metal Matrix Composites By Shock Wave Consolidation", *Acta Metallurgica et Materialia*, January 1995, Vol. 43, No. 1, pp. 235-250.

96. M. Saqib, I. Weiss, G.M. Mehrotra, E. Clevenger, A.G. Jackson and H.A. Lipsitt, "Microstructural and Thermal Stability of Ti-43Al Alloy Containing Dispersoids of Titanium Di-Boride", *Metallurgical Transactions A*, August 1991, Vol. 22A, No. 8, pp. 1721-1728.

97. S.L. Kampe, P. Sadler, L. Christodoulou and D.E. Larsen, "Room Temperature Strength and Deformation of TiB_2-Reinforced Near-γ Titanium Aluminides", *Metallurgical and Materials Transactions A*, October 1994, Vol. 25A, No. 10, pp. 2181-2197.

98. O. Popoola, C. Cordier, P. Pirouz and A.H. Heuer, "On Interface and twin Boundaries in a Forged Ti-47Al/TiB_2 Alloy", *Scripta Metallurgica et Materialia*, October 1992, Vol. 26, No. 10, pp. 1643-1648.

99. C.F. Yolton and J.H. Moll, "Evaluation of a Discontinuously Reinforced Ti-6Al-4V Composite", Titanium '95-Science and Technology, Vol.3, Proceedings of the Eighth World Conference on Titanium, (Birmingham, Great Britain), Eds. P.A. Blenkinsop, W.J. Evans and H.M. Flower, The Institute of Materials, London, United Kingdom, 1996, pp. 2755-2762.

100. P.S. Goodwin, A. Wisbey, H.S. Ubhi, Z. Kulikowski and C.M. Ward-Close, "Synthesis of Particulate Reinforced Titanium MMC By Mechanical Alloying", Titanium '95-Science and Technology, Vol.3, Proceedings of the Eighth World Conference on Titanium, (Birmingham, Great Britain), Eds. P.A. Blenkinsop, W.J. Evans and H.M. Flower, The Institute of Materials, London, United Kingdom, 1996, pp. 2874-2875.

101. T. Saito, T. Furuta and T. Yamaguchi, "Development of Low Cost Titanium Matrix Composite", Recent Advances in Titanium Metal Matrix Composites, (Rosemont, Illinois), Eds. F.H. Froes and J. Storer, TMS, Warrendale, Pennsylvania, USA, 1995, pp. 33-44.

102. T. Saito, H. Takamiya and T. Furuta, "Hot Workability and Mechanical Properties of a TiB Particle Reinforced PM Beta-Titanium Matrix Composite", Titanium '95-Science and Technology, Vol.3, Proceedings of the Eighth World Conference on Titanium, (Birmingham, Great Britain), Eds. P.A. Blenkinsop, W.J. Evans and H.M. Flower, The Institute of Materials, London, United Kingdom, 1996, pp. 2859-2866.

103 T. Furuta, and T. Saito, "Fatigue Properties of TiB Particle Reinforced PM Titanium Matrix Composite", Proceedings of the Fourth International Conference on P/M Aerospace, defense and Demanding applications, Ed. F.H. Froes, Metal Powder Industries Federation, Princeton, New Jersey, USA, 1995, pp. 173-180.

104. Z. Fan, A.P. Miodownik, L. Chandrasekaran and M. Ward-Close, "The Young's Moduli of In Situ Ti/TiB Composites Obtained by Rapid Solidification Processing", *Journal of Materials Science*, Feb 15 1994, Vol. 29, No. 4, pp. 1127-1134.

105. Z. Fan, A.P. Miodownik, L. Chandrasekaran and M. Ward-Close, "The Effect of pre-Consolidation Heat Treatment on TiB Morphology and Mechanical Properties of rapidly Solidified Ti-6Al-4V-XB Alloys", *Scripta Metallurgica et Materialia*, March 15 1995, Vol. 32, No. 6, pp. 833-838.

106. R.L. Sands and C.R. Shakespeare, Powder Metallurgy Practice and Application, George Newnes Limited, London, United Kingdom, 1966, p. 34.

107. T. Saito, T. Furuta and T. Yamaguchi, "A Low Cost Titanium Alloy Matrix Composite", Proceedings of the 1st International Symposium on Metallurgy and Technology of Practical Titanium Alloys, (Chiba, Japan), Eds. S. Fujishiro, D. Eylon and T. Kishi, TMS, Warrendale, Pennsylvania, USA, 1994, pp. 351-362.

108. T.W. Clyne and P.J. Withers, An Introduction to Metal Matrix Composites, Cambridge University Press, Cambridge, United Kingdom, 1993, p. 191.

109. W.D. Callister, Materials Science and Engineering: An Introduction, John Wiley and Sons Inc., New York, New York, USA, 1994, (a) pp. 767-768 and (b) pp. 513-540.

110. D.G. Konitzer and M.H. Loretto, "Microstructural Assessment of Ti6Al4V-TiC Metal-Matrix Composite", *Acta Metallurgica et Materialia*, February 1989, Vol. 37, No. 2, pp. 397-406.

111. M. Gu, E. Jiang and G. Zhang, "Quantitative Analysis of Interfacial Chemistry in TiC/Ti Composite Using Electron-Energy-Loss Spectroscopy", *Metallurgical and Materials Transactions A*, June 1995, Vol. 26A, No. 6, pp. 1595-1597.

112. ASM International Handbook Committee, ASM Handbook - Alloy Phase Diagrams, Vol. 3, ASM International, Materials Park, Ohio, USA, 1992, p. 2·114.

113. I. Cadoff and J.P. Nielson, "Titanium-Carbon Phase Diagram", *Transactions of the AIME (Journal of Metals)*, February 1953, Vol. 197, pp. 248-252.

114. H.R. Ogden, R.I. Jaffee and F.C. Holden, "Structure and Properties of Ti-C Alloys", *Transactions of the AIME (Journal of Metals)*, January 1955, Vol. 203, pp. 73-80.

115. J.L. Murray, "C-Ti (Carbon-Titanium)", Binary Alloy Phase Diagrams, eds. J.L. Murray, L.H. Bennett and H. Baker (Editor-Chief T.B. Massalski), ASM, Metals Park, Ohio, USA, 1986, pp. 593-596.

116. J.L. Murray, "The C-Ti (Carbon-Titanium) System", Phase Diagrams of Binary Titanium Alloys, (Monograph Series on Alloy Phase Diagrams), ed. J.L. Murray (Editor-Chief T.B. Massalski), ASM International, Metals Park, Ohio, USA, 1987, pp. 47-51.

117. H. Goretzki, "Neutron Diffraction Studies on Titanium-Carbon and Zirconium-Carbon Alloys", *Physica Status Solidi*, 1967, Vol. 20 pp. K141-K143.

118. N.N. Kurnakov and M.Ya. Troneva, "Equilibrium Diagram of the Carbon-Titanium Binary System up to 5% Carbon", *Russian Journal of Inorganic Chemistry*, June 1961, Vol. 6, No. 6, pp. 690-694.

119. F.C. Wagner, E.J. Bucur and M.A. Steinberg, "The Rate of Diffusion of Carbon in Alpha and Beta Titanium", *Transactions of the ASM*, 1956, Vol. 48, pp. 742-761.

120. D. Hu, T.P. Johnson and M.H. Loretto, "Titanium Precipitation in Substoichiometric TiC Particles", *Scripta Metallurgica et Materialia*, August 15 1994, Vol. 30, No. 8, pp. 1015-1020.

121. D. Hu and M.H. Loretto, "Coarsening of TiC Particles in a Rapidly Solidified Ti6Al4V-TiC Composite", *Journal of Alloys and Compounds*, July 1994, Vol. 209, No. 1, pp. 167-173.

122. H. Fujii, T. Yamazaki, T. Horiya and K. Takahashi, "High Performance Ti-6Al-4V + TiC Alloy by Blended Elemental Powder Metallurgy", Proceedings of the First Pacific Rim International Conference on Advanced Materials and Processing (PRICM-1), (Hangzhou, China), Eds. C. Shi, H. Li and A. Scott, TMS, Warrendale, Pennsylvania, USA, 1992, pp. 131-135.

123. M.H. Loretto and D.G. Konitzer, "The Effect of Matrix Reinforcement Reaction on Fracture in Ti-6Al-4V-Base Composites", *Metallurgical Transactions A*, June 1990, Vol. 21A, No. 6, pp. 1579-1587.

124. C. Chengwei, Z. Zhiming, T. Xitang, Y. Wang and X.T. Sun, "Influence of Rapidly Solidified Structures on Wear Behavior of Ti-6Al-4V Laser Alloyed with TiC", *Tribology Transactions*, October 1994, Vol. 38, No. 4, pp. 875-878.

125. R.W. Smith and M. Mohanty, "Lightweight TiC/Ti Alloy Wear Resistant Coatings for Lightweight Materials in Aerospace Applications", Proceedings of the 7th National Thermal Spray Conference, (Boston, Massachusetts), Eds. C.C. Berndt and S. Sampath, ASM International, Metals Park, Ohio, USA, 1994, pp. 73-77.

126. M. Mohanty and R.W. Smith, "Lightweight TiC/Ti Wear Resistant Coatings for Lightweight Structural Applications", *Journal of Thermal Spray Technology*, December 1995, Vol. 4, No. 4, pp. 384-394.

127. M. Hagiwara, N. Arimoto, S. Emura, Y. Kawabe and H.G. Suzuki, "Mechanical properties of Particulate Reinforced Titanium-Based Metal Matrix Composites Produced by the Blended Elemental P/M Route", *Transactions of the Iron and Steel Institute (ISIJ) International*, August 1992, Vol. 32, No. 8, pp. 909-916.

128. J.-K. Shang and R.O. Ritchie, "Monotonic and Cyclic Crack Growth in a TiC-Particulate-Reinforced Ti-6Al-4V Metal Matrix Composite", *Scripta Metallurgica et Materialia*, September 1990, Vol. 24, No. 9, pp. 1691-1694.

129. A. Kant, Fatigue and Fracture of Discontinuous TiC Reinforced Ti-6Al-4V, Masters Thesis, University of Texas at Arlington, 1994.

130. G. Liu, D. Zhu and J.-K. Shang, "Temperature Dependence of Fracture Toughness in TiC-Particulate-Reinforced Ti-6Al-4V Matrix Composite", *Scripta Metallurgica et Materialia*, March 15 1993, Vol. 28, No. 6, pp. 729-732.

131. G. Liu, D. Zhu and J.-K. Shang, "Enhanced Fatigue Crack Growth Resistance at Elevated Temperature in TiC/Ti-6Al-4V Composite: Microcrack-Induced Crack Closure", *Metallurgical and Materials Transactions A*, January 1995, Vol. 26A, No. 1, pp. 159-166.

132. S.J. Zhu, Y.X. Lu, Z.G. Wang and J. Bi, "Creep Behavior of TiC-Particulate Reinforced Ti Alloy Composite", *Material Letters*, April 1992, Vol. 13, No. 4-5, pp. 199-203.

133. S.J. Zhu, Y.X. Lu, Z.G. Wang and J. Bi, "Cyclic Creep Behaviour of TiC(Particulate)/Ti-6Al-4V Composite in the Temperature Range of 0.4-0.5 T_m", *Journal of Material Science Letters*, May 1992, Vol. 11, No. 10, pp. 630-632.

134. T.P. Johnson, J.W. Brooks and M.H. Loretto, "Mechanical Properties of a Ti-Based Metal Matrix Composite Produced by a Casting Route", *Scripta Metallurgica et Materialia*, April 1991, Vol. 25, No. 4, pp. 785-789.

135. Y. Lin, R.H. Zee and B.A. Chin, "*In Situ* Formation of Three-Dimensional TiC Reinforcements in Ti-TiC Composites", *Metallurgical Transactions A*, April 1991, Vol. 22A, No. 4, pp. 859-865.

136. R. Zee, C. Yang, Y. Lin and B. Chin, "Effects of Boron and Heat Treatment on Structure of Dual-Phase Ti-TiC", *Journal of Materials Science*, 1991, Vol. 26, pp. 3853-3861.

137. X. Yu, Y. Wang and T. Zhou, "Precipitant Character of TiC in the Metastable β-Ti Alloy", Sixth World Conference on Titanium, (Cannes, France), Eds. P. Lacombe, R. Tricot and G. Béranger, Les Éditions Physique, Les Ulis, France, 1988, pp. 1647-1652.

138. J.H. Abboud and D. R. F. West, "*In Situ* Production of Titanium-TiC Composites by Laser Melting", *Journal of Material Science Letters*, December 1992, Vol. 11, No. 24, pp. 1675-1677.

139. D. Hu and M.H. Loretto, "Microstructural Characterization of Gas Atomized Ti6Al4V-TiC Composite", *Scripta Metallurgica et Materialia*, September 1 1994, Vol. 31, No. 5, pp. 543-548.

140. H.M. Flower, A. Walker and D.R.F. West, "The Structure of Ti-6Al-4V Laser Surface Alloyed with Carbon", *Scripta Metallurgica*, August 1985, Vol. 19, No. 8, pp. 923-926.

141. D. Hu, T.P. Johnson and M.H. Loretto, "Tensile Properties of Gas Atomised Ti6Al4V-TiC Composite", Titanium '95-Science and Technology, Vol. 3, Proceedings of the Eighth World Conference on Titanium, (Birmingham, Great Britain), Eds. P.A. Blenkinsop, W.J. Evans and H.M. Flower, The Institute of Materials, London, United Kingdom, 1996, pp. 2867-2873.

142. D. Hu, T.P. Johnson and M.H. Loretto, "The Forging of a Cast Ti6Al4V/TiC_x Composite", The Processing, Properties and Application of Metallic and Ceramic Materials, Vol. 2, Proceedings of IRC' 92, (Birmingham, Great Britain), Eds. M.H. Loretto and C.J. Beevers, Material and Component Engineering Publications, West Midlands, United Kingdom, 1992, pp. 791-796.

143. D. Hu, T.P. Johnson and M.H. Loretto, "Microstructural Characteristics of Isothermal Forging in Cast Ti-6Al-4V/TiC Composites", *Materials Science and Technology*, May 1994, Vol. 10, No. 5, pp. 421-424.

144. S. Ranganath, M. Vijayakumar and J. Subrahmanyam, "Combustion-Assisted Synthesis of Ti-TiB-TiC Composite Via the Casting Route", *Materials Science and Engineering A: Structural Materials: Properties, Microstructure and Properties*, January 1992, Vol. A149, No. 2, pp. 253-257.

145. S. Ranganath and J. Subrahmanyam, "On the *In Situ* Formation of TiC and Ti_2C Reinforcements in Combustion-Assisted Synthesis of Titanium Matrix Composites", *Metallurgical and Materials Transactions A*, January 1996, Vol. 27A, No. 1, pp. 237-240.

146. H.T. Tsang, C.G. Chao and C.Y. Ma, "*In Situ* Fracture Observation of a TiC/Ti MMC Produced by Combustion Synthesis", *Scripta Materialia*, October 15 1996, Vol. 35, No. 8, pp. 1007-1012.

147. S. Abkowitz, P. Weihrauch and S. Abkowitz, "Advanced Powder Metal Titanium Alloy Matrix Composites Reinforced with Ceramic and Intermetallic Particles", Titanium '92-Science and Technology, Vol.3, Proceedings of the Seventh World Titanium Conference, (San Diego, CA, USA), Eds. F.H. Froes and I.L. Caplan, TMS, Warrendale, Pennsylvania, USA, 1993, pp. 2511-2518.

148. S. Abkowitz, "Titanium Composites for Practical Applications", *Metal Powder Report*, November 1993, Vol. 48, No. 11, pp. 34-35.

149. S. Abkowitz, P. Weihrauch and S.M. Abkowitz, "Particulate-Reinforced Titanium Alloy Composites Economically Formed by Combined Cold and Hot Isostatic Pressing", *Industrial Heating*, September 1993, pp. 32-37.

150. S. Abkowitz, P. Weihrauch, S.M. Abkowitz and H.L. Heussi, "The Commercial Application of Low-Cost Titanium Composites", *Journal of Metals*, August 1995, Vol. 47, No. 8, pp. 40-41.

151. J.-Q. Jiang, T.-S. Lim, Y.-J. Kim, B.-K. Kim and H.-S. Chung, "*In Situ* Formation of TiC-(Ti-6Al-4V) Composites", *Materials Science and Technology*, April 1996, Vol. 12, No. 4, pp. 362-365.

152. H. Liu, B. Yao, L. Wang, A. Wang, B. Ding and Z. Hu, "In Situ Formation of Nanometer Size TiC Reinforcements in Ti Matrix Composites", *Materials Letters*, July 1996. Vol. 27, No. 4, pp. 183-186.

153. C.A. Kelto, B.A. Kosmal, D. Eylon and F.H. Froes, "Titanium Powder Metallurgy - A Perspective", Powder Metallurgy of Titanium Alloys, Proceeding of a Symposium at 109th AIME Annual Meeting, (Las Vegas, Nevada, USA), Eds. F.H. Froes and J.E. Smugeresky, AIME, New York, New York, USA, 1980, pp. 1-19.

154. D. Eylon, "Fatigue Crack Initiation in Hot Isostatically Pressed Ti-6Al-4V", *Journal of Materials Science*, August 1979, Vol. 14, No. 8, pp. 1914-1922.

155. D. Eylon and J.A. Hall, "Fatigue Behavior of Beta Processed Titanium Alloy IMI 685", *Metallurgical Transactions A*, June 1977, Vol. 8A, No. 6, pp. 981-990.

156. D. Shechtman and D. Eylon, "On the Unstable Shear in Fatigue β-Annealed Ti-11 and IMI-685 Alloys", *Metallurgical Transactions A*, July 1978, Vol. 9A, No. 7, pp. 1018-1020.

157. S. Abkowitz and D. Rowell, "Superior Fatigue Properties for Blended Elemental P/M Ti-6Al-4V", *Journal of Metals*, August 1986, Vol. 38, No. 8, pp. 36-39.

158. M. Hagiwara, Y. Kaieda, Y. Kawabe and S. Miura, "Fatigue Property Enhancement of α-β Titanium Alloys by Blended Elemental P/M Approach", *Transactions of the Iron and Steel Institute (ISIJ) International*, August 1991, Vol. 31, No. 8, pp. 922-930.

159. I. Weiss, D. Eylon, M.W. Toaz and F.H. Froes, "Effect of Isothermal Forging on Microstructure and Fatigue Behavior of Blended Elemental Ti-6Al-4V Powder Compacts", *Metallurgical Transactions A*, March 1986, Vol. 17A, No. 3, pp. 549-559.

160. G. Welsch, Y.-T. Lee, P.C. Eloff, D. Eylon and F.H. Froes, "Deformation Behavior of Blended Elemental Ti-6Al-4V Compacts", *Metallurgical Transactions A*, April 1983, Vol. 14A, No. 4, pp. 761-769.

161. F.H. Froes, D. Eylon, G.E. Eichelman and H.M. Burte, "Developments in Titanium Powder Metallurgy", *Journal of Metals*, February 1980, Vol. 32, No. 2, pp. 47-54.

162. S.M. Abkowitz, P.F. Weihrauch, H.L. Heussi, S. Abkowitz, "P/M Titanium Matrix Composites: From War Games to Fun and Games", Titanium '95-Science and Technology, Vol. 3, Proceedings of the Eighth World Conference on Titanium, (Birmingham, Great Britain), Eds. P.A. Blenkinsop, W.J. Evans and H.M. Flower, The Institute of Materials, London, United Kingdom, 1996, pp. 2722-2730.

163. R.F. Lynch and E.N. Aqua, "Characterization of Commercial Titanium Powders", Proceedings of 1971 Powder Metallurgy Conference, (Detroit, Michigan, USA), Ed. S. Mocarski, Metal Powder Industries Federation, Princeton, New Jersey, USA, 1971, pp. 217-229.

164. J.H. Moll, V.C. Petersen and E.J. Dulis, "Powder Metallurgy Parts for Aerospace Applications", Powder Metallurgy - Applications, Advantages and Limitations, Ed. E. Klar, ASM, Metals Park, Ohio, USA, 1983 pp. 279-298.

165. G.I. Friedman, "Titanium Powder Metallurgy", *International Journal of Powder Metallurgy*, April 1970, Vol. 6, No. 2, pp. 43-54.

166. T.P. Johnson, M.H. Loretto, M.J. Walker and M.W. Kearns, "The Forging Characteristics of Two Ti-6Al-4V-Based Particulate Composites", Titanium '92-Science and Technology, Vol.3,

Proceedings of the Seventh World Titanium Conference, (San Diego, CA, USA), Eds. F.H. Froes and I.L. Caplan, TMS, Warrendale, Pennsylvania, USA, 1993, pp. 2585-2592.

167. J.S. Hirschorn, "Chapter 3: Powder Compaction", Introduction to Powder Metallurgy, American Powder Metallurgy Institute, New York, New York, USA, 1969, pp. 96-154.

168. R.M. German, "Chapter 9: Particle Deformation and Compaction", Particle Packing Characteristics, Metal Powder Industries Federation, Princeton, New Jersey, USA, 1989, pp. 219-252.

169. R.L. Sands and C.R. Shakespeare, "Chapter 4: Sintering", Powder Metallurgy Practice and Applications, George Newnes Limited, London, Great Britain, 1966, pp. 78-107.

170. H.H. Hausner, "Discussion of the Definition of the Term "Sintering"", Sintering - New Developments, Elsevier Scientific Publishing Company, New York, New York, 1979, pp. 3-7.

171. F. Thümmler and R. Oberacker, "Chapter 7: Sintering", An Introduction to Powder Metallurgy, Eds. I. Jenkins and J.V. Wood, The Institute of Materials, London, United Kingdom, 1993, pp. 181-240.

172. R.M. German, Powder Metallurgy Science, Metal Powder Industries Federation, Princeton, New Jersey, 1984, pp. 145-255.

173. J.S. Hirschorn, "Chapter 4: Sintering", Introduction to Powder Metallurgy, American Powder Metallurgy Institute, New York, New York, USA, 1969, pp. 155-273.

174. J.S. Reed, "Chapter 26: Firing Processes", Introduction to Principles of Ceramic Processing, John Wiley and Sons, New York, New York, USA, 1988, pp. 449-461.

175. W. Schatt and E. Friedrich, "Progress in the Understanding of Solid Phase Sintering", Powder Metallurgy 1986 State of the Art: Powder Metallurgy in Science and Practical Technology, Vol. 2, Eds. W.J. Huppmann, W.A. Kaysser and G. Petzow, Verlag Schmid GMBH, Freibug, West Germany, 1986, pp. 169-178.

176. G.C. Kuczynski, "Self-Diffusion in Sintering of Metallic Particles", *Transactions of AIME*, February 1949, Vol. 185, pp. 169-178.

177. A.J. Shaler, "Seminar on the Kinetics of Sintering", *Transactions of AIME*, November 1949, Vol. 185, pp. 796-813.

178. W.D. Kingery and M. Berg, "Study of the Initial Stages of Sintering Solids by Viscous Flow, Evaporation-Condensation, and Self-Diffusion", *Journal of Applied Physics*, October 1955, Vol. 26, No. 10, pp. 1205-1212.

179. N. Cabrera, "Sintering of Metallic Particles ", *Transactions of AIME (Journal of Metals)*, April 1950, Vol. 188, pp. 667-668.

180. P. Schwed, "Surface Diffusion in Sintering of Spheres on Planes", *Transactions of AIME (Journal of Metals)*, March 1951, Vol. 188, pp. 169-178.

181. G.C. Kuczynski, "The Mechanism of Densification During Sintering of Metallic Particles", *Acta Metallurgica*, January 1956, Vol. 4, pp. 58-61.

182. H. Ichinose and G.C. Kuczynski, "Role of Grain Boundaries in Sintering", *Acta Metallurgica*, March 1962, Vol. 10, pp. 209-213.

183. F.A. Nichols and W.W. Mullins, "Surface- (Interface-) and Volume-Diffusion Contributions to Morphological Changes Driven by Capillarity", *Transactions of AIME*, October 1965, Vol. 233, pp. 1840-1847.

184. F.A. Nichols, "Coalescence of Two Spheres by Surface Diffusion", *Journal of Applied Physics*, June 1966, Vol. 37, No. 7, pp. 2805-2808.

185. J.G.R. Rockland, "On the Rate Equation for Sintering by Surface Diffusion", *Acta Metallurgica*, October 1966, Vol. 14, pp. 1273-1279.

186. J.G.R. Rockland, "The Determination of the Mechanism of Sintering", *Acta Metallurgica*, February 1967, Vol. 15, pp. 277-286.

187. H.H. Hausner, "Chapter 7: Sintering of Metal Powders", Handbook of Powder Metallurgy, Chemical Publishing Co. Inc., New York, New York, USA, 1973, pp. 144-179.

188. M.F. Ashby, "A First Report on Sintering Diagrams", *Acta Metallurgica*, March 1974, Vol. 22, pp. 275-289.

189. V. Smolej, "How Good Can Sintering Diagrams Be?", *Zeitschrift Für Metallkunde*, October 1983, Vol. 74, No. 10, pp. 689-691.

190. W.A. Kaysser, "Solid State Sintering", Powder Metallurgy: An Overview, Eds. I. Jenkins and J.V. Wood, The Institute of Metals, London, United Kingdom, 1991, pp. 168-181.

191. G. Petzow and H.E. Exner, "Particle Rearrangement in Solid State Sintering", *Zeitschrift Für Metallkunde*, September 1976, Vol. 67, No. 9, pp. 611-618.

192. T. Watanabe and Y. Horikoshi, "The Sintering Phenomenon of Titanium Powders - A Discussion", *International Journal of Powder Metallurgy and Powder Technology*, July 1976, Vol. 12, No. 3, pp. 209-214.

193. B.H. Alexander and R.W. Balluffi, "The Mechanism of Sintering of Copper", *Acta Metallurgica*, November 1957, Vol. 5, pp. 666-677.

194. R.L. Coble, "Sintering Crystalline Solids. I. Intermediate and Final State Diffusion Models", *Journal of Applied Physics*, May 1961, Vol. 32, No. 5, pp. 787-792.

195. W. Beere, "The Second Stage Sintering Kinetics of Powder Compacts", *Acta Metallurgica*, January 1975, Vol. 23, No. 1, pp. 139-145.

196. C.H. Hsueh, A.G. Evans and R.L. Coble, "Microstructure Development During Final/Intermediate Stage Sintering - I. Pore/Grain Boundary Separation", *Acta Metallurgica*, July 1982, Vol. 30, No. 7, pp. 1269-1279.

197. M.F. Ashby, "A First Report on Deformation-Mechanism Maps", *Acta Metallurgica*, July 1972, Vol. 20, No. 7, pp. 887897.

198. F. Thümmler and R. Oberacker, "Chapter 6: Compaction and Shaping", An Introduction to Powder Metallurgy, Eds. I. Jenkins and J.V. Wood, The Institute of Materials, London, United Kingdom, 1993, pp. 154-160.

199. M.F. Ashby and D.R.H. Jones, "Chapter 19: Mechanisms of Creep, and Creep-Resistant Materials", Engineering Materials 1: An Introduction to Their Properties and Applications, Pergamon Press, New York, New York, USA, 1988, pp. 172-175.

200. G.E. Dieter, "Chapter Thirteen: Creep and Stress Rupture", Mechanical Metallurgy, McGraw-Hill Publishing Company, New York, New York, 1986, pp. 445-450.

201. R. Raj and M.F. Ashby, "On Grain boundary Sliding and Diffusional Creep", Metallurgical Transactions, April 1971, Vol. 2, No. 4, pp. 1113-127.

202. M.F. Ashby, "Sintering and Hot Isostatic Pressing Diagrams", Powder Metallurgy: An Overview, Eds. I. Jenkins and J.V. Wood, The Institute of Metals, London, United Kingdom, 1991, pp. 144-166.

203. C. Herring, "Diffusional Viscosity of a Polycrystalline Solid", *Journal of Applied Physics*, May 1950, Vol. 21, No. 5, pp. 437-445.

204. R.L. Coble, "A Model for Boundary Diffusion Controlled Creep in Polycrystalline Materials", *Journal of Applied Physics*, June 1963, Vol. 34, No. 6, pp. 1679-1682.

205. A.C.F. Cocks, "The Structure of Constitutive Laws for the Sintering of Fine Grained Materials", *Acta Metallurgica et Materialia*, July 1994, Vol. 42, No. 7, pp. 2191-2210.

206. R. Suryanarayanan, S.M.L. Sastry and K.L. Jerina, "On the Values of Material Property Data Used in Hot Isostatic Pressing Models", Scripta *Metallurgica et Materialia*, April 1 1993, Vol. 28, No. 7, pp. 797-802.

207. S.M. Doraivelu, H.L. Gegel, J.S. Gunasekera, J.C. Malas, J.T. Morgan and J.F. Thomas Jr., "A New Yield Function for Compressible P/M Materials", *International Journal of Mechanical Sciences*, 1984, Vol. 26, No. 9/10, pp. 527-535.

208. H.A. Kuhn and C.L. Downey, "Deformation Characteristics and Plasticity Theory of Sintered Powder Materials", *International Journal of Powder Metallurgy*, 1973, Vol. 7, No. 1, pp. 15-25.

209. H.A. Kuhn and A. Lawley, Powder Metallurgy Processing, Academic Press, New York, New York, USA, 1978, pp. 99-170.

210. A. Lawley, "Chapter 5: Powder Consolidation", Advances in Powder Technology, Ed. G.Y. Chin, American Society for Metals, Metals Park, Ohio, USA, 1982, pp. 75-97.

211. H.A. Kuhn and C.L. Downey, "Material Behavior in Powder Preform Forging", *Journal of Engineering Materials and Technology (Transactions of the ASME-H)*, January 1973, Vol. 95, No. 1, pp. 41-46.

212. R.E. Dutton, S. Shamasundar and S.L. Semiatin, "Modeling Hot Consolidation of Ceramic and Metal Powders", *Metallurgical and Materials Transactions A*, August 1995, Vol. 26A, No. 8, pp. 2041-2051.

213. R.E. Dutton and M.N. Rahaman, "Sintering, Creep and Electrical Conductivity of Model Glass-Matrix Composites", *Journal of the American Ceramic Society*, August 1992, Vol. 75, No. 8, pp. 2146-2154.

214. R.L. Coble, "Diffusion Models for Hot Pressing with Surface Energy and Pressure Effects as Driving Forces", *Journal of Applied Physics*, November 1970, Vol. 41, No. 12, pp. 4798-4807.

215. G.W. Scherer, "Sintering Inhomogeneous Glasses: Application to Optical Waveguides", *Journal of Non-Crystalline Solids*, October-November 1979, Vol. 34, No. 2, pp. 239-256.

216. G.W. Scherer, "Sintering of Low-Density Glasses", *Journal of the American Ceramic Society*, May-June 1977, Vol. 60, No. 5-6, pp. 236-246.

217. W. Beere, "A Unifying Theory of the Stability of Penetrating Liquid Phases and Sintering Pores", *Acta Metallurgica*, January 1975, Vol. 23, No. 1, pp. 131-138.

218. J.M. Vieira and R.J. Brook, "Kinetics of Hot-Pressing: The Semilogarithmic ", *Journal of the American Ceramic Society*, 1984, Vol. 67, No. 4, pp. 245-249.

219. S. Shima and M. Oyane, "Plasticity Theory for Porous Materials", *International Journal of Mechanical Sciences*, June 1976, Vol. 18, No. 6, pp. 285-291.

220. S. Shamasundar, R.E. Dutton and S.L. Semiatin, "Application of Microhardness testing for the Analysis of Powder Consolidation Processes", *Scripta Metallurgica et Materialia*, September 1994, Vol. 31, No. 5, pp. 521-525.

221. V. Seetharaman, S.M. Doraivelu and H.L. Gegel, "Plastic Deformation Behavior of Compressible Solids", *Journal of Material Shaping and Technology*, 1990, Vol. 8, No. 4, pp. 239-248.

222. D.N. Lee and H.S. Kim, "Plastic Yield Behaviour of Porous Metals", *Powder Metallurgy*, 1992, Vol. 35, No. 4, pp. 275-279.

223. H.F. Fischmeister and E. Arzt, "Densification of Powders by Particle Deformation", *Powder Metallurgy*, 1983, Vol. 26, No. 2, pp. 82-88.

224. A.S. Helle, K.E. Easterling and M.F. Ashby, "Hot-Isostatic Pressing Diagrams: New Developments", *Acta Metallurgica*, December 1985, Vol. 33, No. 12, pp. 2163-2174.

225. E.K.H. Li and P.D. Funkenbusch, "Modeling of the Densification Rates of Monosized and Bimodal-Sized Particle Systems During Hot Isostatic Pressing (HIP)", *Acta Metallurgica*, June 1989, Vol. 37, No. 6, pp. 1645-1655.

226. E.K.H. Li and P.D. Funkenbusch, "Hot Isostatic Pressing (HIP) of Powder Mixtures and Composites: Packing, Densification, and Microstructural Effects", *Metallurgical Transactions A*, June 1993, Vol. 24A, No. 6, pp. 1345-1354.

227. M.N. Rahaman, L.C. De Jonghe and R.J. Brook, "Effect of Shear Stress on Sintering", *Journal of the American Ceramic Society*, January 1986, Vol. 69, No. 1, pp. 53-58.

228. L.C. De Jonghe and M.N. Rahaman, "Sintering Stress of Homogeneous and Heterogeneous Powder Compacts", *Acta Metallurgica*, January 1988, Vol. 36, No. 1, pp. 223-229.

229. R. Raj and R.K. Bordia, "Sintering Behavior of Bi-Modal Powder Compacts", *Acta Metallurgica*, July 1984, Vol. 32, No. 7, pp. 1003-1019.

230. N. Taylor, D.C. Dunand and A. Mortensen, "Initial Stage Hot pressing of Monosized Ti and 90% Ti-10% TiC Powders", *Acta Metallurgica et Materialia*, March 1993, Vol. 41, No. 3, pp. 955-965.

231. R.E. Dutton, (Materials Science and Engineering Laboratory, National Institute of Standards and Technology, Wright Patterson Air Force Base, Dayton, Ohio), Private Communication, November 14, 1997.

232. H. Mecking and G. Gottstein, "Chapter 9: Recovery and Recrystallization During Deformation", Recrystallization of Metallic Materials, Ed. F. Haessner, Dr. Riederer Verlag GmbH, Stuttgart, Germany, 1978, pp. 195-222.

233. N. Hansen and C.Y. Barlow, "Chapter 6: Microstructural Evolution in Whisker- and Particle-Containing Materials", Fundamentals of Metal-Matrix Composites, Eds. S. Suresh, A. Mortensen and A. Needleman, Butterworth-Heinemann, Stoneham, Massachusetts, USA, 1993, pp. 109-118.

234. ASTM E209-65, "Standard Practice for Compression Testing of Metallic Materials at Elevated Temperatures with Conventional or Rapid Heating Rates and Strain Rates".

235. ASTM C373-88, "Standard Test Method for Water Absorption, Bulk Density, Apparent Porosity, and Apparent Specific Gravity".

236. ASM International Handbook Committee, ASM Handbook – Metallography and Microstructures, Vol. 9, ASM International, Materials Park, Ohio, USA, 1985, p. 460.

237. J.I. Goldstein, D.E. Newbury, P. Echlin, D.C. Joy, A.D. Romig Jr., C.E. Lyman, C. Fiori and E. Lifshin, Scanning Electron Microscopy and X-ray Microanalysis, Second Edition, Plenum Press, New York, New York, USA, 1992, p. 81-87.

238. B.D. Cullity, "Chapter 11: Precise Parameter Measurements or Chapter 12: Phase Diagram Determination", Elements of X-ray Diffraction, Second Edition, Addison – Wesley Publishing Company, Reading, Massachusetts, USA, 1978, p. 350-382.

239. J. Foulds and R. Viswanathan, "Small Punch Testing for Determining the Material Toughness of Low Alloy Steel Components in Service", *Journal of Engineering Materials and Technology*, October 1994, Vol. 116, No. 10, pp. 457-464.

240. G.E. Lucas, "Review of Small Specimen Test Techniques for Irradiation Testing", *Metallurgical Transactions A*, May 1990. Vol. 21A, No. 5, pp. 1105-1119.

241. G.E. Lucas, G.R. Odette and J.W. Sheckherd, "Shear Punch and Microhardness Tests for Strength and Ductility Measurements", The Use of Small-Scale Specimens for Testing Irradiated Material, ASTM STP 888, Eds. W.R. Corwin and G.E. Lucas, American Society for Testing and Materials, Philidephia, USA, 1986, pp. 112-140.

242. A. Zarei-Hanzaki, Transformation Characteristics of Si-Mn TRIP Steels After Thermomechanical Processing, Ph.D. Thesis, McGill University, Montreal, Quebec, Canada, 1994.

243. ASTM E8M-94a, "Standard Test Methods for Tension Testing of Metallic Materials [Metric]".

244. T.A. Brzezinski, Squeeze Casting of A356 Aluminum/Discontinuous Saffil Alumina Fibre Composites, Masters Thesis, McGill University, Montreal, Quebec, Canada, 1995.

245. T.A. Brzezinski, R.A.L. Drew and J.E. Gruzleski, "Squeeze Casting of A356/Discontinuous Saffil Alumina Fibre Composites", Recent Developments in Light Metals, Proceedings of the 33rd Conference of Metallurgist (Montreal, Canada, 1994), Eds. M. Gilbert, P. Tremblay and E. Ozberk, CIM, Montreal, Canada, 1994, pp. 3-17.

246. ASM International Handbook Committee, ASM Handbook - Alloy Phase Diagrams, Vol. 3, ASM International, Materials Park, Ohio, USA, 1992, p. 3-22.

247. F.F. Lange, "De-Sintering, A Phenomenon Concurrent with Densification within Powder Compacts: A Review", Sintering Technology, Eds. R.M. German and R.G. Cornwall, Marcel Dekkar Inc., New York, New York, USA, 1996, pp. 1-11.

248. (a) A. Feng, B.J. McCoy, Z.A. Munir and D. Cagliostro, "Wettability of Transition Metal Oxide Surfaces", *Materials Science and Engineering A*, February 1998, Vol. A242, No. 1-2, pp. 50-56. (b) K. Aigner, W. Lengauer and P. Ettmayer, "Interactions in Iron-Based Cermets", *Journal of Alloys and Compounds*, November 1997, Vol. 262-263, pp. 486-491.
(c) F.O. Orumwense, "Estimation of the Wettability of Coal From Contact Angles Using Coagulants and Flocculants", *Fuel*, 1998, Vol. 77, No. 9, pp. 1107-1111.

249. J.F. Murdock and C.J. McHargue, "Self-diffusion in Body-Centered Cubic Titanium-Vanadium Alloys", *Acta Metallurgica*, April 1968, Vol. 16, p.493-500.

250. H. Nakajima and M. Koiwa, "Diffusion in Titanium", *Transactions of the Iron and Steel Institute (ISIJ) International*, August 1991, Vol. 31, No. 8, pp. 757-766.

251. D.A. Porter and K.E. Easterling, "Chapter 2: Diffusion", Phase Transformations in Metals and Alloys, Second Edition, Chapman and Hall, London, United Kingdom, 1992, pp. 78-79.

252. T.S. Touloukian, R.K. Kirby, R.E. Taylor and T.Y.R. Lee, Thermophysical Properties of Matter: Thermal Expansion – Nonmetallic Solids, Vol.13, IFI/Plenum Data Company, New York, New York, USA, 1977.

253. T.S. Touloukian, R.K. Kirby, R.E. Taylor and R.D. Desai, Thermophysical Properties of Matter: Thermal Expansion – Metallic Elements and Alloys, Vol.12, IFI/Plenum Data Company, New York, New York, USA, 1975.

254. ASM International Handbook Committee, Materials Properties Handbook: Titanium Alloys, Eds. R. Boyer, G. Welsch and E.W. Collings, ASM International, Materials Park, Ohio, USA, 1994, pp. 483-635.

255. A.I. Kahveci and G.E. Welsch, "Effect of Oxygen on the Hardness and Alpha/Beta Phase Ratio of Ti-6Al-4V", *Scripta Metallurgica*, September 1986, Vol. 20, No. 9, pp. 1287-1290stm

256. ASTM B817-93, "Standard Specification for Powder Metallurgy (P/M) Titanium Alloy Structural Components".

257. W.B. Pearson, A Handbook of Lattice Spacings and Structures of Metals and Alloys, Pergamon Press Inc., New York, New York, USA, 1964, pp. 948-949.

258. R.J. Kerans, K.S. Mazdiyasni, R. Ruh and H.A. Lipsitt, "Solubility of Metals in Substoichiometric TiC_{1-x}", *Journal of the American Ceramic Society*, January 1984, Vol. 67, No. 1, pp. 34-39.

259. L. Ramqvist, "Preparation, Properties and Electronic Structure of Refractory Carbides and Related Compounds", *Jernkontorets Annaler*, 1969, Vol. 153, p. 159-179.

260. A.M. Brown and M.F. Ashby, "Correlations for Diffusion Constants", *Acta Metallurgica*, August 1980, Vol. 28, No. 8, pp. 1085-1101.

261. S. Sarian, "Diffusion of ^{44}Ti in TiC_x", *Journal of Applied Physics*, August 1969, Vol. 40, No. 9, pp. 3515-3520.

262. S. Sarian, "Diffusion of Carbon in TiC", *Journal of Applied Physics*, June 1968, Vol. 39, No. 7, pp. 3305-3310.

263. S. Sarian, "Anomalous Diffusion of ^{14}C in $TiC_{0.67}$", *Journal of Applied Physics*, October 1968, Vol. 39, No. 11, pp. 5036-5041.

264. D.L. Kohlstedt, W.S. Williams and J.B. Woodhouse, "Chemical Diffusion in Titanium Carbide Crystals", *Journal of Applied Physics*, October 1970, Vol. 41, No. 11, pp. 4476-4484.

265. F.J.J. van Loo and G.F. Bastin, "On the Diffusion of Carbon in Titanium Carbide", *Metallurgical Transactions A*, March 1989, Vol. 20A, No. 3, pp. 403-411.

266. J. Redinger, R. Eibler, P. Herzig, A. Neckel, P. Podloucky and E. Wimmer, "Vacancy Induced Changes in the Electronic Structure of Titanium Carbide – II. Electron Densities and Chemical Bonding", *Journal of Physics and Chemistry of Solids*, 1986, Vol. 47, No. 4, pp. 387-393.

267. S. Otani, T. Tanaka and Y. Ishizawa, "Electrical Resistivities in Single Crystals of TiC_x and VC_x", *Journal of Material Science*, March 1986, Vol. 21, No. 3, pp. 1011-1014.

268. C.M. Sellars and W.J. McG. Tegart, "On the Mechanism of Deformation", *Acta Metallurgica*, September 1966, Vol. 14, pp. 1136-1138.

269. R. Castro and L. Seraphin, "Contribution à l'étude métallographique et structurale de l'alliage de titane TA6V", *Mémoires et Etudes Scientifiques de la Revue de Métallurgie*, 1966, Vol. 63, No. 12, p. 1025-1058.

270. J.G. Malcor and F. Montheillet, "Mechanical and Microstructural Behavior of Ti-6%Al-4%V Alloy in the Hot Working Range," Titanium Science and Technology, Eds. G. Lütjering, U. Zwicker and W. Bunk, Deutsche Gesellschaft für Metallukunde, Germany, Vol.3, 1984, p.1495-1502.

271. J.G. Malcor, "Comportement mécanique et évolution structurale de l'alliage de titane Ti-6%Al-4%v dans la domaine de forgeage à chaud," Ph.D. Thesis, Ecole des Mines de Paris, Sophia Antipolis, France, 1983

272. L. Briottet, J.J. Jonas, and F. Montheillet, "A Mechanical Interpretation of the Activation Energy of High Temperature Deformation in Two Phase Materials", *Acta Metallurgica*, April 1996, Vol. 44, No. 4, pp. 1665-1672.

273. W.A. Bryant, "Correlation of Data on the Hot Deformation of Ti-6Al-4V", *Journal of Material Science*, October 1975, Vol. 10, No. 10, pp. 1793-1797.

274. F. Dyment, "Self and Solute Diffusion in Titanium and Titanium Alloys", Titanium 80' Science and Technology, Proceedings of the Fourth International Conference on Titanium, (Kyoto, Japan), Eds. H. Kimura and O. Izumi, AIME, Warrendale, Pennsylvania, USA, 1980, pp. 519-528.

275. H.C. Braga, R. Barbosa and J. Breme, "Hot Strength of Ti and Ti6Al4V Deformed in Axial Compression", *Scripta Metallurgica et Materialia*, August 1993, Vol. 28, No. 8, pp. 979-983.

276. T. Sheppard and J. Norley, "Deformation Characteristics of Ti-6Al-4V", *Materials Science and Technology*, October 1988, Vol. 4, No. 10, pp. 903-908.

277. M.J. Donachie, Titanium and Titanium Alloys:Source Book, American Society for Metals, Metals Park, Ohio, USA, 1982, pp. 23-280.

278. S. Ranganath, "A Review on Particulate-Reinforced Titanium Matrix Composites", *Journal of Materials Science*, 1997, Vol. 32, No. 1, pp. 1-16.

279. I. Weiss, G.E. Welsch, F.H. Froes, and D. Eylon "Mechanisms of Microstructuer Refinement in Ti-6Al-4V Alloy", Titanium Science and Technology, Eds. G. Lütjering, U. Zwicker and W. Bunk, Deutsche Gesellschaft für Metallukunde, Germany, Vol.3, 1984, p.1503-1510.

APPENDIX I

HOT DEFORMATION TESTING PROGRAM

```
10   REM
20   REM---CONSTANT TRUE STRAIN RATE INTERRUPTED COMPRESSION TEST---
30   REM
40   REM************PROGRAMMED BY A. ZAREI-HANZAKI*****************
50   REM**********MODIFIED BY T.MACCAGNO AND P.WANJARA***********
60   REM
70   REM
80   ERASE
90   DIM X(50,1),Y(50,1)
100  COMMON A(350,3),C(350,3),D(350,3),Z(350),T(350)
110  COMMON F(15),E(15)
120  COMMON H0,A0,D1,D2,D5,B,S0,I1,I2,D
130  COMMON C1,S1,S2,L0,A,J,N$,M$,T$
140  PRINT "SAMPLE IDENTIFICATION"; \ INPUT N$
150  PRINT \ PRINT "MATERIAL"; \ INPUT M$
160  PRINT \ PRINT "TEST TEMPERATURE": \ INPUT T$
170  PRINT \ PRINT "INITIAL HEIGHT (mm)": \ INPUT H0
180  PRINT \ PRINT "INITIAL DIAMETER (mm)"; \ INPUT D0 \ A0=PI*(D0)^2/4
190  PRINT \ PRINT "NUMBER OF DEFORMATIONS:"; \ INPUT D5
200  PRINT \ PRINT "FIRST DEFORMATION": \ INPUT D1
205  PRINT \ PRINT "FIRST STRAIN RATE (1/s)": \ INPUT S1
210  IF D5=1 THEN GO TO 240
220  PRINT \ PRINT "SECOND DEFORMATION": \ INPUT D2
235  PRINT \ PRINT "SECOND STRAIN RATE (1/s)"; \ INPUT S3
240  PRINT \ PRINT "TIME INTERPASS (s)": \ INPUT T
250  PRINT \ PRINT "LOAD RANGE (kip)": \ INPUT L \ L0=L*4.4482*1000
260  PRINT \ PRINT "STROKE RANGE (mm)"; \ INPUT S0
270  PRINT \ PRINT "NO. OF DATA YOU WANT (MAX. 300) "; \ INPUT D \ D9=D/D5
280  ERASE
290  GTIME(,M,H)
300  PRINT "DATE                              :"; \ PRINT DAT$
```

```
310   PRINT "TIME                                :"; \ PRINT H; ":"M
320   PRINT
330   PRINT "************************EXPERIMENTAL DATA*************************"
340   PRINT  \ PRINT
350   PRINT "FILE NAME                           :"; \ PRINT N$
360   PRINT "MATERIAL                            :"; \ PRINT M$
370   PRINT
380   PRINT "TEST TEMPERATURE                    :"; \ PRINT T$
390   PRINT "INITIAL HEIGHT                      :"; \ PRINT H0; \ PRINT "    (mm)"
400   PRINT "INITIAL DIAMETER                    :"; \ PRINT D0; \ PRINT "    (mm)"
410   PRINT
420   PRINT "NUMBER OF DEFORMATIONS              :"; \ PRINT D5
430   PRINT "NUMBER OF REQUESTED DATA            :"; \ PRINT D
440   PRINT
450   PRINT "FIRST DEFORMATION                   :"; \ PRINT D1
455   PRINT "1ST STRAIN RATE                     :"; \ PRINT S1; \ PRINT "    1/SEC"
460   PRINT "SECOND DEFORMATION                  :"; \ PRINT D2
475   PRINT "2ND STRAIN RATE                     :"; \ PRINT S3; \ PRINT "    1/SEC"
480   PRINT "TIME INTERPASS                      :"; \ PRINT T; \ PRINT "    SEC"
490   PRINT
500   PRINT "LOAD RANGE                          :"; \ PRINT L; \ PRINT "    kip"
510   PRINT "STROKE RANGE                        :"; \ PRINT S0; \ PRINT "    (mm)"
520   W=SYS(4)
530   PRINT  \ PRINT
540   PRINT "PRESS RETURN TO START THE TEST";    INPUT G$
550   PRINT  \ PRINT
560   PRINT  "STARTING THE AUTOMATIC POSITIONING OF THE ACTUATOR"
570   FGARG(1, "R", TIME 100,-0.4)
580   ADIMMED(1,A)
590   FGGO
600   IF A<-3.00000E-03 THEN GO TO 620
610   GO TO 580
620   FGSTOP
630   S2=A*L0/A0
640   PRINT  \ PRINT "THE STRESS ON THE SAMPLE IS: "; \ PRINT  S2; \ PRINT "MPa"
650   ETIME \ SLEEP(1)
660   ADIMMED(3,B)
670   T1=D1/S1/50 \ T2=D2/S3/50
675   PRINT  "T1=  "; T1, "T2=  "; T2
680   REM
690   FOR  I=1 TO 50
700   H1=H0/EXP(D1*I/50)
710   X(I,0)=(H1-H0)/S0+B
720   NEXT I
730   REM
740   H1=H0/EXP(D1)+0.254
750   H=(H0-H1)/S0
760   FOR  I=1 TO 50
770   H3=H2/EXP(D2*I/50)
780   Y(I,0)=(H3-H2)/S0+.02+(B-H)
790   NEXT I
800   REM
810   CKTIME(1,.01)
```

```
820   V1=D1/S1/.01 \ T8=V1/D9 \ IF T8<1 THEN T8=1
830   V2=D2/S3/.01 \ T9=V2/D9 \ IF T9<1 THEN T9=1
880   ADTIMED(1,A,,1,T8,3,4)
890   ADTIMED(2,A,,1,10000,3,4)
900   ADTIMED(3,A,,1,T9,3,4)
910   ADTRIGGER(3,F5,-1)
920   REM----------------------SET UP THE SYSTEM------------------------------------------
930   FGARB(1,"R", TIME T1, ARRAY X)
940   FGARB(1,"R", TIME 1.00000E-03,.02+(B-H))
950   PRINT \ PRINT "PRESS RETURN TO START THE DEFORMATION":   INPUT G$
955   PRINT \ PRINT "TO INTERRUPT THE TEST, PRESS Ctrl^C, ":
957   PRINT "AND TYPE 'GOTO 1060'    "
960   ADINIT \ FGGO \ ADGO(1)
970   FGSTATUS(1,W) \ IF W< > 0 THEN GO TO 970
980   ADSTOP(1)
990   PRINT \ PRINT "1ST DEFORMATION DONE"
1000   IF D5=1 THEN GO TO 1060
1010   ETIME \ SLEEP(T)
1020   PRINT \ PRINT "INTERPASS FINISHED"
1030   FGARB(1,"R", TIME T2, ARRAY Y)
1040   FGGO \ ADGO(3)
1050   FGSTATUS(1,S) \ IF S< >0 THEN GO TO 1050
1060   ADSTOP \ FGSTOP \ CKSTOP
1070   REM
1080    FGIMMED(1,"R", TIME .5,0)
1090    PRINT \ PRINT \ PRINT
1100    PRINT "****** THE EXPERIMENT IS FINISHED ******":   INPUT G$
1105    REM-----C1 IS THE MTS COMPLIANCE-------------
1110    FOR I=1 TO A
1130    C2= -ELEVEL(A(I,1))*L0
1140    C1= .198769*(1-EXP(-1.15596E-07*C2^2))+2.0006E-05*C2
1150    Z(I)=H0+(ELEVEL(A(I,2))-B)*S0
1160    REM --- PRINT I,LOG(H0/Z(I))
1170    NEXT I
1180    PRINT \ PRINT
1190    X0=1.00000E-05
1200    FOR I=10 TO A
1210    X1=LOG(H0/Z(I))
1220    IF X1<X0 THEN 1250
1230    X0=X1
1240    NEXT I
1250    PRINT "I1=";I-1 \ I1=I-1
1254    G2= -ELEVEL(A(I1,1))*L0*Z(I1)/A0/H0
1256    G3=.1*G2
1260    FOR J=I1 TO A
1270    X2= -ELEVEL(A(J,1))*L0*Z(J)/A0/H0
1280    IF X2 > G3 THEN 1300
1290    NEXT J
1300    PRINT "I2=";J \ I2=J
1310    J=0
1380    FOR I=0 TO A
1390    IF I > I1 THEN IF I < I2 GO TO 1420
1400    D(J,0)=A(I,0) \ D(J,1)=A(I,1) \ D(J,2)=A(I,2) \ D(J,3)=A(I,3)
```

```
1410    J=J+1
1420    NEXT I
1430    REM
1440    ERASE
1450    PRINT \ PRINT
1460    PRINT “RESULTS FROM THE EXPERIMENT:”
1470    PRINT \ PRINT
1480    PRINT “INITIAL POSITION:”; \ PRINT B
1490    PRINT “TOTAL NUMBER OF DATA POINTS:”; \ PRINT J
1500    PRINT “NUMBER OF POINTS FOR THE FIRST DEFORMATION:”; \ PRINT I1
1510    F(1)=J \ F(2)=I1
1520    F(3)=I2 \ F(4)=H0 \ F(5)=D0 \ F(6)=D5 \ F(7)=D1 \ F(8)=S1
1530    F(9)=T \ F(10)=D2 \ F(11)=L \ F(12)=S0
1540    F(13)=B \ F(14)=S3
1550    PRINT \ PRINT \ PRINT
1560    W=SYS(4)
1570    PRINT “DO YOU WANT TO SAVE THE DATA”; \ INPUT G$
1580    PRINT \ PRINT
1590    IF G$=“N” THEN GO TO 1650
1600    OPEN “DU1:T”&N$ FOR OUTPUT AS FILE #1
1610    OPEN “DU1:K”&N$ FOR OUTPUT AS FILE #2
1620    FOUT(1,D(0,0), ,0,F) \ CLOSE #1
1630    FOUT(2,F(1), ,0,F) \ CLOSE #2
1640    REM ---
1650    PRINT \ PRINT “DO YOU WANT TO SEE THE DATA”; \ INPUT G$
1660    IF G$=“N” THEN GO TO 1910
1670    OPEN “DU1:T”&N$ FOR INPUT AS FILE #1
1680    OPEN “DU1:K”&N$ FOR INPUT AS FILE #2
1690    FINP(1,C(0,0), ,0,F) \ CLOSE #1
1700    FINP(2,E(1), ,0,F) \ CLOSE #2
1710    J=E(1) \ I1=E(2) \ I2=E(3) \ H0=E(4)
1720    D0=E(5) \ D5=E(6) \ D1=E(7) \ S1=E(8)
1730    T=E(9) \ D2=E(10) \ L=E(11) \ S0=E(12) \ B=E(13)
1740    REM ---
1750    T(0)=0
1760    FOR I=1 TO J
1770    T(I) = C(I,0)*.01+T(I-1)
1780    NEXT I
1790    L0=L*4.4482*1000
1800    A0=PI*(D0)^2/4
1810    PRINT \ PRINT “TEST= ”; N$
1820    PRINT \ PRINT “TIME(sec)  :”, “HEIGHT(mm)  :”, “LOAD(kN)  :”, “TEMP(C)”
1830    FOR I=1 TO J
1840    H1=H0+(ELEVEL(C(I,2))-B)*50; “;”,
1850    PRINT T(I); “;”,
1860    PRINT H1; “;”,
1870    PRINT (ELEVEL(C(I,1))*L*4.4482; “;”,
1880    PRINT (ELEVEL(C(I,3))*2794-25
1890    NEXT I
1900    PRINT \ PRINT “B=”; E(13), “J=”; E(1), “I1=”; E(2)
1910    PRINT \ PRINT “DO YOU WANT TO SEE THE GRAPHICS”; \ INPUT F$
1920    IF F$=“Y” THEN CHAIN “BAI5T.BAS” LINE 270
1930    END
```

APPENDIX II

SHEAR PUNCH TESTING PROGRAM

```
10   REM---CONSTANT ACTUATOR VELOCITY PUNCH TEST---
20   REM---PROGRAMMED BY A. ZAREI-HANZAKI & A. ROHATGI---
25   REM---MODIFIED BY T.MACCAGNO AND P.WANJARA---
30   ERASE
40   DIM A(1000.2),B(1000.1),F(5)
50   J=0 \ M0=0
60   PRINT "OLD TEST (O) OR NEW TEST(N) ":   INPUT A$
70   PRINT "FILE NAME: ": \ INPUT N$
80   IF A$="N" GO TO 100
90   GOSUB 600 \ GO TO 530
100  PRINT "MATERIAL        :":  INPUT S$
110  PRINT \ PRINT "ENTER LOAD RANGE (kips)":   INPUT L   L0=L*4.4482*1000
120  PRINT \ PRINT "ENTER STROKE RANGE (mm)":   INPUT S
130  F(1)=L \ F(2)=S
140  ERASE
150  GTIME(,M.H)
160  PRINT "DATE                              :":   PRINT DAT$
170  PRINT "TIME                              :":   PRINT H: ":"M
180  PRINT
190  PRINT "********************PUNCH EXPERIMENTAL DATA***********************
200  PRINT \ PRINT
210  PRINT "FILE NAME                         :":   PRINT N$
220  PRINT
230  PRINT "TOTAL EXPERIMENT TIME (sec)        ":   INPUT T$
240  PRINT "TOTAL STROKE DISPLACEMENT (mm)           ":   INPUT D
250  PRINT
260  PRINT "LOAD RANGE                        :":   PRINT L:   PRINT "   kip"
270  PRINT "STROKE RANGE                      :": \ PRINT S: \ PRINT "  (mm)"
280  REM-----------------------SET  UP  THE  SYSTEM-----------------------------------
290  CKTIME(1,.03)
300  ADTIMED(1,A, .3.10,1)
```

```
310  FGARB(1, "R", TIME T, -D/S)
320  PRINT "DO YOU WANT 'ONSCREEN' DISPLAY (Y/N): "; \ INPUT A$
330  IF A$="N" THEN GOSUB 1280
340  PRINT "AFTER THE GRAPH AXIS HAVE BEEN PLOTTED, PRESS RETURN TO START"
350  W=SYS(4)
360  GOSUB 970
370  GOSUB 1170
380  FGIMMED(1, "R", TIME 0.5, 0)
390  PRINT "****** THE EXPERIMENT IS FINISHED ******"
400  W=SYS(4) \ ERASE
410  FOR I=0 TO A
420  M1= -(ELEVEL(A(I,2)))*L0
430  IF M1 > M0 THEN M0 = M1
440  PRINT I, (ELEVEL(A(0,1))-ELEVEL(A(I,-1)))*S.M1
450  PRINT
460  NEXT I
470  PRINT "REFERENCE ROW #: "; \ INPUT R
480  PRINT "IF YOU WILL not SAVE THE DATA, YOU WILL EXIT FROM THE PROGRAM"
490  PRINT "DO YOU WANT TO SAVE THE DATA"; \ INPUT G$
500  PRINT \ PRINT
510  IF G$="N" THEN GO TO 580
520  GOSUB 840
530  PRINT \ PRINT "DO YOU WANT TO SEE THE GRAPHICS"; \ INPUT G$
540  IF G$="N" THEN GO TO 560
550  GOSUB 760
560  PRINT \ PRINT "ANOTHER OLD FILE (O) OR FINISH (F)"; \ INPUT A$
570  IF A$="O" THEN GO TO 70
580  STOP
590  END
600  REM-------------SUBROUTINE FOR PRINTING THE DATA---------------
610  OPEN "DU1:M"&N$ FOR INPUT AS FILE #2
620  FINP(2,F(0), ,0,F) \ CLOSE #2
630  M0=0 \ J=F(0)/2 \ L=F(1) \ S=F(2)
640  OPEN "DU1:T"&N$ FOR INPUT AS FILE #1
650  FINP(1,B(0,0),F(0),0,F) \ CLOSE #2
660  PRINT "PRESS RETURN TO SEE THE DATA"; \ W=SYS(4)
670  PRINT "LOAD RANGE      :";L; "Kips"
680  PRINT "STROKE RANGE    :";S; "mm"
690  PRINT "NO. OF ROWS     :";J
700  PRINT
710  FOR I=0 TO (J-1)
720  M1=B(I,1) \ PRINT I,B(I,0),B(I,1)
730  IF M1 > M0 THEN M0=M1
740  NEXT I
750  RETURN
760  REM----SUBROUTINE FOR PRINTING THE GRAPH OF LOAD VS DISPLACEMENT----
770  GOSUB 970
780  FOR I=0 TO J
790  MARK(1,4,B(I,0),B(I,1))
800  NEXT I
810  W=SYS(4)
820  ERASE
830  RETURN
```

```
840   REM----------------------SUBROUTINE FOR SAVING THE DATA--------------------------
850   FOR I=R  TO  J
860   B(J,0)=(ELEVEL(A(R,1))-ELEVEL(A(I,-1)))*S
870   B(J,1)=-(ELEVEL(A(I,-2)))*L0
880   J=J+1
890   NEXT I
900   K=J*2
910   F(0)=K
920   OPEN "DU1:T"&N$  FOR OUTPUT AS FILE #1
930   OPEN "DU1:M"&N$  FOR OUTPUT AS FILE #2
940   FOUT(1,B(0,0),K,0,F) \ CLOSE #1
950   FOUT(2,F(1), ,0,F) \ CLOSE #2
960   RETURN
970   REM-----------------SUBROUTINE FOR PLOTTING THE GRAPH AXIS ETC.---------------
980   ERASE
990   PHYL(1,5,95,0,99)
1000   PRINT  \ PRINT  "MAXIMUM LOAD RECORDED                        : ";  \ PRINT M0; "N"
1010   PRINT  \ PRINT  "ENTER THE MAXIMUMLOAD (N) ON Y AXIS          : ";    INPUT U
1020   PRINT  \ PRINT  "ENTER THE LOAD INTERVALS ON Y AXIS           : ";    INPUT U1
1030   PRINT  \ PRINT  "ENTER THE MAXIMUM DISPLACEMENT (mm)          : ";    INPUT V
1040   PRINT  \ PRINT  "ENTER THE INTERVALS ON X AXIS                : ";    INPUT V1
1050   ERASE
1060   SCALE(1,0,-.01,V+.01,0,U)
1070   INVEC(1) \ PLOT(1,-.01,0)
1080   PLOT(1,-.01,U)
1090   PLOT(1,V+.01,U)
1100   PLOT(1,V+.01,0)
1110   PLOT(1,-.01,0)
1120   LABEL(1,"DISPLACEMENT (mm)","LOAD (N)",V1, U1,1)
1130   LABEL(1," "," ",V1/5,U1/5,3)
1140   COMM(1,"TEST :",.05*(V),.95*U)
1150   COMM(1,N$,.2,*(V),.95*U)
1160   RETURN
1170   REM--------SUBROUTINE FOR "ONSCREEN" DISPLAY OF THE CURRENT TEST------
1180   W=SYS(4)
1190   ADIMMED(3,B0)
1200   ADINIT \ FGGO \ ADGO(1)
1210   ADIMMED(1,A1) \ ADIMMED(3,B1)
1220   X=(B0-B1)*S \ Y=-A1*L0
1230   MARK(1,4,X,Y)
1240   FGSTATUS(1,W) \ IF W < > 0 THEN GO TO 1210
1250   ADSTOP \ FGSTOP \ CKSTOP
1260   FGIMMED(1,"R", TIME 5,0) \ W=SYS(4) \ ERASE
1270   RETURN
1280   REM----------SUBROUTINE TO PERFORM THE TEST WHEN 'VISUAL' NOT ON--------
1290   PRINT  "PRESS RETURN TO START THE TEST" \ W =SYS(4)
1300   ADINIT \ FGGO \ ADGO(1)
1310   FGSTATUS(1,W) \ IF W < > 0 THEN GO TO 1310
1320   ADSTOP \ FGSTOP \ CKSTOP
1330   GO TO 380
1340   RETURN
```

APPENDIX III

LATTICE PARAMETER CALCULATIONS

Lattice parameter determination from diffraction data involves a number of calculations and a proper analysis technique to ensure high precision in the computed values. In general, the lattice parameter, a_o, of a cubic substance is directly proportional to the spacing d of any particular set of lattice planes according to the following equation,

$$a = d_{hkl}\sqrt{h^2+k^2+l^2} \tag{AIII.1}$$

where *hkl* are the Miller indices of the diffracting plane, *a* is the lattice spacing of the cubic substance and d_{hkl} is the crystallographic plane spacing.

From the diffraction data, a measurement of the Bragg angle, θ_{hkl}, for each set of diffracting planes, can be used to calculate d_{hkl}, according to Bragg's law.

$$d_{hkl} = \frac{\lambda}{2\sin\theta_{hkl}} \tag{AIII.2}$$

where λ is the neutron de Broglie wavelength for the neutron diffraction data analysis. Hence obtaining d_{hkl} from equation AIII.2, *a* can be calculated from equation AIII.1. Precision in either d_{hkl} or *a* depends on precision in sin θ, a derived quantity and not on precision in θ, the measured quantity. Hence, the error in sin θ caused by a given error in the measured θ has been found to decrease with increasing θ, (Fig. AIII.1).

Thus, the angular position of a diffracted beam will be more sensitive to a change in crystallographic plane spacing or lattice parameter when θ is large. Precision in lattice parameter measurements therefore lies in the use of backward-reflected beams having scattering angle, 2θ, values close to 180°. Although the error in sin θ disappears as the scattering angle approaches 180°, no observable reflected beams exist at this angle. However, since the values of *a* calculated for the various diffraction planes approach the *true value* more closely as the scattering angle increases,[238] it may be possible to obtain the *true value* of the lattice parameter by simply plotting the measured *a* values against θ and extrapolating to 2θ = 180°. Unfortunately, a plot of the *a* values against the scattering angle directly gives a nonlinear curve which is difficult to extrapolate accurately. However, extrapolation functions giving a linear behavior have been derived by considering the various effects that can generate systematic errors in the measured values of the scattering angle.[238] (A systematic error is one that varies in a regular manner with some particular parameter such as off-center specimen and absorption).

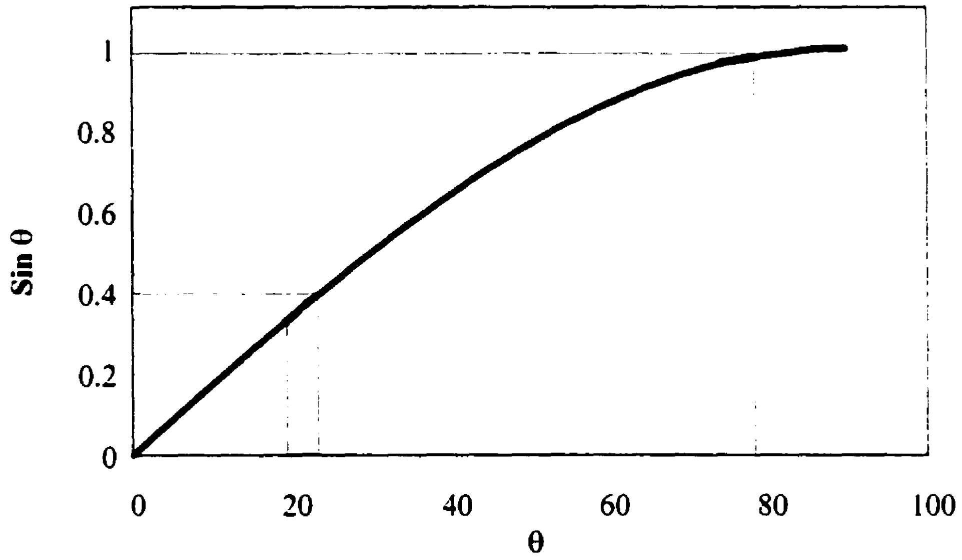

Figure AIII.1 Variation in sin θ with θ illustrating that the uncertainty in sin θ decreases as θ increases.

In this work, the *a* values were plotted against $\cos^2\theta$ and the true value of the lattice parameter, a_0, of a particular phase was found by extrapolating to $\cos^2\theta = 0$. In general, the use of the extrapolation function enables the elimination of systematic errors in *a* which approach zero as θ approaches 90°. In addition, there is an increasing drift in the *a* values with increasing θ and this gives an indication as to the nature of the systematic error, as shown in Figure AIII.2. Comparing Figure AIII.2a with AIII2b, it is observed that in the former plot the calculated *a* values exhibit a strong correlation to the regression line, indicating small random errors, however, the line itself is quite steep due to large systematic errors. The random errors occur inevitably during measurement of the scattering angles of the diffracted peaks. These random errors in *a* also decrease in magnitude as θ increases, essentially due to the slow variation of sinθ with θ at large angles, as shown in Figure AIII.1. In both cases, the a_0 value remains the same. However, inasmuch as the reliability of the regression line decreases with the degree of scatter, great effort must be taken to minimize both random and systematic errors.

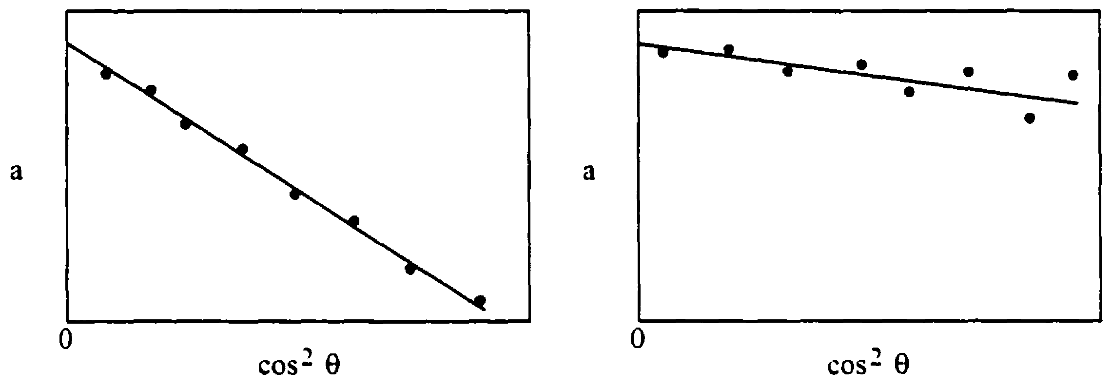

(a) (b)

Figure AIII.2 Schematic of extreme forms of extrapolation curves illustrating (a) large systematic errors, small random errors and (b) small systematic errors and large random errors.

In the present work, at the commencement of consolidation, at any isothermal sintering temperature in the range of 1100°C to 1350°C, two phases existed: a BCC phase corresponding to the β-Ti-6%Al-4%V and a FCC phase corresponding to the TiC. The mean scattering angles for the diffraction peaks were identified from the neutron diffraction data. These were then fitted to the *hkl* Miller indices of the various diffracting planes of each phase. Using equation AIII.2, the crystallographic plane spacing was calculated. From these values the corresponding *a* values were obtained using equation AIII.2, as summarized in Table AIII.1 and AIII.2 for β-Ti-6%Al-4%V and TiC, respectively. The *true* lattice parameters at 1100°C for these phases were then obtained by plotting the *a* values against $\cos^2\theta$. As illustrated in Figure A.III.3 and A.III.4, the *true* lattice parameter, a_0, for β-Ti-6%Al-4%V and TiC was determined be 3.3043 Å and 4.3609Å, respectively.

Table AIII.1 - Diffraction Peak Angles of Beta-Ti-6%Al-4%V at 1100°C

h k l	2θ (°)	$d_{(hkl)}$ (Å)	$a_{(hkl)}$ (Å)
1 1 0	37.900	2.310	3.266
2 0 0	54.550	1.637	3.273
2 1 1	68.189	1.338	3.277
2 2 0	80.560	1.160	3.281
3 1 0	92.501	1.038	3.283
2 2 2	104.359	0.949	3.289

Table AIII.2 - Diffraction Peak Angles of TiC at 1100°C

h k l	2θ (°)	$d_{(hkl)}$ (Å)	$a_{(hkl)}$ (Å)
1 1 0	34.721	2.514	4.3537
2 0 0	40.299	2.177	4.3544
2 2 0	58.291	1.540	4.3557
3 1 1	69.640	1.313	4.3563
2 2 2	73.222	1.258	4.3565
4 0 0	87.039	1.089	4.3566
3 3 1	97.221	1.000	4.3576
4 2 0	100.638	0.975	4.3581

With consolidation, two new peaks were observed to form at the higher scattering angles. From previous work with the Ti-6%Al-4%V/TiC composite system, it is expected that the formation of the interfacial reaction product would be a non-stoichiometric TiC_x phase.[26,86-89,110-121] It has been found that TiC, crystallizing in a NaCl crystal structure, displays deviations from stoichiometry over a wide composition range (TiC_x: $0.5 \leq x \leq 0.97$). These deviations are caused by vacancies on the carbon lattice sites. Moreover the carbon vacancies are disordered in the lattice. Thus, the analysis performed for the lattice parameter of the TiC_x phase was similar to that of TiC.

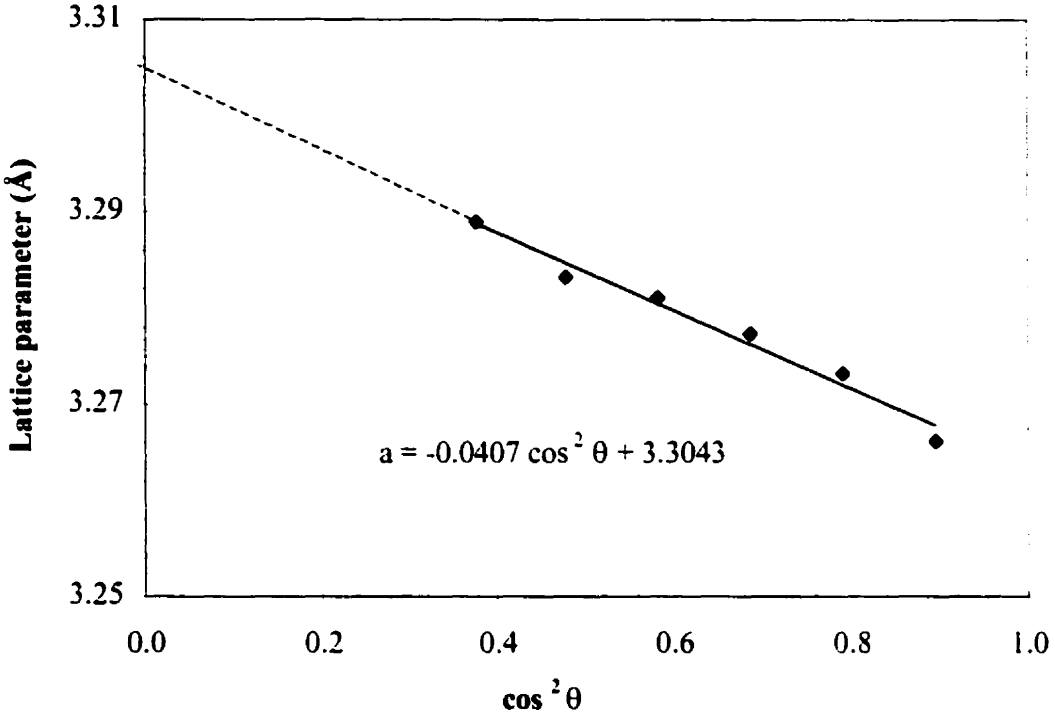

Figure AIII.3 Extrapolation curve for determining the *true* lattice parameter of β-Ti-6%Al-4%V at 1100°C.

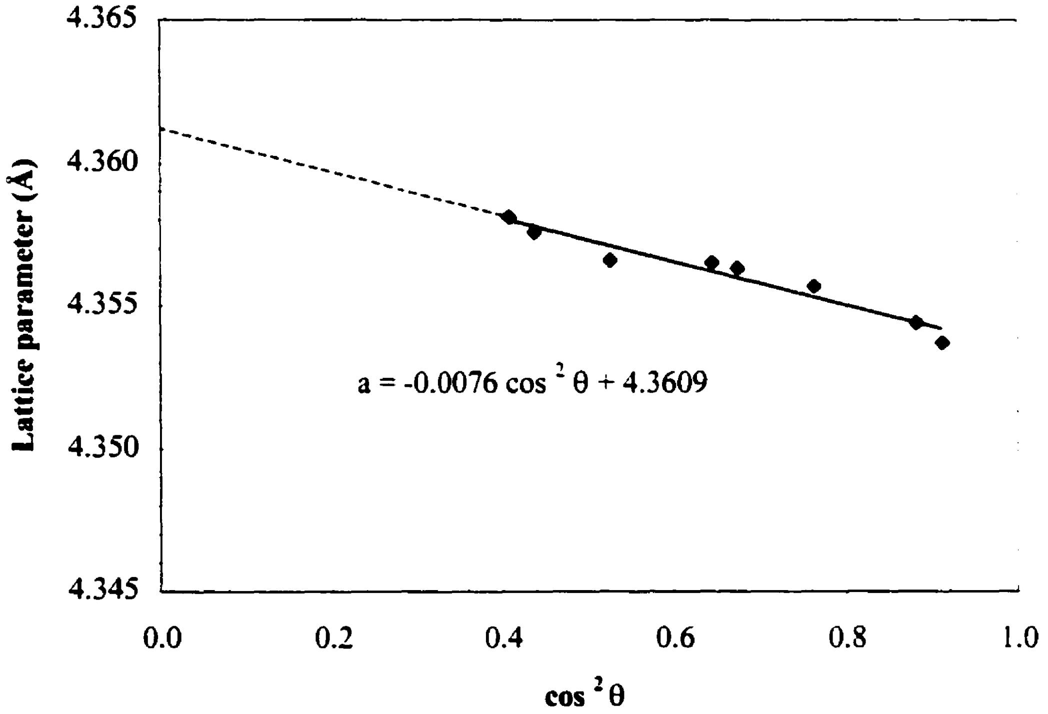

Figure AIII.4 Extrapolation curve for determining the *true* lattice parameter of TiC at 1100°C.

APPENDIX IV

SINGLE PEAK GAUSSIAN FITTING PROGRAM

```
C  THIS IS A PROGRAM TO TAKE A RANGE OF DATA FROM C2 DIFFRACTION PATTERN
C  AND FIT WITH A GAUSSIAN FUNCTION.
    DIMENSION X(100), Y(100), D(100), PARMS(5)
    DIMENSION C(5), F1INV(5,5), CERR(5)
    OPEN (UNIT=1,FILE='c:PRITI1.IN', STATUS='OLD')
    OPEN (UNIT=2,FILE='c:PRITI1.PRN',STATUS='UNKNOWN')
    open (unit=3,file='c:PRITI1.OUP',status='unknown')
C  INITIAL GUESSES OF PEAK POSITIONS
    WRITE(*,*) 'INITIAL GUESSES OF PEAK ANGLE        '
    READ (*,*) C2
C  ANALYZE SPECTRA UNTIL EOF
   1 CONTINUE
C  INPUT THE DATA FROM DISKETTE OR HARD DISK FILE, AND MODIFY IT INTO (X,Y)
C  FORM.  ALSO KEEP TRACK OF THE VARIOUS EXPERIMENTAL R PARAMETERS FOR THIS
C  RUN SUCH AS RUN#, XPOS, YPOS WHICH ARE NECESSARY FOR OUTPUT FILE. NX IS
C  THE NUMBER OF EXPERIMENTAL DATA C POINTS TO BE FIT.
    CALL DATAIN (X,Y,NX,PARMS,AMON,IMDONE,IERR,C2)
    IF (IMDONE.EQ.1) GOTO 999
    IF (IERR.EQ.1) GOTO 990
C  CALCULATE INITIAL VALUES OF THE COEFFICIENTS OF THE MODEL FUNCTION
C  REPRESENTING THE PEAK DATA. (THE MODEL IS A GAUSSIAN SUPERIMPOSED ON A
C  SLOPED BACKGROUND: HENCE THE COEFFICIENTS ARE THE GAUSSIAN AMPLITUDE,
C  MEAN SIGMA, AND THE LINE SLOPE AND Y INTERCEPT, LABELLED C(1) THROUGH C(5)
C  RESPECTIVELY. RETURNS AN ERROR FLAG IF THE DATA IS NOT LIKELY TO BE WELL
C  ANALYSED BY A GAUSSIAN,.EG NO DISCERNIBLE PEAK AGAINST BACKGROUND
    CALL PREFIT (C,X,Y,NX,IERR)
    IF (IERR.EQ.1) goto 990
C  REFINE THESE ESTIMATES OF THE COEFFICIENTS OF THE MODEL FUNCTION USING
C  A LEAST-SQUARES PROCEDURE (NEWTON-RAPHSON SOLUTION).  THIS YIELDS THE
C  BEST MODEL FUNCTION, D, AND A FINAL INVERSE MATRIX USED FOR UNCERTAINTY
C  ESTIMATES, F1INV.  IF THE N-R MATRIX CANNOT BE INVERTED, FLAG IERR IS SET TO 1.
```

```
      CALL REFINE (C,X,Y,D,F1INV,NX,IERR)
      IF (IERR.EQ.1) GOTO 900
C  CALCULATE THE UNCERTAINTIES ASSOCIATED WITH THE FINAL VALUES OF THE
C  COEFFICIENTS, AND THE GENERAL QUALITY OF FIT OF THE MODEL TO THE DATA, CHI.
      CALL UNCERT (Y,D,F1INV,CERR,CHI,NX)
C  OUTPUT RESULTS IN THE FORMAT REQUIRED FOR THE SPREADSHEET PROGRAM.
      CALL DATOUT (X,Y,D,NX.C,CERR,CHI,PARMS.AMON)
      GOTO 1
  900 CONTINUE
      WRITE (*,500) PARMS(1)
  500 FORMAT(' RUN# ',F8.0,'   ***** MATRIX NOT INVERTIBLE *******')
      GOTO 1
  990 CONTINUE
      WRITE(*,555) PARMS(1)
  555 FORMAT(' RUN# ',F8.0,'   DATA NOT SUITABLE FOR GAUSSIAN FIT')
      GOTO 1
C  END-OF-FILE ENCOUNTERED. STOP PROGRAM
  999 CONTINUE
      WRITE(*.550)
  550 FORMAT(' END OF FILE FOUND... STOP')
      CLOSE(1)
      CLOSE(2)
      STOP
      END
SUBROUTINE DATAIN (X.Y.NX.PARMS.AMON.IMDONE.IERR.C2)
      DIMENSION X(100).Y(100),PARMS(5).YIN(800)
      IERR=0
      IMDONE=0
C  CLEAR OUT BLANK LINES, TRANS HEADER AND SPECTROMETER IDENTIFIER
      DO 11 K=1,4
      READ (1,*,END=999)
   11 CONTINUE
C  READ RUN NUMBER AND NUMBER OF DATA POINTS IN SCAN
      READ (1,480,END=999) INPT
  480 FORMAT(5X,I4)
C  CLEAR OUT MODE LINE AND SPECTROMETER SETUP LINES
      DO 12 K=1,5
      READ (1,*.END=999)
   12 CONTINUE
C  READ phi1
      READ (1,461.END=999) PHI1
  461 FORMAT(31X,F8.3)
      DO 121 K=1,8
      READ (1,*,END=999)
  121 CONTINUE
C  READ TIME, MONITOR, TEMPERATURES
      READ (1,482.END=999) TIME.AMON.CTEMP. RTEMP
  482 FORMAT(15X,F5.0,F9.0,F10.4,F10.4)
      READ (1,*,END=999)
      PARMS(1) = INPT
      PARMS(2) = CTEMP
      PARMS(3) = RTEMP
      PARMS(4) = TIME
```

```
C  READ IN THE DATA
      READ (1,*,END=999) (YIN(K),K=1,800)
C  CORRECT THE BAD CHANNELS
      YIN(162) = (YIN(161)+YIN(163))/2.
      YIN(449) = (YIN(448)+YIN(450))/2.
      YIN(681) = (YIN(680)+YIN(682))/2.
C  EXTRACT THE PEAK OFF THE DIFFRACTION PATTERN
      ICENTR=(C2-PHI1)*10+1
      ILOW=ICENTR-15
      IHI =ICENTR+15
C  CONSTRUCT THE X,Y ARRAYS
      DO 15 I=ILOW,IHI
      K = (I-ILOW)+1
      X(K) = PHI1 + (ILOW+K-2)*0.1
   15 Y(K) = YIN(I)
      NX = 31
      RETURN
C  EOF FLAG SET IF END-OF-FILE WAS ENCOUNTERED
  999 IMDONE=1
      RETURN
      END
SUBROUTINE PREFIT (C,X,Y,NX,IERR)
      DIMENSION C(5),X(300),Y(300)
      IERR=0
C  FIND THE MAXIMUM VALUE OF DATA Y, AND ITS POSITION
      YMAX=0.
      YMIN=1.0E6
      DO 10 I=1,NX
      IF (Y(I).LE.YMAX) GOTO 9
      YMAX=Y(I)
      INDX=I
    9 CONTINUE
      IF (Y(I).LT.YMIN) YMIN=Y(I)
   10 CONTINUE
C  FIND THE FULL WIDTH AT HALF MAX
      HMAX=(YMAX-YMIN)/2.
      DO 20 I=INDX,NX
      IF ((Y(I)-YMIN).LE.HMAX) GOTO 21
   20 CONTINUE
   21 XMAX=X(I)
      DO 30 J=1,INDX
      I=INDX-J+1
      IF ((Y(I)-YMIN).LE.HMAX) GOTO 31
   30 CONTINUE
   31 XMIN=X(I)
C  (FWHM=XMAX-XMIN  SIGMA = FWHM/2.35)
      C(1)=YMAX-YMIN
      C(2)=X(INDX)
      C(3)=(XMAX-XMIN)/2.35
      C(4)=(Y(NX)-Y(1))/(X(NX)-X(1))
      C(5)=Y(1)
      IF ((INDX.EQ.NX).OR.(INDX.EQ.1)) IERR=1
      IF (YMAX.LT.(1.2*YMIN)) IERR=1
```

```
    IF (YMAX.LE.10.0) IERR=1
    IF (NX.LT.10) IERR=1
    RETURN
    END
SUBROUTINE REFINE (C,VECX,VECY,VECD,F1INV,N,IERR)
    DIMENSION VECX(300),VECY(300),VECD(300)
    DIMENSION C(5),F(5),F1(5,5),F1INV(5,5),DF(5),DF1(5,5)
    SUMSAV=1.0E10
    IERR=0
    X0=VECX(1)
C   CLEAR NEWTON-RAPHSON FUNCTION AND ITS DERIVATIVE WITH RESPECT TO COEFFS
  1 DO 10 I=1,5
    F(I)=0.
    DO 10 J=1,5
 10 F1(I,J)=0.
C   COMPOSE N-R FUNCTION AND DERIVATIVE MATRIX BY SUMMING INCREMENTS ARISING
C   FROM EACH DATA POINT
    DO 20 I=1,N
    X=VECX(I)
    Y=VECY(I)
C   CALCULATE INCREMENTS OF F AND F1 FOR THIS, THE ITH DATA POINT AND THE
C   VALUE OF THE MODEL FUNCTION, D, FOR THE CURRENT COEFFS VALUES
    CALL FINC (C,X,X0,Y,D,DF,DF1)
    VECD(I) = D
    DO 15 J=1,5
    F(J) = F(J) + DF(J)
    DO 15 K=1,5
 15 F1(J,K) = F1(J,K) + DF1(J,K)
 20 CONTINUE
C   SEE IF SUM(F**2) IS SMALL ENOUGH SO THAT WE HAVE CONVERGENCE
    SUMF=0.
    DO 30 I=1,5
 30 SUMF = SUMF + (F(I)/F1(I,I))**2
    IF (SUMF.LT.1.E-4) RETURN
C   CONVERSELY, IF THERE WAS NO PROGRESS OVER THE LAST ITERATION, THEN QUIT
    TEST=ABS((1.-SUMF/SUMSAV))
    IF (TEST.LT.0.01) RETURN
    SUMSAV=SUMF
C   IF FURTHER ITERATIONS ARE NEEDED, COEFF VALUES MUST BE UPDATED BY
C   INVERTING THE N-R MATRIX
    CALL MINV (F1,IERR)
    IF (IERR.EQ.1) RETURN
C   (SAVE MATRIX INVERSE IN CASE THIS IS THE LAST ITERATION)
    DO 50 I=1,5
    CORR=0.
    DO 40 J=1,5
    F1INV(I,J)=F1(I,J)
 40 CORR = CORR + F1(I,J)*F(J)
 50 C(I) = C(I) - CORR/2.
    GOTO 1
    END
SUBROUTINE FINC (C,X,X0,Y,D,DF,DF1)
    DIMENSION C(5), DF(5), DF1(5,5), D1(5)
```

```
      CA =C(1)
      CMU=C(2)
      CS =C(3)
      CM =C(4)
      CB =C(5)
C  CALCULATE DERIVATIVES OF MODEL FUNCTION AT THIS X WITH RESPECT TO COEFF(N)
      EXPARG = 0.5*((X-CMU)/CS)**2
      D1(1) = 0.
      IF (EXPARG.LT.20.0) D1(1) = EXP ((0.-EXPARG))
      D1(2) = CA*D1(1)*(X-CMU)/CS/CS
      D1(3) = D1(2)*(X-CMU)/CS
      D1(4) = X-X0
      D1(5) = 1.0
C  CALCULATE THE MODEL FUNCTION WITH PRESENT COEFFICIENTS
      D = CM*D1(4) + CB + CA*D1(1)
C  WEIGHT OF EACH CONTRIBUTION TO THE INCREMENT, AND WEIGHTED DIFFERENCE
C  BETWEEN DATA AND MODEL ARE:
      W = 1./(Y+1.)
      WDIFF = W*(D-Y)
C  CALCULATE THE INCREMENTS OF F
      DO 10 I=1,5
   10 DF(I) = WDIFF*D1(I)
C  CALCULATE THE INCREMENTS OF F1
      DO 20 I=1,5
      DO 20 J=1,5
   20 DF1(I,J) = W*D1(I)*D1(J)
C  COMPLETE THE SYMMETRIC MATRIX
      DO 30 I=1,4
      J1=I+1
      DO 30 J=J1,5
   30 DF1(J,I) = DF1(I,J)
      RETURN
      END
   SUBROUTINE UNCERT (Y,D,F1INV,CERR,CHI,N)
      DIMENSION Y(300), D(300), F1INV(5,5), CERR(5)
      XN=N
      CHISQ=0.
      DO 10 I=1,N
   10 CHISQ = CHISQ + (Y(I) - D(I))**2/(Y(I)+1.)
      CHI = SQRT((CHISQ/(XN-5.)))
      DO 20 I=1,5
   20 CERR(I) = SQRT(F1INV(I,I))*CHI
      RETURN
      END
   SUBROUTINE DATOUT (X,Y,D,NX,C,E,CHI,PARMS,AMON)
      DIMENSION C(5), E(5), PARMS(5),X(300),Y(300),D(300)
C  SUM THE COUNTS OVER ALL CHANNELS
      SUM=0.
      DO 111 KN=1,NX
  111 SUM=SUM+Y(KN)
C  CONVERT AMPLITUDE TO INTEGRATED INTENSITY
      FCT=SQRT(6.283186)*C(3)
      C(1)=ABS((C(1)*FCT))/AMON*1.0E5
```

```
   E(1)=ABS((E(1)*FCT))/AMON*1.0E5
   C(5)=ABS((C(5)*FCT))/AMON*1.0E5
   E(5)=ABS((E(5)*FCT))/AMON*1.0E5
   C(4)=ABS((C(4)*FCT))/AMON*1.0E5
   E(4)=ABS((E(4)*FCT))/AMON*1.0E5
C  CONVERT SIGMA TO FWHM
   C(3)=ABS((2.35482*C(3)))
   E(3)=ABS((2.35482*E(3)))
   WRITE (2,500) (PARMS(I),I=1,4),(C(I),E(I),I=1,5),CHI
 500 FORMAT(' ',F12.0,3F12.2,11F12.4)
   WRITE(*,497) NX
 497 FORMAT (' NUMBER OF DATA POINTS =',I3)
C  PUT INPUT/OUTPUT DATA TO FILE
   WRITE(3,*) ' '
   WRITE(3,697) (PARMS(I),I=1,4), AMON
 697 FORMAT(' ',4F12.3,F12.1)
   DO 10 K=1,NX
   WRITE(3,498) X(K),Y(K),D(K)
 498 FORMAT(' ',F12.3,2F12.3)
  10 CONTINUE
   WRITE (*,501) PARMS(1),(C(I),I=1,3),CHI
 501 FORMAT(' RUN# I  MEAN  FW  CHI:',F6.0,4F12.4)
   RETURN
   END
C  SUBROUTINE TO INVERT A 5X5 MATRIX F1.  RETURNS INVERTED MATRIX IN ORIGINAL
C  SPACE OF F1 AND SETS FLAG (IERR=1 IF MATRIX SINGULAR, 0 IF INVERSION SUCCESS)
   SUBROUTINE MINV (F1,IERR)
   DIMENSION F1(5,5), A(5,10), ID(5)
   N=5
   NN=N+1
   N2=2*N
   DO 200 I=1,N
   DO 200 J=1,N
 200 A(I,J)=F1(I,J)
   K=1
   DO 1 I=1,N
   DO 1 J=NN,N2
  1 A(I,J) = 0.
   DO 21 I=1,N
   A(I,N+I) = 1.
  21 ID(I) = I
2 CONTINUE
   KK = K+1
   IS = K
   IT = K
   B = ABS (A(K,K))
   DO 3 I = K,N
   DO 3 J = K,N
   IF (ABS(A(I,J)).LE.B) GOTO 3
   IS = I
   IT = J
   B = ABS(A(I,J))
  3 CONTINUE
```

```
      IF (IS.LE.K) GOTO 4
      DO 42 J=K,N2
      C=A(IS,J)
      A(IS,J) = A(K,J)
   42 A(K,J) = C
    4 CONTINUE
      IF (IT.LE.K) GOTO 5
      IC = ID(K)
      ID(K) = ID(IT)
      ID(IT) = IC
      DO 52 I=1,N
      C = A(I,IT)
      A(I.IT) = A(I,K)
   52 A(I,K) = C
    5 CONTINUE
  IF (A(K.K).EQ.0.) GOTO 120
      DO 7 J=KK,N2
      A(K,J) = A(K,J)/A(K,K)
      DO 7 I = KK.N
      W=A(I,K)*A(K.J)
      A(I,J) = A(I,J) - W
      IF (ABS(A(I,J)).GE.0.0001*ABS(W)) GOTO 7
      A(I,J) = 0.
    7 CONTINUE
      K=KK
      IF (K.LT.N) GOTO 2
      IF (K.GT.N) GOTO 120
      IF (A(N,N).EQ.0.) GOTO 120
      DO 9 J=NN,N2
    9 A(N,J) = A(N,J)/A(N.N)
      N1 = N-1
      DO 10 M=1,N1
      I = N-M
      II= I+1
      DO 10 K=II,N
      DO 10 J=NN,N2
   10 A(I.J) = A(I.J) - A(I,K)*A(K,J)
      DO 11 I=1,N
      DO 11 J=1,N
      IF (ID(J) .NE. I) GOTO 11
      DO 112 K=NN,N2
  112 F1(I,K-N) = A(J.K)
   11 CONTINUE
      IERR = 0
      RETURN
  120 IERR = 1
      RETURN
      END
```

APPENDIX V

DOUBLE PEAK GAUSSIAN FITTING PROGRAM

```
C  THIS IS A PROGRAM TO TAKE A RANGE OF DATA FROM C2 DIFFRACTION PATTERN
C  AND FIT WITH A GAUSSIAN FUNCTION.
   DIMENSION X(100), Y(100), D(100), PARMS(4)
   DIMENSION C(6), F1INV(6,6), CERR(6)
   OPEN (UNIT=1,FILE='c:PRITI2.IN', STATUS='OLD')
   OPEN (UNIT=2,FILE='c:PRITI2.PRN',STATUS='UNKNOWN')
   open (unit=3,file='c:PRITI2.OUP',status='unknown')
C  INITIAL GUESSES OF PEAK POSITIONS
   WRITE(*,*) 'INITIAL GUESSES OF DOUBLET ANGLES      '
   WRITE(*,*) 'FIRST PEAK                       '
   READ (*,*) C3
   WRITE(*,*) 'SECOND PEAK                       '
   READ (*,*) C4
   CAVG = (C3+C4)/2.
C  ANALYZE SPECTRA UNTIL EOF
  1 CONTINUE
C  INPUT THE DATA FROM DISKETTE OR HARD DISK FILE, AND MODIFY IT INTO (X,Y) FORM
C  ALSO KEEP TRACK OF THE VARIOUS EXPERIMENTAL PARAMETERS FOR THIS RUN SUCH
C  RUN#, XPOS, YPOS WHICH ARE NECESSARY FOR OUTPUT FILE. NX IS THE NUMBER OF
C  EXPERIMENTAL DATA POINTS TO BE FIT.
CALL DATAIN (X,Y,NX,PARMS,AMON,IMDONE,IERR,CAVG)
   IF (IMDONE.EQ.1) GOTO 999
   IF (IERR.EQ.1) GOTO 990
C  CALCULATE INITIAL VALUES OF THE COEFFICIENTS OF THE MODEL FUNCTION
C  REPRESENTING THE PEAK DATA. (THE MODEL IS A GAUSSIAN SUPERIMPOSED ON A
C  SLOPED BACKGROUND: HENCE THE COEFFICIENTS ARE THE GAUSSIAN AMPLITUDE,
C  MEAN SIGMA, AND THE LINE SLOPE AND Y INTERCEPT, LABELLED C(1) THROUGH C(5)
C  RESPECTIVELY. RETURNS AN ERROR FLAG IF THE DATA IS NOT LIKELY TO BE WELL
C  ANALYSED BY A GAUSSIAN,.EG NO DISCERNIBLE PEAK AGAINST BACKGROUND
   C(3)=C3
   C(4)=C4
```

```
      CALL PREFIT (C,X,Y,NX,IERR)
      IF (IERR.EQ.1) goto 990
C  REFINE THESE ESTIMATES OF THE COEFFICIENTS OF THE MODEL FUNCTION USING
C  A LEAST-SQUARES PROCEDURE (NEWTON-RAPHSON SOLUTION). THIS YIELDS THE
C  BEST MODEL FUNCTION, D, AND A FINAL INVERSE MATRIX USED FOR UNCERTAINTY
C  ESTIMATES, F1INV. IF THE N-R MATRIX CANNOT BE INVERTED, FLAG IERR IS SET TO 1.
CALL REFINE (C,X,Y,D,F1INV,NX,IERR)
      IF (IERR.EQ.1) GOTO 900
C  CALCULATE UNCERTAINTIES ASSOCIATED WITH FINAL VALUES OF THE COEFFS, AND
C  THE GENERAL QUALITY OF FIT OF THE MODEL TO THE DATA, CHI.
      CALL UNCERT (Y,D,F1INV,CERR,CHI,NX)
C  OUTPUT RESULTS IN THE FORMAT REQUIRED FOR THE SPREADSHEET PROGRAM.
      CALL DATOUT (X,Y,D,NX,C,CERR,CHI,PARMS,AMON)
      GOTO 1
  900 CONTINUE
      WRITE (*,500) PARMS(1)
  500 FORMAT(' RUN# ',F8.0,'  ***** MATRIX NOT INVERTIBLE *******')
      GOTO 1
  990 CONTINUE
      WRITE(*,555) PARMS(1)
  555 FORMAT(' RUN# ',F8.0,'  DATA NOT SUITABLE FOR GAUSSIAN FIT')
      GOTO 1
C  END-OF-FILE ENCOUNTERED. STOP PROGRAM
  999 CONTINUE
      WRITE(*,550)
  550 FORMAT(' END OF FILE FOUND... STOP')
      CLOSE(1)
      CLOSE(2)
      STOP
      END
SUBROUTINE DATAIN (X,Y,NX,PARMS,AMON,IMDONE,IERR,CAVG)
      DIMENSION X(100),Y(100),PARMS(4),YIN(800)
      IERR=0
      IMDONE=0
C  CLEAR OUT BLANK LINES, TRANS HEADER AND SPECTROMETER IDENTIFIER
      DO 11 K=1,4
      READ (1,*,END=999)
   11 CONTINUE
C  READ RUN NUMBER AND NUMBER OF DATA POINTS IN SCAN
      READ (1,480,END=999) INPT
  480 FORMAT(5X,I4)
C  CLEAR OUT MODE LINE AND SPECTROMETER SETUP LINES
      DO 12 K=1,5
      READ (1,*,END=999)
   12 CONTINUE
C  READ phi1
      READ (1,461,END=999) PHI1
  461 FORMAT(31X,F8.3)
      DO 121 K=1,8
      READ (1,*,END=999)
  121 CONTINUE
C  READ TIME, MONITOR, TEMPERATURES
      READ (1,482,END=999) TIME,AMON,CTEMP, RTEMP
```

```
  482 FORMAT(15X,F5.0,F9.0,F10.4,F10.4)
      READ (1,*,END=999)
      PARMS(1) = INPT
      PARMS(2) = CTEMP
      PARMS(3) = RTEMP
      PARMS(4) = TIME
C  READ IN THE DATA
      READ (1,*,END=999) (YIN(K),K=1,800)
C  CORRECT THE BAD CHANNELS
      YIN(162) = (YIN(161)+YIN(163))/2.
      YIN(449) = (YIN(448)+YIN(450))/2.
      YIN(681) = (YIN(680)+YIN(682))/2.
C  EXTRACT THE PEAK OFF THE DIFFRACTION PATTERN
      ICENTR=(CAVG-PHI1)*10+1
      ILOW=ICENTR-20
      IHI =ICENTR+20
C  CONSTRUCT THE X,Y ARRAYS
      DO 15 I=ILOW,IHI
      K = (I-ILOW)+1
      X(K) = PHI1 + (ILOW+K-2)*0.1
   15 Y(K) = YIN(I)
      NX = 41
      RETURN
C  EOF FLAG SET IF END-OF-FILE WAS ENCOUNTERED
  999 IMDONE=1
      RETURN
      END
C SUBROUTINE PREFIT (C,X,Y,NX,IERR)
      DIMENSION C(6),X(100),Y(100)
      IERR=0
C  FIND THE MAXIMUM VALUE OF DATA Y, AND ITS POSITION
      YMAX=0.
      YMIN=1.0E6
      DO 10 I=1,NX
      IF (Y(I).LE.YMAX) GOTO 9
      YMAX=Y(I)
      INDX=I
    9 CONTINUE
      IF (Y(I).LT.YMIN) YMIN=Y(I)
   10 CONTINUE
      IF ((INDX.EQ.NX).OR.(INDX.EQ.1)) IERR=1
      IF (YMAX.LT.(1.2*YMIN)) IERR=1
      IF (NX.LT.10) IERR=1
      RETURN
      END
SUBROUTINE REFINE (C,VECX,VECY,VECD,F1INV,N,IERR)
      DIMENSION VECX(100),VECY(100),VECD(100)
      DIMENSION C(6),F(6),F1(6,6),F1INV(6,6),DF(6),DF1(6,6)
      SUMSAV=1.0E10
      IERR=0
      X0=VECX(1)
C  CLEAR NEWTON-RAPHSON FUNCTION, AND ITS DERIVATIVE WITH RESPECT TO COEFFS
    1 DO 10 I=1,6
```

```
    F(I)=0.
    DO 10 J=1,6
  10 F1(I,J)=0.
C  COMPOSE N-R FUNCTION, AND DERIVATIVE MATRIX BY SUMMING INCREMENTS
C  ARISING FROM EACH DATA POINT
    DO 20 I=1,N
    X=VECX(I)
    Y=VECY(I)
C  CALCULATE THE INCREMENTS OF F AND F1 FOR THIS, THE ITH DATA POINT AND THE
C  VALUE OF THE MODEL FUNCTION, D, FOR THE CURRENT VALUES OF THE COEFFS.
    CALL FINC (C,X,X0,Y,D,DF,DF1)
    VECD(I) = D
    DO 15 J=1,6
    F(J) = F(J) + DF(J)
DO 15 K=1,6
  15 F1(J,K) = F1(J,K) + DF1(J,K)
  20 CONTINUE
C  SEE IF SUM(F**2) IS SMALL ENOUGH SO THAT WE HAVE CONVERGENCE
    SUMF=0.
    DO 30 I=1,6
  30 SUMF = SUMF + (F(I)/F1(I,I))**2
    IF (SUMF.LT.1.E-6) RETURN
C  CONVERSELY, IF THERE WAS NO PROGRESS OVER THE LAST ITERATION, THEN QUIT
TEST=ABS((1.-SUMF/SUMSAV))
    IF (TEST.LT.0.001) RETURN
    SUMSAV=SUMF
C  IF FURTHER ITERATIONS ARE NEEDED, COEFF VALUES MUST BE UPDATED BY
C  INVERTING THE N-R MATRIX
    CALL MINV (F1,IERR)
    IF (IERR.EQ.1) RETURN
C  NEW COEFFS = OLD COEFFS - INV(F1) . F
C  (SAVE MATRIX INVERSE IN CASE THIS IS THE LAST ITERATION)
    DO 50 I=1,6
    CORR=0.
    DO 40 J=1,6
    F1INV(I,J)=F1(I,J)
  40 CORR = CORR + F1(I,J)*F(J)
  50 C(I) = C(I) - CORR/2.
    GOTO 1
    END
SUBROUTINE FINC (C,X,X0,Y,D,DF,DF1)
    DIMENSION C(6), DF(6), DF1(6,6), D1(6)
    CA1 =C(1)
    CA2 =C(2)
    CM1 =C(3)
    CM2 =C(4)
    CS  =C(5)
    CB  =C(6)
C  CALCULATE DERIVATIVES OF MODEL FUNCTION AT THIS X WITH RESPECT TO COEF (N)
    EXPARG= 0.5*((X-CM1)/CS)**2
    D1(1) = 0.
    IF (EXPARG.LT.20.0) D1(1) = EXP ((0.-EXPARG))
    D1(3) = CA1*D1(1)*(X-CM1)/CS/CS
```

```
    EXPARG= 0.5*((X-CM2)/CS)**2
    D1(2) = 0.
    IF (EXPARG.LT.20.0) D1(2) = EXP ((0.-EXPARG))
    D1(4) = CA2*D1(2)*(X-CM2)/CS/CS
    D1(5) = D1(3)*(X-CM1)/CS + D1(4)*(X-CM2)/CS
    D1(6) = 1.0
C   CALCULATE THE MODEL FUNCTION WITH PRESENT COEFFICIENTS
    D = CB + CA1*D1(1) + CA2*D1(2)
C   WEIGHT OF EACH CONTRIBUTION TO THE INCREMENT, AND WEIGHTED DIFFERENCE
C   BETWEEN DATA AND MODEL ARE:
    W = 1./(Y+1.)
    WDIFF = W*(D-Y)
C   CALCULATE THE INCREMENTS OF F
    DO 10 I=1,6
  10 DF(I) = WDIFF*D1(I)
C   CALCULATE THE INCREMENTS OF F1
    DO 20 I=1,6
    DO 20 J=I,6
  20 DF1(I,J) = W*D1(I)*D1(J)
C   COMPLETE THE SYMMETRIC MATRIX
    DO 30 I=1,5
    J1=I+1
    DO 30 J=J1,6
  30 DF1(J,I) = DF1(I,J)
    RETURN
    END
SUBROUTINE UNCERT (Y,D,F1INV,CERR,CHI,N)
    DIMENSION Y(100), D(100), F1INV(6,6), CERR(6)
    XN=N
    CHISQ=0.
    DO 10 I=1,N
  10 CHISQ = CHISQ + (Y(I) - D(I))**2/(Y(I)+1.)
    CHI = SQRT((CHISQ/(XN-6.)))
    DO 20 I=1,6
  20 CERR(I) = SQRT(F1INV(I,I))*CHI
    RETURN
    END
    SUBROUTINE DATOUT (X,Y,D,NX,C,E,CHI,PARMS,AMON)
    DIMENSION C(6), E(6), PARMS(4),X(100),Y(100),D(100)
C   SUM THE COUNTS OVER ALL CHANNELS
    SUM=0.
    DO 111 KN=1,NX
  111 SUM=SUM+Y(KN)
C   CONVERT AMPLITUDE TO INTEGRATED INTENSITY
    FCT=SQRT(6.283186)*C(5)
    C(1)=ABS((C(1)*FCT))/AMON*1.0E5
    E(1)=ABS((E(1)*FCT))/AMON*1.0E5
    C(2)=ABS((C(2)*FCT))/AMON*1.0E5
    E(2)=ABS((E(2)*FCT))/AMON*1.0E5
    C(6)=C(6)/AMON*1.0E5
    E(6)=E(6)/AMON*1.0E5
C   CONVERT SIGMA TO FWHM
    C(5)=ABS((2.35482*C(5)))
```

```
      E(5)=ABS((2.35482*E(5)))
      WRITE (2,500) (PARMS(I),I=1,4),(C(I),E(I),I=1,6),CHI
  500 FORMAT(' ',F10.0,3F10.2,13F10.4)
      WRITE(*,497) NX
  497 FORMAT (' NUMBER OF DATA POINTS =',I3)
C  PUT INPUT/OUTPUT DATA TO FILE
      WRITE(3,697) (PARMS(I),I=1,3)
  697 FORMAT('0',3F10.3)
      DO 10 K=1,NX
      WRITE(3,498) X(K),Y(K),D(K)
  498 FORMAT(' ',3F10.3)
   10 CONTINUE
      WRITE (*,501) PARMS(1),(C(I),I=1,5,2),CHI
  501 FORMAT(' RUN# INT MEAN FWHM CHISQ:',F8.0,4F10.4)
      RETURN
      END
C  SUBROUTINE TO INVERT A 6X6 MATRIX F1. RETURNS INVERTED MATRIX IN ORIGINAL
C  SPACE OF F1 AND SETS A FLAG (IERR=1 IF MATRIX SINGULAR, 0 IF INVERSION SUCCESS)
      SUBROUTINE MINV (F1,IERR)
      DIMENSION F1(6,6), A(6,12), ID(6)
      N=6
      NN=N+1
      N2=2*N
      DO 200 I=1,N
      DO 200 J=1,N
  200 A(I,J)=F1(I,J)
      K=1
      DO 1 I=1,N
      DO 1 J=NN,N2
    1 A(I,J) = 0.
      DO 21 I=1,N
      A(I,N+I) = 1.
   21 ID(I) = I
2     CONTINUE
      KK = K+1
      IS = K
      IT = K
      B = ABS (A(K,K))
      DO 3 I = K,N
      DO 3 J = K,N
      IF (ABS(A(I,J)).LE.B) GOTO 3
      IS = I
      IT = J
      B = ABS(A(I,J))
    3 CONTINUE
      IF (IS.LE.K) GOTO 4
      DO 42 J=K,N2
      C=A(IS,J)
      A(IS,J) = A(K,J)
   42 A(K,J) = C
    4 CONTINUE
      IF (IT.LE.K) GOTO 5
      IC = ID(K)
```

```
    ID(K) = ID(IT)
    ID(IT) = IC
    DO 52 I=1,N
    C = A(I,IT)
    A(I,IT) = A(I,K)
  52 A(I,K) = C
   5 CONTINUE
IF (A(K,K).EQ.0.) GOTO 120
    DO 7 J=KK,N2
    A(K,J) = A(K,J)/A(K,K)
    DO 7 I = KK,N
    W=A(I,K)*A(K,J)
    A(I,J) = A(I,J) - W
    IF (ABS(A(I,J)).GE.0.0001*ABS(W)) GOTO 7
    A(I,J) = 0.
   7 CONTINUE
    K=KK
    IF (K.LT.N) GOTO 2
    IF (K.GT.N) GOTO 120
    IF (A(N,N).EQ.0.) GOTO 120
    DO 9 J=NN,N2
   9 A(N,J) = A(N,J)/A(N,N)
    N1 = N-1
    DO 10 M=1,N1
    I = N-M
    II= I+1
    DO 10 K=II,N
    DO 10 J=NN,N2
  10 A(I,J) = A(I,J) - A(I,K)*A(K,J)
    DO 11 I=1,N
    DO 11 J=1,N
    IF (ID(J) .NE. I) GOTO 11
    DO 112 K=NN,N2
  112 F1(I,K-N) = A(J,K)
  11 CONTINUE
    IERR = 0
    RETURN
```